



UNIVERSITÀ
DEGLI STUDI
FIRENZE

DOTTORATO DI RICERCA IN SCIENZE CHIMICHE

CICLO XXXV

COORDINATORE Prof. Anna Maria Papini

*THE NANO-BIO INTERFACE AS A PLATFORM FOR TECHNOLOGICAL
APPLICATIONS*

Settore Scientifico Disciplinare CHIM/02

Dottorando

Dott. Jacopo Cardellini

(firma)

Tutore

Prof. Berti Debora

(firma)

Co-tutore

Prof. Marco Laurati

(firma)

Coordinatore

Prof. Papini Anna Maria

(firma)

Anni 2019/2022

ABSTRACT

Despite the potentially revolutionary impact of the use of nanomaterials in medical applications, the number of nanoparticles (NPs) approved for clinical trials is still very limited. This limitation is also attributed to a lack of fundamental knowledge on the biological fate of NPs once introduced in the complex and heterogeneous environment of living systems. To fill this gap, a vast research area focuses on disentangling the intricate nature of the nano-bio interface, i.e., the interface between NPs and biological systems, to predict the NPs' biological impact and potential cytotoxicity. With this purpose, synthetic lipid membranes rapidly emerged as biomimics to study the nano-bio interface in simplified and controlled conditions, providing a simplistic yet comprehensive understanding of membrane-related phenomena.

In this field, recent reports showed that citrate-capped gold nanoparticles (AuNPs) spontaneously aggregate on synthetic zwitterionic membranes with a membrane-templated process dependent on the rigidity of the membranes and the surface functionalization of the inorganic NPs. Despite the potential relevance of this peculiar aggregative phenomenon, its mechanistic and kinetic aspects were not completely understood. In the present thesis, the interaction between citrated inorganic nanoparticles and synthetic and natural membranes was thoroughly investigated, aiming at: i) contributing to improving the fundamental knowledge on the nano-bio interface; ii) designing straightforward approaches for the synthesis of novel engineered hybrid nanomaterials; iii) demonstrating that the NPs-membrane interaction can be exploited for the characterization of free-standing vesicles and inorganic NPs-vesicles hybrids.

Accordingly, the first section of this work focuses on unveiling the roles of viscoelastic properties of bilayers as well as the chemical nature of the particles in the membrane-templated aggregative phenomenon. Then, in the second section we demonstrate that the plasmonic properties of AuNPs can be conveniently exploited as nanoprobe for determining the stiffness of synthetic and natural vesicles and estimating the extent of lipid coverage of membrane-camouflaged NPs for targeted nanomedical applications. Finally, the last part of the work shows that magneto-plasmonic citrated NPs can be easily combined with liposomes through spontaneous self-assembly to produce multifunctional materials which combine the properties of inorganic particles with the biocompatibility of lipid scaffolds.

In conclusion, the results presented in this work provide an overall description of the association of citrated NPs with lipid structures, shedding light on the main energetic contributions that drive the interaction and demonstrating its technological relevance, paving the way for the development of novel strategies for the production and characterization of nanomaterials.

List of Publications

Contributions included in this thesis:

Membrane Phase Drives the Assembly of Gold Nanoparticles on Biomimetic Lipid Bilayers (Paper I)

Jacopo Cardellini, Lucrezia Caselli, Enrico Lavagna, Sebastian Salassi, Heinz Amenitsch, Martino Calamai, Costanza Montis, Giulia Rossi, and Debora Berti, *J. Phys. Chem. C* 2022, 126, 9, 4483–4494.

Lipid-polymer assemblies as biomimetic platforms for the spontaneous clustering of AuNPs (Paper II)

Jacopo Cardellini*, Arianna Balestri*, Luca Comparini, Costanza Montis, Debora Berti (*equally contributed) (Manuscript in preparation)

Interaction of Metallic Nanoparticles With Biomimetic Lipid Liquid Crystalline Cubic Interfaces (Paper III)

Jacopo Cardellini, Costanza Montis, Francesco Barbero, Ilaria De Santis, Lucrezia Caselli, and Debora Berti, *Front. Bioeng. Biotechnol.* 2022; 10, 848687.

A plasmon-based nanoruler to probe the mechanical properties of synthetic and biogenic nanosized lipid vesicles (Paper IV)

Lucrezia Caselli, Andrea Ridolfi, Jacopo Cardellini, Lewis Sharpnack, Lucia Paolini, Marco Brucale, Francesco Valle, Costanza Montis, Paolo Bergese, and Debora Berti, *Nanoscale Horizons*, 2021, 6, 543–550.

Probing the coverage of nanoparticles by biomimetic membranes via nanoplasmonics (Paper V)

Jacopo Cardellini, Andrea Ridolfi, Melissa Donati, Valentina Giampietro, Mirko Severi, Marco Brucale, Francesco Valle, Paolo Bergese, Costanza Montis, Lucrezia Caselli, and Debora Berti (Manuscript in preparation)

Self-assembly of magneto-plasmonic NPs on synthetic vesicles: hybrid nanomaterials for medical applications (Paper VI)

Jacopo Cardellini, Alessandro Surpi, Beatrice Muzzi, Valentina Pacciani, Claudio Sangregorio, Costanza Montis, Alek Dediu, and Debora Berti (Manuscript in preparation)

Other contributions:

A Martini Coarse Grained Model of Citrate-Capped Gold Nanoparticles Interacting with Lipid Bilayers

Sebastian Salassi, Lucrezia Caselli, Jacopo Cardellini, Enrico Lavagna, Costanza Montis, Debora Berti, and Giulia Rossi, *J. Chem. Theory Comput.*, 2021, 17, 6597–6609.

Advanced Static and Dynamic Fluorescence Microscopy Techniques to Investigate Drug Delivery Systems

Jacopo Cardellini*, Arianna Balestri*, Costanza Montis, and Debora Berti, *Pharmaceutics*, 2021, 13.6: 861. (*equally contributed)

Link between Morphology, Structure, and Interactions of Composite Microgels

Rodrigo Rivas-Barbosa, José Ruiz-Franco, Mayra A. Lara-Peña, Jacopo Cardellini, Angel Licea-Claverie, Fabrizio Camerin, Emanuela Zaccarelli, and Marco Laurati, *Macromolecules* 2022, 55, 5, 1834–1843.

Compositional profiling of extracellular vesicles/lipoproteins mixtures by AFM nanomechanical imaging

Andrea Ridolfi, Laura Conti, Marco Brucale, Roberto Frigerio, Jacopo Cardellini, Angelo Musicò, Miriam Romano, Andrea Zandrini, Laura Polito, Greta Bergamaschi, Alessandro Gori, Costanza Montis, Lucio Barile, Debora Berti, Annalisa Radeghieri, Paolo Bergese, Marina Cretich, and Francesco Valle, *bioRxiv*, 2022.

Contents

Contents	5
1. Introduction	8
1.1 Gold Nanoparticles as prototypical inorganic nanoparticles.....	10
1.2 Lipid-based biomimetic interfaces	12
1.3 The nano-bio interface: Interaction between inorganic Nanoparticles and biomimetic membranes	15
1.3.1 Fundamental understanding of the nano-bio interface	17
1.3.2 Engineered NPs-lipid assemblies for technological purposes	20
2. Results	23
2.1 Interaction of inorganic NPs with model membranes	23
2.1.1 Interaction of AuNPs with zwitterionic lipid vesicles of different rigidity	23
2.1.2 Interaction of AuNPs with polymer-lipid hybrid vesicles with raft- like domains.....	32
2.1.3 Interaction of AuNPs and AgNPs with non-lamellar model membranes.....	39
2.2 Colorimetric assays for the characterization of lipid-based assemblies	46
2.2.1 AuNPs plasmonics to probe the rigidity of synthetic and biogenic vesicles.....	47
2.2.2 AuNPs plasmonics to estimate the lipid coverage of inorganic NPs	51
2.3 Hybrid lipid-inorganic functional Nanomaterials	58
2.3.1 Self-assembly of magnetoplasmonic NPs on synthetic liposomes	59
3. Conclusions	67
4. Methods	69
4.1 Small Angle X-ray Scattering	69
4.2 Dynamic Light Scattering.....	70
4.2 Zeta Potential.....	71
4.3 Quartz Crystal Microbalance With Dissipation Monitoring.....	72
4.4 Confocal Laser Scanning Microscopy	73
4.5 Atomic Force Microscopy	74

4.6 Computational Methods	75
4.7 Cryogenic electron microscopy.....	76
Bibliography.....	77

List of Abbreviations

AFM	Atomic Force Microscopy
AFM-FS	Force Spectroscopy-based
AgNPs	Silver Nanoparticles
AuNPs	Gold Nanoparticles
Cryo-EM	Cryogenic electron microscopy
DLS	Dynamic Light Scattering
DOPC	1,2-dioleoyl-sn-glycero-3-phosphocholine
DPPC	1,2-dipalmitoyl-sn-glycero-3-phosphocholine
DSPC	1,2-distearoyl-sn-glycero-3-phosphocholine
EVs	Extracellular Vesicles
GMO	Glycerol Monooleate
LSCM	Laser Scanning Confocal Microscopy
MD	Molecular Dynamics
NPs	Nanoparticles
POPC	1-Palmitoyl-2-oleoyl-sn-phosphocholine
QCM-D	Quartz Crystal Microbalance with Dissipation monitoring
SASA	Solvent Accessible Surface Area
SAXS	Small Angle X-ray Scattering
SiNPs	Silica Nanoparticles
SLB	Supported Lipid Bilayer
UV-Vis	UV-visible
2D	Two-dimensional
3D	Three-dimension

1. Introduction

Over the last decade, the impressive development of synthetic bottom-up strategies to produce nanostructured materials has boosted the use of nanomaterials in several applicative areas. Among the various fields, Nanomedicine emerges as one of the most promising ones, providing unparalleled benefits compared to traditional medicine.¹

The present medical methods, including surgery, chemotherapy, and radiation therapy, are generally characterized by significant side effects and involve typically invasive procedures, causing severe damage to healthy tissues or the immune system. In this context, the attractive promise of nanomedicine concerns the development of safer and more effective modalities for treating pathologies while minimizing side effects.^{2,3} With this purpose, nanoparticles (NPs) can be finely engineered with convenient physicochemical properties for precise medical treatments, tuning their stability to prolong the circulation in biological fluids and simultaneously improving their drug delivery characteristics and diagnostic and therapeutic abilities.³⁻⁵ However, despite the intense research in the field, the number of approved NP formulations in clinical trials is still poor and almost limited to lipid formulations.^{6,7} A significant factor contributing to the gap between the design/development of nanomaterials for nanomedicine applications and their translation into medical practice is the lack of fundamental knowledge of their behavior and fate in biological fluids and living organisms.⁸⁻¹⁰ Once introduced into a living system, nanostructured materials interact with proteins, membranes, cells, DNA, and other biomolecules and biological interfaces, undergoing several transformations that can affect their functionalities.¹¹

For this reason, a complete understanding of the interfacial interactions between the nanomaterial and the biological objects, i.e. the nano-bio interface, is required to improve both the safety and the efficiency of nanomaterials designed for biomedical applications.¹¹ In this thesis, the interactions between NPs and simplified biomimetic membranes have been investigated to improve the fundamental knowledge of the nano-bio interfaces and shed light on the main non-specific energetic

contributions that rule the NPs' fate in biological environments (**papers I, II, III**). From an applicative point of view, a comprehensive understanding of the interactions occurring at the nano-bio interface can be exploited for both the production of intelligent nanomaterials for nanomedical applications (**paper VI**) as well as for the development of colorimetric assays for the characterization of lipid-inorganic structures (**papers IV, V**), paving the way for new technologies in the biomedical field.

Among the vast library of nanomaterials, the present thesis is focused on metallic NPs (gold and silver nanoparticles, AuNPs and AgNPs, respectively), silica nanoparticles (SiO₂NPs), and magnetic NPs. Concerning the biomimetic interface, the most common lipid-based systems are considered in the form of lipid vesicles and supported lipid bilayers; however, more complex biomimetic interfaces are also studied, such as polymer vesicles, cubosomes, and extracellular vesicles.

1.1 Gold Nanoparticles as prototypical inorganic nanoparticles

Gold nanoparticles (AuNPs) represent one of the most important nanomaterials for biomedical applications.¹² They are easy to synthesize, and their size and morphology can be finely controlled from a few to several hundred nanometers.¹³ Typically, AuNPs are obtained from the reduction of gold salts, which starts the nucleation and growth of the particles. The high stability of gold makes AuNPs an excellent candidate to face the biological environment without undergoing significant modifications, such as dissolution and degradability due to the surrounding media. Although AuNPs are composed of an inert metal, biocompatibility studies must be performed to allow their safe and effective application.⁹ However, thanks to the well-known chemistry of gold, the AuNPs' surface chemistry can be specifically tailored, improving their biocompatibility, and introducing targeting properties while maximizing their stability.^{14,15} In the medical field, AuNPs are currently studied for imaging purposes. By properly functionalizing their surface, they can be preferentially directed and accumulated in specific tissues, providing high contrast for imaging techniques.^{16–18} AuNPs also represent a powerful tool for the photothermic treatment of cancer.^{19,20} They can adsorb and convert the incident radiation into thermal energy, locally increasing the temperature and provoking the necrosis of diseased cells.²¹ In their nanometric form, AuNPs absorb the visible light due to the resonance between the incident radiation and the frequency of oscillation of the conduction electrons across the particle. Such phenomenon, namely Localized Surface Plasmon Resonance (LSPR), which confers to the colloidal spherical gold its characteristic red color, is extremely sensitive to the particle size, surface functionalization, chemical environment, and aggregative state.^{22–24}

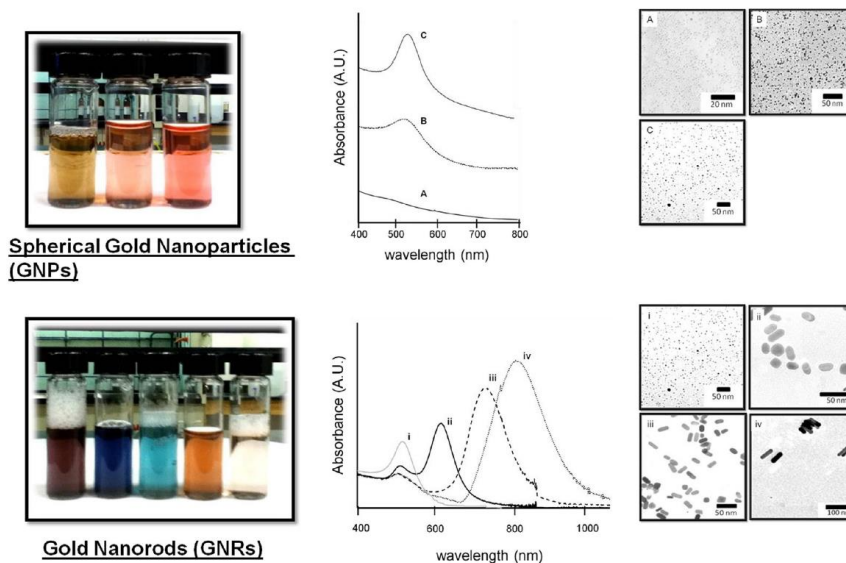


Figure 1.1: Gold nanoparticles possess size- and shape-dependent optical properties. (Top panel): Spherical gold nanoparticles (GNPs) of diameter 3 nm (A) are too small to support a plasmon band; GNPs of 5 (B) and 20 nm (C) possess a single plasmon absorption band. (Bottom panel): Gold nanorods (GNRs) possess two plasmonic absorption bands corresponding to the transverse and longitudinal dimensions of the rod. The longitudinal plasmon absorbance band is aspect ratio-dependent (i-iv). Reprinted with permission from ²⁵. Copyright 2013, American Chemical Society.

When the spacing between two particles is approximately lower than the particle's size, plasmons on distinct NPs reciprocally influence each other.²⁶ This “plasmon coupling” causes the change of the solution's color, which, depending on the fractality of the aggregate, is associated with the occurrence of a red-shifted shoulder to a new red-shifted peak, or the enlargement of the original signal in the UV-visible spectrum.^{27–29} The dependence of the SPR on the NP aggregative state, intensively investigated in the present thesis, makes the AuNPs optical variations a unique tool for monitoring their interactions in biological medium.³⁰ Altogether these properties make the AuNPs an ideal probe to investigate how the physicochemical properties of NPs (such as size, shape, and surface functionalization) affect their interaction with

biological barriers, contributing to disentangling fundamental aspects of the nano-bio interface.^{25,31}

1.2 Lipid-based biomimetic interfaces

Lipids are among the most abundant biomolecules in the composition of cell membranes. They are amphiphilic molecules characterized by hydrophilic and hydrophobic moieties. Depending on their molecular structure and environmental conditions, lipids in water self-assemble in different ordered geometrical structures.³² The architecture of the lipid assembly can be predicted using the so-called “critical packing parameter p ”, a geometrical parameter that considers the length (l) and the volume of the hydrophobic tails (v) and the area per polar head (a).

$$P = \frac{v}{a \times l} \quad (1.1)$$

Depending on the geometrical characteristics of lipids, the assembly could originate spherical micelles ($p \leq \frac{1}{3}$), non-spherical micelles ($\frac{1}{3} \leq p \leq \frac{1}{2}$), bilayer ($\frac{1}{2} \leq p \leq 1$), and inverted structures ($p > 1$).³³

This unique variety of liquid crystalline phases originating from lipid assembly results from the combination of hydrophobic forces and weak intermolecular interactions. Among the plethora of different structures arising from the extraordinary lipid polymorphism, lipid bilayers represent the simplest and most common outcome. Natural membranes are, for instance, heterogeneous lipid (and other biomolecules) assemblies, possessing a critical parameter close to 1, which mainly organize in lamellar structures composed of two lipid monolayers that separate and protect the inner environment (cytosol) and membrane-bound organelles. The structure of cell membranes can be synthetically mimicked by a wide variety of lamellar structures such as free-standing vesicles (liposomes), supported planar bilayer (SLB), vesicles on planar support, and unsupported planar bilayer (figure 1.2)^{34–37}.

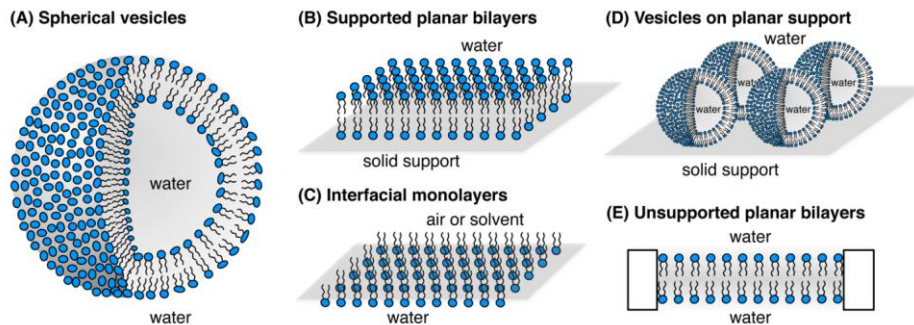


Figure 1.2: Schematic representation of biomimetic membranes: (A) spherical vesicles (dispersed), (B) supported planar bilayers, (C) interfacial monolayers, (D) vesicles on planar supports, and (E) unsupported planar bilayers (i.e., spanning an orifice). Spherical vesicles (A) can consist of freestanding bilayers, bilayers supported on microparticles or nanoparticles, or intact vesicles deposited on supports (D). Reprinted with permission from³⁵. Copyright 2014, American Chemical Society.

Liposomes are phospholipid vesicles characterized by a bilayer that separates the aqueous core from the external environment.^{38–40} Thanks to their ability to solubilize both hydrophobic -in the bilayer- and hydrophilic -in the aqueous core- molecules, as well as to their highly biocompatible composition, facilitating the cargo transport through membranes, liposomes are commonly used in cosmetics and pharmaceutical formulation as powerful drug carriers with precise control of the cargo release. For instance, depending on their lipid compositions, membranes exhibit a characteristic phase transition occurring at different melting chain temperatures T_m .⁴¹ Below the T_m , lipids are orderly packed together due to the van der Waals attraction between the hydrophobic tails, constituting a rigid membrane (gel phase). Above the T_m , the fluidity of the membranes increases, and lipids exhibit high lateral and inter-layer mobility (fluid or liquid-crystalline phase). Since during the phase transition, the permeability of the membranes increases, causing the release of encapsulated molecules, the temperature can be exploited as an external stimulus for the controlled release in drug delivery applications.^{42–44} Furthermore, this physical state of the membranes, which in turn affects the bilayer bending elasticity, i.e., the energy cost required to modify the natural curvature

of the membrane in response to an external stimulus, plays a crucial role during the interaction with nanoparticles and in internalization mechanisms.^{45–48}

In addition, as demonstrated in a recent work, synthetic lamellar lipid assembly can be used for mimicking the non-specific interaction between inorganic NPs and natural cells. Montis et al., testing the interaction of a library of AuNPs with different sizes, shapes, charges, and surface coating with both synthetic giant unilamellar vesicles and eukaryotic cells, highlighted that biomimetic membranes represent reliable but simple models to investigate and predict the outcome of the interaction between inorganic nanoparticles and cell membranes.^{49,50}

In the present work (**papers IV and V**), liposomes have been used as a simplistic model of Extracellular Vesicles (EVs), i.e., lipid vesicles naturally secreted by cells, currently considered fundamental vectors in intercellular communication.

More recently, block-copolymer-composed artificial vesicles and hybrid lipid-polymer vesicles emerged as powerful tools both as drug delivery platforms, addressing several drawbacks of pure lipid assemblies, such as limited long-term stability and low mechanical resistance, as well as from a biomimetic standpoint.^{51,52} Indeed, lipid-polymer hybrid scaffolds allow generating complex organized domains with different fluidity, resembling raft-like patches, i.e., micro- and nano-ordered immiscible domains with the surrounding liquid disordered phase, which mediate essential processes in cells, including mechanisms of internalization and production of biogenic vesicles, and act as sites for selective adsorption of particles.⁵³ In this context, here (**paper II**) lipid-polymer hybrid membranes have been used as mimetic scaffolds for improving our knowledge of the role of raft-like domains in the interaction with nanoparticles.

On the other hand, depending on composition, temperature, and concentration, lipids self-assemble into non-lamellar architectures featuring different degrees of complexity and symmetry^{54,55}. Among them, the so-called “cubic” structures, formed by folding a continuous lipid bilayer on gyroid (G), diamond (D), and primitive (P) periodic

minimal surfaces, are gaining growing interest in the formulation of drug carriers for nanomedical applications, thanks to their large surface-to-volume ratio as well as their ability to load a large number of hydrophilic molecules in the bicontinuous aqueous channels and hydrophobic molecules in the bilayer, providing stability and structural integrity for loaded cargo.^{56–58} Only recently, the biologically relevant nature of 3D cubic membranes, permanently or transiently occurring in cells under specific biological conditions (starvation, oxidative stress, viral infection, and other pathologies) and playing crucial roles in membrane fusion and fission, has been proved.^{59,60}

In this thesis (**paper III**), for the first time, synthetic cubic membranes have been prepared as a biomimetic platform to explore the specific behavior of naturally occurring non-lamellar membranes in the interaction with nanoparticles, thus contributing to improve our fundamental knowledge on the nano-bio interface.

1.3 The nano-bio interface: Interaction between inorganic Nanoparticles and biomimetic membranes

The biological fate of nanoparticles is determined by their interaction with biological interfaces in a biological medium, and, specifically, with cell membranes, the external envelope separating the internal cell compartmentalization from the environment.⁶¹ To address the biological impact of NPs, their behavior, and their relative cytotoxic effects, a deep understanding of NPs-membrane interactions is required.^{62,63}

Besides the nature and physico-chemical characteristics of NPs^{64–67}, the outcome of the NPs-membrane interaction can be affected by multiple parameters of cell membranes, such as the local curvature, elasticity, permeability, and the presence of segregated raft-like domains^{43,45,48,68–70}. In addition, the high heterogeneity in the composition of cell membranes (composed of thousands of different types of lipids, proteins, and carbohydrates non-homogeneously distributed in the membrane), resulting in the extreme variability of nanotoxicity and internalization

efficiency studies, highly complicates the prediction of NPs destiny.⁷¹⁻⁷³ Additionally, once introduced into biological fluids, the NP's surface is rapidly coated by a shell of proteins and other biomolecules, forming the so-called protein corona, which redefines the NPs' biological identity, including internalization processes and interaction mechanisms (figure 1.3).^{74,75}

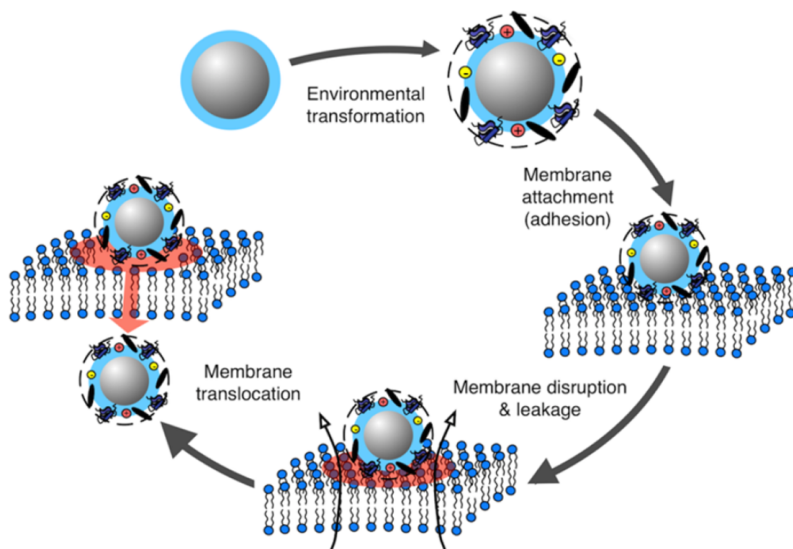


Figure 1.3: Schematic representation of the interaction of NPs with lipid membranes in biological fluids. Reprinted with permission from³⁵. Copyright 2014, American Chemical Society.

In this context, synthetic membranes, mimicking the size composition, and elastic and mechanical properties of natural membranes, rapidly emerged as fundamental tools to study the nano-bio interface in simplified conditions.⁷⁶ As mentioned, simpler lipid structures, such as liposomes, giant unilamellar vesicles, and supported lipid bilayers, can be prepared from biologically relevant lipids, disentangling the biological aspects of the interaction from the physicochemical ones and providing a simplistic yet comprehensive understanding of the membrane-related phenomena.⁷⁷

1.3.1 Fundamental understanding of the nano-bio interface

The interaction mechanism between NPs and membranes depends on the physicochemical features of both the inorganic object and the lipid scaffold. In a simplistic view, the non-specific NP-membrane interaction involves the NPs adhesion to the bilayer, the complete or partial wrapping of the NPs by the membrane, and the possible clustering of the NPs, which represent relevant phenomena in internalization mechanisms. In first approximation, the total interaction energy of the processes occurring at the nano-bio interface can be described by the following contributions:

$$E_{int} = E_{NP-NP} + E_{NP-m} + E_m \quad (1.2)$$

E_{NP-NP} accounts for the electrostatic and steric interactions between NPs and defines their colloidal stability. E_{NP-m} , which defines whether the adhesion of a NP on a membrane is thermodynamically favored ($E_{NP-m} < 0$), depends on the interaction energy between the particles and the lipid surface and can be evaluated according to the DLVO theory, as a combination of van der Waals (E_{vdw}) and electrostatic interactions (E_{el}). In the ideal case of a spherical NPs with radius R_1 interacting with a liposome with a radius R_2 and a thick shell h , the van der Waals contribution is given by:

$$E_{vdw} = -A \frac{R_1 R_2}{6(R_1 + R_2)} \left(\frac{1}{d} - \frac{1}{d+h} \right) - \frac{A}{6} \ln \left(\frac{d}{d+h} \right) \quad (1.3)$$

Where d is the distance between the two interacting surfaces and A is the Hamaker constant which can be either positive or negative, leading to attractive or repulsive energy, respectively. On the other hand, the electrostatic contribution between two unequal surfaces is approximately given by:

$$E_{el} = \frac{\varepsilon R_1 R_2 (\psi_1^2 + \psi_2^2)}{4(R_1 + R_2)} \left[\frac{2\psi_1 \psi_2}{\psi_1^2 + \psi_2^2} \ln \left(\frac{1+e^{-kd}}{1-e^{-kd}} \right) + \ln (1 - e^{-2kd}) \right] \quad (1.4)$$

That can be either positive or negative depending on the surface potentials ψ_1 and ψ_2 and the Debye length k .

E_m represents the energy cost required to the membrane to wrap the NPs and depends on the physico-chemical properties of the bilayer, including its fluidity, spontaneous curvature, and bending modulus. This latter term, representing the membrane ability to bend, modifying its natural curvature, dominates the interactions when considering small NPs compared to the length scales of the membranes.

$$E_m \approx E_{be} = \int (2\kappa M^2 + \bar{\kappa}K) dA \quad (1.5)$$

Where A is the membrane area, M and K are the local mean and Gaussian membrane curvatures, κ the bending rigidity, and $\bar{\kappa}$ the Gaussian curvature modulus. Overall, the energetic balance between the adhesion energy, which is maximized by increasing the NP-membrane contact area, and the bending energy, define the interaction outcomes, ranging from the unwrapped to the fully wrapped NP conformation, leading to the NPs clustering and determining their cell internalization pathways.^{43,50,77}

An interesting example of NPs-membrane interaction conveniently exanimated to provide an overall description of the main contributions involved in the nano-bio interactions is the spontaneous association of Turkevich-Frens AuNPs on synthetic zwitterionic membranes.⁷⁸⁻⁸³ This work proposes that citrate-capped AuNPs aggregate on lipid bilayers as the result of a membrane-templated process dependent on the membrane rigidity and the NPs surface coating.^{78,79} The schematic representation of the theorized iterative interaction mechanisms is represented in figure 1.4 and can be summarized in the following steps:

- i) Adhesion, an AuNP adheres to the lipid bilayer due to van der Waals attractions.
- ii) Wrapping, the membrane bends (depending on the particle size and on the membrane bending modulus) around the particle to increase the contact area, leading to an irreversible ligand exchange and citrate release.
- iii) Citrate trail, the release of citrate provokes a transient local increase of the ionic strength.

- iv) Membrane-templated aggregation, the decrease of the electrostatic barrier, which stabilizes the particle, leads to the aggregation of neighboring NPs on the membrane.

Although this mechanism physicochemically explains the AuNPs clustering on zwitterionic membranes, a thorough mechanistic demonstration of the origin of this intriguing process, its dependence on the physical state of the membranes, and the physico-chemical characterization of the resulting suprastructures are still needed.

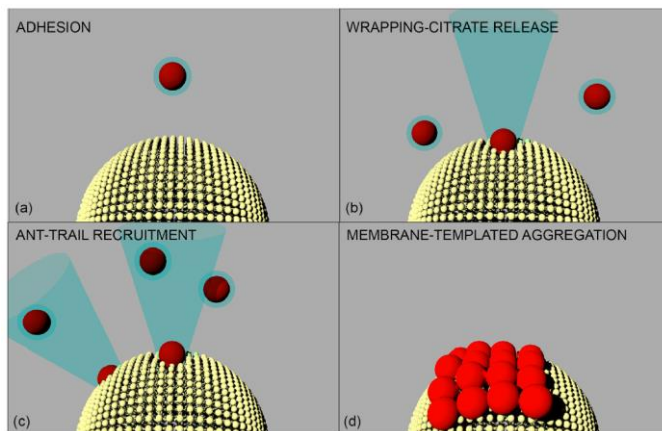


Figure 1.4: Mechanism of interaction between AuNP and the lipid membrane. (a) Adhesion-docking; (b) wrapping-ligand exchange; (c) citrate-trail recruitment (ant-trail); (d) membrane-templated aggregation. Reprinted with permission from ⁷⁸. Copyright 2020, Elsevier.

In this thesis, we investigate the self-assembly of citrate-capped NPs on lipid membranes over different time and length scales by combining complementary experimental and computational measurements (**paper I**). Moreover, to address the influence of raft-like domains (i.e. domains with different rigidities) on this membrane-templated phenomenon and on the resulting NPs-vesicle suprastructures, more complex hybrid lipid-copolymer-based assemblies have been employed as templating scaffolds for the particles' clustering (**paper II**). Finally, in the last part of this section, the influence of the NP core is addressed by monitoring the interaction of AuNPs and AgNPs with similar size and surface coating with cubic membranes, selected as an emergent mimic of bio-relevant lipid architectures (**paper III**).

1.3.2 Engineered NPs-lipid assemblies for technological purposes

From a general standpoint, the scarce applicability of inorganic NPs in medical practice can be related to their size range and exogenous nature, which trigger their recognition and uptake by macrophages, mediating host inflammatory and immunological biological responses. In this context, besides the necessity to understand the main energetic contributions which govern the nano-bio interface, the combination of inorganic nanoparticles with lipid membranes is instrumental to developing smart engineered nanomaterials which not only retain the inherent properties of each building block (biocompatibility of lipid scaffolds and electric, optical, magnetic, and catalytic properties of inorganic NPs) but also feature novel functionalities.⁸⁴⁻⁸⁶

Among the lipid structures, liposomes are the most exploited scaffolds for the preparation of hybrid materials, thanks to their already large success in pharmaceutical applications. Interfacing liposomes with inorganic NPs results in the production of biocompatible engineered nanomaterials for biological imaging, stimuli-triggered drug delivery, photothermal and hyperthermic therapies, sensing, and biolabeling.^{85,87} In these suprastructures, liposomes can bind hydrophilic particles to their shell, encapsulate them in the aqueous core and embed hydrophobic particles in the bilayer. Depending on the localization of the inorganic nanoparticles in the lipid assembly, the hybrids can be classified into different categories, rationally designed according to the final application (figure 1.5): i) liposomes with surface-bound NPs, ii) liposomes with bilayer-embedded NPs, iii) liposomes with core encapsulated NPs, and iv) lipid bilayer coated NPs.⁸⁵

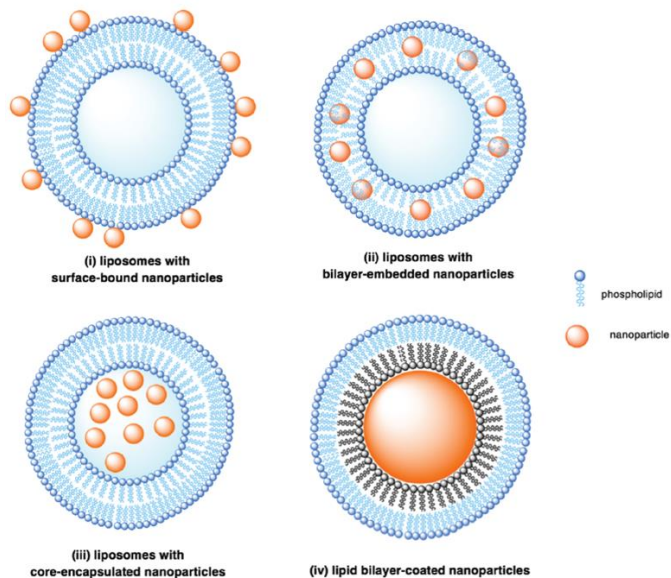


Figure 1.5: Illustration of the five classes of liposome-NPs hybrids: (i) liposomes with surface-bound nanoparticles, (ii) liposomes with bilayer-embedded nanoparticles, (iii) liposomes with core-encapsulated nanoparticles, and (iv) lipid bilayer-coated nanoparticles. Adapted with permission from⁸⁵. Copyright 2019, The Royal Society of Chemistry.

NPs embedded within the lipid bilayer or fully covered with synthetic or natural membranes circumvent the macrophage clearance, augmenting the circulation time and decreasing the probability of their non-specific uptake.^{88–90} Such membrane-camouflaged biomimetic hybrids retain the physicochemical properties of the inorganic hosts, providing at the same time specific molecular recognition and targeting, enhanced cell adhesion, and reduced toxicity thanks to the mediating action of the lipid bilayer.^{91,92} On the other hand, NPs bounded to the external liposomal shell can be used to stabilize the liposomes' dispersions, preventing their fusion thanks to the introduction of electrostatic repulsions.^{43,93,94} Additionally, the interaction with the bilayer can locally concentrate the NPs inducing novel collective properties and enhancing the material potentiality.^{49,84,86,95} In this context, recent works demonstrate the applicability of liposomes with surface-bounded NPs as biocompatible nanomotors or as practical nanomaterials for deep-tissue cancer immunotherapy.^{80,96}

Aiming at producing novel nanomaterials for medical applications, in the present thesis, we took advantage of the membrane-templated clustering of citrated NPs to associate magnetic-plasmonic NPs (AuMNPs) to lipid vesicles, forming hybrid suprastructures with controlled size, morphology, and colloidal stability which features enhanced magnetic properties compared to the starting unassembled objects (**paper VI**).

The interaction between NPs and lipid membranes can also be employed in analytical applications to get various kinds of qualitative and quantitative information. A prominent example is represented by the plasmonic properties of AuNPs, often used in colorimetric assays.^{97,98} As discussed in the previous section, citrate AuNPs aggregate on zwitterionic lipid membranes of synthetic and natural origin. The color of the dispersion changes depending on the extent of gold clustering. This peculiar behavior was exploited in colorimetric assays for determining both the concentration and purity of natural vesicle dispersion since the presence of proteins, or other biomolecules prevents gold aggregation and, accordingly, color variation.

In this context, we exploited the plasmonic properties of AuNPs and their characteristic assembly on synthetic and biogenic membranes to develop a plasmonic assay to estimate the rigidity of natural vesicles (**paper IV**). Additionally, such characteristic assembly was conveniently used to monitor the extent of lipid coverage of inorganic NPs during the production of membrane-camouflaged inorganic NPs for biomedical applications (**paper V**).

2. Results

2.1 Interaction of inorganic NPs with model membranes

The first part of this thesis focuses on the interaction between inorganic NPs and mimetic lipid systems aiming at improving our knowledge of the nano-bio interfaces and gaining novel insights to predict the biological fate of nanomaterials.

More specifically, this section deeply investigates the non-specific interaction occurring at the interfaces between synthetic zwitterionic membranes and citrated NPs, previously introduced in section 1.3. First (section 2.1.1), as detailed described in a recent publication (**paper I**), liquid-crystalline and gel phase liposomes have been selected to address, through experimental and computational tools, the effect of the membrane rigidity on the characteristic self-association of Turkevich-Frens AuNPs on the membrane of zwitterionic lipid vesicles. Then (section 2.1.2), in a study that is the subject of a manuscript in preparation (**paper II**), the investigation has been extended to synthetic membranes featured by raft-like domains with different rigidity; in this case, the investigation of NPs-hybrid membrane interaction is considered both from a fundamental perspective, to gain information on the nano-bio interfaces, and for applicative purposes, to unveil the main guidelines for the controlled production of smart vesicle-NPs suprastructures. Finally, the last part of this section (section 2.1.3) summarizes the results of a recent publication (**paper III**) where the role of the NP chemical nature in the interaction of citrate Au and AgNPs with lipid cubic interfaces has been addressed.

2.1.1 Interaction of AuNPs with zwitterionic lipid vesicles of different rigidity (Paper I)

First, we investigated the interaction between Turkevich-Frens gold nanoparticles and synthetic liposomes with different rigidities (see

materials and methods and supporting information sections of paper I for the liposomes and AuNPs preparation and characterization). The spontaneous association of 12 nm citrate-capped AuNPs on lipid vesicles was studied over different lengths- and time scales, starting from the very first AuNP-membrane contact, monitored through Molecular Dynamics Simulations performed in collaboration with the department of physics of the University of Genova. Then, the morphological characteristics of liposomes-AuNPs hybrids were assessed with cryogenic electron microscopy (Cryo-EM). Finally, the evolution of the AuNPs-liposomes suprastructures was monitored through UV-vis spectroscopy, Dynamic Light Scattering, and Small Angle X-ray Scattering, unveiling the kinetics of the AuNPs clustering on the lipid surface as a function of the membrane rigidity.

With these purposes, 1,2-Dioleoyl-sn-glycero-3-phosphocholine (DOPC) and 1-dipalmitoyl-sn-glycero-3-phosphocholine (DPPC) vesicles have been selected for their well-known different stiffness^{99–101}. As sketched in figure 2.1a, at room temperature in water, DOPC lipids self-assemble into soft and fluid phase bilayers, while DPPC lipids form rigid and gel phase bilayers.

The selected liposomes were challenged with the AuNPs dispersion. The UV-vis spectra reported in figure 2.1b were recorded after 10 minutes of incubation. The interaction of AuNPs with soft DOPC liposomes leads to the variation of the color of the colloidal gold dispersion from red to blue. As discussed in paragraph 1.1, this optical phenomenon, associated with the appearance of a red-shifted plasmonic peak, is determined by the coupling of the plasmonic signals of different AuNPs and highlights the AuNPs clustering. Conversely, the incubation with DPPC liposomes leads just to a slight bathochromic shift and broadening of the AuNPs original peak profile, highlighting that the AuNPs aggregation is highly inhibited on rigid membranes.

Direct images of the formed suprastructures were obtained by Cryo-EM imaging. The collected images, reported in figures 2.1c and 2.1d, show that AuNPs adhere to both DOPC and DPPC membranes without membrane disruption. However, the morphology of the structures is dramatically affected by the vesicle rigidity. Specifically, AuNPs

extensively aggregate on DOPC membranes forming densely packed clusters, in line with the plasmonic variation observed in the UV-vis spectrum. Moreover, almost all the objects appear as singles vesicles decorated by compact AuNPs aggregates (red arrows in figure 2.1c). On the other hand, AuNPs adhere to DPPC vesicles as separated particles with a larger average NP-NP distance. Additionally, the hybrids are connected to each other by AuNPs bridges, giving rise to micron-sized aggregates (figure 2.1d). In line with the UV-vis spectroscopy, this experimental evidence underlines that the membrane phase plays a pivotal role in AuNPs-vesicles interactions, leading to completely different hybrid morphologies.

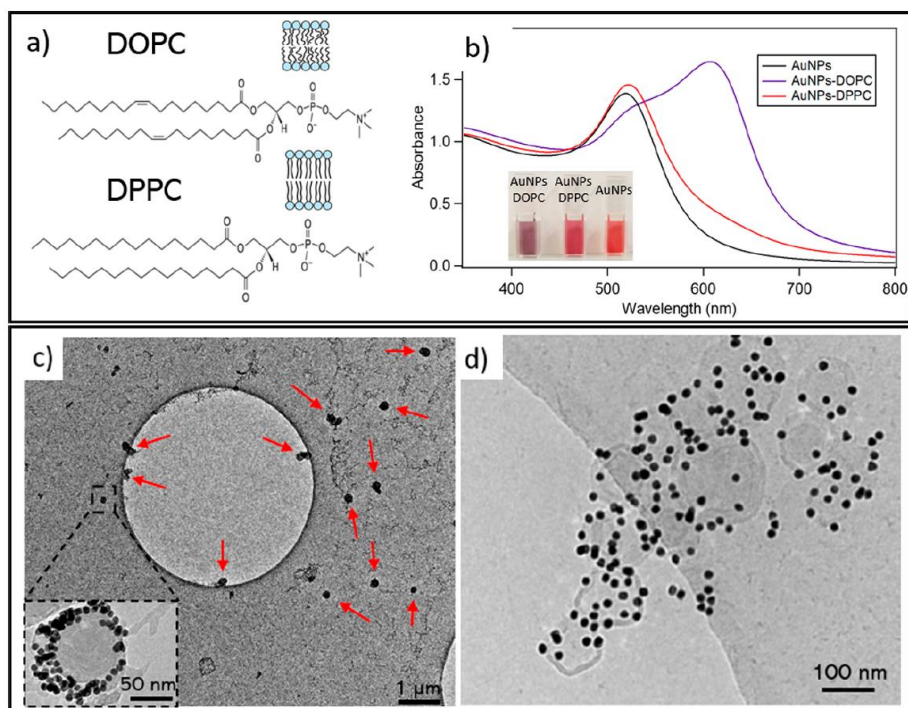


Figure 2.1: (a) Molecular structures of DOPC (1,2-dioleoyl-*sn*-glycero-3-phosphocholine) with a sketch of the fluid bilayer portion and DPPC (1,2-dipalmitoyl-*sn*-glycero-3-phosphocholine) with a sketch of the gel bilayer portion. (b) UV-visible spectra of AuNPs, AuNPs-DPPC hybrid, and AuNPs-DOPC hybrid collected after 10 min of incubation. Cryo-EM images of (c) AuNPs-DOPC composites and (d) AuNPs-DPPC composites.

AuNP-membrane first contact: MD simulation

To understand how the different behavior of AuNPs-vesicles originates at the molecular level, in collaboration with the department of physics of the university of Genova, we performed molecular dynamic (MD) simulations according to a recently developed coarse-grained model⁷⁹ (figure 2.2). The interaction of a single citrate-capped AuNP has been simulated with both DOPC and DPPC flat bilayers. On the DOPC membrane, the NP rapidly penetrates the bilayer. The NP is wrapped by the membrane until the formation of a complete bilayer around the particle, which provokes the fast release of citrate molecules toward the solution. On the other hand, the interaction of AuNPs with the gel phase DPPC bilayer is slower. In this case, the wrapping of the NP is irregular, the system dynamic slows down dramatically, and the simulation gets stacked at an intermediate state of NP penetration. The tables in the bottom panel of figure 2.2, which report the number of contacts between the citrate molecules and the NP, confirm the slower release of citrate from the gold surface after the interaction with the DPPC bilayer.

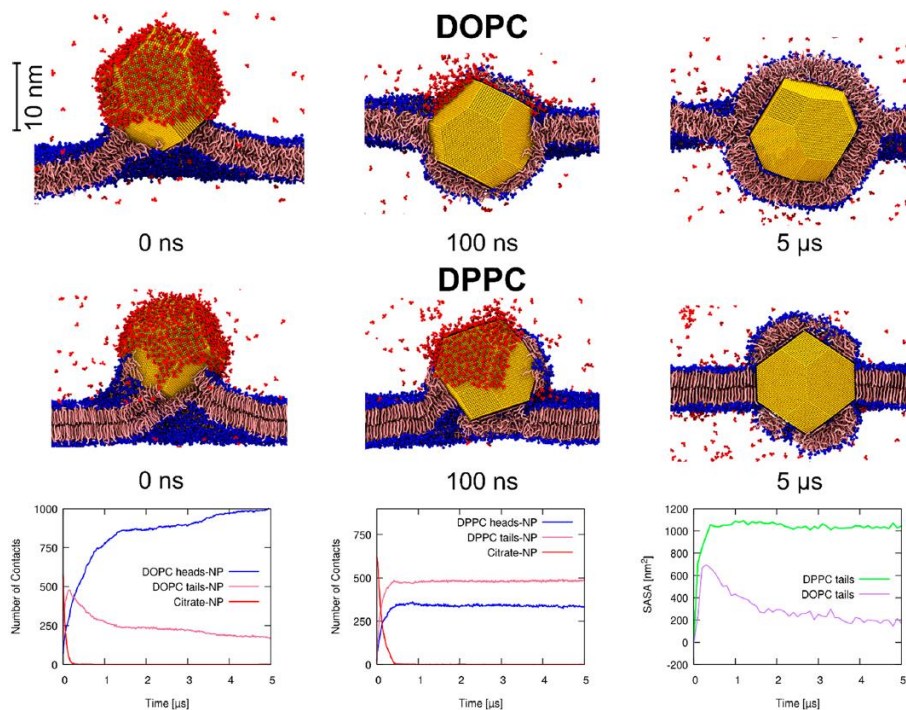


Figure 2.2: *Difference between the penetration process of a citrate AuNP in DOPC and DPPC flat bilayers. For each kind of bilayer, we show three snapshots at significant moments of the wrapping process, where the NP is represented in yellow, the citrate is represented in red, the lipid headgroups are represented in blue, and the lipid tails are represented in pink. In the bottom row, we show the time evolution of the number of contacts between the NPs and citrate molecules (in red), lipid headgroups (blue), and lipid tails (pink) for both simulations, in addition to the time evolution of the solvent accessible surface area (SASA) plots of the lipid tails. In the SASA plots, the area is set to 0 for the unperturbed membrane. Time $t = 0$ corresponds to the first NP– membrane contact. The time series are shown only up to $5.0 \mu\text{s}$ to better highlight the fast initial time evolution, although the simulations reached $10.0 \mu\text{s}$ in both cases.*

AuNP-vesicles: morphology of the aggregates

The temporal evolution of the AuNPs-vesicles hybrid structures following the first AuNP bilayer contact was investigated through UV-vis spectroscopy and high-resolution SAXS, monitoring the interaction during the first 10 minutes of incubation. Figure 2.3 reports the absorbance evaluated at 610 nm, the hallmark wavelength of the plasmonic signal of clustered NPs. The incubation of AuNPs with soft DOPC vesicles leads to the sudden absorbance increase associated with the appearance of a red-shifted shoulder, which becomes a well-defined secondary peak in a few seconds. In the case of DPPC, the signal manifests just a very modest increase, reasonably due to the variation of AuNPs chemical environment. The different AuNPs behavior can be considered as the outcome of the first AuNP-bilayer contact illustrated in the MD simulations. As hypothesized in paragraph 1.3⁷⁸, it's reasonable to assume that the gold clustering process is triggered by the release of citrate towards the surrounding aqueous medium. As shown here, the membrane rigidity modulates the ability of the bilayer to bend around the particles, leading to different kinetics of citrate release. Accordingly, on the DOPC membrane, the fast NP wrapping and citrate release can induce a transient local increase of the ionic strength and trigger AuNPs aggregation, while the more gradual citrate release in the case of DPPC extremely limits such NPs recruitment.

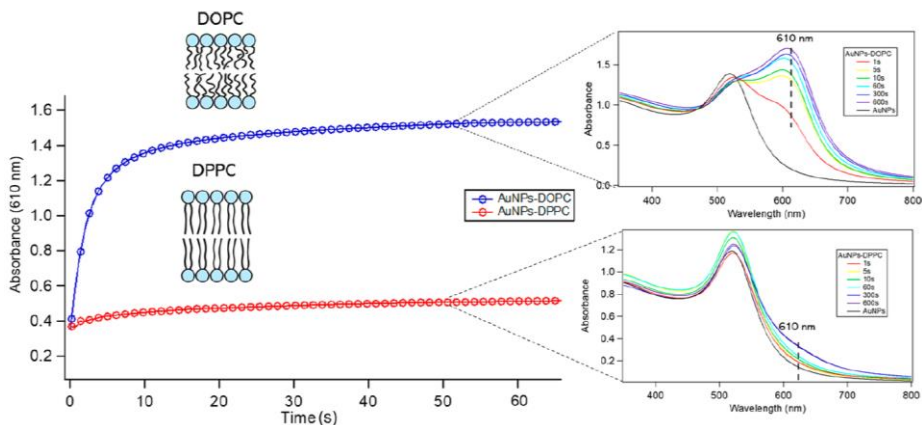


Figure 2.3: Time evolution of the absorbance of AuNPs-DOPC and AuNPs-DPPC aqueous dispersions (10 μ L of 12 nM DOPC or DPPC liposomal dispersions mixed with 300 μ L of 6.3 nM AuNPs) at 610 nm. The inset shows UV-visible absorption profiles of AuNPs-DOPC (top) and AuNPs-DPPC (bottom) collected after 1, 5, 10, 60, 300, and 600 s of incubation.

To determine the evolution of AuNPs-vesicles structures, we performed high-resolution SAXS. The collected scattering profiles are reported in figure 2.4. It's worth noticing that in our experimental conditions, the scattering signal of the vesicles is negligible, and each variation in the scattering curves is the result of the evolution of AuNPs cluster on the lipid surface (see figure S4 in the supporting information of paper I for details). From each spectrum, we extracted the structure factor $S(Q)$, reported in the insets of Figure 2.4, by dividing the measured scattered intensity of the hybrids by the profile of the AuNPs acquired at the same concentration (see Paper I for details). The $S(Q)$ peak position reflects the average distance between the particles. In line with cryo-EM images, for AuNPs-DOPC samples, the particles are in direct contact with each other. Additionally, the $S(Q)$ peak intensity increases with time, while its Q -position is time-invariant, indicating that AuNPs are already in contact 1 s after incubation and the number of aggregated particles gradually increases. On the other hand, regarding AuNPs-DPPC hybrids, the $S(Q)$ signal is just slightly visible, suggesting a minor AuNPs positional correlation.

Furthermore, the slope of the scattering profiles in the low Q region of the $I(Q)$ vs. Q plots can be associated with the dimensionality of the AuNPs cluster. In AuNPs-DOPC sample, the slope evolution suggests that the cluster becomes larger and more compact with time, passing from a 1D aggregate to a 2D aggregate (see paper I for details). This fast Kinect of the gold aggregation is in line with UV-vis results and is consistent with the hypothesis that the fluidity of the membranes controls AuNPs clustering.

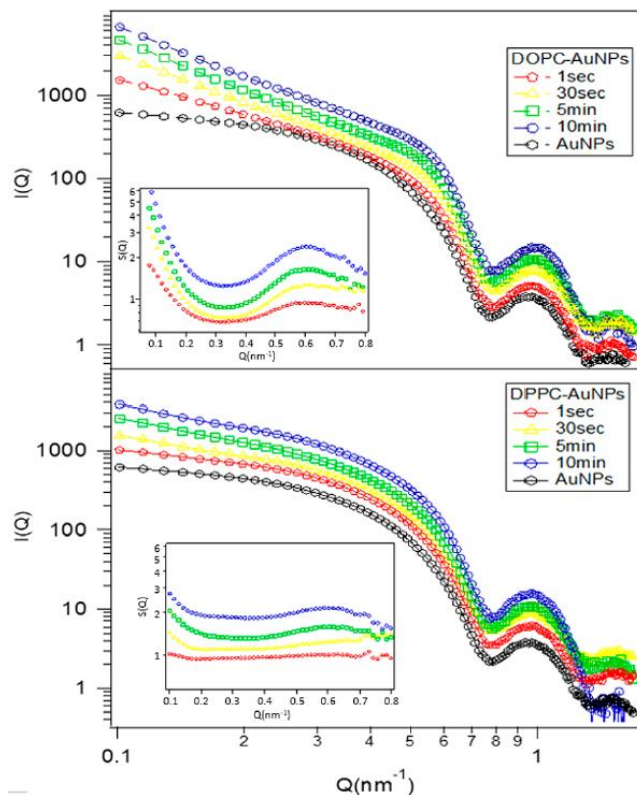


Figure 2.4: Log-log SAXS profiles of AuNPs-DOPC (top) and AuNPs-DPPC (bottom) hybrids collected after 1 s, 30 s, 5 min, and 10 min of incubation. The inset shows the structure factor $S(Q)$ of the samples, with correlation peaks related to the center-to-center interparticle distances.

AuNP-vesicles: colloidal stability

Finally, to shed light on the colloidal stability of the hybrid structures during the first hour of incubation, we performed Dynamic Light

Scattering measurements. Figure 2.5 (a,b,c) displays the normalized autocorrelation functions collected for DOPC-AuNPs and DPPC-AuNPs samples and the evaluated hydrodynamic diameters. As shown, the interaction of AuNPs with DOPC liposomes leads to the formation of metastable suprastructures of 180 nm in diameter. The evaluated size is consistent with the size of single liposomes surrounded by a AuNPs crust. Conversely, the interaction with rigid DPPC vesicles leads to the immediate destabilization of the system, forming micron-sized aggregates, which eventually precipitate as the result of an aggregative phenomenon where AuNPs act as bridging agents between the DPPC hybrids.

To address these dramatic differences in the colloidal stability, we performed ζ -potential measurements. As shown in figure 2.5d, DOPC and DPPC vesicles possess a slightly negative ζ -potential. After their incubation with the AuNPs dispersion, the ζ -potential decreases as a consequence of the particles adhesion to the lipid membranes. However, the ζ -potential of DOPC-AuNPs hybrids is significantly lower, justifying their enhanced colloidal stability. This difference can be related to the different number of particles adsorbed per vesicle. In a recent publication, Gradzielsky et al. proved that the adsorption of negatively charged silica NPs (SiNPs) on liposomes improves the electrostatic stabilization of the structures, increasing the electric charges on the lipid shell.⁹³ However, this enhanced colloidal stabilization is gained only due to the adsorption of a sufficient number of SiNPs. Conversely, when the number SiNPs on the membrane is lower, the system is highly destabilized, eventually leading to liposome bridging and rapid precipitation.^{102,103} Here, we can speculate that the high number of particles per DOPC vesicle is sufficient to electrostatically stabilize the hybrids. In the DPPC case, due to the lower number of AuNPs absorbed per vesicle, the electrostatic repulsion is not sufficient to overcome the attractive interaction between the hybrids, eventually causing the flocculation.

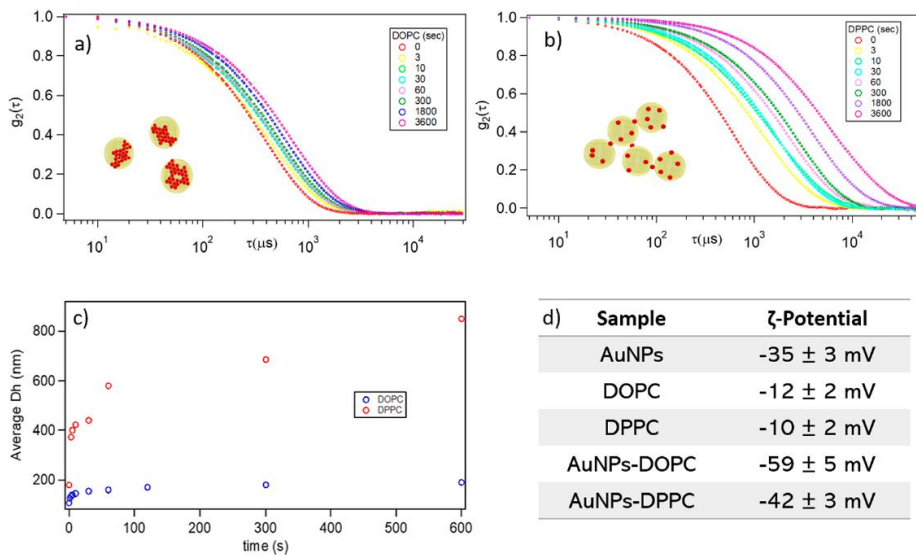


Figure 2.5: 10 μL of 12 nM DOPC or DPPC liposomal dispersions were mixed with 300 μL of 6.3 nM AuNPs and the hydrodynamic dimension of the hybrids was followed up to one hour. (a) Time evolution of the DLS curves of the AuNPs-DOPC hybrid. (b) Time evolution of the DLS curves of the AuNPs-DPPC hybrid. (c) Time evolution of the average hydrodynamic diameter evaluated by the DLS curves for AuNPs-DOPC and AuNPs-DPPC composites. (d) ζ -Potentials of citrate AuNPs, pure DOPC, and DPPC vesicles, and AuNPs-DOPC and AuNPs-DPPC hybrids.

Overall, the hypothesized interaction mechanism is schematized in figure 2.6. First, a AuNP adheres to the lipid membrane, undergoing a membrane-wrapping phenomenon that depends on the stiffness of the vesicle and on the physical state of the membrane (rigid gel phase or soft liquid-crystalline phase). Then, depending on the kinetics of citrate release from AuNP surface, the clustering on the lipid membrane of the neighboring particles can be triggered, leading either to the formation of AuNP clusters (on soft membranes) or to the separate adhesion of single AuNPs (on rigid vesicles). Finally, the resultant different number of particles per vesicle directly affects the colloidal stability of AuNP-lipid vesicle hybrids, forming metastable AuNP-decorated DOPC vesicles and extended DPPC aggregates bridged by AuNPs.

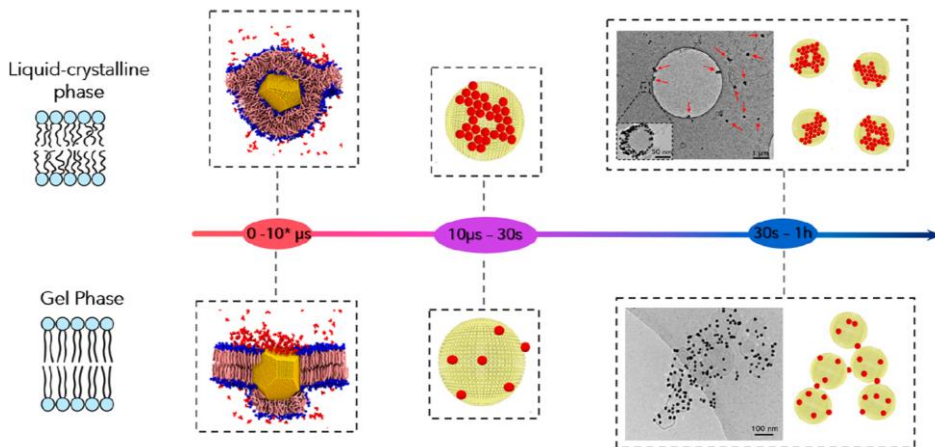


Figure 2.6: Schematic representation of the interaction mechanisms dependent on the vesicle rigidity. First, the adhesion of the particles and the citrate release occur. Second, the AuNPs in the proximity of the interaction site aggregate according to the kinetics of the citrate release. Finally, the hybrids evolve in single vesicles decorated by AuNPs or in flocculated objects where the particles act as a bridge. We remark that the simulated time scale ($10\ \mu\text{s}$) corresponds to $10\text{--}100\ \mu\text{s}$ in real time due to the acceleration of the dynamics that is intrinsic to the use of a coarse-grained model.

2.1.2 Interaction of AuNPs with polymer-lipid hybrid vesicles with raft-like domains (Paper II)

After investigating the interaction of AuNPs with simple zwitterionic lipid membranes, the study was extended to the interaction of AuNPs with more complex target membranes, i.e., hybrid lipid-polymer vesicles characterized by an interfacial membrane containing raft-like patches. The aim of this study is to explore, in simplified conditions, the effects of membrane domains with different rigidity on the nano-bio interactions.

In recent years, the combination of amphiphilic block copolymers and lipids has opened unexplored perspectives in the design of soft assemblies as model membranes.^{104,105} The inclusion of a polymer moiety in a lipid bilayer leads to the formation of complex membranes with nano- or micro-domains of different rigidities. From a simplistic

point of view, these patches resemble lipid rafts of cells that mediate fundamental functions in several biological processes.^{51,106}

In this section, we want to address the influence of raft-like domains with different rigidity in the interaction of copolymer-lipid hybrid vesicles with Turkevich-Frens AuNPs, aiming both at improving the fundamental knowledge of the peculiar aggregative phenomenon of citrated AuNPs on lipid interfaces and, from a technological point of view, at unveiling the main contributions which rule the formation of vesicles-AuNPs suprastructures. With this purpose, we selected as biomimetic membrane a hybrid platform composed of DPPC and poly(butadiene-*b*-ethylene oxide) (PBD-*b*-PEO), which associate in water forming lamellar structures featured by distinct rigid lipid- and soft copolymer-rich domains, as highlighted in a recent publication¹⁰⁶. The interaction of AuNPs with both the supported hybrid bilayers and the free-standing hybrid vesicles was followed through quartz crystal microbalance with dissipation monitoring (QCM-D), confocal laser scanning microscopy (CSLM), UV-vis spectroscopy, and Small-Angle X-rays Scattering (SAXS).

AuNP interaction with supported hybrid bilayers

DPPC SLBs and DPPC-PBD-*b*-PEO hybrid supported bilayers (DPPC PBD-*b*-PEO65%) were formed on a borosilicate coverglass according to a well-established protocol¹⁰⁷ and were labeled with two fluorescent probes with different affinity for the lipid and polymer phase and well-separated emission spectra (see paper II for details of the supported bilayers preparation). The AuNPs dispersion was added to the supported membranes, and the interaction was monitored after 5, 10, and 30 minutes through CLSM, collecting both fluorescence and transmission signals (figure 2.7a). After 5 minutes of incubation, the transmission signal shows the formation of AuNPs clusters on the hybrid bilayer, while small aggregates appear on the DPPC SLB only after 30 minutes, highlighting the slower dynamic of AuNPs clustering on the rigid membrane. This behavior was fully confirmed by QCM-D analysis by monitoring the mass of molecules and particles adsorbed on a hydrophilic quartz sensor by the variation in its resonance frequency (ΔF) (see materials and methods section of paper II for further details).

In fact, the injection of the AuNPs dispersion on both the pure lipid and hybrid supported bilayers provokes a decrease of the quartz crystal frequency shift ΔF , which is the hallmark for mass adsorption on the crystal. The extent of such variation can be directly related to the AuNPs adsorbed mass (figure 2.7b). As shown, the injection of AuNPs in the measurement chamber results in a much higher ΔF (in absolute value) on the DPPC PBD-b-PEO65%. By employing the Sauerbrey equation¹⁰⁸ (see materials and methods section of paper II for calculations), we estimated the adsorbed mass on the bilayer ($1523 \mu\text{g}/\text{cm}^2$ and $212 \mu\text{g}/\text{cm}^2$ on DPPC PBD-b-PEO65% and DPPC substrate, respectively). These results evidence how the presence of soft polymeric domains in the rigid lipid membrane strongly affects the interaction, promoting the AuNPs clustering.

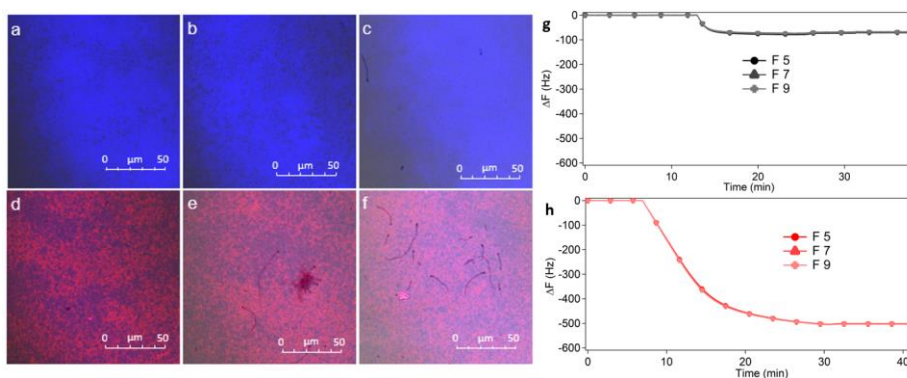


Figure 2.7: Confocal microscopy images of the interaction of 9.93 nM AuNPs with SLB of DPPC and DPPC PBD-b-PEO65%. a) DPPC SLB, image collected 5 minutes after the AuNPs incubation; b) DPPC SLB, image collected 10 minutes after the AuNPs incubation c) DPPC SLB, image collected 30 minutes after the AuNPs incubation; d) DPPC-PBD-b-PEO65% SLB, image collected 5 minutes after the AuNPs incubation, e) DPPC-PBD-b-PEO65% SLB, image collected 10 minutes after the AuNPs incubation, f) DPPC-PBD-b-PEO65% SLB, image collected 30 minutes after the AuNPs incubation. Merged channels PBD(1200)-b-PEO(600) + rhodamine excitation wavelength 561 nm, emission wavelength 571 nm-630 nm (red); β -bodipy excitation wavelength 488 nm, emission wavelength 488 nm-530 nm (blue) and transmission (greyscale). QCM measurements of the deposition of AuNPs' adsorption onto pure DPPC and hybrid DPPC PBD-

b-PEO65% supported bilayers. Frequency variation measured for 5th, 7th, and 9th harmonics (black-red lines, filled circles, and empty triangles). (g) deposition of AuNPs on the SLB of DPPC, AuNPs injection flow 0.1mL/min; (h) deposition of AuNPs on the DPPC PBD-*b*-PEO65% supported bilayer, AuNPs injection flow 0.1mL/min.

AuNPs interaction with free-standing hybrid vesicles

To further address the effect of soft polymer domains in the membrane-template AuNPs aggregation, we studied the interaction of AuNPs and free-standing vesicles with increasing polymer molar percentages (5%, 15%, 35%, 65%, 100%) at different vesicle/NPs ratios (vesicles/NPs ratios approximately 1/5, 1/10, 1/25, 1/50, 1/75, 1/125, 1/150, 1/200, 1/250, 1/350, 1/450, 1/550, 1/850, 1/1250, and 1/1450), monitoring the incubation through UV-vis spectroscopy and SAXS.

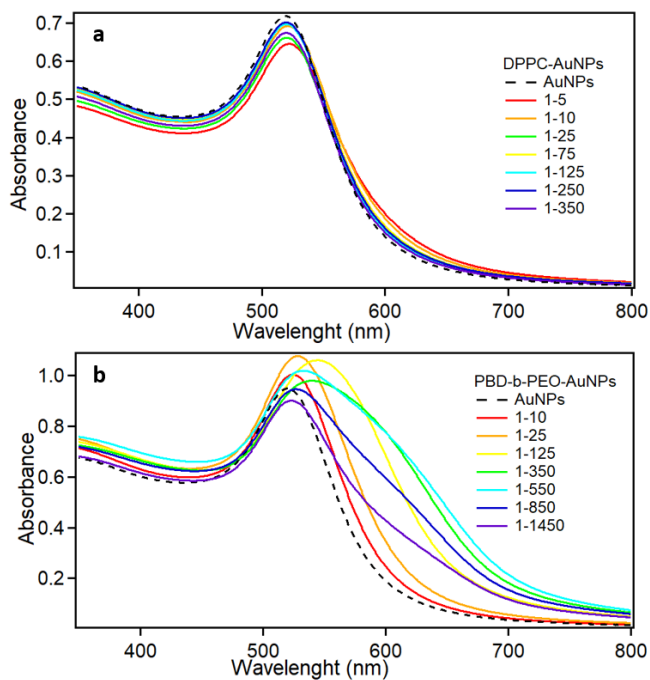


Figure 2.8: 300 μL of 9.93×10^9 M AuNPs was incubated with 10 μL of a) DPPC and b) PBD-*b*-PEO vesicles in the following vesicles/NPs ratios: 1/5, 1/10, 1/25, 1/50, 1/75, 1/125, 1/150, 1/200, 1/250, 1/350, 1/450, 1/550, 1/850, 1/1250, and 1/1450.

As observed in section 2.1 and figure 2.8a, the interaction of AuNPs with DPPC vesicles provokes negligible effects on the original AuNPs plasmonic peak, clearly due to the elevated membrane rigidity. On the contrary, upon incubation with pure PBD-b-PEO vesicles, an immediate color change is visible to the naked eye (from red to purple-blue), associated with the broadening of the plasmonic peak as a consequence of the plasmon coupling of proximal NPs (figure 2.8b), the clear outcome of AuNPs clustering. Importantly, such plasmonic variations are strictly related to the vesicle/AuNPs ratio with a non-monotonic behavior. First, the decrease of the vesicle/AuNPs ratio leads to a progressive enlargement of the plasmonic peak until a maximum (vesicle/AuNPs number ratio approximately 1/550, light blue line in figure 2.8b). Then, a further increase of the NPs number provokes the recovery of the original plasmonic feature. Interestingly, the same non-monotonic trend in the AuNPs aggregation was noticed for the DPPC - PBD-PEO hybrid vesicles (see supporting information of paper II for the UV-vis spectra). To better comprehend this result, we used an aggregation index “A.I.” as the descriptor of the AuNPs aggregation, obtained as follows:

$$A.I. = \frac{Abs_{max} - Abs_{600}}{\Delta\lambda} \quad (2.1)$$

Where Abs_{max} is the absorbance of the plasmonic peak of bare AuNPs, generally located at about 520 nm, Abs_{600} is the absorbance at 600 nm, the hallmark wavelength of AuNPs clusters formation, and $\Delta\lambda$ is the difference between the two plasmonic signals. The A.I.s calculated for each UV-Vis spectrum are then normalized with the one calculated for the bare AuNPs. Accordingly, the A.I. value of bare AuNPs is always equal to 1, and the A.I. decreases with increasing aggregation extent (see paper II for details). Figure 2.9 shows the variation of A.I. versus the vesicle/AuNPs ratio. Clearly, increasing the polymer content in the vesicles formulations results in the shift of the maximum aggregation of AuNPs (i.e., the minimum point in the A.I. vs. vesicle/NP plots) to lower vesicles/AuNPs ratios (values highlighted in the boxes in figure 2.9), underlying the dramatic effect of the PBD-b-PEO content on AuNPs aggregation.

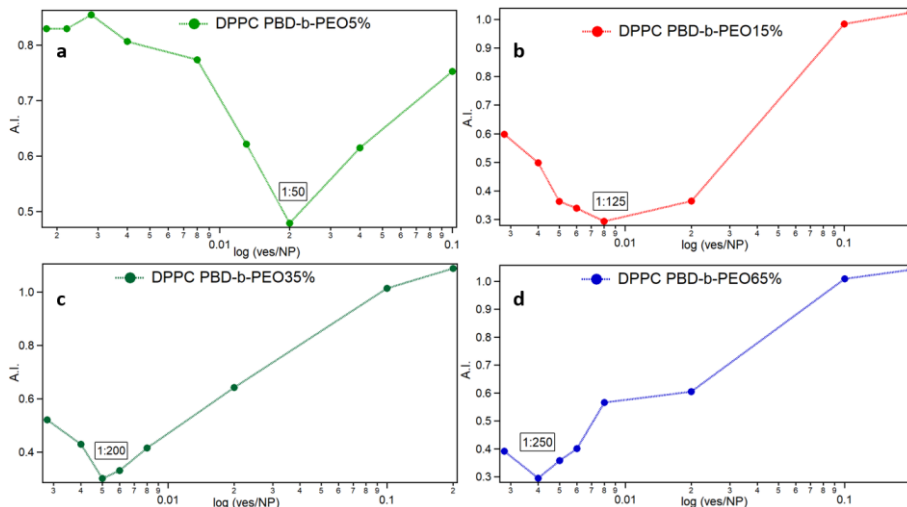


Figure 2.9: 300 μL of 9.93×10^{-9} M AuNPs were incubated with 10 μL of vesicles in the following vesicles/NPs ratios: 1/5, 1/10, 1/25, 1/50, 1/75, 1/125, 1/150, 1/200, 1/250, 1/350, 1/450, 1/550, 1/850, 1/1250, and 1/1450. a) A.I. vs $\log(\text{vesicle/NP})$ plot for DPPC PBD-b-PEO5%, b) A.I. vs $\log(\text{vesicle/NP})$ plot for DPPC PBD-b-PEO15%, c) A.I. vs $\log(\text{vesicle/NP})$ plot for DPPC PBD-b-PEO35%, d) A.I. vs $\log(\text{vesicle/NP})$ plot for DPPC PBD-b-PEO65%, e) A.I. vs $\log(\text{vesicle/NP})$ plot for PBD-b-PEO.

To further explore this phenomenon and gain information on the structure of the AuNPs aggregates, we performed SAXS measurements (figure 2.10). In our experimental conditions, the SAXS signal only originates from the scattering of AuNPs, while the contribution of vesicles is negligible (see Supporting information of paper II). For each sample, we selected specific vesicle/AuNPs ratios (before and after the maximum plasmonic variations). The fractal dimension of the aggregates and the average interparticle spacing obtained from the analysis of SAXS curves confirms the non-monotonic trend of the aggregation, showing higher aggregates size and compactness with increasing polymer content (see paper II for the detailed SAXS analysis).

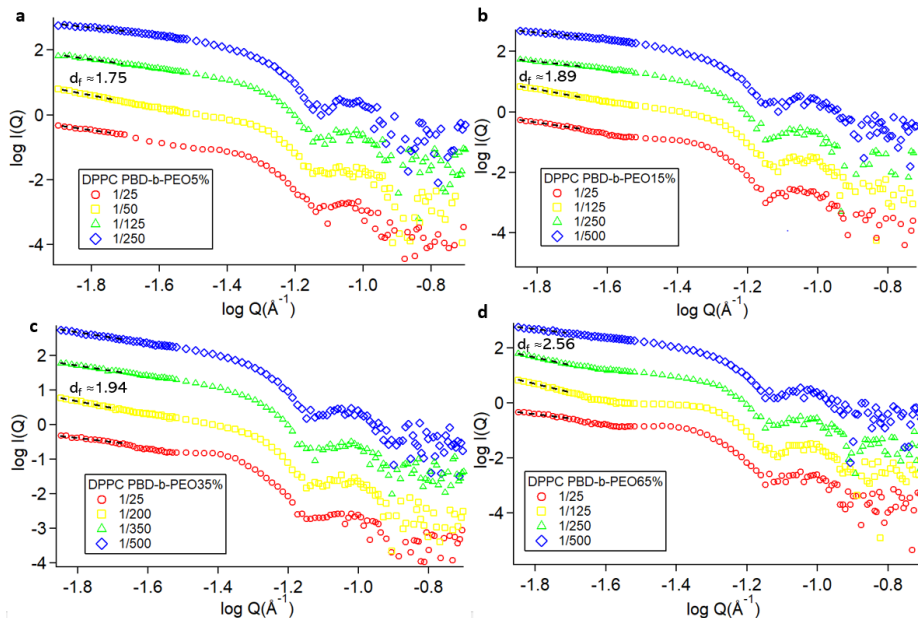


Figure 2.10: Log-log SAXS profiles of AuNPs/vesicles hybrids collected after 10 minutes of incubation of 300 μL AuNPs 9.93 nM with a) DPPC-PBD-b-PEO5%, b) DPPC-PBD-b-PEO15%, c) DPPC-PBD-b-PEO35%, d) DPPC-PBD-b-PEO65% vesicles at different AuNPs/vesicles ratios. Dashed black lines indicate the linear fittings of the low q region.

To summarize, the AuNPs aggregation on rigid membranes is strongly inhibited, independently of the number of vesicles. When a soft polymeric region is introduced in the membrane formulations, the aggregation behavior dramatically changes and is clearly dependent on the vesicle/AuNP ratio. Reasonably, we can assume that for each sample the maximum AuNPs aggregation corresponds to the saturation of the membrane by AuNPs that, in turn, depends on the extension of the soft polymeric domains on the vesicles, as schematized in figure 2.11. Then, for vesicles/AuNPs ratio decreasing, the additional nanoparticles remain freely dispersed, restoring the original plasmonic and scattering features. In line with this assumption, larger and more compact gold aggregates can be obtained by increasing the polymer amounts in the vesicle formulations.

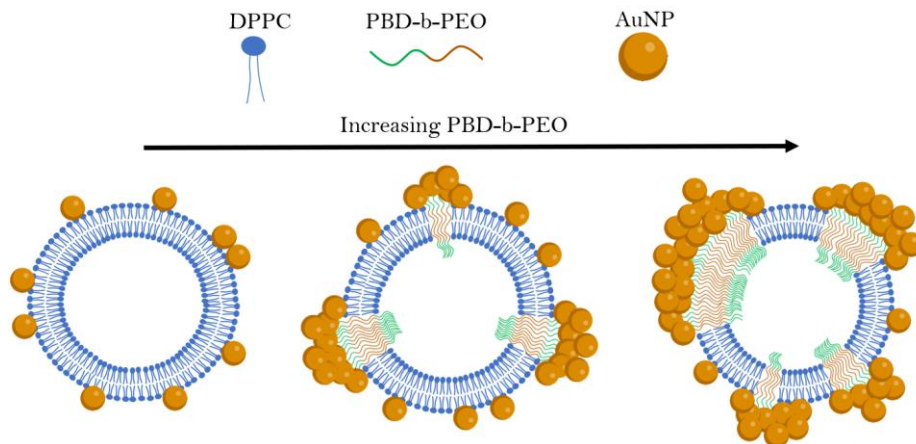


Figure 2.11: Schematic representation of the effect of PBD-b-PEO concentration in AuNPs-vesicle suprastructures. The AuNPs cluster size and compactness increase with the polymer content.

Altogether, our results not only disentangle a peculiar aggregative phenomenon of citrate AuNPs on multidomain membranes, demonstrating the primary role of soft regions but also proved that AuNPs cluster size and morphology can be finely controlled by varying concentration and composition of vesicles, shedding light on novel routes for the preparation of hybrid colloidal adducts with combined properties.

2.1.3 Interaction of AuNPs and AgNPs with non-lamellar model membranes (Paper 3)

To complete our understanding of the peculiar aggregative phenomenon of citrated AuNPs on biomimetic membranes, in this study, we compared for the first time the interaction of a highly curved biomimetic interface of cubic nature with citrate-capped gold and silver nanoparticles (AuNPs and AgNPs) with similar size and shape.

In the past years, the interactions occurring at the nano-bio interface have been studied to shed light on the main parameters that role the biological fate of nanomaterials to contribute to their clinical translation. While lamellar membranes have been intensively investigated to get information on NPs cytotoxicity, more complex

membranous architectures still need to be explored. As described in section 1.2, 3D lipid assemblies possessing a cubic architecture demonstrated to be biologically relevant structures permanently or transiently occurring in cells.^{109–111} In this context, the investigation of the interaction between NPs and cubic membranes offers novel perspectives on the understanding of nano-bio interactions.

In this study, we monitored the interaction of citrate-capped spherical AuNPs and AgNPs with stabilizer-free cubosomes (both dispersed in water and adsorbed onto a solid support). Such artificial lipid models allowed us to study the effect of the NPs composition (i.e. Ag- vs. AuNPs) on cubic phase membranes under controlled conditions, extending our current knowledge on cubic interfaces with high biological relevance.

Interaction of metallic NPs with free-standing cubosomes

First, we studied the interaction of citrate-capped AuNPs¹¹² and AgNPs¹¹³ with dispersed glycerol monooleate (GMO) cubosomes¹¹⁴, by monitoring the optical variation of the metallic NPs through UV-vis spectroscopy (see paper III for the detailed characterization of metallic NPs and cubosomes dispersion preparation). As displayed in figure 2.12, the characteristic color, as well as the plasmonic profile of AgNPs, remain almost unchanged upon incubation with the cubosome dispersion. Conversely, the color of AuNPs dispersion quickly turns from red to purple, and the original plasmonic peak undergoes a prominent red shift and an intense broadening, indicating the formation of gold aggregates, similarly to the phenomenon already highlighted for citrated AuNPs challenging soft lipid vesicles and hybrid lipid-copolymer vesicles. To get insights into the structure of the aggregates, we performed SAXS measurements, which main results are reported in figure 2.12b. Considering that in our experimental conditions the scattering intensity of cubosomes is negligible, any variation in the scattering profiles can be attributed to the particle arrangement. In line with UV-vis spectroscopy results, the presence of cubosomes does not influence the SAXS profile of AgNPs. On the contrary, the incubation of cubosomes with AuNPs provokes an increase in the slope of the scattering curve in the low Q region. This power-law dependence,

observed as a linear trend in the $I(Q)$ vs Q double logarithmic plot, reflects the formation of AuNPs fractal aggregates on the cubosomes membranes, in line with the optical variation of the dispersion. These results highlight that, despite their very similar physico-chemical properties (size, shape, morphology, surface coating), the incubation of AuNPs and AgNPs with cubosomes results in dramatically different outcomes. It has to be noticed that UV-vis spectroscopy and SAXS measurements provide information on the NPs behavior; therefore, in order to gain some hints on their effect on the cubic membrane, we designed and prepared cubosomes-based membranes and investigated their interaction with AuNPs and AgNPs through surface techniques.

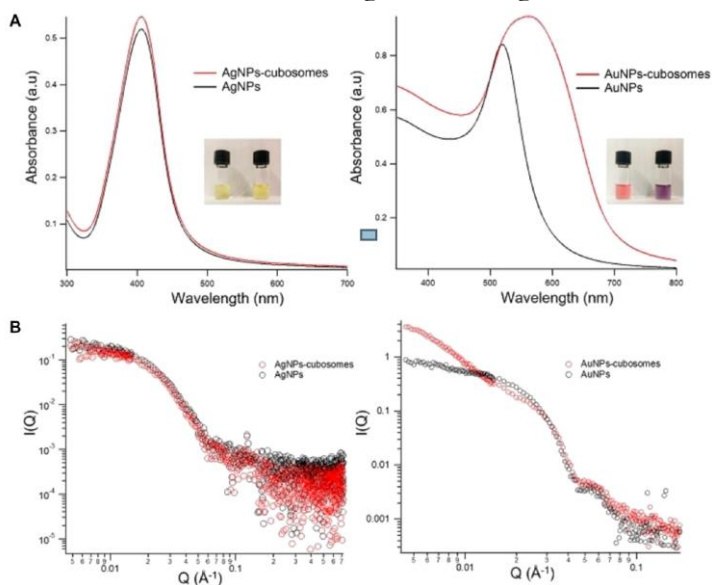


Figure 2.12: (A): UV-Visible absorption profiles of AgNPs-cubosomes (left) and AuNPs-cubosomes (right). (B): Log-log SAXS profiles of AgNPs-cubosomes (left) and AuNPs-cubosomes (right) hybrids. $300 \mu\text{L}$ of NPs ($8.3 \times 10^{-10} \text{ M}$) were mixed with $20 \mu\text{L}$ of 0.4 mg/ml cubosomes (for a final concentration of cubosomes in the mixture of 0.025 mg/ml), and SAXS and UV-vis profiles were collected after 10 min of incubation. The SAXS profile of cubosomes in water at a 0.025 mg/ml lipid concentration has been subtracted from AgNPs cubosomes and AuNPs-cubosomes profiles.

Interaction of metallic NPs with supported cubosomes

To gain information on the response of the cubic membranes to the NPs adhesion, we prepared a thin film of cubosomes adsorbed onto a solid support.

Considering their slightly negative surface charge, cubosomes were deposited on a slightly positive supported lipid bilayer. With this aim, we prepared the SLB through the adsorption and fusion of DOPC/DOTAP (1,2-dioleoyl-3-trimethylammonium-propane) vesicles on a hydrophilic substrate (see paper III for the SLB preparation). To real-time monitor the cubic nanoparticles deposition through Confocal Microscopy, we labelled liposomes and cubosomes with two different fluorescent probes with well-separated emission spectra. Figure 2.13 shows representative 2D and 3D images of the SLB before and after 30 minutes from the addition of cubosomes (fluorescent signals of liposomes and cubosomes are green and red, respectively). As shown, after 30 minutes of incubation, the cubosomes are homogeneously deposited on the lipid substrate. It's worth noticing that, due to the intrinsic resolution limits of confocal microscopy, it's not possible to unambiguously assess whether the deposited particles are single cubosomes or small cubosome clusters (see paper III for the effect of cubosomes concentration on the deposition kinetics and cubosomes packing).

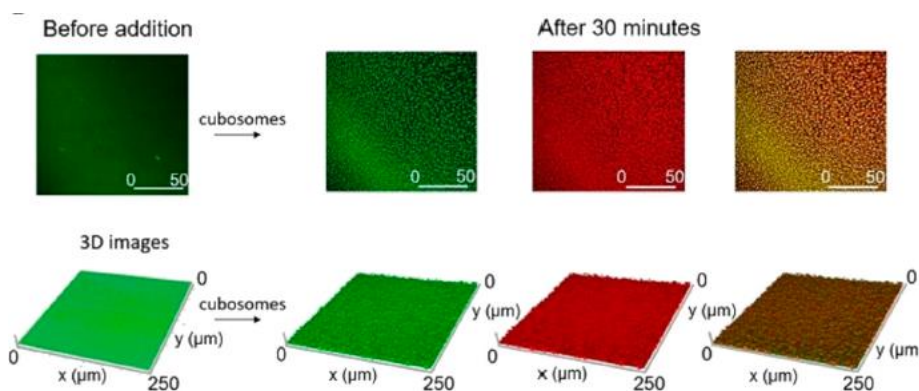


Figure 2.13: Representative 2D and 3D Confocal Microscopy images of the cubosomes deposition on the SLB. SLB and cubosomes were fluorescently labeled with two different probes with well-separated emission spectra.

Specifically, *DOPC/DOTAP* liposomes have been labeled with β -Bodipy (λ_{exc} 488 nm, λ_{em} 493–614 nm), while stabilizer-free *GMO*-based cubosomes with 18:1 Cyanine 5 PE (λ_{exc} 633 nm, λ_{em} 662–732 nm). Cubosomes are imaged in red, the SLB in green, and the colocalization of the probes in yellow.

The interaction of the metallic NPs with the cubosomes film was initially investigated through QCM-D measurements. Once stabilized the cubic film and removed the excess of dispersed cubosomes, AuNPs or AgNPs were injected into the measurement chamber. As shown in figure 2.14a, the resonance frequency shift immediately decreases after the injection of the AuNPs, indicating massive adsorption of particles on the substrate, in line with the results obtained for the dispersed systems. On the other hand, the injection of AgNPs does not provoke any relevant shift of the oscillation frequency, highlighting a negligible or event absent number of particles interacting with the substrate (figure 2.14b).

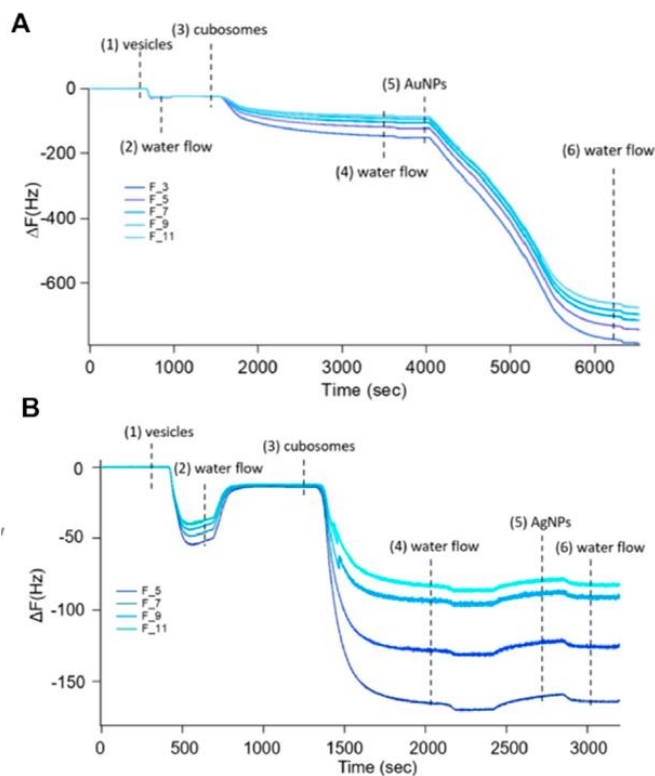


Figure 2.14: QCM experiments describing the adsorption of 0.83 nM AuNPs (Panel (A)) and AgNPs (Panel (B)) on the cubosomes film deposited upon the DOPC/ DOTAP substrate. The vertical lines represent the subsequential injection of DOPC/DOTAP vesicles (1), milliQ water (2), cubosomes (3), milliQ water (4), AuNPs (left) or AgNPs (right) (5), and milliQ water (6).

Finally, the interaction was monitored through confocal microscopy to observe the micron-scale morphological modification of the substrate induced by the interaction with the metallic particles. Figure 2.15a shows the fluorescent signal, originating from the supported DOPC/DOTAP bilayer and the GMO-based cubosomes, and the transmission signal, originating from the presence of NPs clusters, collected at specific time intervals (0 minutes, 30 minutes, and 6 hours after the NPs addition). Before the incubation with the particles, the substrate is characterized by a stable and densely packed layer of cubosomes. Upon AuNPs addition, the cubosomes progressively agglomerate, forming larger lipid clusters, and the intensity of the bilayer fluorescence decreases, suggesting the extraction of lipids from the substrate. After 6 h of incubation, the characteristic cubosome packing is completely lost, and just a few large aggregates are present. At the same time, as visible in the transmission images, micron-sized AuNPs aggregates extensively covered the glass surface. As shown in panel b of figure 2.15, when AgNPs are incubated with the cubic substrate, the morphology of the substrate is not affected after 6 h of interaction, and the transmission image doesn't show any presence of particle clusters.

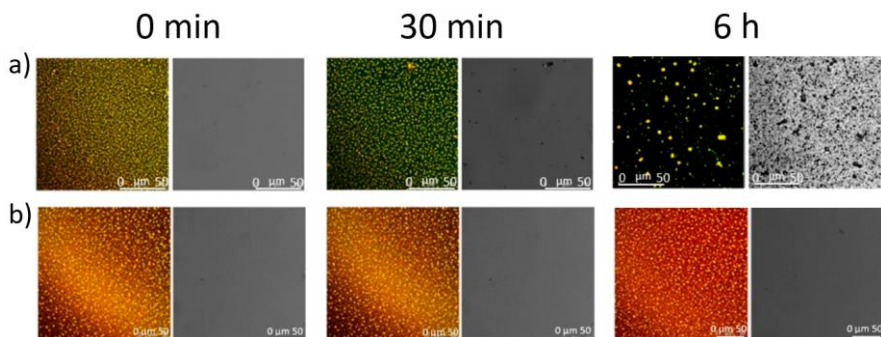


Figure 2.15: Representative 2D Confocal Microscopy images of the interaction of 0.83 nM AuNPs and AgNPs with the film of cubosomes

deposited on the DOPC/DOTAP SLB. Images collected at different incubation times (before and after 30 min and 6 h from AuNPs injection).

Overall, considering that the selected NPs are similar in terms of size, shape, concentration, and surface coating, our experimental results revealed that the interaction is governed by the chemical nature of the particles both at the nano- and the micro-scale. Specifically, at the nanoscale, AuNPs quickly cluster on the cubosomes membrane, leading to the formation of NPs' fractal aggregates, while no aggregation is detected for AgNPs; at the micron scale, AuNPs destroy the ordered array of SLB-supported cubosomes, forming micron-sized cubosome-based agglomerates and AuNPs aggregates. On the contrary, the supported cubic membrane is almost unaffected upon incubation with AgNPs. In agreement with recent works and with the mechanisms hypothesized in paper I, we can hypothesize that the spontaneous aggregation of citrated AuNPs arises from the fast release of citrate molecules that, by locally increasing the ionic strength, causes a loss of AuNPs electrostatic stabilization, leading to their clustering on the membranes. Reasonably, in the present case, the AuNPs aggregation is triggered by a similar mechanism, which ultimately leads to the formation of NPs clusters on the cubic membranes and causes lipid extraction and substrate disruption.

In this framework, the different behavior of AgNPs can be related to the different affinity of the citrate for the silver surface. While citrate molecules can be easily displaced from the gold surface^{79,115}, citrate anions form water-insoluble complexes with Ag(I) ions at the silver surface^{116–118}. Such complexes partially -or completely- bounded to the AgNPs surface cannot be readily displaced. Thus, the formation of these complexes prevents the ligand-exchange process and the citrate anions release, inhibiting the AgNPs aggregation. The schematic representation of the process is displayed in figure 2.16.

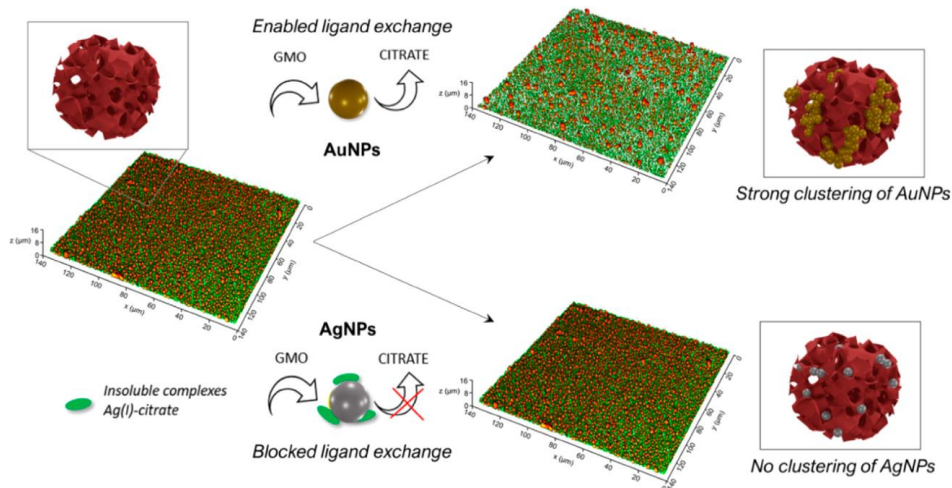


Figure 2.16: Schematic representation of the mechanism and final outcomes of the interaction of AuNPs and AgNPs with water dispersion cubosomes and solid supported films of cubosomes.

Overall, this work reports for the first time a physico-chemical investigation of the interaction of prototypical particles with cubic phase interfaces, addressing the NPs impact from the micro- to the nano-scale point of view. These results further highlight the relevance of understanding the main contributions which determine the events at the nano-bio interface, pointing out the prominent role of the interaction between the surface coating and the particle's surface.

2.2 Colorimetric assays for the characterization of lipid-based assemblies

The second section of this thesis focuses on how the spontaneous interaction occurring at the nano-bio interface between AuNPs and lipid assembly, which mechanism has been thoroughly discussed and disentangled in the previous section, can be exploited for analytical applications. Chapter 2.2.1, the subject of a freshly published paper (**paper IV**), shows that by exploiting the high dependence of the AuNPs clustering on the membrane rigidity, it is possible to develop a colorimetric assay for the determination of the stiffness of natural and synthetic vesicles. Within the same framework, section 2.2.2, showing

the results of a recently submitted paper (**paper V**), demonstrates that the presence of a lipid interface covering an inorganic NPs activates and templates the aggregation of AuNPs. This experimental phenomenon paves the way for the development of a colorimetric assay for determining the degree of lipid coverage in the production of membrane-camouflaged nanomaterials for medical applications.

2.2.1 AuNPs plasmonics to probe the rigidity of synthetic and biogenic vesicles (Paper 4)

As discussed in section 1.2, the mechanical properties of natural membranes play a crucial role in relevant biological properties, ranging from cell fusion and differentiation to the response to pharmacokinetics delivery and internalization mechanisms.^{119–121} Moreover, recent reports displayed that the mechanical properties of Extracellular Vesicles (EVs), natural vesicles secreted by cells and ubiquitous in biological fluids^{122–124}, is a biomarker for pathological conditions of parental cells^{125,126}.

Despite the fundamental relevance of the viscoelastic properties of membranes, to date, their accurate quantification is still challenging.¹²⁷ Indeed, both traditional and more recent methods are time and cost-consuming or require heavy data analysis.¹²⁸

As shown in section 2.1 (**paper I**), AuNPs can spontaneously assemble on lipid vesicles according to a membrane-templated phenomenon driven by the physical state of the membrane. AuNPs can cluster on soft membranes, forming densely packed aggregates, and just adhere to rigid lipid scaffolds.^{78,129,130} Based on these results, in this study we propose Turkevich-Frens AuNPs as colorimetric nanoprobe of the stiffness of membrane-enclosed nano-objects by demonstrating that AuNPs clustering is not an on-off process but is rather continuously modulated by membrane stiffness. Thus, the plasmonic variations of AuNPs can be exploited as a finely sensitive probe to vesicle rigidity, even able to discriminate the rigidity of vesicles in the same physical state. Our findings pave the way for the development of a reproducible,

sensitive, and high-throughput “*plasmon-based stiffness nanoruler*” (paper IV).

With this aim, we synthesized six different liposomal formulations having similar size and polydispersity, and different rigidities (DOPC, POPC(1-palmitoyl-2-oleoyl-glycero-3-phosphocholine), POPC/DPPC, DPPC, DPPC/DSPC, and DSPC(1,2-distearoyl-snglycero-3-phosphocholine)).

First, the stiffness of each vesicle was evaluated through Atomic Force Microscopy-based Force Spectroscopy (AFM-FS) measurements performed in collaboration with the CNR-ISMN group. With this technique, the force experienced by the AFM tip while it is indenting the vesicles is recorded (figure 2.17b). The slope of the force-distance profiles is directly related to the stiffness of the vesicles. In line with the literature¹³¹, as displayed in figure 2.17c, the obtained values of stiffness show that the rigidity monotonically increases from DOPC to DSPC (see paper IV for details).

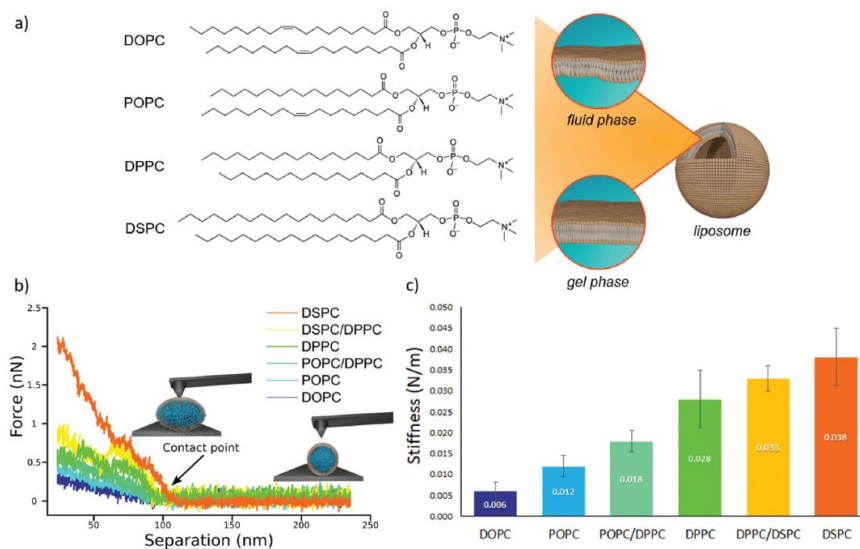


Figure 2.17: AFM characterization of vesicle stiffnesses. (a) Chemical formulas of the four lipids used for the preparation of liposomes (1,2-distearoyl-snglycero-3-phosphocholine (DSPC), 1,2-dipalmitoyl-snglycero-3-phosphocholine (DPPC), 1-palmitoyl-2-oleoyl-glycero-3-phosphocholine (POPC) and 1,2-dioleoyl-snglycero-3-phosphocholine (DOPC)); depending

on the molecular composition, the lipid bilayer enclosing a liposome exhibits a different degree of molecular packing at room temperature, which determines the phase (i.e., fluid or gel) of the membrane. (b) AFM force-distance curves for the different vesicles batches, together with the graphical representation of vesicles deformation induced by the AFM tip at two different separation distances. Liposomes samples are DOPC, POPC, POPC/DPPC (50/50 mol%), DPPC, DPPC/DSPC (50/50 mol%), and DSPC vesicles; (c) stiffness values (Nm^{-1}) of the different vesicles, determined through AFM-FS; All error bars represent the uncertainties obtained by bootstrapping.

Then, the selected vesicles were challenged with the AuNPs dispersion, and the SPR profiles were collected after 15 minutes of incubation. The colour of the dispersions clearly shifts from the characteristic red colour of the colloidal gold to blue, in a continuous fashion passing from DSPC (the most rigid vesicle) to DOPC (the softest vesicle). In the UV-vis spectra (reported in figure 2.18a), such color variations are associated with the occurrence of a red-shifted peak, with increasing intensity with vesicles rigidity decrease. In line with the interaction mechanism proposed in sections 1.3 and 2.1^{78,129}, the aggregation is initiated by the wrapping of the AuNPs by the membranes, which ultimately regulates the extent of particle clustering and their plasmonic variations. For this reason, the optical properties of AuNPs depend on the mechanical properties of the templating vesicles and can be exploited to set up a UV-Vis spectroscopic assay to estimate vesicles rigidity. With this purpose, we selected a stiffness index (S.I.) as a quantitative descriptor of AuNPs spectral variations. Figure 2.18b reports the calculated S.I.s as a function of the vesicles stiffness evaluated through AFM. As shown, the dependence of the S.I. on the stiffness can be expressed by a sigmodal law, according to the following expression:

$$S.I. = \frac{b}{1 + \exp\left(\frac{c-S}{d}\right)} + a \quad (2.2)$$

Where S represents the stiffness and a, b, c, and d constant fitting parameters. This equation, relating the AuNPs optical variations to the membrane rigidity, can be used for estimating the rigidity of vesicles of unknown composition. Additionally, it's worth considering that such a sigmoidal relation provides the maximum sensitivity in the region of

intermediate rigidity ($20\text{-}30 \times 10^{-3} \text{ N/m}$), which is typically the range of rigidity of natural vesicles.

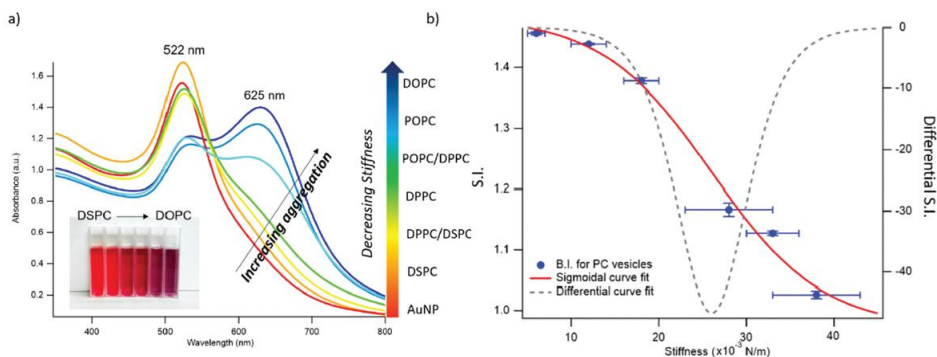


Figure 2.18: *a) UV-Vis spectra of AuNPs (6.7 nM) incubated with synthetic vesicles (0.2 nM) (liposomes/AuNPs number ratio 1/100). Inset: Visual appearance of the same samples. (b) S.I. values (blue spots) with relative error bars plotted as a function of membrane stiffness. The red curve is the sigmoidal curve fit, while the grey dashed curve is the first derivative of the sigmoidal curve fit with respect to stiffness (see supporting information of paper IV for details on fitting parameters).*

To validate our method and demonstrate its applicability on natural and more complex lipid structures, we selected a sample of EVs extracted from the murine cell line TRAMP-C2¹³², characterized by size and Z-potential similar to the ones of the synthetic liposomes selected for the calibration curve. As shown in figure 2.19, the stiffness of this selected EVs batch evaluated with AFM-FS is intermediate between the values obtained for the POPC/DPPC and DPPC vesicles. Accordingly, the S.I. obtained by challenging the EVs dispersion with the AuNPs falls in the middle of the stiffness range determined through AFM.

Overall, the experimental results showed that the nanoplasmonics properties of AuNPs can be used to assess the stiffness of synthetic and natural vesicles. The proposed method allows evaluating the rigidity with a reproducible and sensitive assay, able to discriminate the stiffness of liposomes with very similar mechanical properties usually not distinguishable with other techniques, minimizing the vesicles amount and requiring only standard lab facilities.

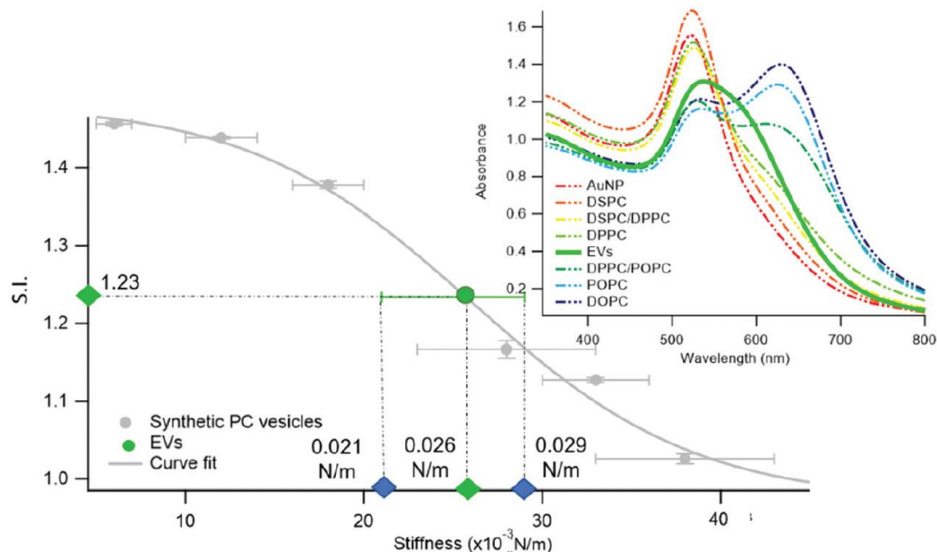


Figure 2.19: Sigmoidal trend of the S.I. as a function of membrane stiffness. The EVs' S.I. (1.23 ± 0.01), evaluated through UV-Vis spectroscopy, and stiffness, predicted by the sigmoidal law (0.026 N m^{-1}), are reported as green points in the graph. The green error bar represents the stiffness interval obtained through AFM-FS for EVs. The right inset reports the UV-Vis spectra of AuNPs (6.7 nM) in the presence of synthetic PC vesicles (dashed curves) and EVs (solid green curve) at a vesicles' concentration of 0.35 nM .

2.2.2 AuNPs plasmonics to estimate the lipid coverage of inorganic NPs (Paper 5)

In the past paragraphs, we deeply investigated the behavior of AuNPs when mixed with lipid membranes, also probing their ability to quantify the rigidity of vesicles. This section extends the interaction of AuNPs to membrane-coated inorganic NPs, aiming both at testing the ability of a lipid bilayer to mediate the aggregation of AuNPs on the surface of inorganic NPs, and at developing a colorimetric assay for the characterization of membrane-coated nanomaterials (**paper V**).

In the past years, inorganic nanoparticles have been intensively investigated thanks to their unique potentiality in biomedical applications. As mentioned, despite the extraordinary advancements in

NPs development and production, their clinical translation is still largely limited due to the lack of knowledge on their biological fate once introduced in living systems.^{133–135} Nowadays, researchers are focusing on solving the main issues of NPs application to promote their use in nanomedicine, including poor colloidal stability and limited circulation time in biological fluids, cytotoxic effects, poor targeting ability, and uncontrolled accumulation in specific tissues, which eventually leads to low efficacy and undesired side effects.¹³⁶

As discussed in section 1.3, the origin of these NPs drawbacks is generally related to their exogenous nature, which leads to uncontrolled behaviors in the biological environment.

A promising approach for enhancing the NPs in-vivo applicability consists in internalizing the particles in lipid membranes, forming lipid-inorganic NPs hybrids, providing a biomimetic surface that hinders the NPs presence from phagocytes, improving their circulation time, and enhancing the cell adhesion and uptake.^{137–140} Despite the wide potential of these biologically promising hybrids, the efficient and accurate characterization of the bilayer formation on the NPs surface is still challenging. Current methodologies for the characterization of the coating integrity, as well as Electron Microscopy, Confocal Laser Scanning Microscopy, Atomic Force Microscopy, Dynamic Light Scattering (DLS), and Zeta Potential measurements, do not provide ensemble-averaged characterization, require heavy data analysis, or fail in providing a quantitative estimate of the coating extent.

Here, based on the spontaneous interaction between AuNPs and zwitterionic membranes discussed in the previous sections^{78,129,141}, we report a plasmonic approach for determining the extent of lipid coverage of NPs. With this aim, we selected SiO₂NPs as a prototypical inorganic core and prepared membrane-coated SiO₂NPs (M-SiO₂NPs) with different degrees of coverage. AuNPs cluster on the portion of the particles covered by the lipid membranes, and the optical variations can be directly exploited to estimate the extent of the lipid coverage.

Interaction of AuNPs with membrane-coated SiO₂NPs

Commercial anionic SiO₂NPs have been coated with a lipid membrane composed of DOPC/Sphingomyelin/ Cholesterol vesicles (0.87/0.38/1 mol%) according to a well-established protocol with slight modifications¹⁴². Briefly, bare SiO₂ NPs in ultrapure water is mixed with a high excess of liposomes ($\geq 1/50$ SiO₂/liposomes number ratio), formed in an aqueous environment of high salinity. First, the vesicles adhere to the SiO₂NPs surface due to van der Waals interactions; then, a transmembrane osmotic shock causes the rupture of the vesicles and the formation of the lipid coating (see section 4.5 of paper V for the preparation of the hybrids). The formation of the lipid bilayers around the SiO₂NPs was first visualized by Cryo-EM microscopy. As shown in figures 2.20a and b, SiO₂NPs are partially covered by an electron-dense nanometric layer faithfully following the particle morphology. Additionally, as a further confirmation of the effective lipid coverage of the SiO₂NPs' surface, M-SiO₂NPs were characterized by liquid-AFM, DLS, and Z-potential measurements (see paper V for the detailed hybrid characterization).

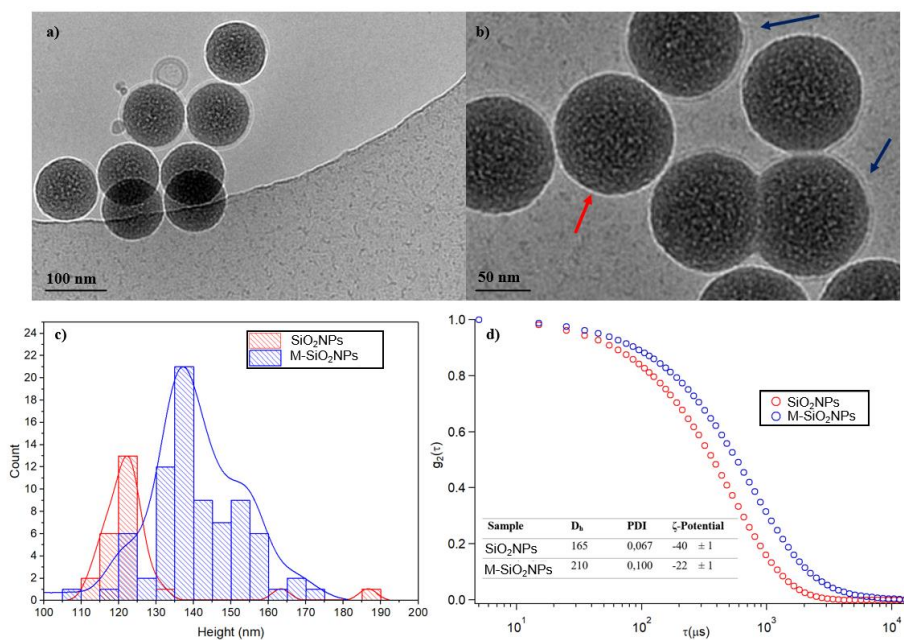


Figure 2.20: a) and b) Cryo-EM images of M-SiO₂NPs at different magnifications (blue and red arrows identify coated and uncoated areas, respectively); c) Size distribution of SiO₂NPs (red) and M-SiO₂NPs (blue)

obtained by liquid-AFM imaging; d) Autocorrelation functions of 0.08 mg/mL water dispersion of SiO₂NPs (red) and M-SiO₂NPs (blue). The inset shows the hydrodynamic diameter (extrapolated by a cumulant fitting) and the ζ -potential values of each sample.

SiO₂NPs and M-SiO₂NPs dispersions were then challenged with Turkevich-Frens AuNPs, and the resulting systems were imaged through Cryo-EM (Figures 2.21 a and b). Given the strong electrostatic repulsion between both negative gold and inorganic silica surfaces, AuNPs do not interact with the naked SiO₂NP. Conversely, when the SiO₂NP is enclosed by a membrane, the AuNPs spontaneously cluster on the lipid bilayer forming AuNPs-decorated M-SiO₂NPs composites. As shown in figures 2.21 c and d, this aggregative phenomenon is reflected by the plasmonic properties of the particles. When AuNPs are mixed with SiO₂NPs, the color of the dispersion, as well as the UV-vis spectrum, remains unchanged. On the contrary, the clustering of the AuNPs on lipid-coated silica nanoparticles clearly causes an evident color change of the dispersion from red to purple/blue, and the occurrence of the red-shifted signal, the hallmark of the AuNPs aggregation. These results show that the membranes can mediate the adhesion of AuNPs on SiO₂NPs, activating the aggregative phenomenon previously observed on synthetic vesicles (papers I, II, IV).

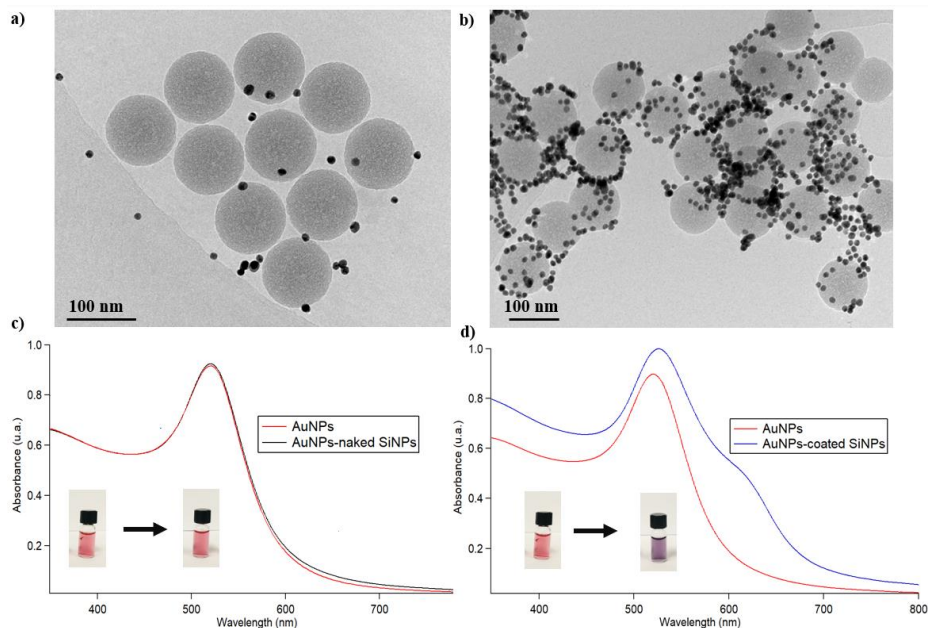


Figure 2.21: Cryo-EM images of (a) $\text{SiO}_2\text{NPs} - \text{AuNPs}$ (b) $\text{M-SiO}_2\text{NPs} - \text{AuNPs}$ composites and UV-visible spectra of AuNPs incubated with (c) SiO_2NPs and (d) $\text{M-SiO}_2\text{NPs}$. The UV-Vis spectrum of bare AuNPs (red curve) is also reported as a control sample. The visual appearance of AuNPs before and after the incubation with SiO_2NPs and SiO_2 NSLBs is reported in the insets of the graphs.

Formation of M-SiO₂NPs with different degrees of coverage

Once proved the role of the membrane in the AuNPs- SiO_2NPs interaction, we explore how the extent of lipid coverage affects the optical properties of the AuNPs. With this purpose, we prepared six batches of M-SiO₂NPs with different coverage by varying the starting number of vesicles in the transmembrane osmotic shock protocol ($\text{SiO}_2\text{NPs}/\text{vesicles}$ employed ratios: 1/50, 1/15, 1/10, 1/5, 1/3, and 1/1, see paper IV for further details). The M-SiO₂NPs were then characterized in terms of hydrodynamic diameter and surface potential and Inductively Coupled Plasma-Atomic Emission Spectrometry (ICP-AES) measurements were used for a rough estimation of the coating degrees. As reported in table 2.1, the total amount of covered SiO_2NPs ranged from 13% to 88% by increasing the starting vesicle amount. In line with this result, the surface ζ -potential of the SiO_2 particles surface

decreases in a continuous trend (-22.7 ± 1.3 mV for the lower SiO₂NP/vesicle ratio (1/50), -36.5 ± 1.5 mV for the higher SiO₂NP/vesicle ratio 1/1). Furthermore, the hydrodynamic size of M-SiO₂NPs (around 200 nm) is stable in the range of 1/50 to 1/5 SiO₂NPs/vesicle ratio, while for higher SiO₂NPs/vesicle ratios (1/3 and 1/1) an abrupt dimensional increase occurs. In agreement with the recent literature^{46,143,144}, this instability can be explained considering that the complete coverage of the particles is not gained with a low number of vesicles, and a surface lipid coverage approximately lower than 40% may induce abrupt precipitation due to the presence of membrane patches on the silica surface which triggers the bridging between partially coated particles (inset in table 2.1).

Sample	D _h (nm)	PDI	ζ-Potential (mV)	SiO ₂ NPs coverage
Vesicles	115	0.115	-11.2 ± 1.1	/
SiO ₂ NPs	165	0.067	-40.2 ± 0.9	0%
1/50	210	0.100	-22.7 ± 1.3	$88 \pm 8\%$
1/15	193	0.122	-26.2 ± 1.2	$68 \pm 7\%$
1/10	189	0.164	-28.6 ± 0.7	$60 \pm 6\%$
1/5	193	0.152	-30.3 ± 1.4	$53 \pm 5\%$
1/3	414	0.363	-37.1 ± 3.2	$33 \pm 3\%$
1/1	621	0.335	-36.5 ± 3.5	$13 \pm 1\%$

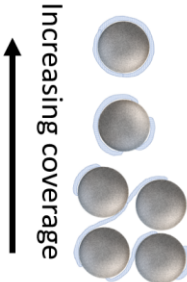


Table 2.1. Hydrodynamic diameter, ζ-potential values of naked SiO₂NPs, bare vesicles, and M-SiO₂NPs obtained using different SiO₂NPs-vesicles ratios. The SiO₂NPs coverage is also reported, calculated from the concentration of P and Si measured with ICP-AES for each composition (see SI section S2.3). The inset displays a schematic representation of how the coverage affects the size and stability of the hybrids.

Relation between AuNPs aggregation and degree of membrane coverage

In the last part of this work, the M-SiO₂NPs with different degrees of coverage were challenged with the Turkevich-Frens AuNPs.

As shown in figure 2.22, the incubation of the so-obtained M-SiO₂NPs provokes a gradual change in the color of the dispersion as well as the occurrence of the characteristic aggregative red-shifted peak whose intensity varies with the fraction of membrane-covered SiO₂NPs surface. Specifically, the intensity of the red-shifted plasmonic peak increases with increasing the extent of membrane coverage. These results, complemented by SAXS analysis (see paper V for the SAXS analysis), showed that AuNPs' clustering on M-SiO₂NPs is spontaneous and strictly modulated by the lipid-coated fraction of the SiO₂NPs surface.

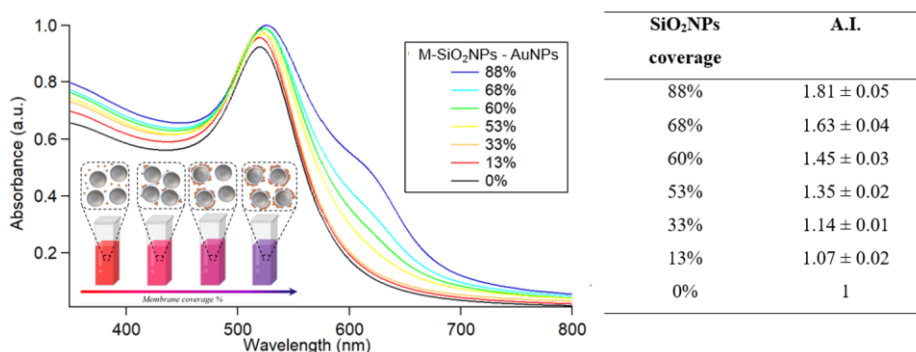


Figure 2.22: (Top) UV-visible spectra of 6.13 nm AuNPs interacting with 1.15 nm M-SiO₂NPs with different degrees of coverage, collected after 10 min of incubation; (bottom) A.I. values obtained for each different membrane coverage of SiO₂NPs.

Therefore, it is possible to estimate the degree of coating by using an aggregation index as the optical descriptor of the plasmonic variation already exploited for the determination of the rigidity of membrane-enclosed nano-objects (paper IV, section 2.2.1). The so-determined A.I.s are reported in figure 2.23. As shown, the A.I. increases linearly with the membrane coverage (r-squared 0.98). The accuracy of the fitting decreases when M-SiO₂NPs with a coverage <35% are included, probably due to the low stability of SiO₂NP with a minor coverage extent (see SI of paper V for further fitting details). With respect to other methodologies, these results pave the way for the development of a high-throughput and ensemble-averaged colorimetric approach for

the quantitative determination of membrane-coated NPs, independently of the chemical nature of the inorganic core.

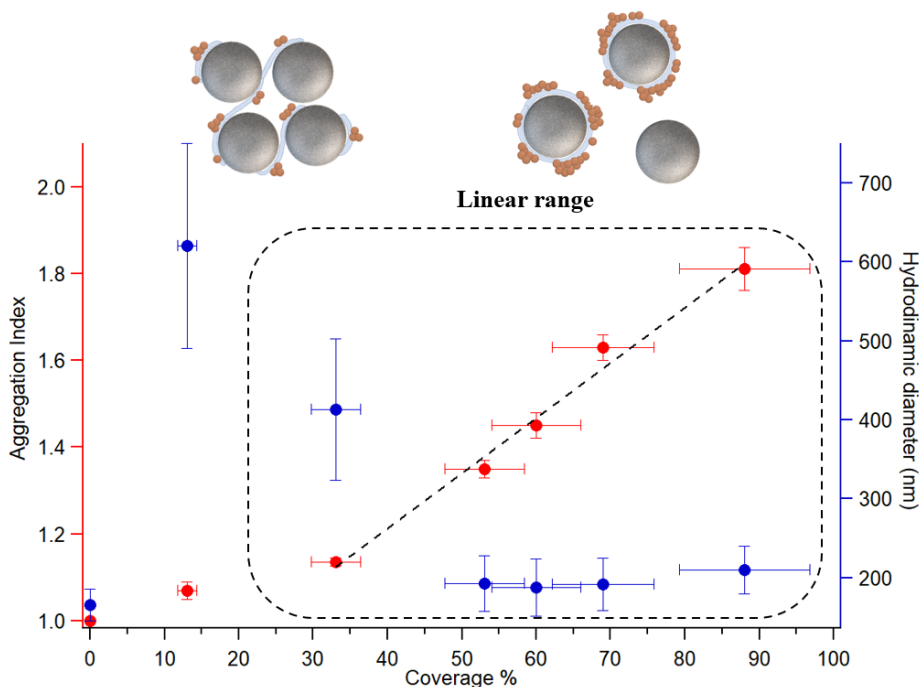


Figure 2.23. A.I. (red) and hydrodynamic diameter (blue) as a function of SiO_2NPs membrane coverage, together with the visual appearance of the AuNPs incubated with SiO_2NPs at different membrane coverages. AuNPs/M- SiO_2 hybrids are also sketched, highlighting how the integrity of the membrane coating affects the binding and aggregation of AuNPs on SiO_2NPs .

2.3 Hybrid lipid-inorganic functional Nanomaterials

In the last section of the thesis (section 2.3.1), the fundamental and mechanistic knowledge of citrated-AuNPs/lipid membranes interaction is exploited to explore the possibility of forming new magnetic and plasmonic materials obtained through the self-assembly of citrated core-shell inorganic nanoparticles on lipid membranes. Thus, the interaction of synthetic liposomes of different rigidity with citrated

hybrid gold-magnetic nanoparticles (AuMNPs) was investigated, aiming at unveiling how these spontaneous events occurring at the nano-bio interface can be implemented as a novel synthetic route for the production of controlled -optical and magnetic- responsive NPs-liposome suprastructures.

2.3.1 Self-assembly of magnetoplasmonic NPs on synthetic liposomes (Paper 6)

As mentioned in the introduction, the combination of inorganic NPs and lipid scaffolds represents a prominent strategy for both improving the biocompatibility of NPs and developing novel nanomaterials with unique properties.^{77,85,145,146} In this context, here we investigated the self-assembly of citrate-capped core-shell magnetic NPs (AuMNPs) on rigid and soft synthetic liposomes. The interaction was firstly monitored through UV-Vis spectroscopy, exploiting the plasmonic properties of nanostructured gold. Then, the morphology and NPs arrangement on the lipid membranes were directly imaged with Cryo Transmission Electron Microscopy, while their colloidal stability was monitored through Dynamic Light Scattering measurements. Finally, the magnetic mobility of the hybrid was tested in collaboration with the CNR-ISMN group, demonstrating that the magnetic responsiveness of the NPs-vesicles suprastructures is enhanced compared to the free dispersed particles.

Physico-chemical characterization of AuMNPs-liposomes suprastructures

The selected AuMNPs, prepared according to a well-known protocol with little modifications¹⁴⁷, display a broad plasmonic signal peaked at about 538 nm, in line with the formation of particles with a gold shell covering a magnetic inorganic core. Briefly, citrate-stabilized Fe₃O₄ NPs were added to a boiling HAuCl₄ solution. In this way, the citrate molecules on the Fe₃O₄ surface provoke the reduction of the Au³⁺ ions and, in turn, induce the growth of a homogeneous gold shell around the magnetic seeds. The hydrodynamic size of the particles probed through DLS shows that the colloidal dispersion is composed of two different

populations of NPs (see paper VI for details). The larger population is peaked at about 45 nm, featuring the hydrodynamic size of core-shell AuMNPs, while the smaller population, which peaked at about 10 nm, perfectly matches the size of the Fe_3O_4 seeds used as the precursor for the growth of the gold shell. The contemporary presence of both ferric seeds and AuMNPs was reasonably expected, considering that the centrifugation and purification steps, commonly employed in core-shell synthesis protocols¹⁴⁷, have been omitted.

First, the interaction of the AuMNPs with zwitterionic liposomes with different rigidities was investigated through cryo-EM microscopy. Figure 2.24 shows representative images resulting from the incubation of the AuMNPs with DOPC and DPPC vesicles for 10 minutes. We noticed that both Fe_3O_4 seeds and AuMNPs adhere to soft and rigid vesicles without membrane disruption. However, as previously observed for AuNPs, the rigidity of the bilayers dramatically affects the morphology of the clusters. On soft DOPC vesicles, the particles adhere to the lipid shell forming densely packed aggregates, with the particles in direct contact with each other. On the other hand, on DPPC vesicles, the particles adhere to the lipid scaffolds, but their clustering on the membrane is hampered. In this latter case, the average spacing between the adsorbed particles is consistently higher, and, importantly, the hybrids present a minor number of adsorbed particles per vesicle.

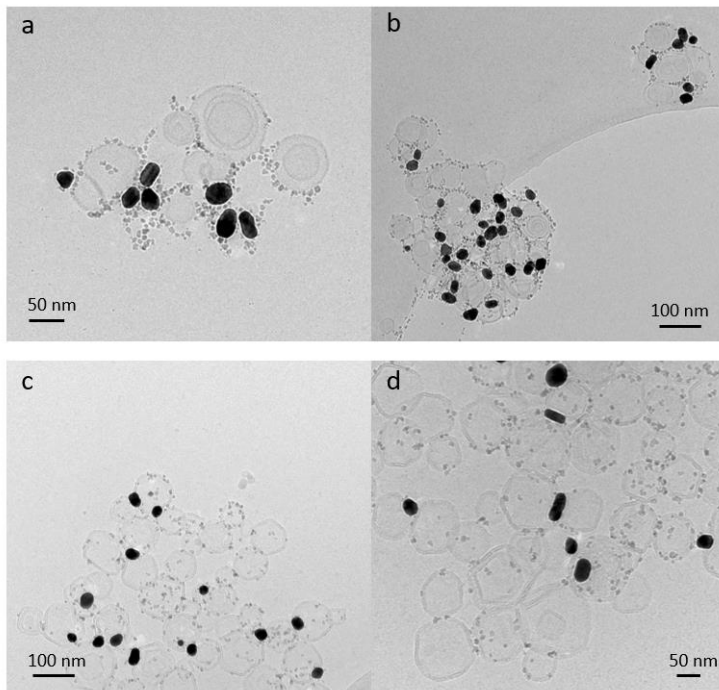


Figure 2.24: Cryo-EM images of (a,b) DOPC-AuMNPs and (c,d) DOPC-AuMNPs composites.

Then, the spectral variations of the particles induced by rigid and soft liposomes were monitored through UV-vis spectroscopy. Figure 2.25 display the UV-vis spectra collected for the AuMNPs dispersion mixed with different concentrations of liposomes. The incubation of AuNPs with DOPC vesicles provokes the red shift and broadening of the original plasmonic peak of the particles. In agreement with cryo-EM images, this phenomenon, ascribable to the plasmonic properties of the gold shell, is provoked by the coupling of the plasmonic peak of AuMNPs due to their spatial proximity and is consistent with particle aggregation. Moreover, the decrease in the vesicle amount leads to a progressive enlargement of the plasmonic peak, pointing out that the particles' aggregation is maximized for lower DOPC amounts. This experimental result suggests that the AuMNPs aggregate on the membrane of fluid phase vesicles according to a membrane-templated process. On the contrary, the interaction with rigid DPPC liposomes provokes a minor bathochromic shift of the original peak, negligibly affected by the vesicle amount. This behavior is consistent with the

change in the chemical environment of the particles upon their adhesion to the DPPC surface. As shown in the inset in figure 2.25b, in this case, the presence of the vesicles does not affect the color of the dispersion, revealing the scarce particle aggregation.

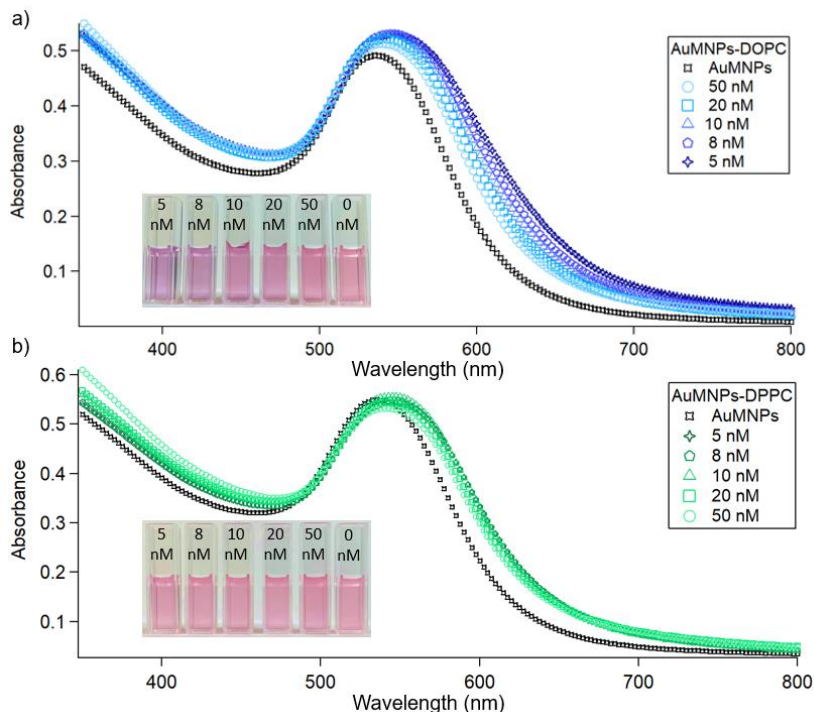


Figure 2.25: UV-Visible absorption profiles of AuMNPs-DOPC (a) and AuMNPs-DPPC (b) as a function of the liposome concentration (5 nM, 8 nM, 10 nM, 20 nM, and 50 nM). The insets in the figures report the color variation in the various sample.

As already demonstrated for citrate AuNP with both experiments and simulations, these results highlight that the rigidity of the membranes drives the aggregation of AuMNPs on zwitterionic membranes, forming completely different suprastructures.^{78,129,148}

To characterize the hybrids in terms of size and colloidal stability, we monitored the aggregative process through DLS (figure 2.26). Concerning the DOPC-AuMNPs system, the hydrodynamic diameter of the hybrids increases with decreasing the liposome concentration due to the formation of NPs-vesicles hybrids characterized by a

progressively larger number of particles per vesicle. The evaluated hydrodynamic size, passing from 160 nm to 350 nm, is consistent with the hydrodynamic dimension of a lipid vesicle surrounded by a crust of nanoparticles. On the other hand, the interaction of AuMNPs with rigid DPPC vesicles leads to the formation of micron-sized objects with dimensions independent of the starting NPs/vesicle ratios. To gain a deep comprehension of the colloidal stability of the systems, the evolution of the hydrodynamic diameter was monitored over time. As a representative example, figures 2.26 c and d show the time evolution of the autocorrelation functions evaluated for AuMNPs interacting with DOPC and DPPC 10 mM (see supporting information for the DLS measurements of the other vesicle concentrations). For what concerns DOPC samples, in all the employed vesicle concentrations, the interaction leads to the formation of metastable objects with constant hydrodynamic sizes in the first hour of incubation. On the contrary, the AuMNPs adhesion on DPPC vesicles provokes the sudden formation of highly unstable objects. As observed in section 2.1.1, the colloidal stability of NPs-vesicles suprastructure is modulated by the number of NPs adsorbed on the vesicles.^{93,103} Specifically, NPs can introduce negative or positive charges on the liposome surface, electrostatically stabilizing the dispersion. Here, the soft bilayer triggers the membrane-templated NPs aggregation, which, in turn, leads to the massive adhesion of NPs to the lipid shell, as confirmed by Cryo-EM images. The presence of this elevated number of negatively charged NPs on the liposomal surface stabilizes the hybrids. In the case of DPPC, the strong membrane rigidity inhibits nanoparticle clustering. Reasonably, in this configuration, the minor number of particles per vesicle is not sufficient to prevent liposome fusion. Thus, NPs adsorbed on the lipid shell interact via van der Waals attractions with the neighboring NPs-vesicles hybrids, ultimately leading to the bridging and the destabilization of the system.

These results demonstrate that the membrane-templated association of citrate-capped NPs can be exploited to easily synthesize NPs decorated liposomes with tunable size, morphology, and stability. Both the obtained hybrid nanomaterials possess intriguing magnetic and plasmonic properties that will be further investigated in next studies.

As proof of concept, here, we focused on DOPC-AuMNPs suprastructures for the investigation of magnetic responsiveness.

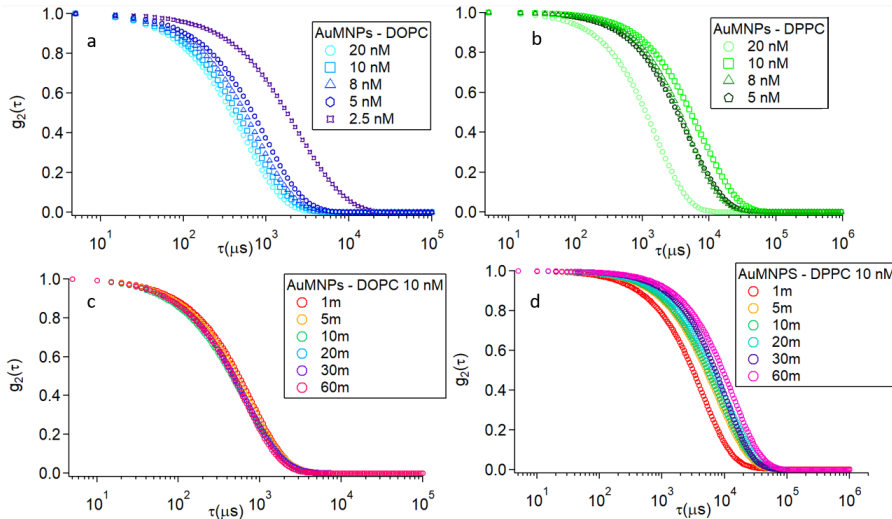


Figure 2.26: Autocorrelation functions collected for AuMNPs-DOPC (a) and AuMNPs-DPPC (b) hybrids as a function of the liposome concentration (20 nM, 10 nM, 8 nM, and 5 nM). Time evolution of the DLS curves of the AuMNPs-DOPC hybrids (c) and of the AuMNPs-DPPC hybrids (d).

Magnetic responsiveness of AuMNPs-DOPC hybrids

The last part of this work focuses on the investigation of the magnetic responsivity of the hybrids when an external magnetic gradient is applied. With this purpose, only the AuMNPs dispersion and stable DOPC-AuMNPs hybrids have been employed. In a dedicated experimental set-up developed at CNR-ISMN, a uniform solution of AuMNPs-liposomes or AuMNPs has been injected into a 500 μm -wide quartz capillary where a high-gradient magnetic field is generated by a couple of cubic permanent magnets placed symmetrically on the sides of the capillary. The transparent quartz capillary allows the optical investigation of the behavior of the magnetic particles under a magnetic field by a microscope-connected CCD camera. The injected batches of NPs-liposomes hybrids, characterized by different DOPC liposome concentrations (5 nM, 8 nM, 20 nM), are expected to display distinct magnetic moments due to the different number of NPs per vesicle.

While the Brownian motion disperses the nanoobjects through the fluid volume, the external magnetic field generates a drift of the magnetic objects towards the highest field region (close to the external magnet). In the absence of hydrodynamic flows, the competition between the chaotic Brownian motion and the directional magnetic force dictates the time scale over which an equilibrium concentration of nanoparticles finally forms in the experimental system.¹⁴⁹

When injected in the capillary, the particles accumulate in the region closest to the magnet forming a disc-shaped dark area. The surface of this area grows over time with clearly distinct time dynamics for unconjugated AuMNPs and AuMNPs-liposome conjugates (figure 2.27a). For the conjugates with low liposome/AuMNP ratios (DOPC 5 nM and 8 nM), the disk grows until it reaches a seeming equilibrium condition in 1 and 3 hours, respectively. For the highest liposome/AuMNPs ratio (DOPC 20 mM) and the bare AuMNPs, the equilibrium condition is not reached within the times experimentally probed, and the surface area keeps growing.

Figure 2.27b displays the time evolution of the disc for all the investigated samples. As highlighted by inspecting the slopes of the linear fittings of the accretion of the disc area during the time, the responsivity of the systems to the external magnetic field increases with decreasing the liposomes concentration. Reasonably, these experimental results can be explained by considering that increasing the number of magnetic particles per vesicle, the magnetic responsivity of the hybrids increases. Overall, albeit with very preliminary measurements, these results demonstrate that the membrane-templated aggregation of citrate-stabilized NPs can be instrumental in the production of novel nanomaterials possessing enhanced and controlled properties with respect to the starting precursors.

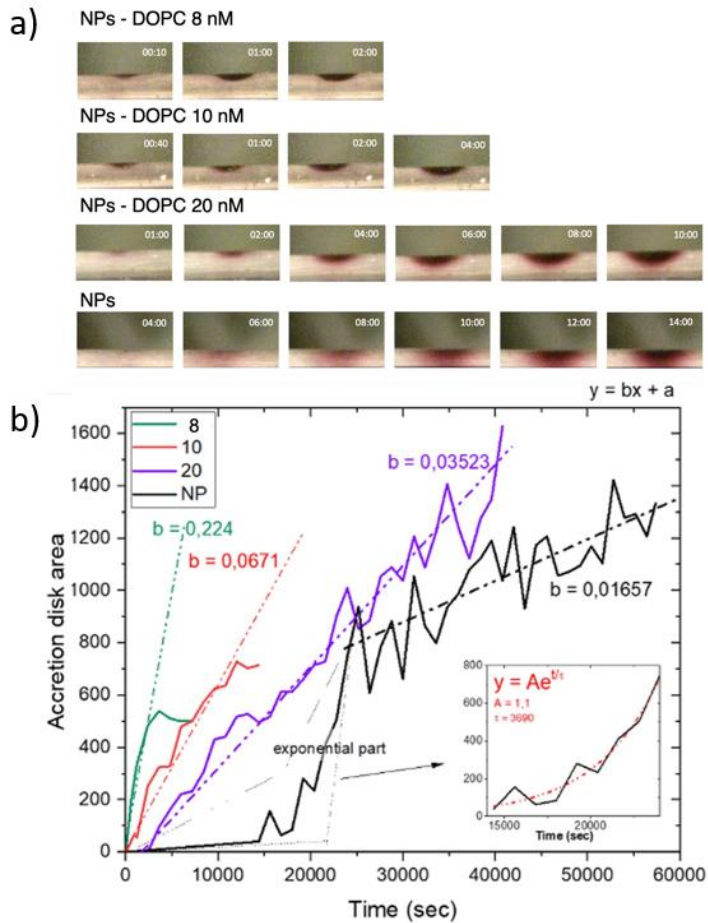


Figure 2.27: a) Representative collected images reporting the time evolution of the area of the accretion disk for AuMNPs-DOPC hybrids (DOPC 8 nM, 10 nM, and 20 nM) and AuMNPs; b) Accretion of the disk areas during the time. The slope of the linear fitting reflects the responsivity of the particles to the external magnetic field.

3. Conclusions

Understanding the interaction of inorganic nanoparticles with biological interfaces is crucial to improve our fundamental knowledge of the main determinant phenomena at the nano–bio interface to predict nanomaterial destiny in living organisms. In this framework, the use of synthetic membranes represents one of the most prominent approaches for investigating the nano-bio interface in simplified conditions. In addition, the understanding of the interaction mechanisms occurring between NPs and lipid scaffolds can pave the way to engineer controlled hybrids where soft and biocompatible vesicles are combined with inorganic NPs.

In the present thesis, we focused on the intriguing self-assembly of Turkevich-Frens AuNPs on synthetic liposomes. Citrate-capped AuNPs spontaneously associate with the bilayer of synthetic liposomes and, in some cases, self-assemble on the membrane. Even if such a membrane-templated aggregation may have relevant implications on NPs uptake and internalization in cells as well as on their bioactivity, the mechanistic and kinetic aspects of this phenomenon still need to be completely understood.

In the first section of the thesis, we have addressed from a physical-chemical standpoint the interaction of citrate-capped AuNPs with synthetic vesicles demonstrating the prominent role of membrane rigidity over different length- and time- scales. We showed that the adhesion pathway of AuNPs to the target membrane is governed at the molecular level by the physical properties of the lipid bilayer. The initial and local AuNP-membrane interaction initiates a cascade of events that regulate and control the structure and functional properties of the final hybrids resulting in dramatic structural, morphological and plasmonic differences. Moreover, by employing a lipid-polymer hybrid scaffold featuring membrane domains with different rigidities, we demonstrate that the presence of soft polymeric regions in rigid vesicle formulations strongly triggers the AuNPs clustering. Interestingly, from a

technological point of view, we showed that the size and the compactness of AuNPs-vesicles suprastructure are finely controlled by varying vesicle concentration and composition. Finally, for the first time, we addressed the interaction of citrate-capped AuNPs and AgNPs with non-lamellar model membranes. Our results not only disentangled the NPs impact on the cubic structures at both the micro- and the nano-scale but also highlighted the relevance of the interaction energy between citrate molecules and the NPs' surface.

In the second section of this thesis, we showed how the spontaneous clustering of AuNPs on lipid membranes, and, in turn, their optical properties could be exploited as a nanoprobe for the characterization of vesicles and NPs-lipid hybrid properties. First, the dependence of the aggregation on the membrane rigidity was exploited to probe the stiffness of -natural and synthetic- membrane-enclosed nanoobjects. Moreover, exploiting the ability of membranes to template the AuNPs aggregation, we build up a colorimetric assay to estimate the degree of lipid coverage in the production of membrane-camouflaged NPs for biomedical applications.

Finally, the last section, supported by preliminary results, shows that citrate-stabilized magnetoplasmonic NPs (i.e., AuMNPs) can aggregate in zwitterionic liposomes forming, in a controlled manner and through simple self-assembly steps, nanomaterials with enhanced optical and magnetic properties.

In conclusion, the herein presented results contribute to the current interest in the biomimetic membranes-NPs interactions showing how the events occurring at the nano-bio interfaces can be used both from a fundamental knowledge point of view and for technological purpose.

4. Methods

4.1 Small Angle X-ray Scattering

Small Angle X-ray Scattering (SAXS) represents one of the most widespread techniques to obtain ensemble-averaged qualitative and quantitative information on dimensions, shape, and structures of colloids, allowing to resolve inhomogeneities of about 1 nm up to hundreds of nanometers.¹⁵⁰ From a basic point of view, when X-ray radiation crosses the sample, it can be partially transmitted, partially absorbed, and transformed into other forms of energy (e.g., heat, fluorescence, etc.), and partially scattered. In the scattering experiment, the transmitted radiation is blocked by the beam stop, while the scattered part is collected by the detector.

The fundamental quantity of the scattering techniques is the scattering vector q , defined as the difference between the wave vector of the diffused radiation k_s , and the wave vector of the incident radiation k_i , which, in the approximation of elastic scattering ($|k| = |k_i| = 2\pi n/\lambda$), can be defined as:

$$|q| = |k_s - k_i| = \left(\frac{4\pi n}{\lambda}\right) \sin\theta \quad (4.1)$$

where n is the refractive index of the sample and 2θ is the scattering angle. Q represents the independent variable of the instrument, which can be expressed as:

$$q = 2\pi/d \quad (4.2)$$

Where d is the characteristic sample distance. The measured variable of the experiment is the scattering intensity, $I(q)$, which is defined by equation 4.3:

$$I(q) = KN_p V_p^2 (\Delta\rho)^2 P(q) S(q) + B \quad (4.3)$$

Where K is a variable that depends on the instrument, N_p is the number of scattering particles in a unit volume, V_p is the particle volume, B is the background, $\Delta\rho$ represents the contrast, defined as the difference

between the scattering length density of dispersed objects and the continuous medium, $P(q)$ and $S(q)$ are the form factor and the structure factor, accounting of size and shape of particles and the interparticle interaction, respectively.¹⁵¹

In the present work, SAXS measurements have been performed for several purposes on aqueous dispersions of AuNPs, AgNPs, dispersions of liposomes, and hybrid systems of AuNPs-liposomes. They were carried out on sealed glass capillaries with 1.5 mm in diameter. The analysis of SAXS curves was performed on Igor Pro. The experimental details are reported in the full text and/or SI of the attached papers.

4.2 Dynamic Light Scattering

Dynamic Light Scattering (DLS), together with SAXS, represents one of the most fundamental techniques in colloidal chemistry, which provides dimensional information on systems ranging from some nanometers to hundreds of nanometers. DLS can be performed in dispersed samples without manipulations.¹⁵² Figure 4.1 shows the scheme of the instrumental set-up. The polarized and monochromatic light emitted from the laser source is focalized by a series of lenses and crosses the sample. The scattered radiation is collected by the detector, typically positioned at 90° .

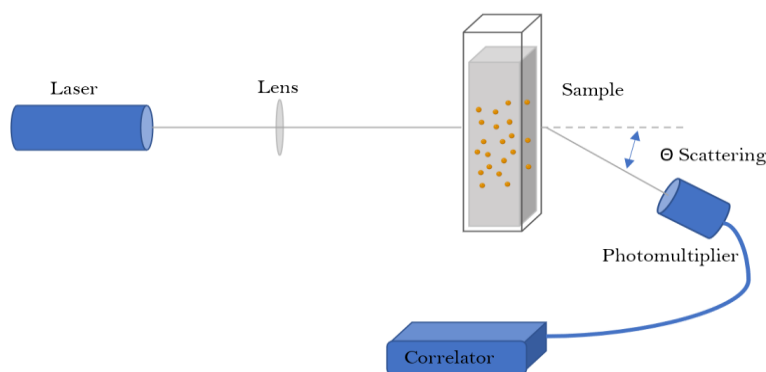


Figure 4.1: Schematic representation of the DLS experiment.

From DLS the characteristic hydrodynamic size of colloidal objects can be determined since the intensity of the scattered light varies as a

function of the Brownian motions of particles. Small particles produce faster fluctuations of the scattered light (they move faster) than big particles. The speed of the Brownian motion is defined by the coefficient of translational diffusion D , which is directly correlated to the hydrodynamic diameter of the structures in solutions by the Stokes-Einstein equation¹⁵³:

$$d(H) = \frac{kT}{3\pi\eta D} \quad (4.4)$$

Where $d(H)$ represents the hydrodynamic diameter, k is the Boltzmann constant, T is the absolute temperature, and η is the viscosity of the solution. The fluctuations of the measured scattering intensity are analysed through the autocorrelation function of the electric field $g^1(\tau)$, which is a function that correlates the signal relative to the scattering intensity with itself at time 0, in a time interval τ . The time that is needed to observe the decay of the correlation depends on the speed of diffusion, and, in turn, on the particle's size.

The simplest method of analysis, extensively used in this thesis, is the cumulant method, which allows for obtaining dimensional information from the autocorrelation function of diluted and monodispersed samples. However, the cumulant method not always can resolve and fit the autocorrelation functions, especially when the dispersed objects are highly polydispersed. In those cases, different analyses can be used such as Contin and NNLS algorithms, employed in the present thesis, which provide the particle size distribution in the investigated samples.¹⁵⁴

4.2 Zeta Potential

The Zeta Potential instrument allows for evaluating the surface potentials of colloidal particles dispersed in a medium. The Zeta potential value is obtained from the electrophoretic mobility of the charged particles under the effect of the applied electric field.¹⁵⁵ The speed at which the particles move is correlated to the electrophoretic mobility through the following equation:

$$v = \mu E \quad (4.5)$$

Where E is the electric field and μ is the electrophoretic mobility. A laser beam crosses the sample, and the scattered light is detected to determine the particle mobility. Through the Helmholtz-Smoluchowski relation, the Zeta potential of the particle can be calculated knowing the electrophoretic mobility of the particle μ , the viscosity of the dispersing liquid η , its dielectric constant ϵ_r , and the dielectric constant in vacuum ϵ_0 permit to calculate the Zeta potential value:

$$\zeta = \frac{\eta\mu}{\epsilon_r\epsilon_0} \quad (4.6)$$

The Zeta Potential measurements are carried out with the Zeta Potential Analyzer (Zeta plus, Brookhaven Instruments Corporation, Holtsville, NY) and processed with the software BIC PALS Ver. 3.54.

4.3 Quartz Crystal Microbalance With Dissipation Monitoring

Quartz Crystal Microbalance with Dissipation Monitoring (QCM-D) is a mass detection technique with the ability to measure very small mass variations in real-time.¹⁵⁶ The instrument consists of a thin sensor formed by a single crystal with metal electrodes on both sides of the sensor. When the crystal is exposed to an external electric field it oscillates at its resonance frequency. When molecules and particles interact with the quartz sensor, the variation in its resonance frequency (ΔF) is directly related to the adsorbed mass. In the case of rigid films uniformly distributed on the surface of the sensor and thin enough compared the weight of the crystal, a linear relation (Sauerbrey equation¹⁰⁸) connects the absorbed mass (m) and the resonance frequency shift (f):

$$\Delta m = \frac{C}{v} \Delta f \quad (4.7)$$

Where C depends on the intrinsic viscoelastic properties of the crystal and on its thickness, while v corresponds to the *overtone* of the crystal.

In the present work, the QCM-D experiments are executed with a Q-sense Explorer (Q-Sense, Gothenburg, Sweden) equipped with a flux cell of the liquid that contains a sensor quartz-coated with a

fundamental resonance of 5 MHz. The active surface of the sensor ($\approx 1 \text{ cm}^2$) is covered with a thin film of SiO_2 ($\approx 100 \text{ nm}$).

4.4 Confocal Laser Scanning Microscopy

Confocal Laser Scanning Microscopy (CLSM) is an imaging technique that allows 3D localization of labelled target molecules. A pinhole is placed in the image plane, so most of the out-of-focus light cannot reach the detector, providing an enhanced signal-to-noise ratio (contrast). The excitation light in confocal microscopy is usually provided by a laser to generate high intensities of fluorescence or reflectance from the focal spot. The focal spot during the analysis is scanned in the X-Y plane, and the signal detected reconstructs an image of the analysed sample.¹⁵⁷

In the case of fluorescence confocal microscopy, it is possible to use simultaneously multiple fluorophores that selectively interact with target molecules to increase the signal-to-noise ratio and obtain an improved sensitivity and specificity of the analysis. The laser emits at a specific wavelength to excite only a selected fluorophore in the sample. The instrument is equipped with a dichroic mirror that reflects the laser light and allows the fluorescent light emitted from the sample to pass through to the light detector, as schematized in Figure 4.2. In the present thesis, we employed a Leica CLSM TCS SP8 confocal microscope, operating in inverted mode, with a 63 x 1.3 numerical aperture water immersion objective. Images were taken with a resolution of 512 x 512 pixels using a 400 Hz bidirectional scan with each scanning line averaged four times. Leica software was used to create three-dimensional reconstructions of the z-stacks. Specific details on the set-up are reported in the full text and/or SI of the attached papers.

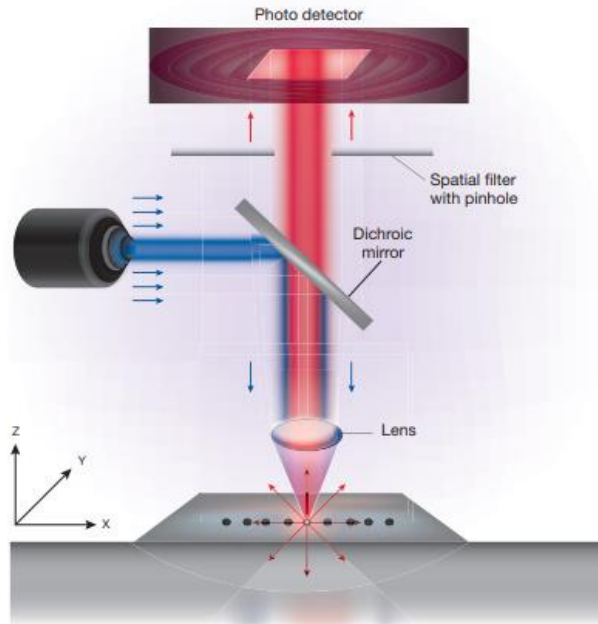


Figure 4.2: Schematic representation of confocal microscopy set-up. Reprinted from¹⁵⁸, Copyright 2012, with permission from Elsevier.

4.5 Atomic Force Microscopy

Atomic force microscopy (AFM) is a non-destructive technique that provides surface maps with nanometric resolution.¹⁵⁹ The instrument measures the forces experienced by the AFM probe, which consists of a cantilever with a tip (with a nanometric radius) at its free end, and the sample. To obtain an AFM surface topography image, the AFM tip is brought close to the sample and maps the sample by measuring the tip-sample interactions at each point. The probe position is finely controlled through a piezoelectric stage, onto which the probe is mounted. While scanning the surface, the AFM tip experiences attractive or repulsive interactions with the sample (e.g., Van der Waals, electrostatic, capillary, magnetic interactions, etc.), leading to a negative or positive bending of the cantilever. The force experienced by the tip while the cantilever is deflected can be described by the Hook law:

$$F = -kx \quad (4.7)$$

with k spring constant of the cantilever and x cantilever deflection. The deflection of the cantilever depends on k (a cantilever-related property) and the strength of its interaction with the sample. A laser beam is reflected from the back of the reflective AFM cantilever and is tracked by a position-sensitive photodetector which records probe vertical and lateral motions.

AFM can operate in different working modes, imaging the samples' structure or probing their physicochemical properties (e.g., magnetic, elastic, electric properties, etc.). The most common APM modes are "contact", "non-contact" and "tapping".¹⁶⁰ In the contact mode, the tip is directly placed in contact with the scanned objects during the measurements. The sample maps of the surface can be obtained by both fixing the tip-sample force and fixing the height of the probe above the sample, monitoring the cantilever deflection during the scanning of the sample's surface (i.e., constant-height mode). On the other hand, in tapping and non-contact modes, the cantilever oscillates close to the sample surface, at the resonance frequency of the cantilever and a defined amplitude. This amplitude is kept constant during scanning, constituting the feedback parameter. We exploited a different approach, named "PeakForce Tapping" mode, to record force spectroscopy data (Paper IV). In "PeakForce Tapping" mode the cantilever oscillates in the proximity of the sample's surface, periodically touching it. The force experienced by the tip while touching the sample is recorded and exploited to regulate the applied force.

4.6 Computational Methods

Coarse-grained simulations represent a computational approach aimed at simulating the behaviour of complex systems using a simplified (coarse-grained) representation of the system itself.¹⁶¹ This approach can be applied to several systems, ranging from water, proteins, and nucleic acids to lipid membranes. Molecules are represented by groups of atoms, decreasing the degrees of freedom, and allowing to simulate much longer simulation times. In the present thesis, all simulations were set up with the coarse-grained Martini force field and run with Gromacs ver. 2020.6. The model for the NPs and citrate was custom developed and described in previous work.⁷⁹

We prepared several configurations containing a flat membrane and a citrate-capped Au NP system. At the start of each simulation, the NP was placed in the water phase a few nanometers away from the surface of the bilayer. The simulation details are reported in the attached papers' full text and/or SI.

4.7 Cryogenic electron microscopy

The Cryogenic Electron Microscopy (Cryo-EM) is a transmission electron microscopy that emerged as powerful technique in structural biology and material science.¹⁶² Compared to traditional transmission electron microscopes (TEM), Cryo-EM is specifically designed to maintain a cryogenic temperature within the sample chamber. In Cryo-EM small aliquots of samples in solution or suspension are quickly cooled to cryogenic temperatures with liquid ethane (around -180°). This very fast freezing process prevents water molecules from crystallizing, preserving the original structure of samples. In the present thesis, Cryo-EM has been exploited to directly image different types of sample (paper I, V, and VI). Generally, 3 μ L of the sample dispersion were applied on glow-discharged Quantifoil Cu 300 R2/2 grids plunge in liquid ethane using an FEI Vitrobot Mark IV (Thermo Fisher Scientific) instrument. Excess liquid was removed by blotting for 1 s (blot force of 1) using filter paper under 100% humidity and 10 $^{\circ}$ C. Cryo-EM data were collected at the Florence Center for Electron Nanoscopy (FloCEN), University of Florence, on a Glacios (Thermo Fisher Scientific) instrument at 200 kV equipped with a Falcon III detector operated in the counting mode. Images were acquired using EPU software with a physical pixel size of 2.5 \AA and a total electron dose of $\sim 50 \text{ e}^{-}/\text{\AA}^2$ per micrograph.

Bibliography

- 1 C. L. Ventola, D. J. Bharali and S. A. Mousa, *Pharmacol. Ther.*, 2010, **128**, 512–525.
- 2 L. Zhang, F. X. Gu, J. M. Chan, A. Z. Wang, R. S. Langer and O. C. Farokhzad, *Clin. Pharmacol. Ther.*, 2008, **83**, 761–769.
- 3 M. J. Mitchell, M. M. Billingsley, R. M. Haley, M. E. Wechsler, N. A. Peppas and R. Langer, *Nat. Rev. Drug Discov.*, 2021, **20**, 101–124.
- 4 M. Liong, J. Lu, M. Kovoichich, T. Xia, S. G. Ruehm, A. E. Nel, F. Tamanoi and J. I. Zink, *ACS Nano*, 2008, **2**, 889–896.
- 5 Y. Liu, H. Miyoshi and M. Nakamura, *Int. J. Cancer*, 2007, **120**, 2527–2537.
- 6 H. Huang, W. Feng, Y. Chen and J. Shi, *Nano Today*, 2020, **35**, 100972.
- 7 C. L. Ventola, *P T*, 2017, **42**, 742–755.
- 8 H. H. Gustafson, D. Holt-Casper, D. W. Grainger and H. Ghandehari, *Nano Today*, 2015, **10**, 487–510.
- 9 A. M. Alkilany and C. J. Murphy, *J. Nanoparticle Res.*, 2010, **12**, 2313–2333.
- 10 S. Barua and S. Mitragotri, *Nano Today*, 2014, **9**, 223–243.
- 11 B. Fadeel and A. E. Garcia-Bennett, *Adv. Drug Deliv. Rev.*, 2010, **62**, 362–374.
- 12 E. C. Dreaden, A. M. Alkilany, X. Huang, C. J. Murphy and M. A. El-Sayed, *Chem. Soc. Rev.*, 2012, **41**, 2740–2779.
- 13 S. Kumar, K. S. Gandhi and R. Kumar, *Ind. Eng. Chem. Res.*, 2007, **46**, 3128–3136.
- 14 J. Zhang, L. Mou and X. Jiang, *Chem. Sci.*, 2020, **11**, 923–936.
- 15 N. Oh and J.-H. Park, *ACS Nano*, 2014, **8**, 6232–6241.
- 16 C. J. Murphy, A. M. Gole, J. W. Stone, P. N. Sisco, A. M. Alkilany, E. C. Goldsmith and S. C. Baxter, *Acc. Chem. Res.*, 2008, **41**, 1721–1730.

- 17 F. Chen, P. Si, A. de la Zerda, J. V. Jokerst and D. Myung, *Biomater. Sci.*, 2021, **9**, 367–390.
- 18 R. Popovtzer, A. Agrawal, N. A. Kotov, A. Popovtzer, J. Balter, T. E. Carey and R. Kopelman, *Nano Lett.*, 2008, **8**, 4593–4596.
- 19 J. B. Vines, J. H. Yoon, N. E. Ryu, D. J. Lim and H. Park, *Front. Chem.*, 2019, **7**, 1–16.
- 20 X. Huang and M. A. El-Sayed, *J. Adv. Res.*, 2010, **1**, 13–28.
- 21 L. Mocan, C. T. Matea, D. Bartos, O. Mosteanu, T. Pop, T. Mocan and C. Iancu, *Med. Pharm. Reports*, 2016, **89**, 199–202.
- 22 M. Hu, J. Chen, Z.-Y. Li, L. Au, G. V. Hartland, X. Li, M. Marquez and Y. Xia, *Chem. Soc. Rev.*, 2006, **35**, 1084.
- 23 H. Chen, L. Shao, Q. Li and J. Wang, *Chem. Soc. Rev.*, 2013, **42**, 2679–2724.
- 24 H. Cha, J. H. Yoon and S. Yoon, *ACS Nano*, 2014, **8**, 8554–8563.
- 25 A. M. Alkilany, S. E. Lohse and C. J. Murphy, *Acc. Chem. Res.*, 2013, **46**, 650–661.
- 26 H. Lange, B. H. Juárez, A. Carl, M. Richter, N. G. Bastús, H. Weller, C. Thomsen, R. von Klitzing and A. Knorr, *Langmuir*, 2012, **28**, 8862–8866.
- 27 A. Capocefalo, T. Bizien, S. Sennato, N. Ghofraniha, F. Bordi and F. Brasili, *Nanomaterials*, 2022, **12**, 1529.
- 28 N. Carl, S. Prévost, J. P. S. Fitzgerald and M. Karg, *Phys. Chem. Chem. Phys.*, 2017, **19**, 16348–16357.
- 29 H. Zhang and D. Wang, *Angew. Chemie - Int. Ed.*, 2008, **47**, 3984–3987.
- 30 W. Zhao, M. A. Brook and Y. Li, *ChemBioChem*, 2008, **9**, 2363–2371.
- 31 A. E. Nel, L. Mädler, D. Velegol, T. Xia, E. M. V. Hoek, P. Somasundaran, F. Klaessig, V. Castranova and M. Thompson, *Nat. Mater.*, 2009, **8**, 543–557.
- 32 C. V. Kulkarni, *Nanoscale*, 2012, **4**, 5779.
- 33 *Intermolecular and Surface Forces*, Elsevier, 2011.

- 34 K. Simons and W. L. C. Vaz, *Annu. Rev. Biophys. Biomol. Struct.*, 2004, **33**, 269–295.
- 35 K. L. Chen and G. D. Bothun, *Environ. Sci. Technol.*, 2014, **48**, 873–880.
- 36 A. L. Ottova and H. Ti Tien, *Bioelectrochemistry Bioenerg.*, 1997, **42**, 141–152.
- 37 A. L. Plant, *Langmuir*, 1999, **15**, 5128–5135.
- 38 S. Vemuri and C. . Rhodes, *Pharm. Acta Helv.*, 1995, **70**, 95–111.
- 39 T. M. Allen, *Drugs*, 1997, **54**, 8–14.
- 40 G. Bozzuto and A. Molinari, *Int. J. Nanomedicine*, 2015, 975.
- 41 J. F. Nagle, *Annu. Rev. Phys. Chem.*, 1980, **31**, 157–196.
- 42 Y. Lee and D. H. Thompson, *WIREs Nanomedicine and Nanobiotechnology*, , DOI:10.1002/wnan.1450.
- 43 R. Michel and M. Gradzielski, *Int. J. Mol. Sci.*, 2012, **13**, 11610–11642.
- 44 S. Dromi, V. Frenkel, A. Luk, B. Traughber, M. Angstadt, M. Bur, J. Poff, J. Xie, S. K. Libutti, K. C. P. Li and B. J. Wood, *Clin. Cancer Res.*, 2007, **13**, 2722–2727.
- 45 R. Michel, E. Kesselman, T. Plostica, D. Danino and M. Gradzielski, *Angew. Chemie*, 2014, **126**, 12649–12653.
- 46 A. H. Bahrami, M. Raatz, J. Agudo-canalejo, R. Michel, E. M. Curtis, C. K. Hall, M. Gradzielski, R. Lipowsky, T. R. Weikl, M. Raphael, C. E. M, H. C. K, G. Michael and L. Rein-, *Adv. Colloid Interface Sci.*, , DOI:10.1016/j.cis.2014.02.012.
- 47 Z. Shen, H. Ye, X. Yi and Y. Li, *ACS Nano*, 2019, **13**, 215–228.
- 48 Y. Hui, X. Yi, D. Wibowo, G. Yang, A. P. J. Middelberg, H. Gao and C. X. Zhao, *Sci. Adv.*, 2020, **6**, 1–11.
- 49 C. Montis, D. Maiolo, I. Alessandri, P. Bergese and D. Berti, *Nanoscale*, 2014, **6**, 6452–6457.
- 50 C. Montis, V. Generini, G. Boccalini, P. Bergese, D. Bani and D. Berti, *J. Colloid Interface Sci.*, 2018, **516**, 284–294.
- 51 M. Schulz and W. H. Binder, *Macromol. Rapid Commun.*, 2015, **36**, 2031–2041.

- 52 F. Meng, Z. Zhong and J. Feijen, *Biomacromolecules*, 2009, **10**, 197–209.
- 53 S.-W. Hu, C.-Y. Huang, H.-K. Tsao and Y.-J. Sheng, *Phys. Rev. E*, 2019, **99**, 012403.
- 54 D. P. Chang, J. Barauskas, A. P. Dabkowska, M. Wadsäter, F. Tiberg and T. Nylander, *Adv. Colloid Interface Sci.*, 2015, **222**, 135–147.
- 55 S. Murgia, S. Biffi and R. Mezzenga, *Curr. Opin. Colloid Interface Sci.*, 2020, **48**, 28–39.
- 56 J. Gustafsson, H. Ljusberg-Wahren, M. Almgren and K. Larsson, *Langmuir*, 1996, **12**, 4611–4613.
- 57 Z. A. Almsherqi, T. Landh, S. D. Kohlwein and Y. Deng, *Int. Rev. Cell Mol. Biol.*, 2009, **274**, 275–342.
- 58 J. Y. T. Chong, X. Mulet, B. J. Boyd and C. J. Drummond, *Steric Stabilizers for Cubic Phase Lyotropic Liquid Crystal Nanodispersions (Cubosomes)*, Elsevier Inc., 1st edn., 2015, vol. 21.
- 59 Q. Xiao, Z. Wang, D. Williams, P. Leowanawat, M. Peterca, S. E. Sherman, S. Zhang, D. A. Hammer, P. A. Heiney, S. R. King, D. M. Markovitz, S. André, H.-J. Gabius, M. L. Klein and V. Percec, *ACS Cent. Sci.*, 2016, **2**, 943–953.
- 60 Z. A. Almsherqi, S. D. Kohlwein and Y. Deng, *J. Cell Biol.*, 2006, **173**, 839–844.
- 61 T. Wang and Y. Luo, *Nanoscale*, 2019, **11**, 11048–11063.
- 62 Y. Wang, R. Cai and C. Chen, *Acc. Chem. Res.*, 2019, **52**, 1507–1518.
- 63 C. J. Murphy, A. M. Vartanian, F. M. Geiger, R. J. Hamers, J. Pedersen, Q. Cui, C. L. Haynes, E. E. Carlson, R. Hernandez, R. D. Klaper, G. Orr and Z. Rosenzweig, *ACS Cent. Sci.*, 2015, **1**, 117–123.
- 64 C. He, Y. Hu, L. Yin, C. Tang and C. Yin, *Biomaterials*, 2010, **31**, 3657–3666.
- 65 K. Yin Win and S.-S. Feng, *Biomaterials*, 2005, **26**, 2713–2722.
- 66 H. Yang, C. Liu, D. Yang, H. Zhang and Z. Xi, *J. Appl. Toxicol.*,

- 2009, **29**, 69–78.
- 67 A. Gojova, B. Guo, R. S. Kota, J. C. Rutledge, I. M. Kennedy and A. I. Barakat, *Environ. Health Perspect.*, 2007, **115**, 403–409.
- 68 A. Ridolfi, L. Caselli, C. Montis, G. Mangiapia, D. Berti, M. Brucale and F. Valle, *J. Microsc.*, 2020, **280**, 194–203.
- 69 E. Sezgin, I. Levental, S. Mayor and C. Eggeling, *Nat. Rev. Mol. Cell Biol.*, 2017, **18**, 361–374.
- 70 L. Caselli, A. Ridolfi, G. Mangiapia, P. Maltoni, J.-F. Moulin, D. Berti, N.-J. Steinke, E. Gustafsson, T. Nylander and C. Montis, *Phys. Chem. Chem. Phys.*, , DOI:10.1039/d1cp03201a.
- 71 Y. Cao, S. Li and J. Chen, *Toxicol. Mech. Methods*, 2021, **31**, 1–17.
- 72 H. C. Fischer and W. C. W. Chan, 2007, 565–571.
- 73 T. Hamada, M. Morita, M. Miyakawa, R. Sugimoto, A. Hatanaka, M. C. Vestergaard and M. Takagi, *J. Am. Chem. Soc.*, 2012, **134**, 13990–13996.
- 74 L. Wang, N. Hartel, K. Ren, N. A. Graham and N. Malmstadt, *Environ. Sci. Nano*, 2020, **7**, 963–974.
- 75 M. I. Setyawati, C. Y. Tay, D. Docter, R. H. Stauber and D. T. Leong, *Chem. Soc. Rev.*, 2015, **44**, 8174–8199.
- 76 E. Rascol, J. M. Devoisselle and J. Chopineau, *Nanoscale*, 2016, **8**, 4780–4798.
- 77 M. Mendoza, L. Caselli, A. Salvatore, C. Montis and D. Berti, *Soft Matter*, 2019, **15**, 8951–8970.
- 78 C. Montis, L. Caselli, F. Valle, A. Zendrini, F. Carlà, R. Schweins, M. Maccarini, P. Bergese and D. Berti, *J. Colloid Interface Sci.*, 2020, **573**, 204–214.
- 79 S. Salassi, L. Caselli, J. Cardellini, E. Lavagna, C. Montis, D. Berti and G. Rossi, *J. Chem. Theory Comput.*, 2021, **17**, 6597–6609.
- 80 Y. Ma, Y. Zhang, X. Li, Y. Zhao, M. Li, W. Jiang, X. Tang, J. Dou, L. Lu, F. Wang and Y. Wang, *ACS Nano*, 2019, **13**, 11967–11980.
- 81 F. Wang and J. Liu, *Nanoscale*, 2015, **7**, 15599–15604.

-
- 82 K. Sugikawa, T. Kadota, K. Yasuhara and A. Ikeda, *Angew. Chemie - Int. Ed.*, 2016, **55**, 4059–4063.
- 83 A. Šarić and A. Cacciuto, *Phys. Rev. Lett.*, 2012, **108**, 1–5.
- 84 L. Caselli, M. Mendoza, B. Muzzi, A. Toti, C. Montis, T. Mello, L. Di Cesare Mannelli, C. Ghelardini, C. Sangregorio and D. Berti, *Int. J. Mol. Sci.*, , DOI:10.3390/ijms22179268.
- 85 K. M. Vargas and Y. S. Shon, *J. Mater. Chem. B*, 2019, **7**, 695–708.
- 86 A. Floris, A. Ardu, A. Musinu, G. Piccaluga, A. M. Fadda, C. Sinico and C. Cannas, *Soft Matter*, 2011, **7**, 6239–6247.
- 87 W. T. Al-Jamal and K. Kostarelos, *Nanomedicine*, 2007, **2**, 85–98.
- 88 Y. Sun, Y. Xu, Y. Sun, B. Hu, L. Wang, Z. Du and Z. Gao, *Biointerphases*, 2022, **17**, 020801.
- 89 D. Lombardo, M. A. Kiselev and M. T. Caccamo, *J. Nanomater.*, , DOI:10.1155/2019/3702518.
- 90 A. E. LaBauve, T. E. Rinker, A. Nouredine, R. E. Serda, J. Y. Howe, M. B. Sherman, A. Rasley, C. J. Brinker, D. Y. Sasaki and O. A. Negrete, *Sci. Rep.*, 2018, **8**, 13990.
- 91 M. Zhou, Y. Xing, X. Li, X. Du, T. Xu and X. Zhang, *Small*, 2020, **16**, 1–11.
- 92 L. Zhang, X. Zhang, G. Lu, F. Li, W. Bao, C. Song, W. Wei and G. Ma, *Small*, 2019, **15**, 1–13.
- 93 R. Michel, T. Plostica, L. Abezgauz, D. Danino and M. Gradzielski, *Soft Matter*, 2013, **9**, 4167–4177.
- 94 Y. Yu, S. M. Anthony, L. Zhang, S. C. Bae and S. Granick, *J. Phys. Chem. C*, 2007, **111**, 8233–8236.
- 95 M. De Cuyper and M. Joniau, *Eur. Biophys. J.*, 1988, **15**, 311–319.
- 96 Z. Wang, Y. Yan, C. Li, Y. Yu, S. Cheng, S. Chen, X. Zhu, L. Sun, W. Tao, J. Liu and F. Wang, *ACS Nano*, , DOI:10.1021/acsnano.2c00327.
- 97 A. Zendrini, L. Paolini, S. Busatto, A. Radeghieri, M. Romano,

- M. H. M. Wauben, M. J. C. van Herwijnen, P. Nejsum, A. Borup, A. Ridolfi, C. Montis and P. Bergese, *Front. Bioeng. Biotechnol.*, 2020, **7**, 1–10.
- 98 D. Maiolo, L. Paolini, G. Di Noto, A. Zandrini, D. Berti, P. Bergese and D. Ricotta, *Anal. Chem.*, 2015, **87**, 4168–4176.
- 99 D. Bochicchio and L. Monticelli, *Adv. Biomembr. Lipid Self-Assembly*, 2016, **23**, 117–143.
- 100 A. Ridolfi, L. Caselli, M. Baldoni, C. Montis, F. Mercuri, D. Berti, F. Valle and M. Brucale, *Langmuir*, 2021, **37**, 12027–12037.
- 101 J. Eid, H. Razmazma, A. Jraj, A. Ebrahimi and L. Monticelli, , DOI:10.1021/acs.jpcc.0c04253.
- 102 S. Thamphiwatana, V. Fu, J. Zhu, D. Lu, W. Gao and L. Zhang, *Langmuir*, 2013, **29**, 12228–12233.
- 103 L. Zhang and S. Granick, *Nano Lett.*, 2006, **6**, 694–698.
- 104 M. Schulz, A. Olubummo and W. H. Binder, *Soft Matter*, 2012, **8**, 4849.
- 105 S.-W. Hu, C.-Y. Huang, H.-K. Tsao and Y.-J. Sheng, *Phys. Rev. E*, 2019, **99**, 012403.
- 106 A. Balestri, L. Chiappisi, C. Montis, S. Micciulla, B. Lonetti and D. Berti, *Langmuir*, 2020, **36**, 10941–10951.
- 107 T. K. Lind, M. Cárdenas and H. P. Wacklin, *Langmuir*, 2014, **30**, 7259–7263.
- 108 G. Sauerbrey, *Zeitschrift für Phys.*, 1959, **155**, 206–222.
- 109 R. Mezzenga, J. M. Seddon, C. J. Drummond, B. J. Boyd, G. E. Schröder-Turk and L. Sagalowicz, *Adv. Mater.*, , DOI:10.1002/adma.201900818.
- 110 Y. Deng and M. Mieczkowski, *Protoplasma*, 1998, **203**, 16–25.
- 111 Y. Deng and A. Angelova, *Front. Cell Dev. Biol.*, 2021, **9**, 1–21.
- 112 N. G. Bastús, J. Comenge and V. Puentes, *Langmuir*, 2011, **27**, 11098–11105.
- 113 N. G. Bastús, F. Merkoçi, J. Piella and V. Puentes, *Chem. Mater.*, 2014, **26**, 2836–2846.

- 114 M. Zabara, B. Senturk, M. Gontsarik, Q. Ren, M. Rottmar, K. Maniura-Weber, R. Mezzenga, S. Bolisetty and S. Salentinig, *Adv. Funct. Mater.*, , DOI:10.1002/adfm.201904007.
- 115 R. Kariuki, R. Penman, S. J. Bryant, R. Orrell-Trigg, N. Meftahi, R. J. Crawford, C. F. McConville, G. Bryant, K. Voitchovsky, C. E. Conn, A. J. Christofferson and A. Elbourne, *ACS Nano*, 2022, **16**, 17179–17196.
- 116 S. Djokić, *Bioinorg. Chem. Appl.*, , DOI:10.1155/2008/436458.
- 117 S. Anees Ahmad, S. Sachi Das, A. Khatoon, M. Tahir Ansari, M. Afzal, M. Saquib Hasnain and A. Kumar Nayak, *Mater. Sci. Energy Technol.*, 2020, **3**, 756–769.
- 118 N. William, F. Bamidoro, P. A. Beales, R. Drummond-Brydson, N. Hondow, S. Key, A. Kulak, A. C. Walsh, S. Winter and L. A. Nelson, *J. Colloid Interface Sci.*, 2021, **594**, 101–112.
- 119 C. M. Beddoes, C. P. Case and W. H. Briscoe, *Adv. Colloid Interface Sci.*, 2015, **218**, 48–68.
- 120 M. Simunovic, C. Prévost, A. Callan-Jones and P. Bassereau, *Philos. Trans. R. Soc. A Math. Phys. Eng. Sci.*, 2016, **374**, 20160034.
- 121 P. B. Canham, *J. Theor. Biol.*, 1970, **26**, 61–81.
- 122 G. Raposo and W. Stoorvogel, *J. Cell Biol.*, 2013, **200**, 373–383.
- 123 H. Saari, E. Lázaro-Ibáñez, T. Viitala, E. Vuorimaa-Laukkanen, P. Siljander and M. Yliperttula, *J. Control. Release*, 2015, **220**, 727–737.
- 124 R. Van Der Meel, M. H. A. M. Fens, P. Vader, W. W. Van Solinge, O. Eniola-Adefeso and R. M. Schiffelers, *J. Control. Release*, 2014, **195**, 72–85.
- 125 A. C. Dumitru, M. A. Poncin, L. Conrard, Y. F. Dufrêne, D. Tyteca and D. Alsteens, *Nanoscale Horizons*, 2018, **3**, 293–304.
- 126 C. Alibert, B. Goud and J.-B. Manneville, *Biol. Cell*, 2017, **109**, 167–189.
- 127 D. Bochicchio and L. Monticelli, 2016, pp. 117–143.
- 128 J. F. Nagle, M. S. Jablin, S. Tristram-Nagle and K. Akabori, *Chem. Phys. Lipids*, 2015, **185**, 3–10.

- 129 J. Cardellini, L. Caselli, E. Lavagna, S. Salassi, H. Amenitsch, M. Calamai, C. Montis, G. Rossi and D. Berti, *J. Phys. Chem. C*, 2022, **126**, 4483–4494.
- 130 F. Wang, D. E. Curry and J. Liu, *Langmuir*, 2015, **31**, 13271–13274.
- 131 J. F. Nagle, *Chem. Phys. Lipids*, 2017, **205**, 18–24.
- 132 L. Paolini, S. Federici, G. Consoli, D. Arceri, A. Radeghieri, I. Alessandri and P. Bergese, *J. Extracell. Vesicles*, 2020, **9**, 1741174.
- 133 S. Gavas, S. Quazi and T. M. Karpiński, *Nanoscale Res. Lett.*, 2021, **16**, 173.
- 134 S. Hua, M. B. C. de Matos, J. M. Metselaar and G. Storm, *Front. Pharmacol.*, , DOI:10.3389/fphar.2018.00790.
- 135 M. Henriksen-Lacey, S. Carregal-Romero and L. M. Liz-Marzán, *Bioconjug. Chem.*, 2017, **28**, 212–221.
- 136 E. Pedziwiatr-Werbicka, K. Horodecka, D. Shcharbin and M. Bryszewska, *Curr. Med. Chem.*, 2020, **28**, 346–359.
- 137 X. Zhen, P. Cheng and K. Pu, *Small*, 2019, **15**, 1804105.
- 138 M. M. Van Schooneveld, E. Vucic, R. Koole, Y. Zhou, J. Stocks, D. P. Cormode, C. Y. Tang, R. E. Gordon, K. Nicolay, A. Meijerink, Z. A. Fayad and W. J. M. Mulder, *Nano Lett.*, 2008, **8**, 2517–2525.
- 139 A. Luchini and G. Vitiello, *Front. Chem.*, 2019, **7**, 1–16.
- 140 P. Fathi, L. Rao and X. Chen, *View*, 2021, **2**, 20200187.
- 141 J. Cardellini, C. Montis, F. Barbero, I. De Santis, L. Caselli and D. Berti, *Front. Bioeng. Biotechnol.*, , DOI:10.3389/fbioe.2022.848687.
- 142 P. J. Chung, H. L. Hwang, K. Dasbiswas, A. Leong and K. Y. C. Lee, *Langmuir*, 2018, **34**, 13000–13005.
- 143 S. Savarala, F. Monson, M. A. Ilies and S. L. Wunder, *Langmuir*, 2011, **27**, 5850–5861.
- 144 S. Mornet, O. Lambert, E. Duguet and A. Brisson, *Nano Lett.*, 2005, **5**, 281–285.

- 145 C.-H. Wu, J. Cook, S. Emelianov and K. Sokolov, *Adv. Funct. Mater.*, 2014, **24**, 6862–6871.
- 146 H. Zhou, F. Zou, K. Koh and J. Lee, *J. Biomed. Nanotechnol.*, 2014, **10**, 2921–2949.
- 147 H. Zhou, J. Lee, T. J. Park, S. J. Lee, J. Y. Park and J. Lee, *Sensors Actuators, B Chem.*, 2012, **163**, 224–232.
- 148 L. Caselli, A. Ridolfi, J. Cardellini, L. Sharpnack, L. Paolini, M. Bruciale, F. Valle, C. Montis, P. Bergese and D. Berti, *Nanoscale Horizons*, 2021, **6**, 543–550.
- 149 S. S. Leong, Z. Ahmad and J. K. Lim, *Soft Matter*, 2015, **11**, 6968–6980.
- 150 M. J. Grimson, *J. Chem. Soc. Faraday Trans. 2*, 1983, **79**, 817.
- 151 J. Brunner-Popela and O. Glatter, *J. Appl. Crystallogr.*, 1997, **30**, 431–442.
- 152 R. Pecora, 2000, 123–131.
- 153 J. T. Edward, *J. Chem. Educ.*, 1970, **47**, 261.
- 154 M. Shibayama, T. Karino and S. Okabe, *Polymer (Guildf.)*, 2006, **47**, 6446–6456.
- 155 J. D. Clogston and A. K. Patri, 2011, pp. 63–70.
- 156 M. Rodahl, F. Höök, C. Fredriksson, C. A. Keller, A. Krozer, P. Brzezinski, M. Voinova and B. Kasemo, *Faraday Discuss.*, 1997, **107**, 229–246.
- 157 J. Cardellini, A. Balestri, C. Montis and D. Berti, *Pharmaceutics*, , DOI:10.3390/pharmaceutics13060861.
- 158 A. Nwaneshiudu, C. Kuschal, F. H. Sakamoto, R. Rox Anderson, K. Schwarzenberger and R. C. Young, *J. Invest. Dermatol.*, 2012, **132**, 1–5.
- 159 N. Jalili and K. Laxminarayana, *Mechatronics*, 2004, **14**, 907–945.
- 160 R. García, *Surf. Sci. Rep.*, 2002, **47**, 197–301.
- 161 S. J. Marrink, H. J. Risselada, S. Yefimov, D. P. Tieleman and A. H. de Vries, *J. Phys. Chem. B*, 2007, **111**, 7812–7824.

- 162 X. Bai, G. McMullan and S. H. Scheres, *Trends Biochem. Sci.*, 2015, **40**, 49–57.

Membrane Phase Drives the Assembly of Gold Nanoparticles on Biomimetic Lipid Bilayers (Paper I)

Jacopo Cardellini, Lucrezia Caselli, Enrico Lavagna, Sebastian Salassi, Heinz Amenitsch, Martino Calamai, Costanza Montis, Giulia Rossi, and Debora Berti, *J.*

Phys. Chem. C 2022, 126, 9, 4483–4494.

Membrane Phase Drives the Assembly of Gold Nanoparticles on Biomimetic Lipid Bilayers

Published as part of *The Journal of Physical Chemistry virtual special issue "Marie-Paule Pileni Festschrift"*.

Jacopo Cardellini, Lucrezia Caselli, Enrico Lavagna, Sebastian Salassi, Heinz Amenitsch, Martino Calamai, Costanza Montis, Giulia Rossi, and Debora Berti*

Cite This: *J. Phys. Chem. C* 2022, 126, 4483–4494

Read Online

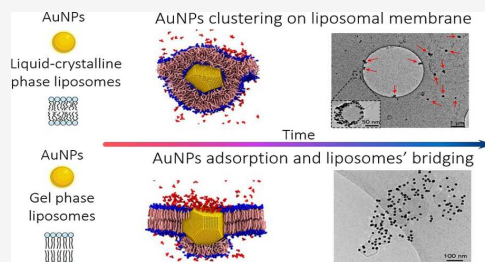
ACCESS |

Metrics & More

Article Recommendations

Supporting Information

ABSTRACT: In recent years, many efforts have been devoted to investigating the interaction of nanoparticles (NPs) with lipid biomimetic interfaces, both from a fundamental perspective aimed at understanding relevant phenomena occurring at the nanobio interface and from an application standpoint for the design of novel lipid–nanoparticle hybrid materials. In this area, recent reports have revealed that citrate-capped gold nanoparticles (AuNPs) spontaneously associate with synthetic phospholipid liposomes and, in some cases, self-assemble on the lipid bilayer. However, the mechanistic and kinetic aspects of this phenomenon are not yet completely understood. In this study, we address the kinetics of interaction of citrate-capped AuNP with lipid vesicles of different rigidities (gel-phase rigid membranes on one side and liquid-crystalline-phase soft membranes on the other). The formation of AuNP–lipid vesicle hybrids was monitored over different time and length scales, combining experiments and simulation. The very first AuNP–membrane contact was addressed through molecular dynamics simulations, while the structure, morphology, and physicochemical features of the final colloidal objects were studied through UV–visible spectroscopy, small-angle X-ray scattering, dynamic light scattering, and cryogenic electron microscopy. Our results highlight that the physical state of the membrane triggers a series of events at the colloidal length scale, which regulate the final morphology of the AuNP–lipid vesicle adducts. For lipid vesicles with soft membranes, the hybrids appear as single vesicles decorated by AuNPs, while more rigid membranes lead to flocculation with AuNPs acting as bridges between vesicles. Overall, these results contribute to a mechanistic understanding of the adhesion or self-assembly of AuNPs onto biomimetic membranes, which is relevant for phenomena occurring at the nano–bio interfaces and provide design principles to control the morphology of lipid vesicle–inorganic NP hybrid systems.



1. INTRODUCTION

The study of interactions between engineered inorganic nanoparticles (NPs) and biomimetic membranes is a very active area of research, inspired by the need to broaden the understanding of the behavior of synthetic nanomaterials at nano–bio interfaces.^{1–3} Over the past several years, the number of reports on the design and application of engineered NPs in nanomedicine has grown exponentially; however, to date the clinical translation of NPs is limited. This limitation is mainly due to a lack of fundamental knowledge on the fate of NPs once in living organisms, which is intimately related to the nature and strength of interactions with biomolecules and biological barriers, such as cell membranes.^{4,5}

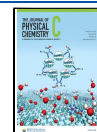
Specifically, NP adhesion to lipid membranes is a pivotal step that regulates endocytic pathways and biological responses. It involves several interfacial processes, such as ligand–receptor binding,⁶ electrostatic interactions,⁷ and membrane wrapping,⁶ each of which is driven by specific or

nonspecific forces.⁸ However, determining the general aspects that govern the nano–bio interaction is not trivial due to the complex and heterogeneous nature of biological membranes. Depending on their composition, biological membranes display different local curvatures, elasticities, and permeabilities, which might affect their response to NP adhesion;^{9–11} moreover, the occurrence of lateral phase-separated domains with different compositions and rigidities (i.e., lipid rafts) is related to cell trafficking phenomena,¹² suggesting that membrane viscoelastic properties are key to controlling the

Received: October 12, 2021

Revised: February 7, 2022

Published: March 1, 2022



phenomena at the nano–bio interfaces (from NP adhesion to NP uptake).

The development of synthetic lipid membranes, such as liposomes, giant unilamellar vesicles (GUV), and supported lipid bilayers (SLB), represents a valuable strategy to systematically investigate how such parameters affect the interaction with NPs in simplified and controlled conditions and to predict the relevant aspects that govern the biological fate of NPs.^{13–15,2} In addition, the interaction of lipid membranes with NPs has attracted considerable interest not only for biomimetic studies but also for application purposes. NPs and lipid scaffolds have been successfully combined to form intelligent drug delivery systems (as magnetoliposomes,^{16,17} or magnetocubosomes^{8,19}) or nanodevices for applications in diagnostics and theranostics.^{20,21} The basic design principles of these devices leverage the spontaneous assembly of NPs with organized lipid assemblies to merge the specific features of inorganic nanoparticles, such as responsivity to magnetic fields²² and optical and thermal properties,^{23,24} with the biocompatibility and pharmacokinetic properties of lipid aggregates.^{25,26} The NPs' response to external forces provides additional control parameters to tune the phase behavior. In addition, the self-organization of lipid assemblies can provide a structural template to control NP–NP interactions and possibly steer the formation of NP suprastructures with enhanced optical or magnetic properties with respect to those of isolated nanoparticles.¹⁹

One interesting example is the spontaneous association of synthetic unilamellar zwitterionic liposomes and citrate-capped gold nanoparticles (AuNPs).^{27–29} After the spontaneous adsorption of NPs on the lipid membrane, the characteristic localized surface plasmon resonance (LSPR) of AuNPs experiences a red-shift accompanied by the appearance of a secondary peak, centered at about 610 nm, which is associated with a color change of the dispersion from red to purple or dark blue. This optical effect is caused by plasmon–plasmon coupling driven by the decrease of the interparticle distance, indicating the membrane-templated aggregation of NPs. By challenging synthetic liposomes of different rigidities with the citrate-stabilized dispersion of AuNPs, we recently demonstrated that the observed LSPR shifts are closely related to the stiffness of the liposomes, which is determined by the lipidic composition of the bilayer.³⁰ In particular, the intensity of the red-shifted peak, i.e., the hallmark of the AuNP aggregation, is minimized for rigid liposomes enveloped by a gel-phase bilayer; in this case, the rigid target membrane is not prone to bend and wrap the NP after NP adhesion, limiting the interfacial NPs–lipid membrane interaction. On the contrary, the lipid membrane–NP interaction and, in turn, the red-shifted peak are maximized for soft liposomes with liquid-crystalline membranes, which are able to efficiently bend and wrap the NPs.³¹

In this work, we address the mechanistic details of this phenomenon by monitoring the interaction of Turkevich–Frens gold nanoparticles with lipid vesicles of different rigidities at different length scales and time scales. Specifically, molecular dynamics (MD) simulations allowed the monitoring of the localized phenomena occurring at the very moment of NP adhesion to the target membranes. Kinetic spectroscopic and scattering data (UV–vis spectroscopy, dynamic light scattering (DLS), and small-angle X-ray scattering (SAXS)) allowed the monitoring the evolution of the NP–lipid vesicle interaction on a colloidal length scale and for longer times

(from a few seconds to a few minutes). Finally, cryogenic electron microscopy (Cryo-EM) allowed the determination of the overall morphological characteristics of NP–lipid vesicle hybrids for a long incubation time. Our approach leverages a detailed comprehension of the energetic contributions that drive the formation of hybrid assemblies over different time and length scales, from a few nanometers, where the membrane rigidity plays the major role, to hundreds of nanometers, where colloidal forces govern the interactions. Specifically, we chose two prototypical synthetic liposomal systems (namely 1,2-dioleoyl-*sn*-glycero-3-phosphocholine (DOPC), characterized by a fluid phase at r.t., and 1-dipalmitoyl-*sn*-glycero-3-phosphocholine (DPPC), characterized by a gel-like phase at r.t.) with markedly different bilayer bending rigidities to show how the first interaction with AuNPs initiates a cascade of colloidal events, which result in completely different hybrid lipid–NP suprastructures.

2. METHODS

2.1. Materials. Tetrachloroauric (III) acid and trisodium citrate dihydrate were provided by Sigma-Aldrich (St. Louis, MO). 1,2-Dioleoyl-*sn*-glycero-3-phosphocholine (DOPC) and 1-dipalmitoyl-*sn*-glycero-3-phosphocholine (DPPC) were provided by Avanti Polar Lipids. All chemicals were used as received. Milli-Q-grade water was used in all preparations.

2.2. Synthesis of AuNPs. Anionic gold nanospheres 12 nm in size were synthesized according to the Turkevich–Frens method.^{27,32} Briefly, 20 mL of a 1 mM HAuCl₄ aqueous solution was brought to the boiling temperature under constant and vigorous magnetic stirring. To the mixture was then added 2 mL of a 1% citric acid solution. The solution was further boiled for 10 min until it acquired a deep red color. The nanoparticle solution was then slowly cooled to room temperature.

2.3. Preparation of Lipid Vesicles. To prepare the DOPC and DPPC liposomes, the proper amount of lipid was dissolved in chloroform, and a lipid film was obtained by evaporating the solvent under a stream of nitrogen and overnight vacuum drying. The film was then swollen and suspended in warm (50 °C) Milli-Q water by vigorous vortex mixing to obtain a final 4 mg/ml lipid concentration. The resultant multilamellar vesicles (MVL) in water were subjected to 10 freeze–thaw cycles and extruded 10 times through two stacked polycarbonate membranes with a 100 nm pore size at room temperature to obtain unilamellar vesicles (ULV) with a narrow and reproducible size distribution. The filtration was performed with the Extruder (Lipex Biomembranes, Vancouver, Canada) through Nuclepore membranes.

2.4. UV–Vis Spectroscopy. UV–vis spectra were recorded with a Cary 3500 UV–vis spectrophotometer.

2.5. Cryo-TEM. On glow-discharged Quantifoil Cu 300 R2/2 grids were applied 3 μL of AuNPs-DOPC and AuNPs-DPPC hybrids. The hybrids were plunge frozen in liquid ethane using an FEI Vitrobot Mark IV (Thermo Fisher Scientific) instrument. Excess liquid was removed by blotting for 1 s (blot force of 1) using filter paper under 100% humidity and 10 °C. Cryo-EM data were collected at the Florence Center for Electron Nanoscopy (FloCEN), University of Florence, on a Glacios (Thermo Fisher Scientific) instrument at 200 kV equipped with a Falcon III detector operated in the counting mode. Images were acquired using EPU software with a physical pixel size of 2.5 Å and a total electron dose of ~ 50 e⁻/Å² per micrograph.

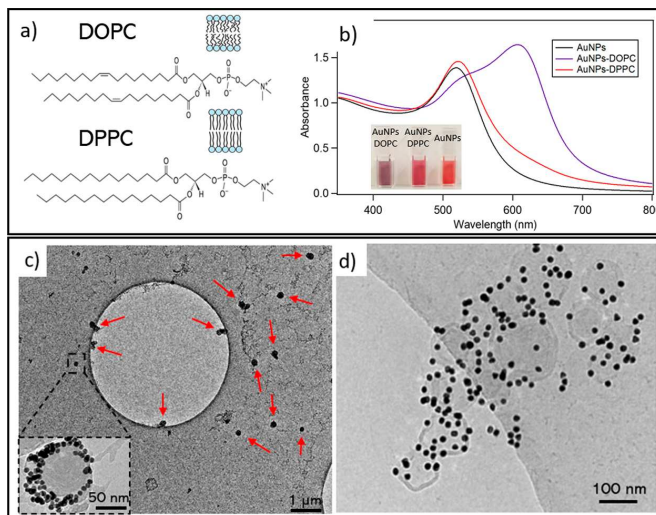


Figure 1. (a) Molecular structures of DOPC (1,2-dioleoyl-*sn*-glycero-3-phosphocholine) with a sketch of the gel bilayer portion and DPPC (1,2-dipalmitoyl-*sn*-glycero-3-phosphocholine) with a sketch of the gel bilayer portion. (b) UV–visible spectra of AuNPs, AuNPs-DPPC hybrid, and AuNPs-DOPC hybrid collected after 10 min of incubation. Cryo-Tem images of (c) AuNPs-DOPC composites and (d) AuNPs-DPPC composites.

2.6. Small-Angle X-ray Scattering. AuNP–liposome dispersions were studied at the SAXS beamline of synchrotron radiation Elettra (Trieste, Italy), which was operated at 2 GeV and a 300 mA ring current. The experiments were carried out with $\lambda = 1.5 \text{ \AA}$, and the SAXS signal was detected with a Pilatus 3 IM detector in the q -range from 0.009 to 0.7 \AA^{-1} . The SAXS curves were recorded in a glass capillary.

2.7. Dynamic Light Scattering. DLS measurements at $\theta = 90^\circ$ and the ζ -potential determination were performed using a Brookhaven Instrument 90 Plus (Brookhaven, Holtsville, NY). Each measurement was an average of 10 repetitions of 1 min each, and measurements were repeated 10 times. The autocorrelation functions (ACFs) were analyzed through cumulant fitting stopped at the second order for samples characterized by a single monodisperse population, allowing an estimate of the hydrodynamic diameter of particles and the polydispersity index. For polydisperse samples, the experimental ACFs were analyzed through the Laplace inversion according to the CONTIN algorithm. ζ -potentials were obtained from the electrophoretic mobility u according to Helmholtz–Smoluchowski equation

$$\zeta = \left(\frac{\eta}{\varepsilon} \right) \times u \quad (1)$$

with η was the viscosity of the medium and ε was the dielectric permittivity of the dispersing medium. The ζ -potential values are reported as averages from 10 measurements.

2.8. Gel Electrophoresis. Custom 0.3% agarose gels made with 0.125× Tris–acetate–EDTA (TAE) buffer, i.e., 5 mM Tris (pH 7.6), 2.5 mM acetic acid, and 0.125 mM EDTA, were run in 0.125× TAE buffer using a Bio-Rad submerged horizontal electrophoresis Mini-Sub Cell GT system at 150 V for 10 min.

The external electric field makes the particles migrate according to their electrophoretic mobility, which is expressed by the following equation:

$$\mu = \frac{2\varepsilon\zeta}{3\eta} f(\kappa R) \quad (2)$$

where ε is the dielectric permittivity of the medium, R the particle radius, $f(\kappa R)$ is the Henry function, and ζ is the particle's ζ -potential.³³

2.9. Computational Methods. **2.9.1. Simulation Parameters.** All simulations were set up with the coarse-grained Martini force field³⁴ and run with Gromacs ver. 2020.6. The cutoff for Van der Waals and electrostatic interactions was set to 1.1 nm, and the dielectric constant was set to $\varepsilon_r = 15$. For equilibration and production runs, we set the time step to 20 fs and used the NpT ensemble, with temperature and pressure set to 300 K and 1 bar, respectively. For temperature coupling, we used the velocity rescale thermostat³⁵ with $\tau_T = 1$ ps. For pressure coupling, we used the Berendsen³⁶ barostat in equilibration runs (with $\tau_p = 4$ ps) and the Parrinello–Rahman barostat in production runs (with $\tau_p = 12$ –18 ps), with compressibility set at $3 \cdot 10^{-4} \text{ bar}^{-1}$. We always used the semi-isotropic pressure-coupling scheme.

2.9.2. Au and Citrate Coarse Grained Model. The model for the NPs and citrate was custom developed and described in a previous work.³⁷ For Au nanoparticles, we used a 1:1 atom-to-bead mapping scheme, and the Lennard-Jones parameters of the Au–Au interaction were set to the Heinz nonpolarizable potential.³⁸ We used two models of Au NPs, both in the shape of a truncated octahedron with diameters of about 8 (12934 beads) and 14 nm (69473 beads). For the 8 nm NP, the size of the largest facets was about 5 nm, comparable to the membrane thickness; for the 14 nm NP, that size was almost doubled (9 nm). The model for citrate was composed of four beads, one representing the hydroxyl terminal group and the others representing the carboxylate terminal groups. Au and citrate non-bonded interactions were parametrized using target properties from atomistic and experimental data, such as the partition coefficient between ether and octanol and adsorption or dimerization free energy profiles.

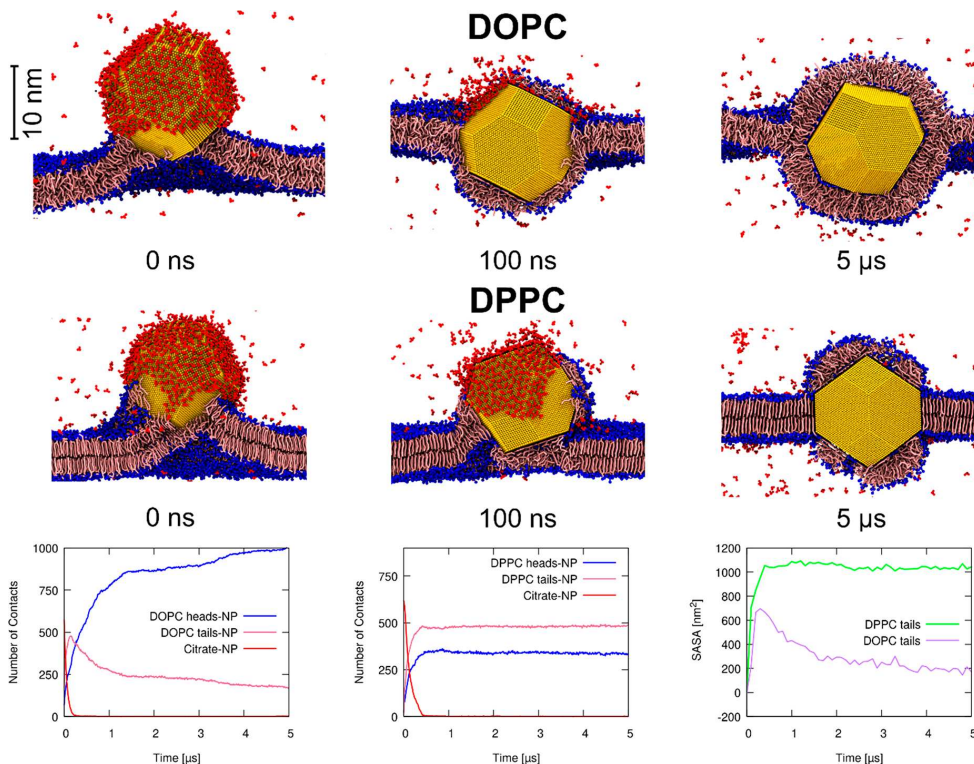


Figure 2. Difference between the penetration process of a citrate AuNP in DOPC and DPPC. For each kind of bilayer, we show three snapshots at significant moments of the wrapping process, where the NP is represented in yellow, citrate is represented in red, the lipid headgroups are represented in blue, and the lipid tails are represented in pink. In the bottom row, we show the time evolution of the number of contacts between the NPs and citrate molecules (in red), lipid headgroups (blue), and lipid tails (pink) for both simulations in addition to the time evolution of the SASA plots of the lipid tails. In the SASA plots, the area is set to 0 for the unperturbed membrane. Time $t = 0$ corresponds to the first NP–membrane contact. The time series are shown only up to $5.0 \mu\text{s}$ to better highlight the fast initial time evolution, although the simulations reached $10.0 \mu\text{s}$ in both cases.

2.9.3. Simulated systems. We prepared several configurations containing a flat membrane and a citrate-capped Au NP system. At the start of each simulation, the NP was placed in the water phase a few nanometers away from the surface of the bilayer. For the 8 nm NPs, we prepared small boxes (1352 lipids) and larger boxes (5408 lipids) both with DOPC and DPPC; for the 14 nm NPs, we set up a box with 8450 DOPC lipids and another with 8480 DPPC lipids. To obtain gel DPPC, we performed a gelification run of $1 \mu\text{s}$ using different temperature couplings for water (300 K) and the membrane (250 K), starting from a fluid DPPC membrane.

3. RESULTS AND DISCUSSION

We selected DOPC and DPPC vesicles with a monodisperse size of 100 nm (see the SI) for their well-known difference in terms of membrane stiffness.^{39–41} As sketched in Figure 1 (upper panel), these lipids have the same zwitterionic polar head (PC) but different acyl tails, which are characterized by the absence of unsaturations for DPPC and the presence of two monounsaturated chains (with 6-unsaturations) for DOPC. Such differences dramatically affect the viscoelastic properties of the membrane. At room temperature, DPPC membranes are in a gel state, with highly ordered lipid acyl

tails. Conversely, DOPC liposomes are lined by a fluid bilayer with a lower bending rigidity and a higher lateral mobility.^{42,43} As anticipated in the introduction, these structural differences in the lipid acyl chains affect the membrane's ability to interact with NPs and, in turn, the extent of the membrane-templated clustering of NPs. Accordingly, in a recent work we were able to exploit the extent of AuNP aggregation to estimate the vesicle's rigidity.³⁰

Figure 1b shows some representative UV–vis spectra obtained for 6.3 nM AuNPs with a 12 nm diameter (black curve),²⁷ compared to the spectra obtained for NP–vesicles hybrids prepared with a liposome–AuNP ratio equal to 1/16 (red curve for NPs–DPPC, blue curve for NPs–DOPC). This liposome–AuNP number ratio was selected on the basis of our previous publication, which highlights that the aggregation of AuNPs is maximized by low liposome amounts within the mix.

The UV–vis spectra were recorded after 10 min of incubation. As displayed in Figure 1b, the interaction of AuNPs with DOPC and DPPC membranes leads to significant variations in the optical properties of the dispersions. Specifically, the aqueous dispersion of AuNPs–DOPC dramatically turns blue or purple (see the pictures in the inset in Figure 1b). The occurrence of a secondary plasmonic peak at

about 610 nm, caused by a decrease in the interparticle distance, reveals AuNPs clustering on the DOPC soft membrane. Conversely, the incubation of AuNPs with rigid DPPC liposomes causes a slight bathochromic shift and a broadening of the characteristic AuNP absorption profile.

To obtain structural information on the AuNP–lipid vesicle hybrid, we performed Cryo-EM imaging. Panels c and d in Figure 1 show representative Cryo-TEM images of DOPC and DPPC vesicles, respectively, challenged with AuNPs. Images were collected after an incubation time of 10 min. The images clearly show that for both liposomes AuNPs adsorb without apparent membrane disruption. However, there is a dramatic morphological difference between these hybrids. Specifically, for fluid DOPC membranes AuNPs adhere to the lipid shell and cluster, in line with the plasmon coupling observed in the UV–vis spectra. In addition, all the lipid vesicles appear as single vesicles, possibly decorated by NP clusters (see red arrows, Figure 1c) without the occurrence of aggregates of the vesicles, giving rise to substantially monodisperse hybrids.

Conversely, for gel vesicles (DPPC, figure 1D) most AuNPs associated the lipid membrane are single particles rather than clusters. Moreover, in all the collected images (see Figures S5 and S6 in the SI for further examples) the DPPC liposomes are connected to each other by AuNP bridges, forming large AuNPs–DPPC vesicle hybrid aggregates.

These results imply that the different degrees of unsaturation of DOPC and DPPC, which lead to the formation of softer or stiffer vesicles, lead not only to different aggregation extents of AuNPs on the lipid membranes but also to the completely different morphologies of AuNP–vesicle hybrids. To understand the mechanistic details of this phenomenon, we monitored this process by combining computational and experimental approaches to access different time scales and length scales

3.1. MD Simulations and Molecular Length Scale Characterization of the AuNP–Lipid Membrane Interaction.

To gain insights on these lipid phase-dependent interactions at the molecular level and in the very first steps of the AuNP–lipid vesicle interaction, we investigated the very first AuNP–membrane contact using MD simulations. Our simulations rely on a recently developed coarse-grained model of citrate-capped Au NPs.³⁷ We have considered two models for the NP. Most of the simulations contain a NP that has a diameter of 8 nm. To rule out significant size effects, we repeated some of the simulations with a larger NP of 14 nm in diameter. Both NPs have the structure of a truncated octahedron, which corresponds to the lowest-energy structure for AuNPs in this size range.⁴⁴ The AuNP citrate coverage in our simulations is 0.97 ± 1.4 citrate/nm², which is consistent with the available experimental literature.³⁷ In ref 37 we calculated the free energy profile for the adsorption of citrate and POPC on the surface of a Au nanoparticle, showing that the interaction with the lipid was thermodynamically favored. Consistently, we observed the spontaneous penetration of Au NPs into POPC fluid bilayers. Here, we ran different sets of unbiased MD simulations in which a single citrate-capped AuNP spontaneously interacts with a DOPC or DPPC lipid bilayer, with the NP starting in the water phase. The list of all simulations and the details of the MD settings are reported in the Methods section.

In the simulations with the DOPC membrane, the penetration of the NP into the bilayer happened in the first tens of nanoseconds. Similarly to what was described for

POPC membranes,^{37,45,46} the membrane wrapped the NP over the following stages (top row of Figure 2): (i) NP–lipid head contact, with the release of citrate in the water phase (ligand exchange); (ii) head–tail flipping of the lipid in contact with the NP; and (iii) the formation of a complete lipid bilayer around the NP, with only heads in contact with its surface. As the figure shows, the head–tail flipping process had already started while the citrate was still being released; overall, the entire process requires less than two microseconds on the coarse-grained time scale of the simulation.

Using similar setups, we performed simulations of a NP interacting with a DPPC bilayer in the gel phase. As a general consideration, we observe that on average the spontaneous onset of the NP–membrane interaction requires more time for NPs–DPPC than for NPs–DOPC, even if the NP starts at the same relative distance from the membrane surface. As the first contact between the Au surface and the lipid headgroups is established, the NP penetrates the DPPC membrane, albeit with significantly different features from the DOPC case. In the central row of Figure 2 we show that the NP pierces the membrane with one of its edges and quickly penetrates the membrane's hydrophobic core. The NP settles in the membrane with its planar facets in a vertical orientation, parallel to the gel-phase lipid tails. Once the NP reaches the midplane of the membrane, the membrane wrapping of the NP is irregular, forming sparse monolayer patches on the NP surface, and leaving several clusters and stripes of lipids with their hydrophobic tails exposed to the water phase. In this situation, the system dynamics slow dramatically. This significant freezing of the system dynamics can be appreciated and quantified by the plot of the temporal evolution of the NP contacts, as shown in Figure 2 for the 14 nm NP model. The NP contacts fully converge after 1 μ s. Furthermore, the plot shows that the initial part of the wrapping process, including the citrate release, is slower than that in DOPC. The gel-phase DPPC lipids adsorbed on the planar NP facets have little to no mobility and do not allow for any further rearrangement of the water-exposed lipid patches. In the plot on the right of the bottom row of Figure 2, we show a time evolution of the solvent accessible surface area (SASA) of the lipid tails. The plot quantifies the water-exposed area of the hydrophobic lipid patches during the interaction of the NP with the two different lipid phases. In DOPC, hydrophobic defects are transient, and their area reaches a maximum during NP penetration and then decreases when a complete DOPC bilayer wraps the NP. On the contrary, in DPPC the hydrophobic defects are permanent on the simulation time scale, as lipid diffusion from the bilayer to the NP surface is almost completely suppressed.

Simulations with 8 nm NPs provide very similar results, as shown in Figure S7 of the SI.

To summarize, molecular dynamics simulations suggest that the outcome of the NP–membrane interaction crucially depends on the membrane lipid phase. Fluid-phase DOPC lipids completely wrap the NP, quickly forming a perfect bilayer around the NP. The external liposome surface would be perturbed little to none by this kind of interaction. On the contrary, the NP interaction with the gel bilayer gets stuck at an intermediate stage of NP penetration. The extremely slow diffusion of lipids in the gel phase freezes the NP–membrane complex in a semiembedded configuration. Neither NP diffusion within the liposome nor further lipid rearrangements would be permitted, leaving significant isolated hydrophobic defects on the surface of the liposome.

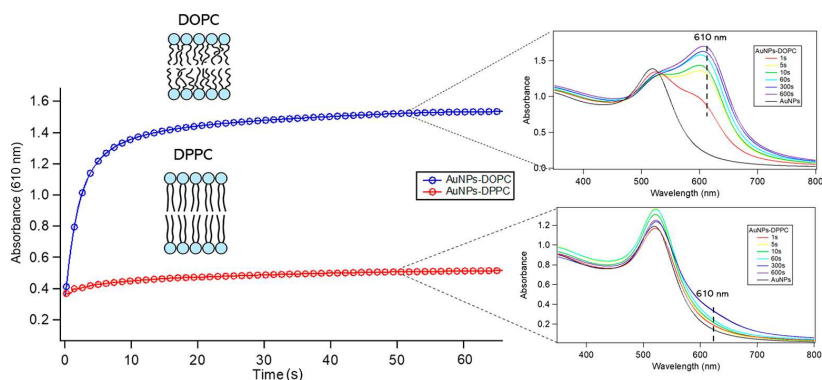


Figure 3. Time evolution of the absorbance of AuNPs-DOPC and AuNPs-DPPC aqueous dispersions ($10 \mu\text{L}$ of 12 nM DOPC or DPPC liposomal dispersions mixed with $300 \mu\text{L}$ of 6.3 nM AuNPs) at 610 nm . The inset shows UV–vis absorption profiles of AuNPs-DOPC (top) and AuNPs-DPPC (bottom) collected after 1, 5, 10, 60, 300, and 600 s of incubation.

3.2. Kinetics of Membrane-Templated AuNP Clustering. Starting from this very localized and short time scale MD investigation of the adhesion of AuNPs to DOPC and DPPC membranes, we performed tailored complementary experiments to monitor the temporal evolution of AuNP–lipid vesicle hybrids. In particular, we used UV–vis spectroscopy and high-resolution SAXS to monitor the evolution of AuNP adhesion and clustering on the target membrane, following the interaction in the first 10 min of incubation (Figures 3 and 4).

Figure 3 reports the increase over time of the UV–vis absorbance at 610 nm , which is diagnostic for NP clustering,³⁰ observed upon the incubation of NPs with DOPC (blue curve)

and DPPC liposomes (red curve). The time evolution of the LSPR when AuNPs are mixed with rigid liposomes (DPPC) is characterized by a constant trend, while for lipid vesicles with a soft membrane (DOPC) a relatively sudden absorbance increase occurs that is associated with the appearance of an additional red-shifted signal in the complete spectrum (Figure 3, upper inset). After a few seconds, this shoulder becomes a well-defined secondary plasmonic peak, the signature of plasmon coupling due to the NPs' close approach. On the other hand, for NPs incubated with DPPC vesicles, the LSPR resonance, peaked at 520 nm for the reference of AuNP dispersion in the same medium, experiences only a very modest absorbance increase at 610 nm . This increase is consistent with the adsorption of NPs onto the liposomal surface, which changes the chemical environment of the NP. In both cases, the absorbance approaches a constant value very rapidly, revealing that NP adhesion to liposomes occurs mostly during the first 30 s of incubation.

The different clustering extent of NPs incubated with DOPC and DPPC liposomes can be interpreted considering the different adhesion modes of NPs, which were previously illustrated for the MD simulations results. Specifically, the membrane's rigidity modulates its ability to bend around the NPs, resulting in different wrapping extents (full wrapping for DOPC and partial wrapping for DPPC) with a markedly different kinetics of citrate/PC exchange and anion release in the two cases (faster citrate release for the AuNPs-DOPC system and slower citrate release for AuNPs-DPPC system). As hypothesized in a recent study,³¹ this burst of citrate release upon AuNP adhesion on a soft membrane can lead to a local transient increase of the ionic strength. Considering the electrostatic origin of the stability of AuNPs¹⁸ versus aggregation, this transient ionic strength increase can trigger the aggregation of the neighboring NPs, with resultant clustering on the lipid membrane³³ in line with UV–vis spectroscopy results. Conversely, for rigid DPPC target membranes the more gradual citrate release strongly limits or completely hampers this effect (see Figures 1 and 3).

We performed high-resolution SAXS at the Elettra synchrotron to determine the structure of AuNP aggregates on the liposomal membrane and to understand the kinetics and mechanism of their formation. The time evolution of the SAXS profiles was followed over the same time frame

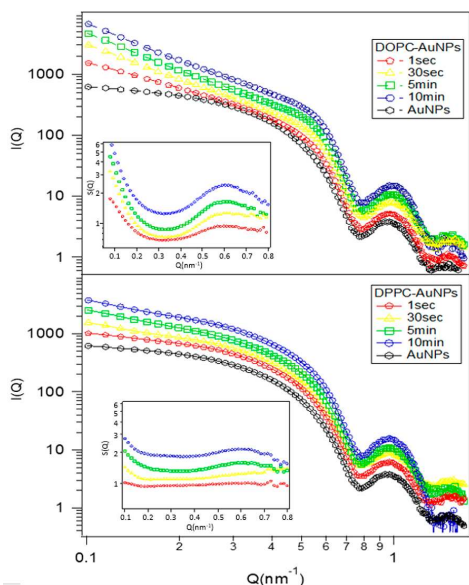


Figure 4. Log–log SAXS profiles of AuNPs-DOPC (top) and AuNPs-DPPC (bottom) hybrids collected after 1 s, 30 s, 5 min, and 10 min of incubation. The inset shows the structure factor of the samples, with correlation peaks related to the center-to-center interparticle distances.

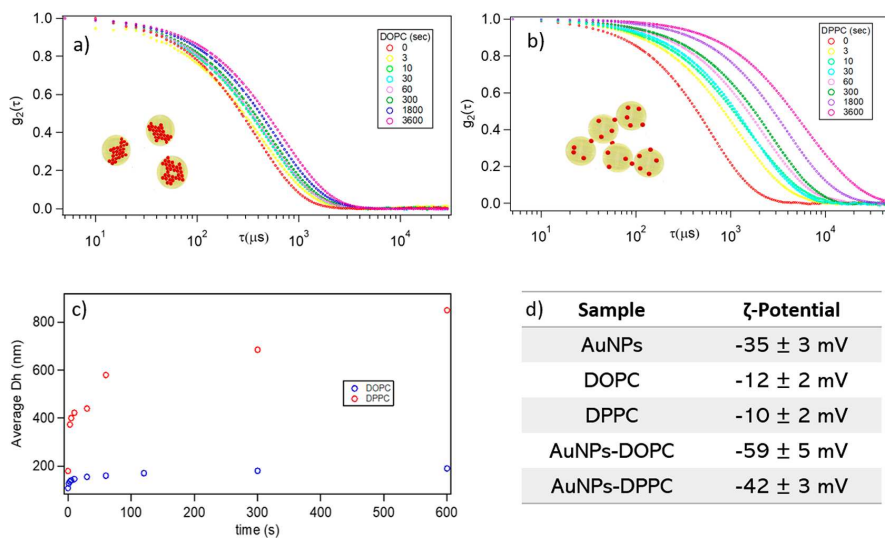


Figure 5. 10 μL of 12 nM DOPC or DPPC liposomal dispersions was mixed with 300 μL of 6.3 nM AuNPs and the hydrodynamic dimension of the hybrids were followed up to one hour. (a) Time evolution of the DLS curves of the AuNPs-DOPC hybrid. (b) Time evolution of the DLS curves of the AuNPs-DPPC hybrid. (c) Time evolution of the average hydrodynamic diameter evaluated by the DLS curves for AuNPs-DOPC and AuNPs-DPPC composites. (d) ζ -Potentials of citrate AuNPs, pure DOPC and DPPC vesicles, and AuNPs-DOPC and AuNPs-DPPC hybrids.

monitored with UV–vis spectrophotometry. Figure 4 displays the SAXS profiles obtained for AuNPs-DOPC systems (top) and AuNPs-DPPC systems (bottom) for increasing incubation times from 1 s to 10 min. A comparison with the reference scattering profiles of the liposomes and the solvent (water) (see Figure S4 in the SI), highlights that in these experimental conditions the scattering intensity of the vesicles is negligible; therefore, SAXS provides specific information on the evolution of the structural arrangement of AuNPs in AuNP–liposome hybrid systems.

For all the samples, the scattered profile is due to a combination of the following: (i) The AuNPs form factor $P(Q)$, accounting for the AuNPs' spherical shape. This contribution is the same in all systems and can be assumed to be equivalent to the SAXS profile obtained for a diluted AuNP dispersion (reported in Figure S1 as a reference). (ii) A structure factor $S(Q)$, which accounts for the interparticle interactions⁴⁷ such as those that lead to AuNPs clustering on the liposomal surface. To understand the evolution of the organization of AuNPs on the lipid shells, we extracted from each spectrum the structure factor $S(Q)$, reported in the inset of Figure 3, by dividing the measured scattered intensity of the hybrids by the profile of the AuNPs at the same concentration. The existence of a structure factor different from unity for such a dilute dispersion of AuNPs constitutes to the evidence of a superstructure of AuNPs. A very coarse-grained analysis provides a correlation between the peak position of $S(Q)$ and an average distance between particles. For AuNPs-DOPC, the Q -position of the peak accounts for an interparticle distance of approximately 11 nm, i.e., particles in direct contact with each other; on the other hand, the weak $S(Q)$ peak of AuNPs-DPPC suggests a lower degree of positional correlation and a larger average interparticle distance, with only a tiny portion of particles in direct contact. These structural results are consistent with Cryo-EM images (shown in Figure 1),

which highlight clusters of AuNPs that are densely packed on the liposomal surface in the case of DOPC and single AuNPs that are separated from each other in the case of DPPC.

The time evolution of the SAXS profiles also provides interesting information on the kinetics of formation of AuNP aggregates on DOPC bilayers. For this hybrid, the $S(Q)$ peak position is time-invariant, but it becomes more and more defined as time increases. This indicates that AuNPs in the AuNPs-DOPC hybrid are in direct contact with each other since 1 s after mixing. As time progresses, the number of clustered particles present in the aggregates increases; however, the interparticle distance within the aggregates does not change, suggesting a fast and irreversible phenomenon without significant structural rearrangements after the first interparticle contacts. On the contrary, the occurrence of the $S(Q)$ signal in AuNPs-DPPC system is slower, and the peak is just slightly visible, revealing slower kinetics of the clustering.

In addition, a clear temporal trend is also apparent in the low- Q region of the $I(Q)$ versus Q plot for AuNPs-DOPC liposomes. Specifically, we notice a power-law signature that appears as a linear dependence in a double logarithmic plot (see Figure 4, upper panel) with a slope that increases (in absolute value) from -0.43 ± 0.02 to -2.01 ± 0.02 with time, reaching a constant value after 30 s (-1.90 ± 0.02 after 30 s and -2.00 ± 0.02 after 5 min). This accounts for the dimensionality of the clusters. A -2 slope is consistent with 2D aggregates, while a -1 slope suggests the presence of elongated 1D structures. The observed slope evolution suggests that the final shape of the AuNP aggregates is a 2D cluster, in line with a full coverage of the liposomal surface by AuNPs (as hypothesized in a recent study³¹). Moreover, it appears that overall the AuNP clusters evolve in dimension, with a progression from a 1D aggregate to a 2D aggregate (see Table S5). Such a rapid variation of the power-law exponent highlights that NP aggregation is a fast process that requires

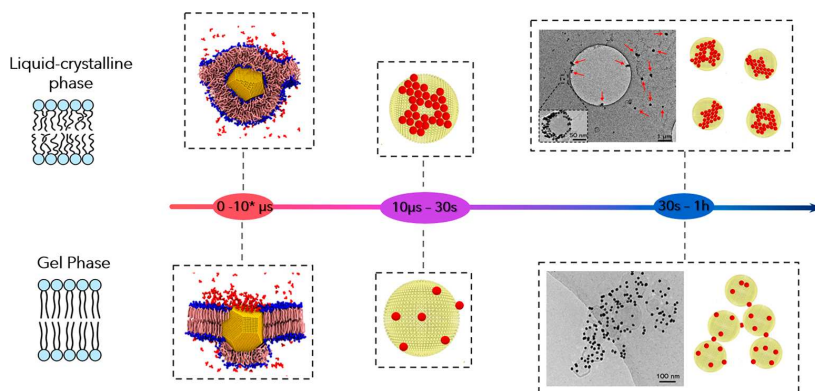


Figure 6. Schematic representation of the interaction mechanisms dependent on the vesicle rigidity. First, the adhesion of the particles and the citrate release occur. Second, the AuNPs in the proximity of the interaction site aggregate according to the kinetics of the citrate release. Finally, the hybrids evolve in single vesicles decorated by AuNPs or in flocculated objects where the particles act as a bridge. We remark that the simulated time scale ($10 \mu\text{s}$) corresponds to $10\text{--}100 \mu\text{s}$ in real time due to the acceleration of the dynamics that is intrinsic to the use of a coarse-grained model.

only a few tens of seconds of incubation to approach an equilibrium arrangement for AuNPs, in line with the time-evolution of the LSPR monitored through UV–vis spectroscopy (Figure 3). A slight slope increase (in absolute value) in the low- Q region can also be noticed for the AuNPs-DPPC hybrids (from -0.43 to -1.02). This variation accounts the absorption and partial aggregation of AuNPs on the DPPC shells, forming much less densely packed AuNPs clusters.

Overall, SAXS and UV–visible measurements are consistent with the hypothesis that the rigidity of the bilayer controls the extent of AuNP clustering. However, in both cases (DOPC and DPPC) the arrangement of AuNPs reaches a stable configuration very rapidly.

We then monitored the hybrids at the colloidal length scale, specifically addressing their colloidal stability with DLS measurements for longer incubation times (up to one hour). The main results are summarized in Figure 5, with details on preparation and data analysis reported in the caption.

Panels a and b in Figure 5 report representative normalized DLS curves obtained for DOPC–AuNPs systems and DPPC–AuNPs systems, respectively, within 1 h of incubation. The average diameters of AuNPs–vesicle hybrids for increasing incubation times (Figure 5c) were determined by analyzing the decay times of the autocorrelation functions through a cumulant fitting stopped at the second order. The hydrodynamic diameters (D_h) of DOPC vesicles and AuNPs show an increasing trend over time upon interaction. In a few minutes, a hybrid system with a D_h of about 180 nm forms, which is consistent with the size of the lipid vesicles surrounded by a shell of inorganic nanoparticles.

On the other hand, the interaction of AuNPs with DPPC membranes leads to a sharp increase in the decay times of the autocorrelation functions, i.e., of the sizes of the hybrids. Despite SAXS and UV–vis point toward a weaker interaction of AuNPs with rigid liposomes, DLS results highlight a dramatic decrease of their colloidal stability, with the relatively fast formation and flocculation of micrometer-sized aggregates and, eventually, precipitation. This result is consistent with the aggregation of vesicles, with AuNPs acting as bridging agents in the case of DPPC (see Cryo-EM images in Figure 1 and the insets in Figure 5 a and b).

To further address such a dramatic difference in the colloidal stability of the AuNPs–DOPC and AuNPs–DPPC hybrids, we also measured the ζ -potential (Figure 5d). The ζ -potential is a quantitative measure of the kinetic colloidal stability⁴⁸ of the hybrids. DOPC and DPPC vesicles have a slightly negative ζ -potential in water, in agreement with the literature,⁴⁹ while hybrid systems display an increase in absolute values toward more negative potentials. In particular, the electrostatic stabilization is very pronounced for the DOPC hybrids and may explain their colloidal stability. Conversely, for DPPC the increase (in absolute value) of the ζ -potential upon the adhesion of AuNPs is significantly lower, suggesting that an overall lower surface charge of AuNPs–DPPC hybrids might be related to a higher colloidal instability.

Gradzielsky et al. have shown that the liposome decoration by anionic inorganic particles causes an increase of the absolute value of the surface ζ -potential due to the increase of electric charges on the lipid shell, resulting in the formation of metastable hybrid nano-objects.⁵⁰ The colloidal stabilization was reached only due to the absorption of a sufficient number of particles. Conversely, a low number of particles cannot prevent the liposome fusion and ensure colloidal stability, leading to the rapid destabilization of the dispersion.

In the present case, we hypothesize that the high number of AuNPs assembled on the DOPC liposomes determines a local increase of the negative charge, stabilizing the colloidal dispersion through electrostatic repulsion. For DPPC vesicles, given the lower number of adsorbed NPs on membrane, the electrostatic repulsion is not sufficient to overcome attractive interactions, leading to liposome bridging and flocculation. The dependence of the liposome's stabilization on the extent of surface coverage by charged nanoparticles is well-known in literature;^{51–54,26} however, in the present case we cannot rule out that the phase of the lipid membrane may also play a role.

Specifically, as shown in the MD simulation, considering that the AuNPs adsorbed on rigid membranes in a semi-embedded state are partially exposed to the external aqueous solution, the attractive interaction with the neighboring vesicles may be favored. Moreover, a hydrophobic interaction between the hydrophobic patches exposed to the water in the AuNPs–DPPC semi-embedded configuration might also have a

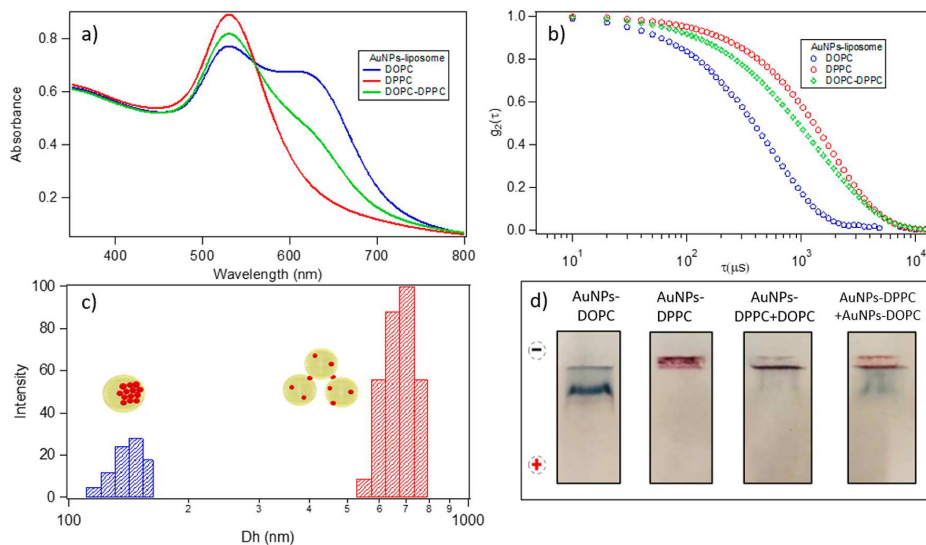


Figure 7. AuNPs-DOPC and AuNPs-DPPC hybrids were prepared mixing 10 μL of 12 nM liposomal dispersions with 300 μL of 6.3 nM AuNPs. To prepare the AuNPs-DOPC+DPPC sample, 300 μL of a 6.3 nM aqueous solution of the AuNPs was added to a mixture of 5 μL of the 12 nM DOPC dispersion and 5 μL of the 12 nM DPPC dispersion. (a) UV-visible spectra of AuNPs-DOPC, AuNPs-DPPC, and AuNPs-DOPC+DPPC samples. (b) DLS curves of AuNPs-DOPC, AuNPs-DPPC, and AuNPs-DOPC+DPPC sample. (c) Double population obtained by the DLS measurement of the AuNPs-DOPC+DPPC composites. (d) Agarose gel electrophoresis analysis of the samples (from left to right: AuNPs-DOPC, AuNPs-DPPC, AuNPs-(DOPC+DPPC), and AuNPs-DOPC+AuNPs-DPPC).

prominent role, eventually leading to the flocculation of the hybrids.

Considering all these results, two different interaction mechanisms can be considered depending on the vesicle's rigidity, starting from the first particle–bilayer contact up to the colloidal regime.

The schematic representation of the processes is reported in Figure 6. (i) First, a AuNP adheres on the lipid membrane, undergoing a membrane-wrapping phenomenon; the extent of AuNP wrapping by the membrane depends on the stiffness of the vesicle, which in turn depends on the state of its membrane, either the gel phase (rigid) or the liquid-crystalline phase (soft). (ii) The first step also controls the kinetics of citrate release upon AuNP adhesion to the target membrane, which is determinant in controlling the interaction of the AuNPs adhered on the liposomal surface with neighboring particles. This in turn leads to the formation of AuNP clusters (on soft membranes) or the separate adhesion of AuNPs (on rigid vesicles). (iii) The different amounts of adhered particles (tight clusters or single particles) and their different natures (protruding from the liposomal surface or wrapped by the lipid membrane) affect the colloidal stability of AuNP–lipid vesicle hybrids, leading to the formation of AuNP-decorated vesicles in the case of soft vesicles and extended vesicles clusters bridged by AuNPs in the case of rigid vesicles.

3.3. Proof of Concept: Separation of Biomimetic Vesicles of Different Stiffnesses. The whole set of experimental measurements that were performed allowed us to discriminate between two interaction mechanisms, which were determined by the composition of the vesicles, i.e., on their membrane rigidity. Such a physicochemical characterization can not only be instrumental in fundamental studies but can also provide a design principle to build novel hybrid

materials with the controlled clustering of both NPs and lipid vesicles and, possibly, different tailored colloidal and functional properties dependent on the rigidity of the lipid vesicles.

In addition, the different sizes and ζ -potentials of hybrid AuNP–lipid vesicle systems for rigid (DPPC) and soft (DOPC) vesicles can be exploited as a separative strategy for dispersions of biogenic vesicles (EVs) of different rigidities, given that the purification and separation of extracellular vesicles is still an open issue.⁵⁵ In the following, we will illustrate a proof-of-concept experiment for the separation of DOPC and DPPC vesicles through incubation with AuNPs, followed by gel electrophoresis (Figure 7). To this aim, we prepared a sample containing both DOPC and DPPC and monitored the interaction with AuNPs via UV-visible spectrometry and DLS measurements over 5 min (Figure 7).

The intensity of the red-shifted peak of the mixed sample is intermediate between those obtained for the DOPC and DPPC samples. This behavior suggests that a portion of the AuNPs clusters on the liquid-crystalline membranes, while the remaining ones adhere to the gel-phase vesicles and initiate the bridging process.

Concerning DLS measurements, the correlation function (Figure 7b) of the AuNPs-DOPC+DPPC hybrid clearly displays two main decay times, suggesting the presence of two populations, one consistent with the size of the AuNPs-DOPC hybrid and the other with a larger and less colloiddally stable population of the AuNPs-DPPC hybrid. The smaller population peaked at around 160 nm (Figure 7c), in line with the size of the lipid vesicles of DOPC with a shell of aggregated AuNPs, and the second one, which was much more polydisperse, was centered at 600 nm, consistent with the presence of bridged DPPC liposomes.

These results show that in dispersions where DOPC and DPPC vesicles are present the overall interaction of AuNPs is a combination of the two mechanisms (decoration of single vesicles with AuNP clusters for DOPC liposomes and the adhesion of single AuNPs on vesicles and subsequent bridging for DPPC liposomes); therefore, once the mixed liposomal dispersion, whose liposomes are characterized by practically identical sizes and surface charges, is incubated with AuNPs, the mixture evolves in a combination of highly charged single vesicles decorated by AuNPs (for DOPC vesicles) and less-charged extended aggregates bridged by AuNPs. After interacting with AuNPs, AuNPs-DOPC and AuNPs-DPPC hybrids possess different ζ -potential values and sizes, making the two hybrids easily separable. To prove this hypothesis, the mixed dispersion was analyzed through agarose gel electrophoresis (AGE). This technique has found multiple applications in the field of colloid and NP characterization to determine the charge and size variations of a dispersed system, allowing the separation of two colloidal populations as a function of their differences in dimension and surface potentials.³³

We prepared an agarose gel with four wells (reported in Figure 7d) to compare the electrophoretic mobility of the mixed samples with respect to the isolated samples of AuNPs-DPPC and AuNPs-DOPC: (1) DOPC-AuNPs hybrids, (2) DPPC-AuNPs hybrids, (3) AuNPs added to the DOPC-DPPC mixture, and (4) a mixture of AuNPs-DOPC and AuNPs-DPPC hybrids (hybrids mixed after their formation) (Figure 7d from left to right: AuNPs-DOPC, AuNPs-DPPC, AuNPs-(DOPC+DPPC), and AuNPs-DOPC+AuNPs-DPPC). Immediately prior to loading in the well, 15 μL of each sample was mixed with 5 μL of glycerol to improve the sample deposition.

In the first well, practically all the objects migrated from the starting position toward the end of the channel after ten minutes. Conversely, the AuNPs-DPPC hybrids in the second well did not move from the deposition point. These differences in electrophoretic mobility are primarily due to the increase of the hydrodynamic diameter, since this sample is composed of micrometer-sized bridged objects (see the **Materials and Methods** section for the gel preparation).

When both DOPC and DPPC liposomes are present (i.e., 3 and 4), gel electrophoresis detects two different populations, one with an electrophoretic mobility very similar to that of DOPC-AuNPs and one with a population that behaves similar to the AuNPs-DPPC hybrid.

Even if very preliminary, this experiment shows that the self-assembly of AuNPs on lipid vesicles, which is highly dependent on the rigidity of the lipid vesicles, can be exploited to separate vesicles of similar surface charge and size based on their rigidity. Overall, this proof-of-principle paves the way to explore several possible applications, such as a semiquantitative assay of the rigidity of membrane-enveloped nano-objects in complex samples of biological or synthetic origin or the real-time monitoring of complex phenomena such as liposome fusion, lipid exchange between liposomes, and transient raft formation.

4. CONCLUSIONS

Understanding the interaction of inorganic nanoparticles with synthetic vesicles is crucial both to improve our fundamental knowledge of the main determinants driving phenomena at the nano-bio interface and to inspire novel design principles to

build functional hybrid nanomaterials for biomedical applications. In this study we have addressed the interaction of citrate-capped AuNPs with synthetic liposomes of different rigidities over different length and time scales. We showed that the adhesion pathway of AuNPs to the target membrane is governed at the molecular level by the physical properties of the lipid bilayer (i.e., its rigidity). This different initial and local interaction mechanism results, for long incubation times and at the colloidal length scale, in dramatic differences in the morphologies, structures, and physicochemical properties of AuNP-liposomes hybrids. Overall, we highlight the multiscale nature of the formation and the properties of AuNP-vesicles hybrids. Depending on the physical state of the bilayer, the energetic balance of NP wrapping is different. This delicate energetic balance, which concerns a phenomenon at the nanometer scale, initiates a cascade of events that regulate the colloidal interactions up to the micrometer scale and control the final morphology of the hybrids, which range from single soft vesicles decorated by AuNP clusters to flocculated rigid liposomes bridged by single AuNPs. In addition, some preliminary results demonstrate the possibility to exploit this interaction cascade to separate mixtures of chemically and colloidally identical vesicles based on their membrane rigidity. This mechanistic understanding paves the way to engineer and finely control hybrids where soft and biocompatible vesicles are combined with the hard properties of citrate-stabilized inorganic NPs through simple self-assembly.

■ ASSOCIATED CONTENT

Supporting Information

The Supporting Information is available free of charge at <https://pubs.acs.org/doi/10.1021/acs.jpcc.1c08914>.

Supplementary SAXS, UV-vis, and cryo-EM data (PDF)

■ AUTHOR INFORMATION

Corresponding Author

Debora Berti – Department of Chemistry “Ugo Schiff” and CSGI, University of Florence, 50019 Sesto Fiorentino, Florence, Italy; orcid.org/0000-0001-8967-560X; Email: debora.beriti@unifi.it

Authors

Jacopo Cardellini – Department of Chemistry “Ugo Schiff” and CSGI, University of Florence, 50019 Sesto Fiorentino, Florence, Italy

Lucrezia Caselli – Department of Chemistry “Ugo Schiff” and CSGI, University of Florence, 50019 Sesto Fiorentino, Florence, Italy

Enrico Lavagna – Department of Physics, University of Genoa, Genoa 16146, Italy; orcid.org/0000-0002-7399-5569

Sebastian Salassi – Department of Physics, University of Genoa, Genoa 16146, Italy

Heinz Amenitsch – Institute of Inorganic Chemistry, Graz University of Technology, 8010 Graz, Austria

Martino Calamai – European Laboratory for Non-Linear Spectroscopy (LENS), 50019 Sesto Fiorentino, Italy; orcid.org/0000-0002-4031-7235

Costanza Montis – Department of Chemistry “Ugo Schiff” and CSGI, University of Florence, 50019 Sesto Fiorentino, Florence, Italy; orcid.org/0000-0001-6960-3772

Giulia Rossi – Department of Physics, University of Genoa, Genoa 16146, Italy

Complete contact information is available at:
<https://pubs.acs.org/10.1021/acs.jpcc.1c08914>

Notes

The authors declare no competing financial interest.

ACKNOWLEDGMENTS

This work has been supported by the European Community through the evFOUNDRY project (H2020-FETOpen, ID 801367) and the BOW project (H2020-EIC-FETPROACT-2019, ID 952183). We also acknowledge MIUR-Italy (“Progetto Dipartimenti di Eccellenza 2018–2022, ref B96C1700020008” allocated to the Department of Chemistry “Ugo Schiff”) and Ente Cassa di Risparmio di Firenze for the economic support. The Elettra Synchrotron SAXS facility (Basovizza, Trieste, Italy) is acknowledged for beam time. We acknowledge the Florence Center for Electron Nanoscopy (FloCEN) at the University of Florence. G.R. acknowledges funding from the ERC BioMNP project (Grant 677513) and from the H2020 SUNSHINE project (952924). G.R. and S.S. acknowledge funding from the University of Genoa via a Curiosity Driven grant (2019–2021). G.R., S.S., and E.L. acknowledge funding by MIUR-DIFI Dipartimento di Eccellenza 2018–2022 for computational resources.

REFERENCES

- (1) Nel, A. E.; Madler, L.; Velegol, D.; Xia, T.; Hoek, E. M. V.; Somasundaran, P.; Klaessig, F.; Castranova, V.; Thompson, M. Understanding Biophysicochemical Interactions at the Nano-Bio Interface. *Nat. Mater.* **2009**, *8* (7), 543–557.
- (2) Wang, Y.; Cai, R.; Chen, C. The Nano-Bio Interactions of Nanomedicines: Understanding the Biochemical Driving Forces and Redox Reactions. *Acc. Chem. Res.* **2019**, *52* (6), 1507–1518.
- (3) Alkilany, A. M.; Lohse, S. E.; Murphy, C. J. The Gold Standard: Gold Nanoparticle Libraries to Understand the Nano-Bio Interface. *Acc. Chem. Res.* **2013**, *46* (3), 650–661.
- (4) Murphy, C. J.; Vartanian, A. M.; Geiger, F. M.; Hamers, R. J.; Pedersen, J.; Cui, Q.; Haynes, C. L.; Carlson, E. E.; Hernandez, R.; Klapper, R. D.; et al. Biological Responses to Engineered Nanomaterials: Needs for the next Decade. *ACS Cent. Sci.* **2015**, *1* (3), 117–123.
- (5) Henriksen-Lacey, M.; Carregal-Romero, S.; Liz-Marzan, L. M. Current Challenges toward in Vitro Cellular Validation of Inorganic Nanoparticles. *Bioconjug. Chem.* **2017**, *28* (1), 212–221.
- (6) Shen, Z.; Ye, H.; Yi, X.; Li, Y. Membrane Wrapping Efficiency of Elastic Nanoparticles during Endocytosis: Size and Shape Matter. *ACS Nano* **2019**, *13* (1), 215–228.
- (7) Sinha, S.; Jing, H.; Sachar, H. S.; Das, S. Surface Charges Promote Nonspecific Nanoparticle Adhesion to Stiffer Membranes. *Appl. Phys. Lett.* **2018**, *112* (16), 163702.
- (8) Hui, Y.; Yi, X.; Wibowo, D.; Yang, G.; Middelberg, A. P. J.; Gao, H.; Zhao, C. X. Nanoparticle Elasticity Regulates Phagocytosis and Cancer Cell Uptake. *Sci. Adv.* **2020**, *6* (16), 1–11.
- (9) Sezgin, E.; Levental, I.; Mayor, S.; Eggeling, C. The Mystery of Membrane Organization: Composition, Regulation and Roles of Lipid Rafts. *Nat. Rev. Mol. Cell Biol.* **2017**, *18* (6), 361–374.
- (10) Hamada, T.; Morita, M.; Miyakawa, M.; Sugimoto, R.; Hatanaka, A.; Vestergaard, M. C.; Takagi, M. Size-Dependent Partitioning of Nano/Microparticles Mediated by Membrane Lateral Heterogeneity. *J. Am. Chem. Soc.* **2012**, *134* (34), 13990–13996.
- (11) Caselli, L.; Ridolfi, A.; Mangiapia, G.; Maltoni, P.; Moulin, J.-F.; Berti, D.; Steinke, N.-J.; Gustafsson, E.; Nylander, T.; Montis, C. Interaction of Nanoparticles with Lipid Films: The Role of Symmetry and Shape Anisotropy. *Phys. Chem. Chem. Phys.* **2022**, *24*, 2762.
- (12) Ridolfi, A.; Caselli, L.; Montis, C.; Mangiapia, G.; Berti, D.; Bruciale, M.; Valle, F. Gold Nanoparticles Interacting with Synthetic Lipid Rafts: An AFM Investigation. *J. Microsc.* **2020**, *280* (3), 194–203.
- (13) Wang, L.; Hartel, N.; Ren, K.; Graham, N. A.; Malmstadt, N. Effect of Protein Corona on Nanoparticle-Plasma Membrane and Nanoparticle-Biomimetic Membrane Interactions. *Environ. Sci. Nano* **2020**, *7* (3), 963–974.
- (14) Chen, K. L.; Bothun, G. D. Nanoparticles Meet Cell Membranes: Probing Nonspecific Interactions Using Model Membranes. *Environ. Sci. Technol.* **2018**, *48*, 873.
- (15) Rascol, E.; Devoisselle, J. M.; Chopineau, J. The Relevance of Membrane Models to Understand Nanoparticles-Cell Membrane Interactions. *Nanoscale* **2016**, *8* (9), 4780–4798.
- (16) De Cuyper, M.; Joniau, M. Magnetoliposomes - Formation and Structural. *Eur. Biophys. J.* **1988**, *15*, 311–319.
- (17) Salvatore, A.; Montis, C.; Berti, D.; Baglioni, P. Multifunctional Magnetoliposomes for Sequential Controlled Release. *ACS Nano* **2016**, *10* (8), 7749–7760.
- (18) Zhang, H.; Wang, D. Controlling the Growth of Charged-Nanoparticle Chains through Interparticle Electrostatic Repulsion. *Angew. Chem.* **2008**, *120* (21), 4048–4051.
- (19) Caselli, L.; Mendoza, M.; Muzzi, B.; Toti, A.; Montis, C.; Mello, T.; Di Cesare Mannelli, L.; Ghelardini, C.; Sangregorio, C.; Berti, D. Lipid Cubic Mesophases Combined with Superparamagnetic Iron Oxide Nanoparticles: A Hybrid Multifunctional Platform with Tunable Magnetic Properties for Nanomedical Applications. *IJMS* **2021**, *22*, 9268.
- (20) Al-Jamal, W. T.; Kostarelos, K. Liposome-Nanoparticle Hybrids for Multimodal Diagnostic and Therapeutic Applications. *Nanomedicine* **2007**, *2* (1), 85–98.
- (21) Luchini, A.; Vitiello, G. Understanding the Nano-Bio Interfaces: Lipid-Coatings for Inorganic Nanoparticles as Promising Strategy for Biomedical Applications. *Front. Chem.* **2019**, *7* (May), 1–16.
- (22) Medeiros, S. F.; Santos, A. M.; Fessi, H.; Elaissari, A. Stimuli-Responsive Magnetic Particles for Biomedical Applications. *Int. J. Pharm.* **2011**, *403* (1–2), 139–161.
- (23) Li, Y.; Schluessener, H. J.; Xu, S. *Gold Nanoparticle-Based Biosensors*. **2010**, *43* (1), 29–41.
- (24) Kennedy, L. C.; Bickford, L. R.; Lewinski, N. A.; Coughlin, A. J.; Hu, Y.; Day, E. S.; West, J. L.; Drezek, R. A. A New Era for Cancer Treatment: Gold-Nanoparticle-Mediated Thermal Therapies. *Small* **2011**, *7* (2), 169–183.
- (25) Immordino, M. L.; Brusa, P.; Rocco, F.; Arpicco, S.; Ceruti, M.; Cattel, L. Preparation, Characterization, Cytotoxicity and Pharmacokinetics of Liposomes Containing Lipophilic Gemcitabine Prodrugs. *J. Controlled Release* **2004**, *100* (3), 331–346.
- (26) Pornpattananakul, D.; Zhang, L.; Olson, S.; Aryal, S.; Obonyo, M.; Vecchio, K.; Huang, C. M.; Zhang, L. Bacterial Toxin-Triggered Drug Release from Gold Nanoparticle-Stabilized Liposomes for the Treatment of Bacterial Infection. *J. Am. Chem. Soc.* **2011**, *133* (11), 4132–4139.
- (27) Turkevich, J.; Stevenson, P. C.; Hillier, J. A Study of the Nucleation and Growth Processes in the Synthesis of Colloidal Gold. *Discuss. Faraday Soc.* **1951**, *11* (0), 55–75.
- (28) Wang, F.; Liu, J. Self-Healable and Reversible Liposome Leakage by Citrate-Capped Gold Nanoparticles: Probing the Initial Adsorption/Desorption Induced Lipid Phase Transition. *Nanoscale* **2015**, *7* (38), 15599–15604.
- (29) Sugikawa, K.; Kadota, T.; Yasuhara, K.; Ikeda, A. Anisotropic Self-Assembly of Citrate-Coated Gold Nanoparticles on Fluidic Liposomes. *Angew. Chemie - Int. Ed.* **2016**, *55* (12), 4059–4063.
- (30) Caselli, L.; Ridolfi, A.; Cardellini, J.; Sharpnack, L.; Paolini, L.; Bruciale, M.; Valle, F.; Montis, C.; Bergese, P.; Berti, D. A Plasmon-Based Nanoruler to Probe the Mechanical Properties of Synthetic and Biogenic Nanosized Lipid Vesicles. *Nanoscale Horizons* **2021**, *6*, 543.
- (31) Montis, C.; Caselli, L.; Valle, F.; Zendrini, A.; Carli, F.; Schweins, R.; Maccarini, M.; Bergese, P.; Berti, D. Shedding Light on

Membrane-Templated Clustering of Gold Nanoparticles. *J. Colloid Interface Sci.* **2020**, *573*, 204–214.

(32) Frens, G. Controlled Nucleation for the Regulation of the Particle Size in Monodisperse Gold Suspensions. *Nat. Phys. Sci.* **1973**, *241*, 20–22.

(33) Surugau, N.; Urban, P. L. Electrophoretic Methods for Separation of Nanoparticles. *J. Sep. Sci.* **2009**, *32* (11), 1889–1906.

(34) Marrink, S. J.; Risselada, H. J.; Yefimov, S.; Tieleman, D. P.; de Vries, A. H. The MARTINI Force Field: Coarse Grained Model for Biomolecular Simulations. *J. Phys. Chem. B* **2007**, *111* (27), 7812–7824.

(35) Bussi, G.; Donadio, D.; Parrinello, M. Canonical Sampling through Velocity Rescaling. *J. Chem. Phys.* **2007**, *126* (1), 014101.

(36) Berendsen, H. J. C.; Grigera, J. R.; Straatsma, T. P. The Missing Term in Effective Pair Potentials. *J. Phys. Chem.* **1987**, *91* (24), 6269–6271.

(37) Salassi, S.; Caselli, L.; Cardellini, J.; Lavagna, E.; Montis, C.; Berti, D.; Rossi, G. A Martini Coarse Grained Model of Citrate-Capped Gold Nanoparticles Interacting with Lipid Bilayers. *J. Chem. Theory Comput.* **2021**, *17*, 6597.

(38) Kanhaiya, K.; Kim, S.; Im, W.; Heinz, H. Accurate Simulation of Surfaces and Interfaces of Ten FCC Metals and Steel Using Lennard-Jones Potentials. *npj Comput. Mater.* **2021**, *7* (1), 17281.

(39) Bochicchio, D.; Monticelli, L. Chapter Five - The Membrane Bending Modulus in Experiments and Simulations: A Puzzling Picture. *Adv. Biomembr. Lipid Self-Assembly* **2016**, *23* (April), 117–143.

(40) Ridolfi, A.; Caselli, L.; Baldoni, M.; Montis, C.; Mercuri, F.; Berti, D.; Valle, F.; Brucale, M. Stiffness of fluid and gel phase lipid nanovesicles: weighting the contributions of membrane bending modulus and luminal pressurization. *Langmuir* **2021**, *37* (41), 12027–12037.

(41) Eid, J.; Razmazma, H.; Jraj, A.; Ebrahimi, A.; Monticelli, L. On Calculating the Bending Modulus of Lipid Bilayer Membranes from Buckling Simulations. *J. Phys. Chem. B* **2020**, *124*, 6299.

(42) Nagle, J. F. Introductory Lecture: Basic Quantities in Model Biomembranes. *Faraday Discuss.* **2013**, *161*, 11–29.

(43) Koynova, R.; Caffrey, M. Phases and Phase Transitions of the Phosphatidylcholines. *Biochim. Biophys. Acta - Rev. Biomembr.* **1998**, *1376* (1), 91–145.

(44) Baletto, F.; Ferrando, R. Structural Properties of Nanoclusters: Energetic, Thermodynamic, and Kinetic Effects. *Rev. Mod. Phys.* **2005**, *77*, 371–423.

(45) Al-Johani, H.; Abou-Hamad, E.; Jedidi, A.; Widdifield, C. M.; Viger-Gravel, J.; Sangaru, S. S.; Gajan, D.; Anjum, D. H.; Ould-Chikh, S.; Hedhili, M. N.; et al. The Structure and Binding Mode of Citrate in the Stabilization of Gold Nanoparticles. *Nat. Chem.* **2017**, *9* (9), 890–895.

(46) Park, J. W.; Shumaker-Parry, J. S. Structural Study of Citrate Layers on Gold Nanoparticles: Role of Intermolecular Interactions in Stabilizing Nanoparticles. *J. Am. Chem. Soc.* **2014**, *136* (5), 1907–1921.

(47) Carl, N.; Prévost, S.; Fitzgerald, J. P. S.; Karg, M. Salt-Induced Cluster Formation of Gold Nanoparticles Followed by Stopped-Flow SAXS, DLS and Extinction Spectroscopy. *Phys. Chem. Chem. Phys.* **2017**, *19* (25), 16348–16357.

(48) Bhattacharjee, S. DLS and Zeta Potential - What They Are and What They Are Not? *J. Controlled Release* **2016**, *235*, 337–351.

(49) Morini, M. A.; Sierra, M. B.; Pedroni, V. I.; Alarcon, L. M.; Appignanesi, G. A.; Disalvo, E. A. Influence of Temperature, Anions and Size Distribution on the Zeta Potential of DMPC, DPPC and DMPE Lipid Vesicles. *Colloids Surfaces B Biointerfaces* **2015**, *131*, 54–58.

(50) Michel, R.; Plostica, T.; Abezgauz, L.; Danino, D.; Gradzielski, M. Control of the Stability and Structure of Liposomes by Means of Nanoparticles. *Soft Matter* **2013**, *9* (16), 4167–4177.

(51) Yu, Y.; Anthony, S. M.; Zhang, L.; Bae, S. C.; Granick, S. Cationic Nanoparticles Stabilize Zwitterionic Liposomes Better than Anionic Ones. *J. Phys. Chem. C* **2007**, *111* (23), 8233–8236.

(52) Mohanraj, V. J.; Barnes, T. J.; Prestidge, C. A. Silica Nanoparticle Coated Liposomes: A New Type of Hybrid Nanocapsule for Proteins. *Int. J. Pharm.* **2010**, *392* (1–2), 285–293.

(53) Thamphiwatana, S.; Fu, V.; Zhu, J.; Lu, D.; Gao, W.; Zhang, L. Nanoparticle-Stabilized Liposomes for Ph-Responsive Gastric Drug Delivery. *Langmuir* **2013**, *29* (39), 12228–12233.

(54) Zhang, L.; Granick, S. How to Stabilize Phospholipid Liposomes (Using Nanoparticles). *Nano Lett.* **2006**, *6* (4), 694–698.

(55) Paolini, L.; Zendrini, A.; Noto, G. Di; Busatto, S.; Lottini, E.; Radeghieri, A.; Dossi, A.; Caneschi, A.; Ricotta, D.; Bergese, P. Residual Matrix from Different Separation Techniques Impacts Exosome Biological Activity. *Sci. Rep.* **2016**, *6*, 1–11.

Supporting Information for:

Membrane Phase Drives the Assembly of Gold Nanoparticles on Biomimetic Lipid Bilayers

Jacopo Cardellini^a, Lucrezia Caselli^a, Enrico Lavagna^b, Sebastian Salassi^b,

Heinz Amenitsch^c, Martino Calamai^d, Costanza Montis^a, Giulia Rossi^b, Debora

Berti^{a*}

^a Department of Chemistry “Ugo Schiff” and CSGI, University of Florence, via della Lastruccia 3, 50019 Sesto Fiorentino, Florence, Italy;

^b Department of Physics, University of Genoa, Genoa 16146, Italy;

^c Institute of Inorganic Chemistry, Graz University of Technology, 8010 Graz, Austria;

^d European Laboratory for Non-linear Spectroscopy (LENS), 50019 Sesto Fiorentino, Italy;

	Page
Supplementary Characterization of Gold Nanoparticles	S2
<i>Small Angle X-Ray Scattering</i>	<i>S2</i>
<i>Dynamic Light Scattering and Z-Potential</i>	<i>S3</i>
<i>UV-Vis Spectroscopy</i>	<i>S4</i>
Supplementary Characterization of Liposomes	S5
<i>Dynamic Light Scattering and Z-Potential</i>	<i>S6</i>
<i>Evaluation of liposomes concentration</i>	<i>S6</i>
<i>Small Angle X-Ray Scattering</i>	<i>S7</i>
Supplementary Characterization of liposomes/AuNPs hybrids	S8
<i>Preparation of liposomes/AuNPs hybrids</i>	<i>S8</i>
<i>Cryo-TEM</i>	<i>S9</i>
<i>MD simulations</i>	<i>S10</i>
<i>Small-Angle X-Ray Scattering</i>	<i>S10</i>

<i>Agarose gel electrophoresis</i>	<i>S13</i>
Bibliography	S14

Supplementary Characterization of Gold Nanoparticles

Small Angle X-ray Scattering

SAXS measurements on AuNPs aqueous dispersion were carried out in sealed glass capillaries of 1,5 mm diameter.

The structural parameters (Table S1) of citrated gold nanoparticles were evaluated from the SAXS profile of their diluted water dispersion (Figure S1), according to a spherical form factor and a Schulz size distribution. In this concentration range, we can safely assume that there are no interparticle interactions are present, and that the structure factor $S(Q)$ equals in the whole range of scattering vectors. Thus, the scattering profile of the particles derives from their form factor, $P(Q)$. The SAXS spectrum reported in Figure S1 is fully consistent with the characteristic $P(Q)$ of spherical particles with an average diameter of about 5.8 nm. The clear presence of $P(Q)$ oscillations in the high Q

region is consistent with a relatively low polydispersity of the synthesized AuNPs.

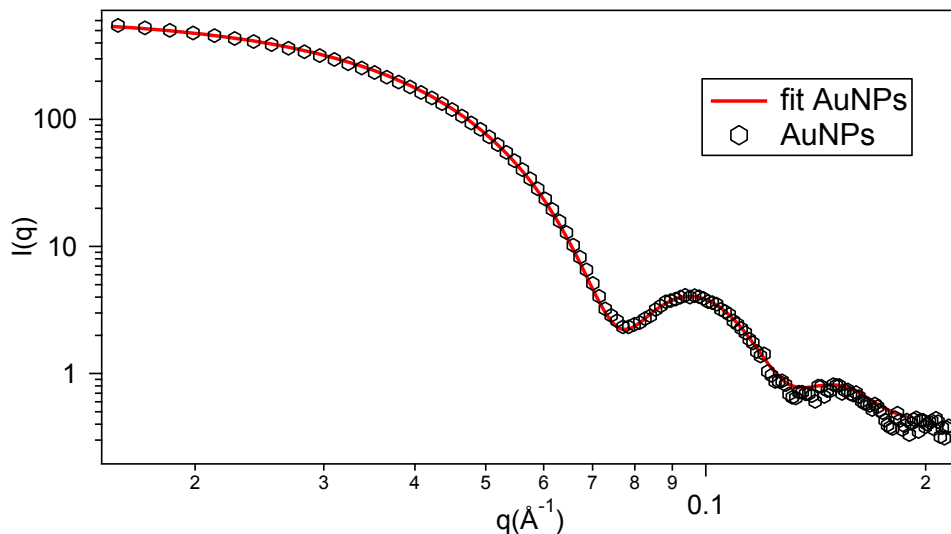


Figure S1 Experimental SAXS curve (red markers) obtained for AuNPs and curve fit (solid black line) according to the Schulz spheres model from the analysis software package SasView. The size and polydispersity obtained from the fitting procedure are summarized in the Table S1 below.

	R_{core} (nm)	poly
AuNP	5,78	0,095

Table S1 Structural parameters of the nanoparticles obtained from the analysis of SAXS curves according to the Schulz spheres model.

Dynamic Light Scattering and Z-Potential

AuNPs hydrodynamic diameter and surface charge in MilliQ water were evaluated through Dynamic Light Scattering and Zeta-Potential, respectively, and reported in Table S2.

	D_h (nm)	Z-Potential (mV)
AuNPs	$20 \pm 0,6$	-35 ± 3

Table S2 *Hydrodynamic diameter obtained from Dynamic Light Scattering and Zeta Potential values of AuNPs.*

UV-vis Spectroscopy

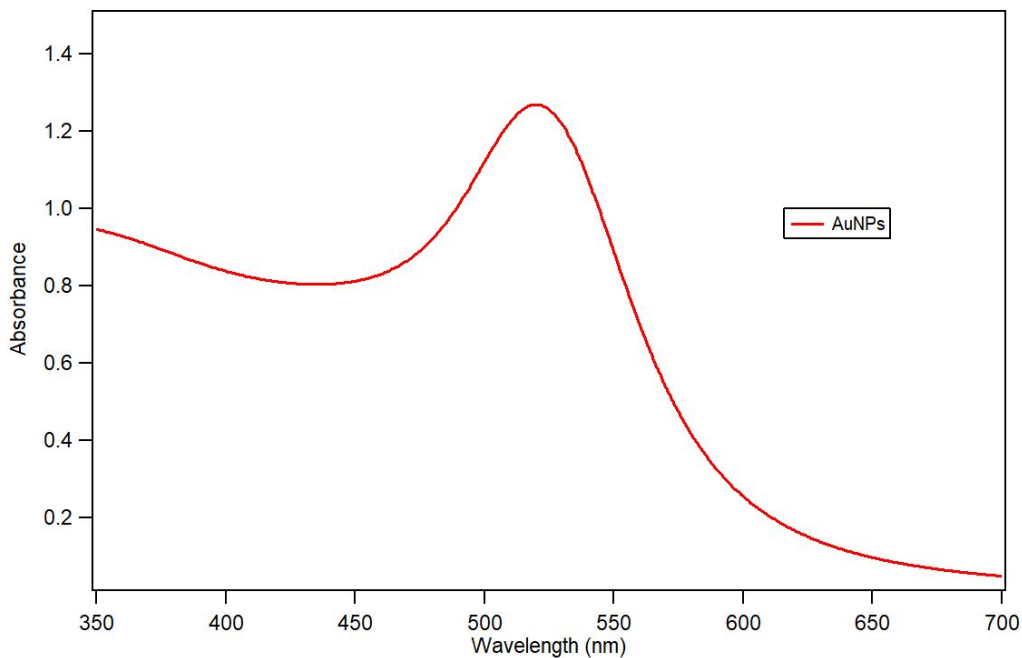


Figure S3 UV-Vis absorption spectra of AuNPs after 1:3 dilution in water. The plasmon absorption peak is at around 520 nm.

To further evaluate the AuNPs size through UV-Vis spectroscopy we exploited the following equation¹:

$$d = \exp \left(B_1 \frac{A_{spr}}{A_{450}} - B_2 \right)$$

with d diameter of gold nanoparticles, A_{spr} absorbance at the surface plasma resonance peak, A_{450} absorbance at the wavelength of 450 nm and B_1 and B_2 are dimensionless parameters, taken as 3 and 2,2, respectively. The diameter value obtained is of 12,3 nm.

The concentration of citrated gold nanoparticles was determined via UV-Vis spectrometry, using the Lambert-Beer law ($E(\lambda) = \varepsilon(\lambda)lc$), taking the extinction values $E(\lambda)$ at the LSPR maximum, i.e. $\lambda = 521$ nm. The extinction coefficient $\varepsilon(\lambda)$ of gold nanoparticles dispersion was determined by the method reported in literature², by the following equation:

$$\ln(\varepsilon) = k \ln(d) + a$$

with d core diameter of nanoparticles, and k and a dimensionless parameters ($k = 3,32111$ and $a = 10,80505$). The arithmetic mean of the sizes obtained by optical and scattering analyses was selected, leading to a $\varepsilon(\lambda)$ of $2.0 \cdot 10^8 \text{ M}^{-1} \text{ cm}^{-1}$. The final concentration of the citrated AuNPs is therefore $\sim 6.3 \cdot 10^{-9} \text{ M}$.

Supplementary Characterization of Liposomes

Dynamic Light Scattering and Zeta-Potential

	D_h (nm)	Zeta P
DOPC	$118,6 \pm 0.2$	-12 ± 2
DPPC	$178,7 \pm 0.1$	-10 ± 2

Table S3 *Hydrodynamic diameter obtained from Dynamic Light Scattering and Zeta Potential values of synthetic liposomes.*

Evaluation of Liposomes concentration

The lipid concentration in the starting colloidal dispersion was estimated to be 4 mg/mL from the initial lipid and water amounts employed in the formation and swelling of lipid films, assuming the absence of lipid loss due to the extrusion procedure. The liposomes concentration in the final dispersion was subsequently calculated considering the hydrodynamic diameter of each liposomal batch (Table S3 of SI). In particular, the liposomal surface area (surface area= $4\pi r^2$) can be calculated from the liposome diameters; the doubled surface can be subsequently divided by the lipid cross section ($0,5 \text{ nm}^2$) in order to obtain the lipid number per liposome, assuming that approximately one half of the lipids is localized in the external leaflet of a liposome, since the bilayer thickness, about 4-5 nm, is negligible with respect to the liposomes' average diameter. Eventually, the total weighted lipid concentration was divided by the total number of lipids per liposome, yielding the real liposome concentration, which is reported in Table S4 for each liposomes' dispersion.

	Concentration (M)
DOPC	$3,2 \cdot 10^{-8}$
DPPC	$2,1 \cdot 10^{-8}$

Table S4 Final liposomes' concentration in each liposomal batch.

The liposomal dispersions were diluted to reach a final concentration of $1,2 \cdot 10^{-8}$ M before use.

Small Angle X-Ray Scattering

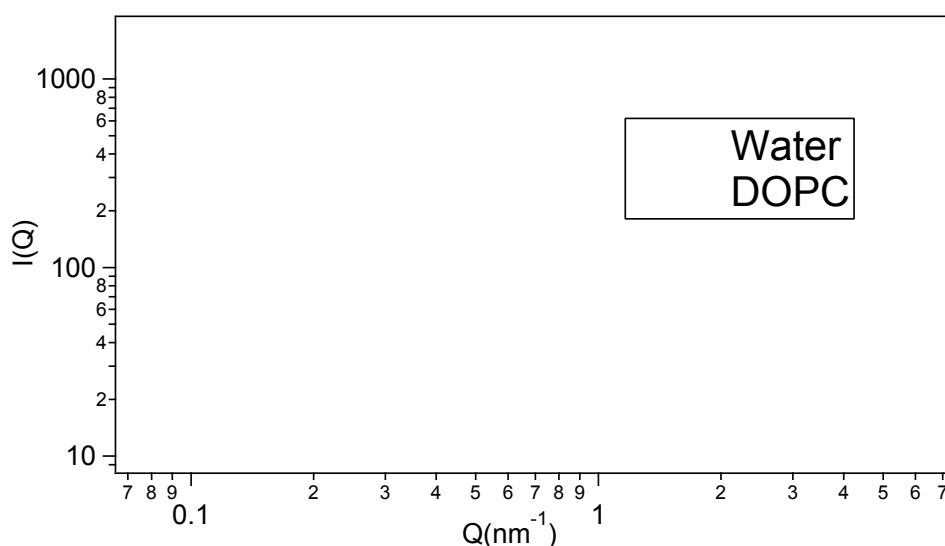


Figure S4 Comparison between the scattering intensity of water and the scattering intensity of $10 \mu\text{L}$ of liposome dispersions (12 nM) in $300 \mu\text{L}$ of water.

Supplementary Characterization of liposomes/AuNPs hybrids

Preparation of liposomes/AuNPs hybrids

The hybrid samples were prepared as follow: $10 \mu\text{L}$ of liposome dispersions (12 nM) were incubated with $300 \mu\text{L}$ of AuNPs $6,3 \text{ nM}$, in order to have a

liposomes/AuNPs number ratio of $\sim 1/16$. This liposomes/AuNPs number ratio was selected on the basis of our previous publication^{3,4} which highlights that the aggregation of AuNPs on zwitterionic vesicles is promoted by low liposome amounts within the mix.

Cryo-TEM

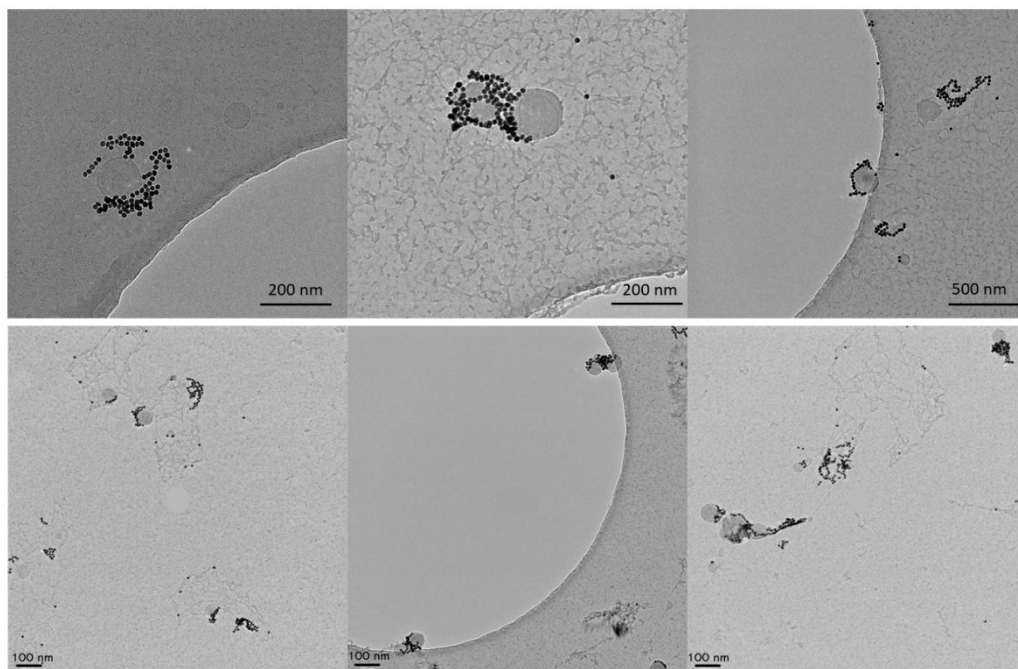


Figure S5 Further examples of cryo-TEM images of AuNPs-DOPC hybrids.

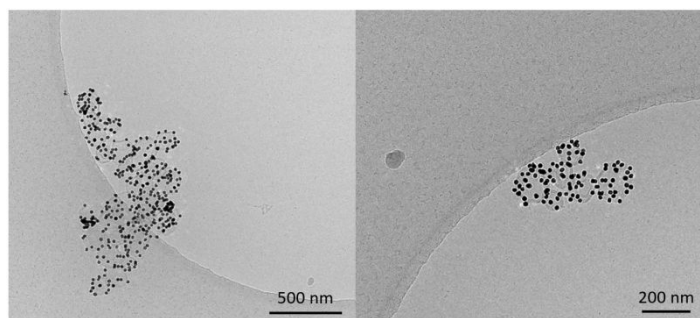


Figure S6 Further examples of cryo-TEM images of AuNPs-DPPC hybrids.

MD Simulations

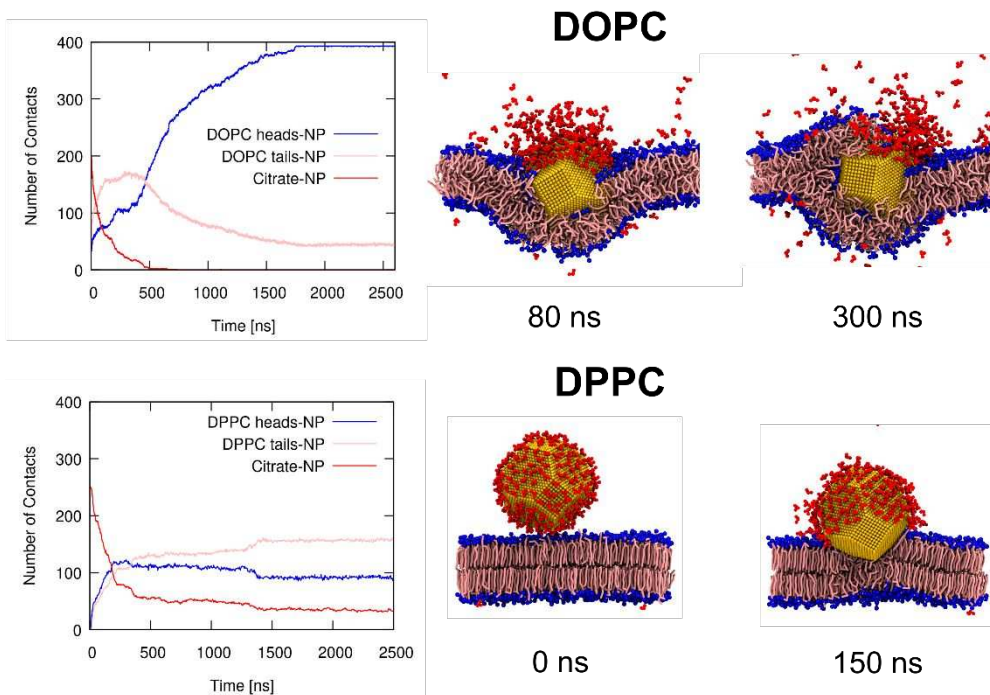


Figure S7: *Difference between the penetration process of a citrate 8 nm AuNP in DOPC and DPPC. For each kind of bilayer, we show the time evolution of the number of contacts between the NP and citrate molecules (in red), lipid headgroups (blue) and lipid tails (pink), and three snapshots from the corresponding simulations; in the snapshots, the NP is represented in yellow, the citrate in red, the lipid headgroups in blue and the lipid tails in pink. Time $t=0$ corresponds to the first NP-membrane contact. The contact time series is shown only up to 2,5 μs ; afterwards, the values are stable.*

Small-Angle X-Ray Scattering

To characterize the NPs- vesicles hybrids' formation, 10 μL of 12 nM DOPC or DPPC liposomal dispersions were challenged with 300 μL of 6.3 nM citrate-stabilized AuNPs. In order to gain information on the kinetic of AuNPs

aggregation, the SAXS profiles have been collected after 1s, 30s, 5m and 10 minutes of the incubation.

In the low q region, plotting $\log_{10}(I(q))$ vs $\log_{10}(q)$ it's possible to obtain the fractal dimension of the aggregates by the slope of the scattering profile⁵, according to:

$$\log_{10}(I(q) - B) = -p \log_{10}(q)$$

Where B is the background and p the Porod exponent. Generally, $p=1$ represents the fractal dimension of a linear aggregate and $p=2$ represents the fractal dimension of a 2D object.⁵

The SAXS profiles of DOPC liposomes/AuNPs and DPPC liposomes/AuNPs in Figure 3 were fitted through a linear fit in the 0,1-0,3 nm^{-1} q -range, to obtain the slope values reported in table S5.

Incubation time	AuNPs-DOPC	AuNPs-DPPC
1s	-1,32 ± 0.02	-0,53 ± 0.03
30s	-1,90 ± 0.02	-0,94 ± 0.01
5m	-2,00 ± 0.02	-1,02 ± 0.01

10m	$-2,01 \pm 0.02$	$-1,06 \pm 0.01$
------------	------------------	------------------

Tab S5: Slopes of the linear fits of the SAXS profiles;

The Structure factors for the scattering profiles reported in the insets of figure 4 (main text) were obtained as follow.

The scattering intensity ($I(q)$) is defined by the following equation:

$$I(q) = KN_p V_p^2 (\Delta\rho)^2 P(q) S(q) + B$$

With k instrumental constant, N_p scattering nanoparticles' number per unit volume, V_p nanoparticle's volume, $\Delta\rho$ contrast of the experiment, B background intensity, $P(q)$ e $S(q)$ form and structure factors, respectively.

In order to obtain the structure factor of the liposome/AuNPs complex, we divided the scattering intensity of the liposomes/AuNPs hybrid by the scattering intensity of the neat AuNPs dispersion:

$$\frac{I(q)_{Hyb}}{I(q)_{NP}} \sim \frac{S(q)_{Hyb} P(q)_{Hyb}}{S(q)_{NP} P(q)_{NP}}$$

For a diluted AuNPs dispersion the structure factor can be considered equal to 1. In addition, in the high- q region ($0,1-1,6 \text{ nm}^{-1}$), the form factor of liposomes/AuNP hybrids can be approximated to the one of neat AuNPs, leading to the following equation:

$$\frac{I(q)_{Hyb}}{I(q)_{NP}} = S(q)_{Hyb}$$

The mean interparticle distance between the AuNPs within the aggregates (d) can be obtained from the $S(q)$ vs q (nm^{-1}) plot (see inset of Figure 2b of the main text), by the following equation:

$$d = \frac{2\pi}{q_{max}}$$

With q_{max} value corresponding to the maximum of the correlation peaks reported in the insets of figure 4 (main text).

Agarose gel electrophoresis

In order to perform gel electrophoresis, the AuNPs and DOPC or DPPC dispersions were mixed as previously reported. The AuNPs-DOPC+DPPC sample were prepared as follow: 300 μL of 6,3 nM AuNPs aqueous solution were added to the mixture of 5 μL of 12 nM DOPC and 5 μL of 12 nM DPPC dispersions. The AuNPs-DOPC + AuNPs-DPPC sample was prepared mixing AuNPs-DOPC and AuNPs-DPPC hybrids after their formation. 15 μL of each sample were a mixed with 5 μL of glycerol in order to improve their deposition at the bottom of the wells.

Bibliography

- 1 W. Haiss, N. T. K. Thanh, J. Aveyard and D. G. Fernig, 2007, **79**, 4215–4221.
- 2 X. Liu, M. Atwater, J. Wang and Q. Huo, 2007, **58**, 3–7.
- 3 L. Caselli, A. Ridolfi, J. Cardellini, L. Sharpnack, L. Paolini, M. Brucale, F. Valle, C. Montis, P. Bergese and D. Berti, *Nanoscale Horizons*, , DOI:10.1039/d1nh00012h.
- 4 C. Montis, L. Caselli, F. Valle, A. Zendrini, F. Carlà, R. Schweins, M. Maccarini, P. Bergese and D. Berti, *J. Colloid Interface Sci.*, 2020, **573**, 204–214.
- 5 T. A. Ezquerra, M. Garcia-Gutierrez, A. Nogales and M. Gomez, *Applications of synchrotron light to scattering and diffraction in materials and life sciences*, 2009.

Lipid-polymer assemblies as biomimetic platforms for the spontaneous clustering of AuNPs (Paper II)

Jacopo Cardellini*, Arianna Balestri*, Luca Comparini, Costanza Montis, Debora Berti (*equally contributed) (Manuscript in preparation)

Lipid-polymer assemblies as biomimetic platforms for the spontaneous clustering of AuNPs

Authors: Jacopo Cardellini, Arianna Balestri, Luca Comparini, Costanza Montis, Debora Berti

Affiliation

Abstract

Despite their extraordinary applicative potential in medicine, the limited use of inorganic nanoparticles (NPs) in the biomedical field relies on the lack of knowledge of their biological fate. In this context, a detailed description of the interaction between nanoparticles and membrane interfaces is required. Gold nanoparticles (AuNPs), thanks to their unique optical properties, can be used as representative model nanosystem to shed lights on the aspecific interaction between NPs and biological membranes. On the other side, synthetic free-standing vesicles, and supported lipid bilayers (SLBs) can mimic natural membranes, allowing to extremely simplify the interaction environment. Recently, amphiphilic copolymers were included in phospholipid bilayer systems to improve their physical properties and tailor their chemical function, as well as to reproduce raft-like patches which represent an important feature of natural membranes.

Recent reports revealed that citrated AuNPs spontaneously self-assemble onto liposomal membranes, depending on their rigidity. Specifically, AuNPs aggregate on soft bilayers, forming large and compact clusters, while their interaction is strongly limited on rigid lipid scaffolds. In this work, we perform a physico-chemical study of the interaction of citrated AuNPs with hybrid synthetic supported and free-standing bilayers with different lipid-copolymer compositions, to assess the effects of the presence of raft-like domains on the membrane-induced aggregation of NPs. Confocal Laser Scanning Microscopy and Quartz Crystal Microbalance analysis, performed on hybrid SLBs, showed that the presence of the copolymer leads to a much higher number of deposited AuNPs. On the other hand, UV-Vis spectroscopy revealed specific trends in the AuNPs clustering, which strongly depends on the molar concentration of the copolymer in the liposomal formulations, while Small Angle X-ray Scattering provides a further characterization of the structure of AuNPs aggregates.

Overall, these results provide opportunities both from a fundamental perspective, to understand the phenomena occurring at the nano-bio interface, and from an

applicative point of view, to unveil the main principles to design novel lipid and polymer-nanoparticles hybrid materials.

1. Introduction

To date, engineered nanoparticles (NPs) rule the biotechnological research ranging their applications from drug delivery [1], [2] and imaging [3], [4] to hyperthermia [5], [6],[7] encouraging great advancements in their design.[8] A crucial step to enhance the clinical use of NPs is unravelling their fate in biological environments.[9][10][11] As previously reported [12], the crossing of biological barriers regulates the success of the nanoparticles' functions [13]. However, the deep comprehension of the physico-chemical parameters that govern the NPs fate is often tricky with in-vivo and in-vitro experiments, due to the cell complexity. In this context, synthetic membranes are instrumental to unveil the nano-bio interfacial phenomena in controlled and simplified conditions [14][15][16].

Model membranes consisting of biologically relevant lipid can reproduce different geometries, like giant unilamellar vesicles (GUVs)[17], monolayers [18], free-standing and supported bilayers [19]. However, recent progresses in the design of lipid assemblies mixed with synthetic polymer have opened novel perspectives for the use of hybrid assemblies in bio-applications [20]. For instance, hybrid systems composed of lipid mixed with amphiphilic block copolymers represents a new milestone for the realization of bio-platforms possessing tailored interaction with natural and synthetic hydrophobic species [21]. Moreover, the inclusion of polymers into the lipid bilayer architecture can promote the formation of complex membranes, with lateral phase separation and domains with different fluidities, resembling lipid rafts which mediate various processes in cells [20], [22], [23].

On the other hand, Turkevich-Frens gold nanoparticles[24][25] coated by citrate anions (AuNPs) represent one of the most studied classes of inorganic nanoparticles both in nanomedical applications and as prototypical beads in fundamental studies [26][27][7][28]. They are easy to synthesize and possess intriguing optical properties due to the Surface Plasmon Resonance (SPR) effect. The plasmonic properties of AuNPs mostly depends on their chemical environment and aggregative state, and can be used for monitoring their interactions.[29][30] As recently reported, AuNPs aggregate upon incubation with lipid membranes according to a membrane-templated phenomenon which strictly depends on the rigidity of the bilayers.[31] [32][33][34][35] Being such aggregation on zwitterionic liposomes ruled by the vesicle's stiffness and concentration, the AuNPs plasmonic

variations have been exploited for the development of colorimetric assays to characterize natural and synthetic vesicle dispersions. [36][37][38] Furthermore, from the nanotechnological point of view, AuNPs-liposomes suprastructures have already demonstrated their potentiality as nanomedical tool for the photothermal treatment of immunogenic cancer cells.[39]

In this contribution, we address the study of this prototypical inorganic NPs in the presence of a new promising hybrid platform consisting of the natural phospholipid 1,2-dipalmitoyl-sn-glycero-3-phosphocholine (DPPC) mixed with the polymer poly(butadiene-b-ethyleneoxide) (PBD-b-PEO), to extend the AuNPs clustering mechanism to complex biomimetic models. As previously demonstrated, the two building blocks associate in lamellar structures featured by distinct lipid- and copolymer-rich domains at the nano- and micro-scale, opening new strategies for a selective NPs-membrane interaction [40]. In this work, we performed a complete physico-chemical investigation of the AuNPs interactions with supported hybrid membranes, through quartz crystal microbalance (QCM) and confocal laser scanning microscopy (CSLM), and free-standing hybrid vesicles, through UV-vis spectroscopy and Small-Angle X-rays Scattering (SAXS).

We demonstrate the pivotal role of the soft polymeric domains in the NPs-membrane aspecific interactions, as well as that the AuNPs clustering can be modulated by varying the concentration and composition of synthetic vesicles.

Overall, considering that only a few reports[41] investigated the NPs interaction with hybrid lipid/polymer interfaces, this study provides a further contribution to the topic and a first insight into the AuNPs clustering onto complex membranes. Furthermore, our results introduced fundamental information to build-up novel and finely controlled engineered nanomaterials, which combine the drug delivery potentiality of vesicles-like structures with the powerful diagnostic and therapeutic properties of metallic nanoparticles.

2. Materials and Methods

2.1 Materials

The lipid DPPC, 1-dipalmitoyl-sn-glycero-3-phosphocholine, and the β -bodipy(2-(4,4-difluoro-5,7-dimethyl-4-bora-3a,4a-diazasindacene-3-pentanoyl)) lipophilic dye were purchased from AVANTI Polar Lipids, Inc. (Alabaster, AL). The copolymer PBd(2500)-b-PEO(1500), poly(butadiene-b-ethylene oxide), PBdPEO, and the

rhodamine-labeled copolymer polybutadiene ($M_n = 1200$ g/mol)- block-poly(ethylene oxide) ($M_n = 600$ g/mol), RhodPEBD-b-PEO, were provided from Polymer Source. Tetrachloroauric acid (HAuCl_4 , $M_n=393.83$ g/mol) and sodium citrate ($\text{Na}_3\text{C}_6\text{H}_5\text{O}_7$, $M_n=258.06$ g/mol) were provided from Sigma Aldrich (St. Louis, MO), using MilliQ as solvent. All chemicals were used as received.

2.2 Synthesis of AuNPs

The Turkevich-Frens method[25] was used to obtain a stable dispersion of AuNPs with a diameter of 12 nm. A specific solution of tetrachloroauric acid was prepared dissolving 20.0 mg in 50 mL of MilliQ water, and then brought to boil under constant agitation. Meanwhile, a solution of citric acid 1% was prepared (0.153 g in 15 mL of MilliQ water) and added rapidly to the gold solution under agitation. The reaction continued for 15 minutes and then left cool down at room temperature.

2.3 Preparation of Lipid vesicles

The DPPC, PBD-b-PEO, and hybrids DPPC PBD-b-PEO vesicles were prepared with different molar percentages of PBD-b-PEO (DPPC PBD-b-PEO 5%, DPPC PBD-b-PEO 15%, DPPC PBD-b-PEO 35%, and DPPC PBD-b-PEO 65%). Lipid and polymer vesicles were produced according to the thin-film hydration method. First, the phospholipid and the copolymer were dissolved in chloroform. Then a thin film was obtained by evaporating the solvent through exposition to a N_2 flux and overnight vacuum drying. The films were hydrated with MilliQ water at 50 °C under vigorous stirring to reach a lipid and copolymer concentration of 4 mg/mL. The obtained Multilamellar Vesicles (MLVs) were tip sonicated with a with a Digital Sonifier Model 450 (Branson, Hampton, NH), provided with a horn tip (diameter 25.4 mm), in an intermittent-pulse mode (5 s), with a power of 40 kHz (amplitude 30%). Then, they were subjected to 10 Freeze and Thaw cycles.[42] Finally, to limit the polydispersity[43], the vesicles were extruded through two stacked polycarbonate membranes with pores diameter of 100 nm for 10 times at a temperature of 50°C. At the end of the process unilamellar vesicles (LUV) with a narrow and reproducible size distribution were obtained. The filtration was performed with the Extruder (Lipex Biomembranes, Vancouver, Canada) through Nuclepore membranes.

2.4 Preparation of Supported bilayers

Solid-supported bilayers were prepared by vesicles' spontaneous rupture on hydrophilic substrates. SLBs were obtained by adding a 10 mM CaCl₂ aqueous solution to a dilute (1 mg/mL) dispersions of vesicles in a 0.1 M NaCl solution and subsequently deposited onto a silicon substrate at T = 50 °C for 30 min. After the deposition, the substrate was washed 15 times with 1 mL of Milli-Q water and then cooled to ambient temperature.

2.5 Confocal Laser Scanning Microscopy

A Leica CLSM TCS SP8 confocal microscope, operating in inverted mode, with a 63 x 1.3 numerical aperture water immersion objective, was used to image the morphology of polymer and lipid-based surface structures in water excess. The β -bodipy(2-(4,4-difluoro-5,7-dimethyl-4-bora-3a,4a-diazasindacene-3-pentanoyl) lipophilic dye was used to label DPPC liposomes; the fluorescence of this probe was excited at 488 nm and collected in the 498–530 nm emission range with a Phomultiplier tube (PMT). The fluorescence of a rhodamine-labelled copolymer polybutadiene (Mn = 1200 g/mol)- block-poly(ethyne oxide) (Mn = 600 g/mol), RhodPEBD-b-PEO was used to label PBdPEO polymersomes, employing an excitation wavelength of 633 nm, while the fluorescence was collected in the 650-700 nm emission range with a PMT detector. Images were taken with a resolution of 512 x 512 pixels using a 400 Hz bidirectional scan with each scanning line averaged four times. Leica software was used to create three-dimensional reconstructions of the z-stacks.

2.6 Quartz Crystal Microbalance

The QCM experiments were executed with a Q-sense Explorer (Q-Sense, Gothenburg, Sweden) instrument equipped with a flux cell that contains a quartz-coated sensor with a fundamental resonance of 5 MHz. The active surface of the sensor ($\approx 1 \text{ cm}^2$) is covered with a thin film of SiO₂ ($\approx 100 \text{ nm}$). The sensors were cleaned before use by washing in pure ethanol and bath sonication for 15 min, nitrogen drying, and finally ozone cleaning for 10 min. The experiments were performed at 40 °C. The sensor was placed in the chamber, and Milli-Q water was injected at a low flow rate (0.1 mL/min). The fundamental resonance frequencies (f) were measured for the odd overtones (5th–9th). A stable baseline of the different harmonics was ensured before the injection of the vesicles at a low flow rate (0.1 mL/min). The QCM curves reported are normalized by the overtone number.

In the case of rigid films uniformly distributed on the surface of the sensor and thin enough with respect to the weight of the crystal, a linear relation, called Sauerbrey equation, connects the absorbed mass (m) and the resonance frequency shift (f):

$$\Delta m = \frac{c}{v} \Delta f \quad (1)$$

with mass sensitivity constant $C = 17.7 \text{ ng}/(\text{cm}^2 \text{ Hz})$ for a 5 MHz sensor crystal.

2.7 UV-Vis spectroscopy

The UV-Vis measures were effectuated with a spectrophotometer Cary 3500 Multizone UV-Vis. The instrument is equipped with a Xenon lamp that emits in the range of wavelengths 190-1100 nm. The lamp emits radiations with 250 Hz frequency transmitted through an optic fibre beam to the 8 positions for the samples, each one equipped with its own detector. To each couple of cuvette holders is associated a Peltier block for the temperature control.

2.8 Small Angle X-ray Scattering

Small Angle X-Ray Scattering profiles were measured on AuNPs, and hybrid AuNPs-vesicles dispersions using a Xeuss 3.0HR (Xenocs) instrument equipped with a Genix3D (Cu) X-Ray source and a Dectris 1 M Eiger detector. Samples were put in glass capillary tubes of thickness 1.5 mm. Data from each sample were acquired at Sample-Detector (S-D) distances of 450 and 1800 mm for 300 s. The scattering signal was detected in the Q range $0.015 \text{ \AA}^{-1} < Q < 0.6 \text{ \AA}^{-1}$ and in Figure 4 the results are reported in $\log I(Q)$ vs $\log Q$ plots. Intensities were normalized with respect to transmission and sample thickness. After data reduction, the contribution of the sample holder and solvent (water) was subtracted from the sample intensity. The data were analysed with the Igor software.

To obtain the structure factor $S(Q)$ from the scattering profiles, the scattering intensity of the mixed samples ($I(Q)_{\text{mix}}$) was divided by the scattering intensity of the bare AuNPs ($I(Q)_{\text{AuNPs}}$), as follows:

$$\frac{I(Q)_{\text{mix}}}{I(Q)_{\text{AuNPs}}} = \frac{P(Q)_{\text{mix}} S(Q)_{\text{mix}}}{P(Q)_{\text{AuNPs}} S(Q)_{\text{AuNPs}}} \sim S(Q)_{\text{mix}}$$

Where the structure factor of bare AuNPs ($S(Q)_{\text{AuNPs}}$) is equal to 1, and the form factor of the mixed system ($P(Q)_{\text{mix}}$) is equal to the form factor of bare AuNPs ($P(Q)_{\text{mix}}$), considering that the $P(Q)$ of the AuNPs cluster does not affect the scattering intensity in the selected Q range.[44]

3. Results and discussions

3.1 AuNPs interaction with hybrid membranes

The aggregation of AuNPs on bio-membranes consisting of organized supported bilayers onto a hydrophilic support, was initially studied through confocal laser scanning microscopy (CLSM). We investigated the interaction between 12 nm AuNPs and hybrid lipid-polymer membrane, composed by 1,2-dipalmitoyl-sn-glycero-3-phosphocholine (DPPC) and poly(butadiene-*b*-ethyleneoxide) (PBD-*b*-PEO), compared to the pure DPPC system. According to the recent literature[45], at room temperature, DPPC molecules associate in water in gel phase structures, characterized by an elevated rigidity due to the high order of the hydrophobic tails, while the PBD-*b*-PEO copolymer forms softer polymeric bilayers. The assembly in water of the two selected building blocks produces hybrid bilayers with phase separated soft and rigid regions. The effect of raft-like domains with different rigidities on the AuNPs interaction was monitored using model membranes at a polymer molar composition 65%mol PBD-*b*-PEO.

The hybrid lipid-polymer interface was labelled with two different fluorescent probes: a rhodamine-modified copolymer (RhodPBD-*b*-PEO) and a lipid β -bodipy dye. The selected probes differ in their affinity to the lipid and copolymer phases, and they are characterized by well-separated absorption and emission spectra, allowing the simultaneous acquisition of both probes. Specifically, RhodPBD-*b*-PEO spontaneously accumulate in the polymeric domains, while lipid β -bodipy possesses a higher affinity for the lipid moiety.

DPPC and DPPC-PBD-*b*-PEO65% supported bilayers were formed by spontaneous vesicles' rupture and fusion onto borosilicate confocal wells, according to a well-established protocol[46]. The AuNPs dispersion was added into the wells and the interaction was monitored after 5, 10 and 30 minutes.

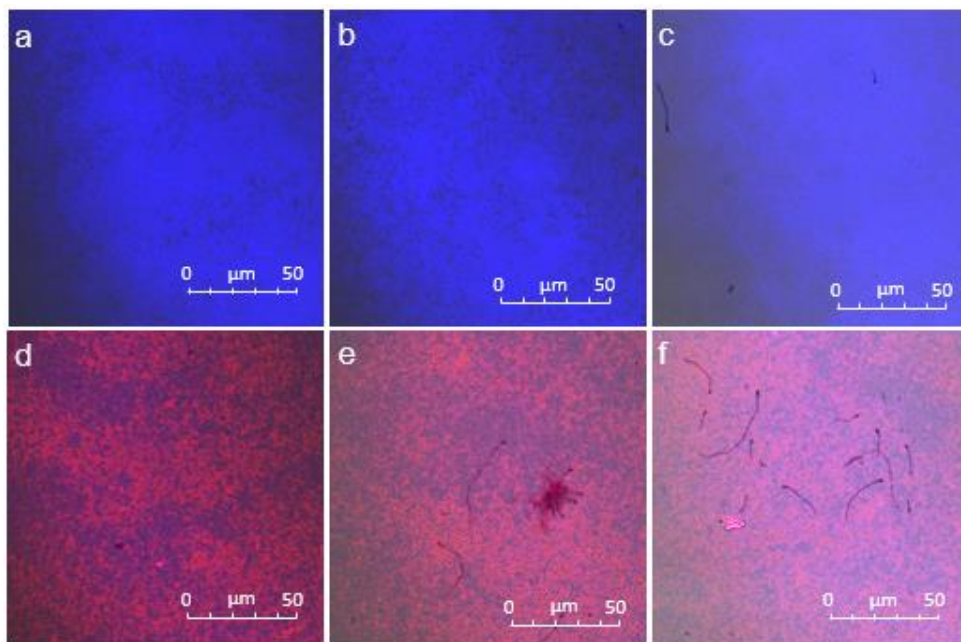


Figure 1. 2D confocal microscopy images of the interaction of 9.93 nM AuNPs with SLB of DPPC and DPPC PBD-b-PEO65%. a) DPPC SLB, image collected 5 minutes after the AuNPs incubation; b) DPPC SLB, image collected 10 minutes after the AuNPs incubation c) DPPC SLB, image collected 30 minutes after the AuNPs incubation; d) DPPC-PBD-b-PEO65% SLB, image collected 5 minutes after the AuNPs incubation, e) DPPC-PBD-b-PEO65% SLB, image collected 10 minutes after the AuNPs incubation, f) DPPC-PBD-b-PEO65% SLB, image collected 30 minutes after the AuNPs incubation. Merged channels PBD(1200)-b-PEO(600) + rhodamine excitation wavelength 561 nm, emission wavelength 571 nm-630 nm (red); β -bodipy excitation wavelength 488 nm, emission wavelength 488 nm-530 nm (blue) and transmission (greyscale).

As shown in the CLSM images (Figure 1), we observed a faster AuNPs aggregation onto the hybrid SLB of DPPC PBD-b-PEO65% than on the pure DPPC one. Initially (5-10 minutes), the AuNPs aggregation, visible in the transmission signal, only occurs in the presence of the polymer (see Figure 1 a, d, b and e). 30 minutes after the incubation, small aggregates start to grow onto the pure lipid interface, while big clusters are already formed onto the hybrid lipid-polymer substrate (reported in Figure 1c and f), pointing out the slower dynamic of the AuNPs clustering on the rigid membranes.

As expected, the CSLM results show that the presence of soft polymer regions strongly affects the AuNPs behavior. However, the resolution of the technique

cannot neither allow us to clearly discriminate the regions where the particles aggregate, nor visualize the presence of single AuNPs and even small clusters.

To get a further comprehension of the interaction between AuNPs and hybrid lipid-polymer systems, we performed a surface sensitive technique, namely Quartz Crystal Microbalance (QCM). In this technique, molecules and particles are adsorbed on a hydrophilic SiO₂ sensor varying its resonance frequency. The resonance frequency shift (Δf) of the sensor can then be associated with the adsorbed mass.[47] Pure DPPC and hybrid SLBs were formed onto the sensor at a temperature close to the gel-liquid crystalline phase transition of the DPPC membrane ($T = 41^{\circ}\text{C}$) (consistently with literature[48], PBD-b-PEO does not form a stable film, see SI). The AuNPs were injected in the measurement chamber after cooling down the temperature to restore the gel phase of the DPPC membrane [49].

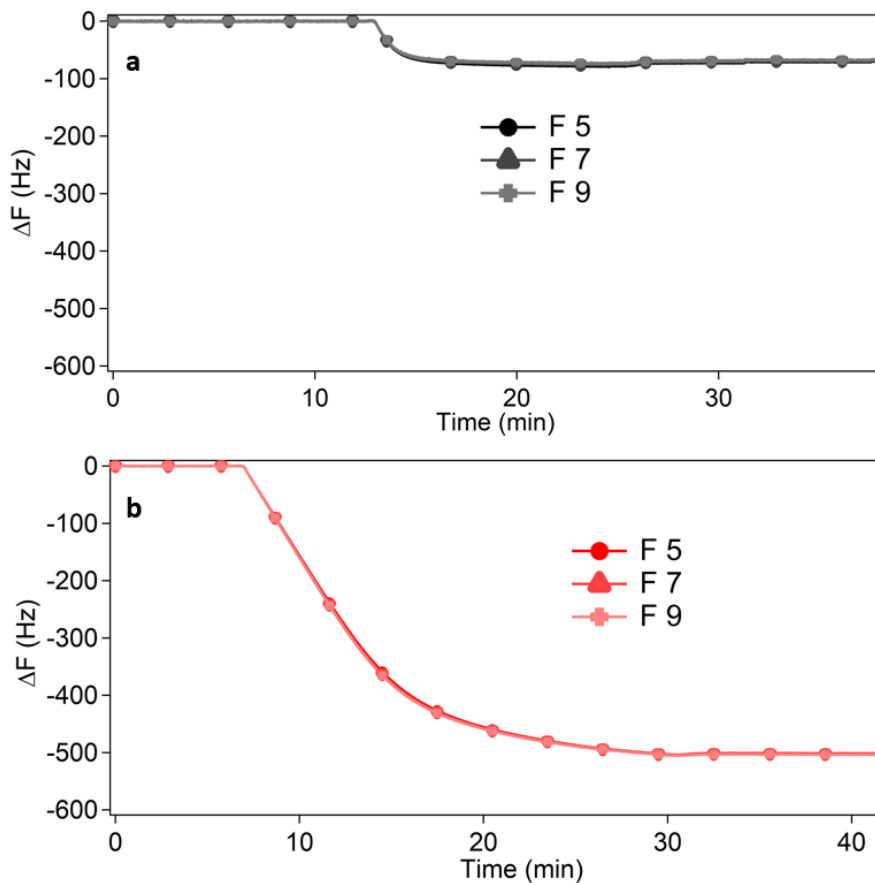


Figure 2. QCM measurements of the deposition of AuNPs' adsorption onto pure DPPC (a) and hybrid DPPC PBD-b-PEO65% (b) supported lipid bilayers. Frequency variation measured for 5th, 7th, and 9th harmonics (black-red lines, filled circles and empty triangles). a) deposition of AuNPs on the SLB of DPPC, (1) AuNPs injection flow 0.1mL/min incubation, (2) rinse with water flow 0.1mL/min H₂O. b) deposition of AuNPs on the SLB of DPPC PBD-b-PEO65%, (1) AuNPs incubation, (2) rinse with water flow 0.1mL/min H₂O.

As reported in Figure S1 (see SI), the formation of a complete DPPC and DPPC-PBDPEO65% bilayers leads to frequency shifts of $\Delta f = -30$ Hz and $\Delta f = -60$ Hz, respectively. As shown in Figure 2, the AuNPs injection results in an increase of the absolute value of the frequency shifts ($\Delta f = -70$ Hz for the deposition of AuNPs on pure DPPC SLB, $\Delta f = -500$ Hz on the hybrid SLB), suggesting a significant mass adsorption on the membrane. The larger Δf observed for the hybrid SLB demonstrate the much higher affinity of AuNPs for the hybrid bilayer. To gain quantitatively information about the AuNPs interaction with the membranes, the Sauerbrey equation was applied (Material and methods section, equation 1). We compared the amount of AuNPs interacting with the hybrid membrane to the pure

lipid system. The calculated adsorbed mass on the DPPC PBD-b-PEO65% bilayer is 1522.9 $\mu\text{g}/\text{cm}^2$, while only 212.0 $\mu\text{g}/\text{cm}^2$ adhere to the DPPC one (see Table 1). These results evidenced that the inclusion of the polymer into the lipid membrane strongly promotes the membrane-templated aggregation of AuNPs, opening new perspectives for the use of complex hybrid membranes for selective interaction with inorganic nanoparticles.

Sample	AuNPs mass absorbed ($\mu\text{g}/\text{cm}^2$)	Number of AuNPs absorbed (AuNPs/cm^2)
DPPC	212.0	7.6×10^9
DPPC PBD-b-PEO 65%	1522.9	5.4×10^{10}

Table 3. Mass and number of AuNPs absorbed on the SLBs of pure DPPC and hybrid DPPC PBD-b-PEO 65% systems calculated through the Sauerbrey equation.

3.2 AuNPs interaction with free-standing hybrid vesicles

3.3

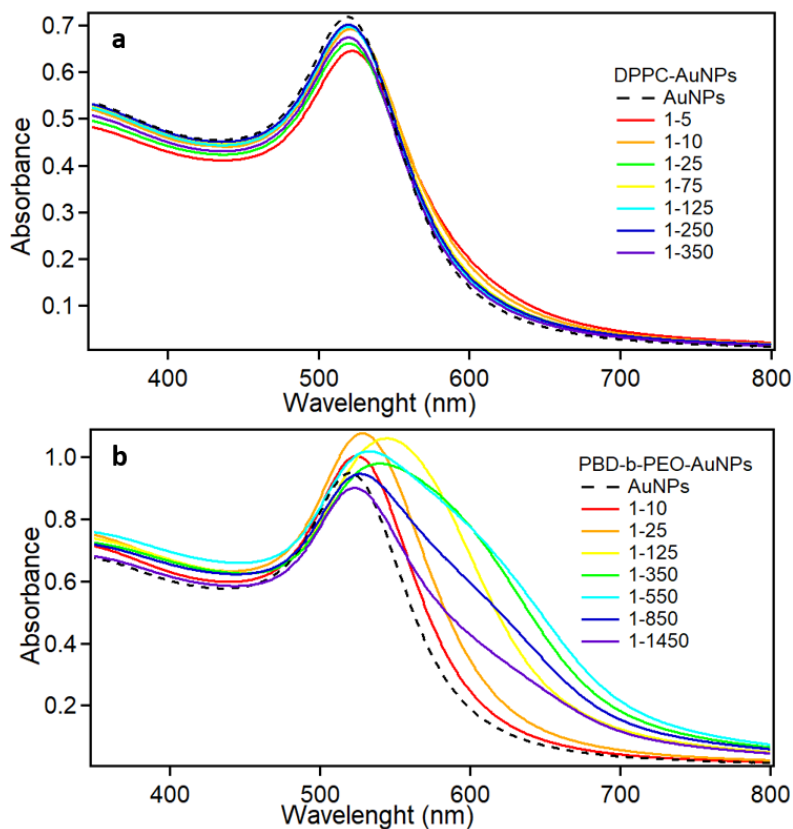


Figure 4. 300 μL of 9.93×10^{-9} M AuNPs were incubated with 10 μL of a) DPPC and b) PBD-b-PEO vesicles in the following vesicles/NPs ratios: 1/5, 1/10, 1/25, 1/50, 1/75, 1/125, 1/150, 1/200, 1/250, 1/350, 1/450, 1/550, 1/850, 1/1250, and 1/1450.

Recent works demonstrated that AuNPs plasmonic variations can be exploited to monitor the aggregation of AuNPs on the liposomes surface as a function of their concentration and membrane rigidity.[36][37] However, such studies focused on vesicles with a homogeneous surface, while the effect of membrane domains still need to be assessed.

To better understand the polymer role, we performed UV-vis spectroscopy, monitoring the variation of the optical properties of citrate AuNPs following the incubation with 100 nm vesicles at different PBD-b-PEO molar composition (DPPC, DPPC PBD-b-PEO5%, DPPC PBD-b-PEO15%, DPPC PBD-b-PEO35%, DPPC PBD-b-PEO65%, PBD-b-PEO) and vesicle/NPs ratios.

Concerning rigid DPPC vesicles (Figure 3a), the interaction with AuNPs provokes negligible effects to the plasmonic peak, completely in agreement with the recent literature[31][50]. In our hypothesis, the elevated rigidity of DPPC membranes inhibits the AuNPs clustering, and the nanoparticles just randomly adhere to the lipid surface as single particles. On the contrary, the AuNPs incubation with pure PBD-b-PEO vesicles leads to a significant variation of the characteristic color of the gold dispersion (from red to purple-blue), associated to the broadening of the plasmonic peak (Figure 3b). This experimental evidence, clear consequence of the plasmon coupling effect, points out that citrate AuNPs cluster on the polymeric membrane. Moreover, the decrease in the vesicle/AuNPs ratio corresponds to a progressive enlargement of the plasmonic peak, until a maximum. A further increase in the number of NPs per vesicle determines a progressive restoration of the original plasmonic properties, highlighting a non-monotonic behavior of the AuNPs aggregation with the vesicle concentration.

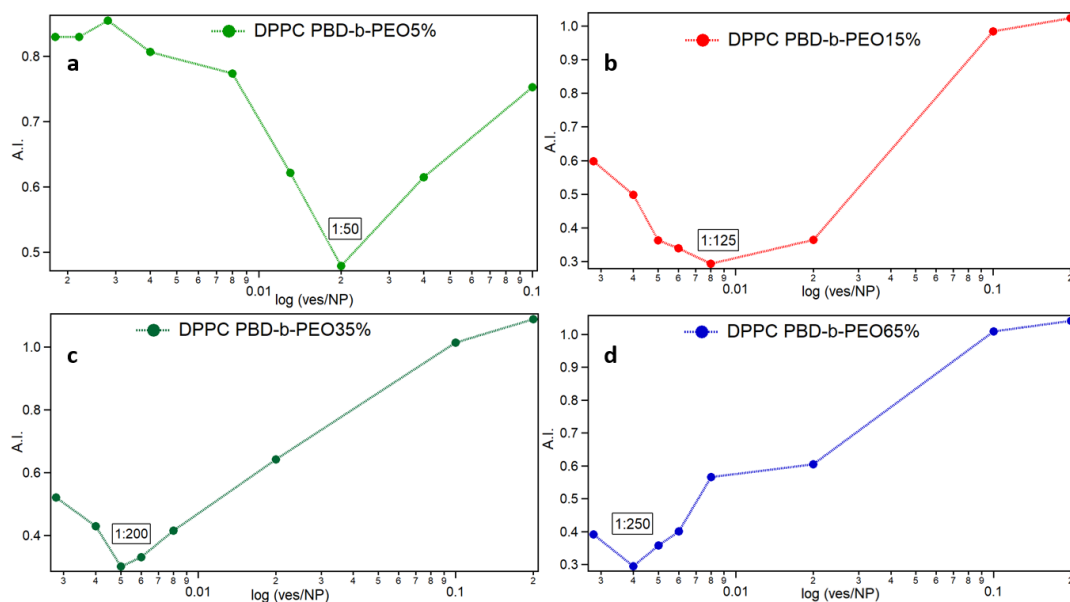


Figure 4. 300 μ L of 9.93×10^{-9} M AuNPs were incubated with 10 μ L of vesicles in the following vesicles/NPs ratios: 1/5, 1/10, 1/25, 1/50, 1/75, 1/125, 1/150, 1/200, 1/250, 1/350, 1/450, 1/550, 1/850, 1/1250, and 1/1450. a) A.I. vs log(vesicle/NP) plot for DPPC PBD-b-PEO5%, b) A.I. vs log(vesicle/NP) plot for DPPC PBD-b-PEO15%, c) A.I. vs log(vesicle/NP) plot for DPPC PBD-b-PEO35%, d) A.I. vs log(vesicle/NP) plot for DPPC PBD-b-PEO65%, e) A.I. vs log(vesicle/NP) plot for PBD-b-PEO.

For what concerns the hybrid vesicles containing PBD-b-PEO, we noticed the same non-monotonic specific trend in the AuNPs aggregation (see SI for full spectra). To better visualize the results and rationalize this behavior, we defined a so-called Aggregation Index (A.I.), already exploited as descriptor of the AuNPs clustering:

$$A. I. = \frac{Abs_{max} - Abs_{600}}{\Delta\lambda} \quad (2)$$

Where Abs_{max} is the absorbance of the AuNPs characteristic peak, generally located about 520 nm, Abs_{600} is the absorbance at 600 nm, the wavelength ascribed to the contribution of the AuNPs clusters, and $\Delta\lambda$ is the difference between 600 nm and 520 nm. The A.I.s calculated for each UV-Vis spectrum were normalized for the one calculated for the bare AuNPs. According to the so-calculated A.I., the A.I. value of bare AuNPs is always equal to 1, and the higher are the plasmonic variations (and consequently the AuNPs aggregation), the lower is the aggregation index.

In Figure 4 the calculated A.I.s are plotted as a function of the vesicle/NP ratio in a logarithmic scale. As already shown for pure PBD-b-PEO vesicles, the A.I. displays a similar non-monotonic behavior for all the hybrid samples as a function of the vesicle concentration.

Sample	Vesicles/AuNPs ratio	A.I.
DPPC	1-5	0.93
DPPC5%PBD-b-PEO	1-50	0.48
DPPC15%PBD-b-PEO	1-125	0.29
DPPC35%PBD-b-PEO	1-200	0.30
DPPC65%PBD-b-PEO	1-250	0.29
PBD-b-PEO	1-450	0.33

Table 2. Ratios Vesicles/AuNPs at which the maximum aggregation of nanoparticles for each sample is observed, reported with their respective A.I.

The vesicles/AuNPs ratios at which the maximum aggregation of nanoparticles occurs are summarized in Table 2. Interestingly, the maximum plasmonic variation in each sample occurs for lower vesicles/AuNPs ratios as the polymer molar

concentration increases, underlying the major effect of the PBD-b-PEO on the nanoparticle clustering (Table 2). However, UV-vis analysis cannot provide a direct information on the cluster structure since the plasmon coupling mostly depends on the interparticle distance and local cluster morphology.[51][52]

To gain insight into the structure of the AuNPs aggregates, we performed Small Angle X-ray Scattering measurements. In our experimental conditions, the SAXS signal only originates from the scattering of AuNPs, while the contribution of vesicles is negligible (see SI). In this way, we directly monitor the influence of the composition and concentration of hybrid vesicles on the AuNPs cluster structure. For each sample, we selected specific concentration ranges covering the vesicle/AuNPs ratios before and after the maximum plasmonic variations. In the low Q region ($\log Q < 1.7$) the power-law of the scattering profiles takes in account the dimensionality of the AuNPs clusters, and the slope of the $\log I(Q)$ vs $\log(Q)$ curves can be associated to their fractal dimensions (d_f), which increases with increasing size and compactness. The fractal dimensions obtained from the linear fittings are reported in the SI. The d_f increases with decreasing the vesicles/AuNPs ratio until a maximum, following the non-monotonic trend of the A.I.s. In fact, in agreement with the AuNPs plasmonics, the vesicles/AuNPs ratio associated to the maximum aggregation of AuNPs is strictly dependent on the vesicle composition (Table 3). Furthermore, such maximum d_f increases with the polymer content, passing from 0.5 for the pure DPPC liposomes to 2.9 for the pure PBD-b-PEO vesicles, highlighting the formation of larger and more compact gold aggregates.

Sample	Vesicles/AuNPs ratio	d_f
DPPC	1-5	0.50
DPPC PBD-b-PEO5%	1-50	1.75
DPPC PBD-b-PEO15%	1-125	1.89
DPPC PBD-b-PEO35%	1-200	1.94
DPPC PBD-b-PEO65%	1-250	2.56
PBD-b-PEO	1-450	2.90

Table 3. Maximum fractal dimensions of each composition of vesicles extrapolated by the linear fitting of the scattering profiles in the low Q region ($\log Q < 1.7$).

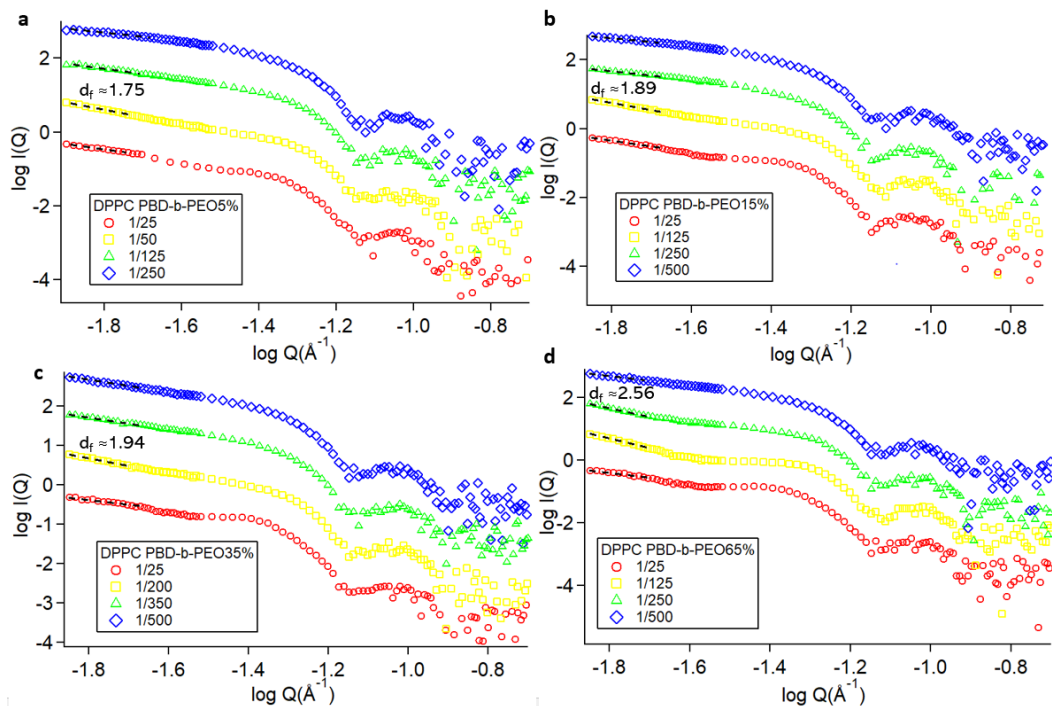


Figure 5. Log – log SAXS profiles of AuNPs/vesicles hybrids collected after 10 minutes of incubation of 300 μL AuNPs 9.93 nM with a) DPPC-PBDPEO5%, b) DPPC-PBDPEO15%, c) DPPC-PBDPEO35%, d) DPPC-PBDPEO65% vesicles at different AuNPs/vesicles ratios. Dashed black lines indicate the linear fittings of the Porod region.

As a further analysis, the AuNPs interparticle distances were extrapolated from the $S(Q)$ of the aggregates (see material and methods section). The $S(Q)$ (Figure 6) shows intensity peaks associated with the interparticle distance in the reciprocal space ($d = \frac{2\pi}{Q}$). For each sample, the peak position shifts towards higher Q values (lower distances) with increasing the number of particles per vesicle. The evaluated minimum interparticle distance, constant for each vesicle formulation (≈ 11.6 nm), is consistent with the AuNPs size, denoting that the AuNPs are in contact with each other. Moreover, this NP-NP minimum spacing is firstly reached for the vesicle/AuNPs ratios characterized by the higher plasmonic variations and fractal dimension. Importantly, the ulterior decrease of the number of vesicles per particle leads to a reduction of the intensity of the $S(Q)$ peaks without altering their position.

To rationalize this clustering behavior, it's worth considering the AuNPs aggregation on pure DPPC lipid membrane. We observed that the aggregation of AuNPs on rigid

membranes is strongly inhibited, independently of the number of vesicles. However, once introduced a soft polymeric domain, the aggregation behavior dramatically changes. For high vesicle amount, the plasmonic variation is still low, consistently with a high average AuNP-AuNP distance (red peaks in Figure 5). Then, reducing the vesicle concentration, the plasmonic variation increases together with the decrease of the interparticle distance, until a certain vesicle/particle ratio (yellow peaks in Figure 5). The maximum AuNPs aggregation can be ascribed to the saturation of the membrane by AuNPs. With a further decrease of vesicles/AuNPs ratio, the additional nanoparticles remain freely dispersed in the solution, restoring the original plasmonic and scattering features. According to this hypothesis, the maximum aggregation depends on the polymer amount, and the number of AuNPs required to saturate the soft polymer rafts increases with the PBD-b-PEO content.

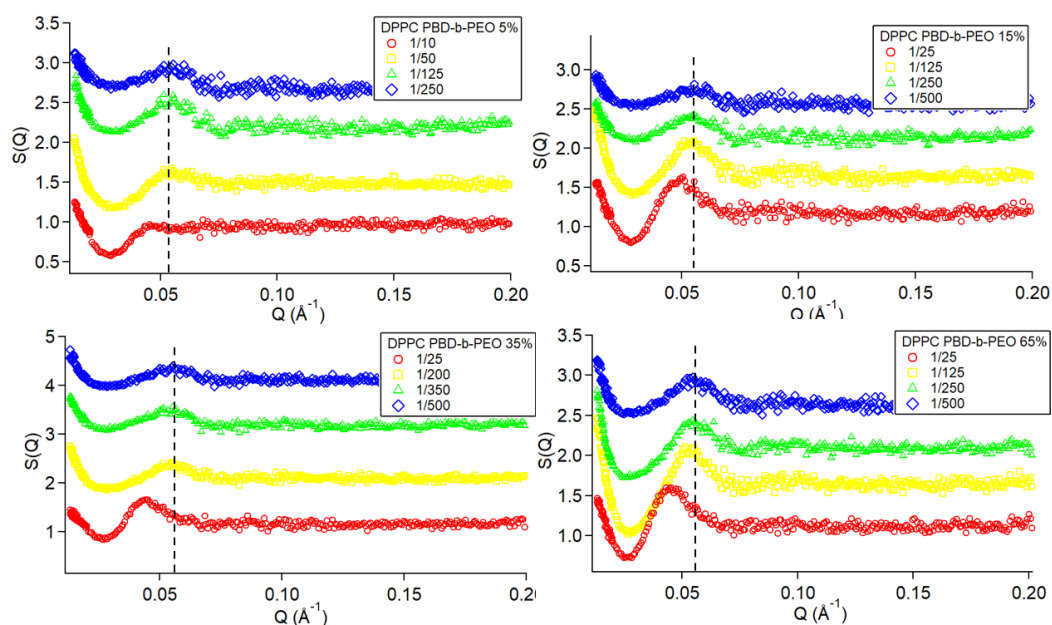


Figure 6. Structure factors ($S(Q)$) evaluated for the samples at 4 different vesicle/AuNPs ratios by dividing the $I(Q)_{\text{mix}}$ by $I(Q)_{\text{AuNPs}}$. The correlation peaks are related to the AuNPs-AuNPs center-to-center interparticle distances. The q -position of the dashed black lines correspond to 11.6 nm.

Altogether, these results, investigating the aspecific interaction between AuNPs and lipid-polymer hybrid membranes, demonstrated that the AuNPs cluster size

and packing can be easily modulated by varying the composition and concentration of the supported and free-standing soft scaffolds.

Conclusions

The investigation of the interaction between inorganic nanoparticles and bio-inspired barriers represents a crucial step for boosting the medical translation of nanomaterials. A common approach for improving the understanding of the chemical-physical parameters that govern the nano-bio interface involves synthetic model membranes as biomimetic platform. Our recent works focused on the spontaneous self-assembly of Turkevich-Frens AuNPs on zwitterionic vesicles, underlying the large applicability of this phenomenon, ranging from the improvement of the fundamental knowledge on nano-bio interfaces[32][54][50], to the development of colorimetric assays for the characterization of natural and synthetic vesicle dispersions[55][38], and the introduction of novel perspectives in the synthesis of controlled colloidal nanohybrids for multiple applications.

Here, to the best of our knowledge, we for the first time deeply investigated the AuNPs clustering on hybrid lipid-polymeric substrates. These brand-new scaffolds found their bio-relevance in the medical field thanks to their ability to mimic cell membranes featured by raft-like domains with well distinct rigidity, which represents a fundamental parameter in the membrane-templated AuNPs processes. The study of the interaction of AuNPs with these complex and heterogeneous membranes was carried out on both supported bilayers, using surface sensitive techniques as Confocal Microscopy and Quartz Crystal Microbalance, and free-standing vesicles, by monitoring the AuNPs aggregation through UV-Vis spectroscopy and Small Angle X-ray Scattering. Our experimental results pointed out that the presence of soft polymeric domains strongly induces the formation of gold clusters onto the lipid-polymer interface. Moreover, we demonstrated that the size and the compactness of AuNPs aggregates strictly depends on the vesicle concentration and polymer content.

In conclusion, our results not only disentangle a peculiar aggregative phenomenon of citrate AuNPs on multidomain membranes, but also proved that the AuNPs cluster size and morphology can be finely controlled, shedding light on novel routes for the preparation of hybrid colloidal adducts with combined properties.

Reference

- [1] K. Cho, X. Wang, S. Nie, Z. (Georgia) Chen, and D. M. Shin, "Therapeutic Nanoparticles for Drug Delivery in Cancer," *Clin. Cancer Res.*, vol. 14, no. 5, pp. 1310–1316, Mar. 2008, doi: 10.1158/1078-0432.CCR-07-1441.
- [2] A. Z. Wilczewska, K. Niemirowicz, K. H. Markiewicz, and H. Car, "Nanoparticles as drug delivery systems," *Pharmacol. Reports*, vol. 64, no. 5, pp. 1020–1037, Sep. 2012, doi: 10.1016/S1734-1140(12)70901-5.
- [3] G. Pillai, "Nanomedicines for Cancer Therapy: An Update of FDA Approved and Those under Various Stages of Development," *SOJ Pharm. Pharm. Sci.*, 2014, doi: 10.15226/2374-6866/1/2/00109.
- [4] M. Liong *et al.*, "Multifunctional Inorganic Nanoparticles for Imaging, Targeting, and Drug Delivery," *ACS Nano*, vol. 2, no. 5, pp. 889–896, May 2008, doi: 10.1021/nn800072t.
- [5] P. Cherukuri, E. S. Glazer, and S. A. Curley, "Targeted hyperthermia using metal nanoparticles," *Adv. Drug Deliv. Rev.*, vol. 62, no. 3, pp. 339–345, 2010, doi: 10.1016/j.addr.2009.11.006.
- [6] M. Bañobre-López, A. Teijeiro, and J. Rivas, "Magnetic nanoparticle-based hyperthermia for cancer treatment," *Reports Pract. Oncol. Radiother.*, vol. 18, no. 6, pp. 397–400, Nov. 2013, doi: 10.1016/j.rpor.2013.09.011.
- [7] S. Balakrishnan, F. A. Bhat, and A. Jagadeesan, "Applications of gold nanoparticles in cancer," *Biomed. Eng. Concepts, Methodol. Tools, Appl.*, pp. 780–808, 2017, doi: 10.4018/978-1-5225-3158-6.ch035.
- [8] M. Seleci, D. Ag Seleci, R. Jonczyk, F. Stahl, C. Blume, and T. Scheper, "Smart multifunctional nanoparticles in nanomedicine," *BioNanoMaterials*, vol. 17, no. 1–2, pp. 33–41, 2016, doi: 10.1515/bnm-2015-0030.
- [9] J. M. Metselaar and T. Lammers, "Challenges in nanomedicine clinical translation," *Drug Deliv. Transl. Res.*, vol. 10, no. 3, pp. 721–725, 2020, doi: 10.1007/s13346-020-00740-5.
- [10] Z. Chu *et al.*, "Unambiguous observation of shape effects on cellular fate of nanoparticles," *Sci. Rep.*, vol. 4, pp. 1–9, 2014, doi: 10.1038/srep04495.
- [11] T. Wang and Y. Luo, "Biological fate of ingested lipid-based nanoparticles: Current understanding and future directions," *Nanoscale*, vol. 11, no. 23, pp. 11048–11063, 2019, doi: 10.1039/c9nr03025e.
- [12] J. Jia, Z. Wang, T. Yue, G. Su, C. Teng, and B. Yan, "Crossing Biological

- Barriers by Engineered Nanoparticles,” *Chem. Res. Toxicol.*, vol. 33, no. 5, pp. 1055–1060, May 2020, doi: 10.1021/acs.chemrestox.9b00483.
- [13] N. Feliu *et al.*, “In vivo degeneration and the fate of inorganic nanoparticles,” *Chem. Soc. Rev.*, vol. 45, no. 9, pp. 2440–2457, 2016, doi: 10.1039/C5CS00699F.
- [14] K. L. Chen and G. D. Bothun, “Nanoparticles meet cell membranes: Probing nonspecific interactions using model membranes,” *Environ. Sci. Technol.*, vol. 48, no. 2, pp. 873–880, 2014, doi: 10.1021/es403864v.
- [15] C. Montis, V. Generini, G. Boccalini, P. Bergese, D. Bani, and D. Berti, “Model lipid bilayers mimic non-specific interactions of gold nanoparticles with macrophage plasma membranes,” *J. Colloid Interface Sci.*, vol. 516, pp. 284–294, 2018, doi: 10.1016/j.jcis.2018.01.064.
- [16] E. Rascol, J. M. Devoisselle, and J. Chopineau, “The relevance of membrane models to understand nanoparticles-cell membrane interactions,” *Nanoscale*, vol. 8, no. 9, pp. 4780–4798, 2016, doi: 10.1039/c5nr07954c.
- [17] C. Montis, D. Maiolo, I. Alessandri, P. Bergese, and D. Berti, “Interaction of nanoparticles with lipid membranes: a multiscale perspective,” *Nanoscale*, vol. 6, no. 12, pp. 6452–6457, 2014, doi: 10.1039/C4NR00838C.
- [18] A. K. Sachan, R. K. Harishchandra, C. Bantz, M. Maskos, R. Reichelt, and H.-J. Galla, “High-Resolution Investigation of Nanoparticle Interaction with a Model Pulmonary Surfactant Monolayer,” *ACS Nano*, vol. 6, no. 2, pp. 1677–1687, Feb. 2012, doi: 10.1021/nn204657n.
- [19] C. Montis *et al.*, “Biogenic supported lipid bilayers as a tool to investigate nano-bio interfaces,” *J. Colloid Interface Sci.*, vol. 570, no. June 2019, pp. 340–349, 2020, doi: 10.1016/j.jcis.2020.03.014.
- [20] M. Schulz and W. H. Binder, “Mixed Hybrid Lipid/Polymer Vesicles as a Novel Membrane Platform,” *Macromol. Rapid Commun.*, vol. 36, pp. 2031–2041, Dec. 2015.
- [21] M. Schulz, A. Olubummo, and W. H. Binder, “Beyond the lipid-bilayer: interaction of polymers and nanoparticles with membranes,” *Soft Matter*, vol. 8, no. 18, p. 4849, 2012, doi: 10.1039/c2sm06999g.
- [22] S. K. Patra, “Dissecting lipid raft facilitated cell signaling pathways in cancer,” *Biochim. Biophys. Acta - Rev. Cancer*, vol. 1785, no. 2, pp. 182–206, 2008, doi: 10.1016/j.bbcan.2007.11.002.
- [23] S.-W. Hu, C.-Y. Huang, H.-K. Tsao, and Y.-J. Sheng, “Hybrid membranes of

- lipids and diblock copolymers: From homogeneity to rafts to phase separation," *Phys. Rev. E*, vol. 99, no. 1, p. 012403, Jan. 2019, doi: 10.1103/PhysRevE.99.012403.
- [24] G. Frens, "Controlled Nucleation for the Regulation of the Particle Size in Monodisperse Gold Suspensions," *Nat. Phys. Sci.*, vol. 241, pp. 20–22, 1973, doi: 10.1038/physci241020a0.
- [25] J. Turkevich, P. C. Stevenson, and J. Hillier, "A study of the nucleation and growth processes in the synthesis of colloidal gold," *Discuss. Faraday Soc.*, vol. 11, no. 0, pp. 55–75, 1951, doi: 10.1039/DF9511100055.
- [26] S. B. Yaqoob, R. Adnan, R. M. Rameez Khan, and M. Rashid, "Gold, Silver, and Palladium Nanoparticles: A Chemical Tool for Biomedical Applications," *Front. Chem.*, vol. 8, no. June, pp. 1–15, 2020, doi: 10.3389/fchem.2020.00376.
- [27] E. C. Dreaden, A. M. Alkilany, X. Huang, C. J. Murphy, and M. A. El-Sayed, "The golden age: Gold nanoparticles for biomedicine," *Chem. Soc. Rev.*, vol. 41, no. 7, pp. 2740–2779, 2012, doi: 10.1039/c1cs15237h.
- [28] A. M. Alkilany, S. E. Lohse, and C. J. Murphy, "The gold standard: Gold nanoparticle libraries to understand the nano-bio interface," *Acc. Chem. Res.*, vol. 46, no. 3, pp. 650–661, 2013, doi: 10.1021/ar300015b.
- [29] V. Amendola, R. Pilot, M. Frasconi, O. M. Maragò, and M. A. Iatì, "Surface plasmon resonance in gold nanoparticles: A review," *J. Phys. Condens. Matter*, vol. 29, no. 20, 2017, doi: 10.1088/1361-648X/aa60f3.
- [30] A. H. R. Koch *et al.*, "Probing Nanoparticle/Membrane Interactions by Combining Amphiphilic Diblock Copolymer Assembly and Plasmonics," *J. Phys. Chem. B*, vol. 124, no. 5, pp. 742–750, 2020, doi: 10.1021/acs.jpcc.9b10469.
- [31] K. Sugikawa, T. Kadota, K. Yasuhara, and A. Ikeda, "Anisotropic Self-Assembly of Citrate-Coated Gold Nanoparticles on Fluidic Liposomes," *Angew. Chemie - Int. Ed.*, vol. 55, no. 12, pp. 4059–4063, 2016, doi: 10.1002/anie.201511785.
- [32] C. Montis *et al.*, "Shedding light on membrane-templated clustering of gold nanoparticles," *J. Colloid Interface Sci.*, vol. 573, pp. 204–214, 2020, doi: 10.1016/j.jcis.2020.03.123.
- [33] J. Cardellini *et al.*, "Membrane Phase Drives the Assembly of Gold Nanoparticles on Biomimetic Lipid Bilayers," *J. Phys. Chem. C*, vol. 126, no.

- 9, pp. 4483–4494, 2022, doi: 10.1021/acs.jpcc.1c08914.
- [34] Z. Wang *et al.*, “Fluidity-Guided Assembly of Au@Pt on Liposomes as a Catalase-Powered Nanomotor for Effective Cell Uptake in Cancer Cells and Plant Leaves,” *ACS Nano*, 2022, doi: 10.1021/acsnano.2c00327.
- [35] J. Cardellini, C. Montis, F. Barbero, I. De Santis, L. Caselli, and D. Berti, “Interaction of Metallic Nanoparticles With Biomimetic Lipid Liquid Crystalline Cubic Interfaces,” *Front. Bioeng. Biotechnol.*, vol. 10, no. March, pp. 1–15, 2022, doi: 10.3389/fbioe.2022.848687.
- [36] B. Lucrezia Caselli *et al.*, “A plasmon- based nanoruler to probe the mechanical properties of synthetic and biogenic nanosized lipid vesicles,” *Nanoscale Horiz.*, 2021.
- [37] D. Maiolo *et al.*, “Colorimetric nanoplasmonic assay to determine purity and titrate extracellular vesicles,” *Anal. Chem.*, vol. 87, no. 8, pp. 4168–4176, 2015, doi: 10.1021/ac504861d.
- [38] A. Zendrini *et al.*, “Augmented COlorimetric NANoplasmonic (CONAN) Method for Grading Purity and Determine Concentration of EV Microliter Volume Solutions,” *Front. Bioeng. Biotechnol.*, vol. 7, no. February, pp. 1–10, 2020, doi: 10.3389/fbioe.2019.00452.
- [39] Y. Ma *et al.*, “Near-infrared II phototherapy induces deep tissue immunogenic cell death and potentiates cancer immunotherapy,” *ACS Nano*, vol. 13, no. 10, pp. 11967–11980, 2019, doi: 10.1021/acsnano.9b06040.
- [40] A. Balestri, L. Chiappisi, C. Montis, S. Micciulla, B. Lonetti, and D. Berti, “Organized Hybrid Molecular Films from Natural Phospholipids and Synthetic Block Copolymers: A Physicochemical Investigation,” *Langmuir*, vol. 36, no. 37, pp. 10941–10951, 2020, doi: 10.1021/acs.langmuir.0c01544.
- [41] K. Jaskiewicz *et al.*, “Incorporation of nanoparticles into polymersomes: Size and concentration effects,” *ACS Nano*, vol. 6, no. 8, pp. 7254–7262, 2012, doi: 10.1021/nn302367m.
- [42] R. C. MacDonald, F. D. Jones, and R. Qui, “Fragmentation into small vesicles of dioleoylphosphatidylcholine bilayers during freezing and thawing,” *BBA - Biomembr.*, vol. 1191, no. 2, pp. 362–370, 1994, doi: 10.1016/0005-2736(94)90187-2.
- [43] F. Olson, C. A. Hunt, F. C. Szoka, W. J. Vail, and D. Papahadjopoulos, “Preparation of liposomes of defined size distribution by extrusion through

- polycarbonate membranes," *BBA - Biomembr.*, vol. 557, no. 1, pp. 9–23, 1979, doi: 10.1016/0005-2736(79)90085-3.
- [44] S. Kim, K. Hyun, B. Struth, K. H. Ahn, and C. Clasen, "Structural Development of Nanoparticle Dispersion during Drying in Polymer Nanocomposite Films," *Macromolecules*, vol. 49, no. 23, pp. 9068–9079, 2016, doi: 10.1021/acs.macromol.6b01939.
- [45] Z. V. Leonenko, E. Finot, H. Ma, T. E. S. Dahms, and D. T. Cramb, "Investigation of temperature-induced phase transitions in DOPC and DPPC phospholipid bilayers using temperature-controlled scanning force microscopy," *Biophys. J.*, vol. 86, no. 6, pp. 3783–3793, 2004, doi: 10.1529/biophysj.103.036681.
- [46] T. K. Lind, M. Cárdenas, and H. P. Wacklin, "Formation of supported lipid bilayers by vesicle fusion: Effect of deposition temperature," *Langmuir*, vol. 30, no. 25, pp. 7259–7263, 2014, doi: 10.1021/la500897x.
- [47] G. Sauerbrey, "Verwendung von Schwingquarzen zur Wägung dünner Schichten und zur Mikrowägung," *Zeitschrift für Phys.*, vol. 155, no. 2, pp. 206–222, 1959, doi: 10.1007/BF01337937.
- [48] K. L. Willes, J. R. Genchev, and W. F. Paxton, "Hybrid lipid-polymer bilayers: PH-mediated interactions between hybrid vesicles and glass," *Polymers (Basel)*, vol. 12, no. 4, 2020, doi: 10.3390/POLYM12040745.
- [49] B. Tenchov, R. Koynova, and G. Rapp, "New Ordered Metastable Phases between the Gel and Subgel Phases in Hydrated Phospholipids," *Biophys. J.*, vol. 80, no. 4, pp. 1873–1890, Apr. 2001, doi: 10.1016/S0006-3495(01)76157-7.
- [50] J. Cardellini *et al.*, "Membrane Phase Drives the Assembly of Gold Nanoparticles on Biomimetic Lipid Bilayers," *J. Phys. Chem. C*, 2022, doi: 10.1021/acs.jpcc.1c08914.
- [51] L. M. Liz-marza, "In V ited Feature Article," *Langmuir*, vol. 22, no. 22, pp. 32–41, 2006.
- [52] N. Carl, S. Prévost, J. P. S. Fitzgerald, and M. Karg, "Salt-induced cluster formation of gold nanoparticles followed by stopped-flow SAXS, DLS and extinction spectroscopy," *Phys. Chem. Chem. Phys.*, vol. 19, no. 25, pp. 16348–16357, 2017, doi: 10.1039/c7cp01807j.
- [53] L. A. Feigin and D. I. Svergun, *Structure Analysis by Small-Angle X-Ray and Neutron Scattering*. Boston, MA: Springer US, 1987.

- [54] S. Salassi *et al.*, "A Martini Coarse Grained Model of Citrate-Capped Gold Nanoparticles Interacting with Lipid Bilayers," *J. Chem. Theory Comput.*, 2021, doi: 10.1021/acs.jctc.1c00627.
- [55] L. Caselli *et al.*, "A plasmon-based nanoruler to probe the mechanical properties of synthetic and biogenic nanosized lipid vesicles," *Nanoscale Horizons*, 2021, doi: 10.1039/d1nh00012h.

Lipid-polymer assemblies as biomimetic platforms for the spontaneous clustering of AuNPs

Jacopo Cardellini, Arianna Balestri, Luca Comparini, Costanza Montis, Debora Berti

Department of Chemistry “Ugo Schiff” and CSGI, University of Florence, via della
Lastruccia 3, 50019 Sesto Fiorentino, Florence, Italy;

	Page
Supplementary Information for Liposomes Preparation	S2
Supplementary Characterization of Gold Nanoparticles	S2
<i>Small Angle X-Ray Scattering</i>	S2
<i>Dynamic Light Scattering and Z-Potential</i>	S3
<i>UV-Vis Spectroscopy</i>	S3
Supplementary Characterization of Liposomes	S4
<i>Dynamic Light Scattering and Z-Potential</i>	S4
<i>Evaluation of liposomes concentration</i>	S5
Supplementary Characterization of Solid Bilayers/AuNPs Hybrids	S7
<i>Confocal Laser Scanning Microscopy</i>	S7
<i>Quartz Crystal Microbalance</i>	S7
Supplementary Characterization of vesicles/AuNPs Hybrids	S8
<i>Preparation of Liposomes/AuNPs Hybrids</i>	S8
<i>UV/Vis Spectroscopy</i>	S11

Supplementary Information for Liposomes Preparation

SAMPLE	DPPC mass (mg)	PBd-b-PEO mass (mg)
DPPC	4.00	/
DPPC PBd-b-PEO5%	3.00	0.82
DPPC PBd-b-PEO15%	2.00	1.63
DPPC PBd-b-PEO35%	2.00	3.82
DPPC PBd-b-PEO65%	1.00	3.54
PBd-b-PEO	/	4.00

Table S1. Quantities in mg used to produce the vesicles.

Supplementary Characterization of Gold Nanoparticles

Small Angle X-ray Scattering

SAXS measurements on AuNPs aqueous dispersion were carried out in sealed glass capillaries of 1,5 mm diameter.

The structural parameters (Table S2) of citrated gold nanoparticles were evaluated from the SAXS profile of their diluted water dispersion (Figure S1), according to a spherical form factor and a Schulz size distribution. In this concentration range, we can safely assume that there are no interparticle interactions are present, and that the structure factor $S(Q)$ equals in the whole range of scattering vectors. Thus, the scattering profile of the particles derives from their form factor, $P(Q)$. The SAXS spectrum reported in Figure S1 is fully consistent with the characteristic $P(Q)$ of

spherical particles with an average diameter of about 6.0 nm. The clear presence of $P(Q)$ oscillations in the high Q region is consistent with a relatively low polydispersity of the synthesized AuNPs.

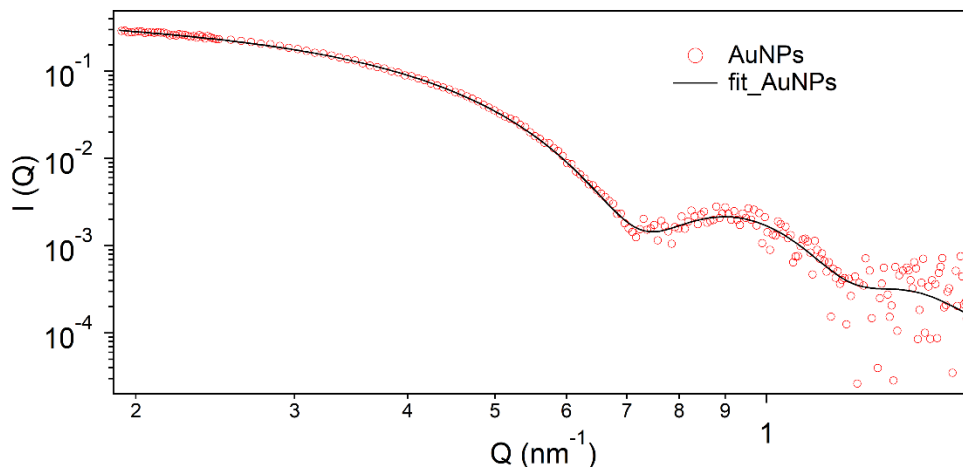


Figure S1. Experimental SAXS curve (red markers) obtained for AuNPs and curve fit (solid black line) according to the Schulz spheres model from the analysis software package Igor. The size and polydispersity obtained from the fitting procedure are summarized in the Table S1 below.

	R_{core} (nm)	poly
AuNP	6.02	0,095

Table S2. Structural parameters of the nanoparticles obtained from the analysis of SAXS curves according to the Schulz spheres model.

Dynamic Light Scattering and Z-Potential

AuNPs hydrodynamic diameter and surface charge in MilliQ water were evaluated through Dynamic Light Scattering and Zeta-Potential, respectively, and reported in

Table S3.

	D _h (nm)	Z-Potential (mV)
AuNPs	20 ± 0,6	-35 ± 3

Table S3. Hydrodynamic diameter obtained from Dynamic Light Scattering and Zeta Potential values of AuNPs.

UV-vis Spectroscopy

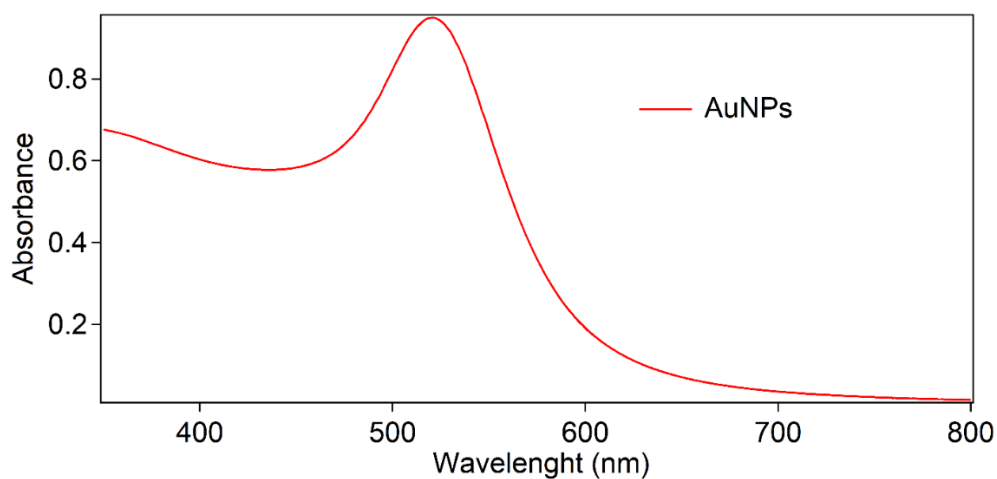


Figure S2 UV-Vis absorption spectra of AuNPs.

To further evaluate the AuNPs size through UV-Vis spectroscopy we exploited the following equation:

$$d = \exp \left(B_1 \frac{A_{spr}}{A_{450}} - B_2 \right)$$

with d diameter of gold nanoparticles, A_{spr} absorbance at the surface plasma resonance peak, A_{450} absorbance at the wavelength of 450 nm and B_1 and B_2 are dimensionless parameters, taken as 3 and 2,2, respectively. The diameter value obtained is of 12.0 nm.

The concentration of citrated gold nanoparticles was determined via UV-Vis spectrometry, using the Lambert-Beer law ($E(\lambda) = \varepsilon(\lambda)lc$), taking the extinction values $E(\lambda)$ at the LSPR maximum, i.e. $\lambda = 520.5$ nm. The extinction coefficient $\varepsilon(\lambda)$ of gold nanoparticles dispersion was determined by the method reported in literature², by the following equation:

$$\ln(\varepsilon) = k \ln(d) + a$$

with d core diameter of nanoparticles, and k and a dimensionless parameters ($k = 3,32111$ and $a = 10,80505$). The final concentration of the citrated AuNPs is therefore $\sim 9.93 \cdot 10^{-9}$ M.

Supplementary Characterization of Liposomes

Dynamic Light Scattering and Zeta-Potential

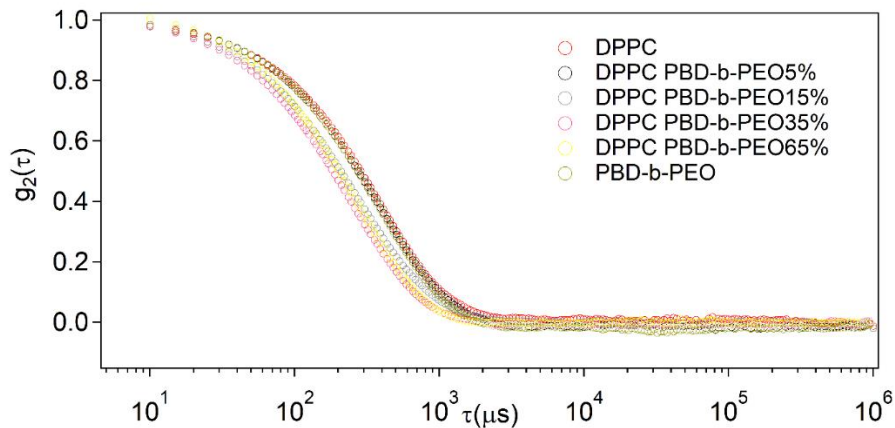


Figure S3. Autocorrelation functions of the liposomes, polymersomes, hybrid systems, and AuNPs

The liposomes dimensions were investigated with DLS (Figure S3). These data can be obtained by fitting the autocorrelation function of the scattering intensity, $g(\tau)$, as a function of time (τ). The decay rate of $g(\tau)$, is strictly related to the dimension of the scattering objects (the smaller they are, the more the autocorrelation function decay rapidly). In the following image are reported the DLS curves normalized in the form of $g_2(q, \tau)$ vs τ (in microseconds), measured for each sample. Each curve was analyzed with the cumulants fitting, and the obtained results highlight the formation of monodispersed vesicles.

	D_h (nm)	Zeta P
DPPC	124.0 ± 1.0	-4.2 ± 0.6
DPPC PBD-b-PEO5%	115.6 ± 1.0	-5.7 ± 0.7
DPPC PBD-b-PEO15%	88.3 ± 0.5	-10.2 ± 0.7
DPPC PBD-b-PEO35%	80.0 ± 0.5	-16.8 ± 0.9
DPPC PBD-b-PEO65%	85.0 ± 1.0	-23.1 ± 2.6
PBD-b-PEO	125.5 ± 1.0	-36.1 ± 2.0

Table S4. Hydrodynamic diameter obtained from Dynamic Light Scattering and Zeta Potential values of synthetic liposomes.

Evaluation of Liposomes Concentration

The lipid concentration in the starting colloidal dispersion was estimated to be 4 mg/mL from the initial lipid and water amounts employed in the formation and swelling of lipid films, assuming the absence of lipid loss due to the extrusion procedure. The liposomes concentration in the final dispersion was subsequently calculated considering the hydrodynamic diameter of each liposomal batch (Table S5). In particular, the liposomal surface area (surface area= $4\pi r^2$) can be calculated from the liposome diameters; the doubled surface can be subsequently divided by the lipid cross section ($0,5 \text{ nm}^2$) in order to obtain the lipid number per liposome, assuming that approximately one half of the lipids is localized in the external leaflet of a liposome, since the bilayer thickness, about 4-5 nm, is negligible with respect to the liposomes' average diameter. Eventually, the total weighted lipid concentration was divided by the total number of lipids per liposome, yielding the real liposome concentration, which is reported in Table S5 for each liposomes' dispersion.

	Concentration (M)
DPPC	$2.8 \cdot 10^{-8}$
DPPC PBD-b-PEO5%	$2,1 \cdot 10^{-8}$
DPPC PBD-b-PEO15%	$3.8 \cdot 10^{-8}$
DPPC PBD-b-PEO35%	$4.0 \cdot 10^{-8}$
DPPC PBD-b-PEO65%	$3.0 \cdot 10^{-8}$

PBD-b-PEO	$1.1 \cdot 10^{-8}$
-----------	---------------------

Table S5. Final liposomes' concentration in each liposomal batch.

The liposomal dispersions were diluted to reach a final concentration of $1,1 \cdot 10^{-8}$ M before use.

Supplementary Characterization of Solid Bilayers/AuNPs Hybrids

Confocal Laser Scanning Microscopy (CLSM)

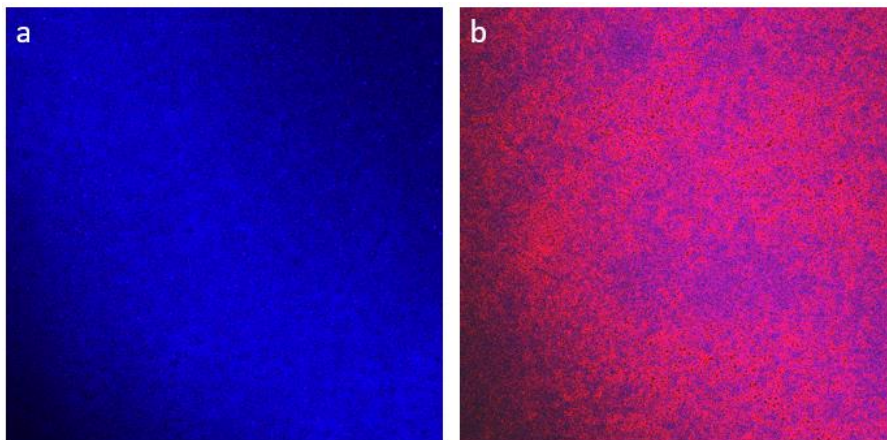


Figure S4. CSLM images of DPPC and 65% mol PBD-b-PEO. a) top image of the DPPC SLB, b) top image of the DPPC 65% mol PBD-b-PEO SLB.

Quartz Crystal Microbalance (QCM)

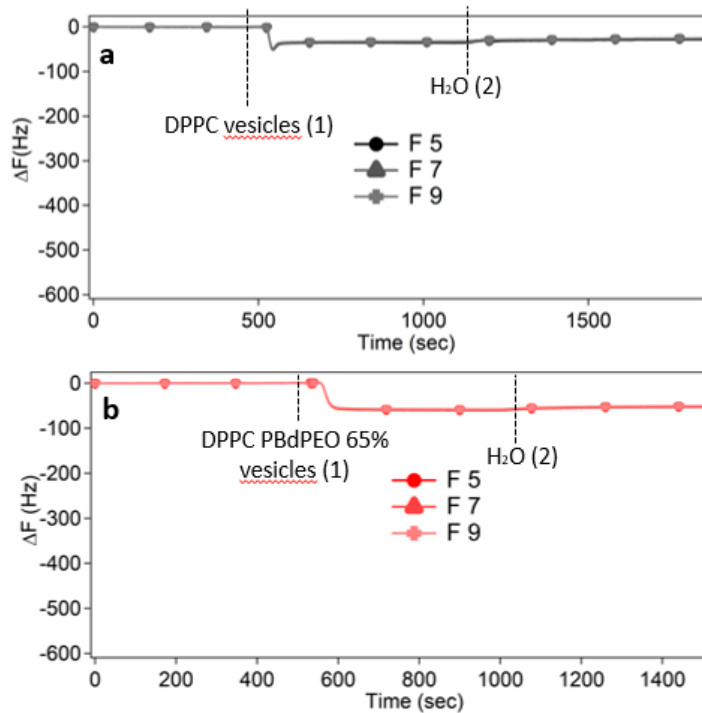


Figure S5. Formation of lipid and copolymer bilayers through QCM measurements of the deposition and rupture of DPPC (a) and DPPC PBD-b-PEO65% (b) vesicles onto SiO₂ sensor.

Frequency variation measured for 5th, 7th, and 9th harmonics (black-red lines, filled circles and empty triangles). a) deposition of DPPC SLB, (1) DPPC vesicles injection flow 0.1mL/min, (2) rinse with water flow 0.1mL/min H₂O. b) deposition of DPPC PBD-b-PEO65% SLB, (1) DPPC PBD-b-PEO65% vesicles injection flow 0.1mL/min, (2) rinse with water flow 0.1mL/min H₂O.

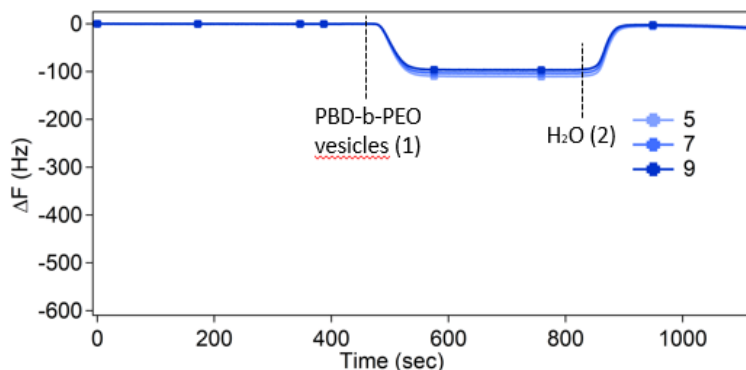


Figure S6. Failed formation of copolymer bilayer through QCM measurements of the deposition and rupture of PBD-b-PEO vesicles onto SiO₂ sensor. Frequency variation measured for 5th, 7th, and 9th harmonics (blue lines, filled circles and empty triangles). (1) DPPC vesicles injection flow 0.1mL/min, (2) rinse with water flow 0.1mL/min H₂O

Supplementary Characterization of vesicles/AuNPs hybrids

Preparation of liposomes/AuNPs hybrids

The hybrid samples were prepared as follow: 10 μL of liposome dispersions (12 nM) were incubated with 300 μL of AuNPs 6,3 nM, to have a liposomes/AuNPs number ratio of ~1/16. This liposomes/AuNPs number ratio was selected on the basis of our previous publication^{3,4} which highlights that the aggregation of AuNPs on zwitterionic vesicles is promoted by low liposome amounts within the mix.

UV-Vis Spectroscopy

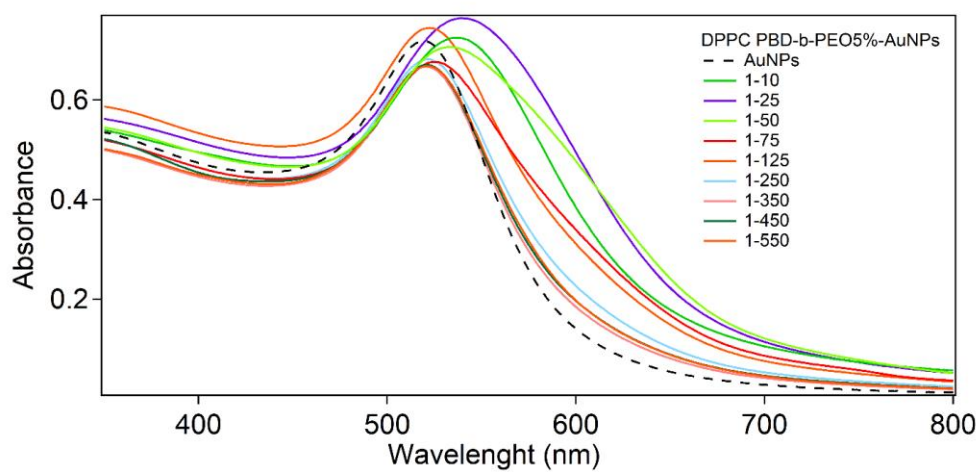


Figure S7. UV-Vis spectra of DPPC PBD-b-PEO 5% at decreasing vesicles/AuNPs ratios.

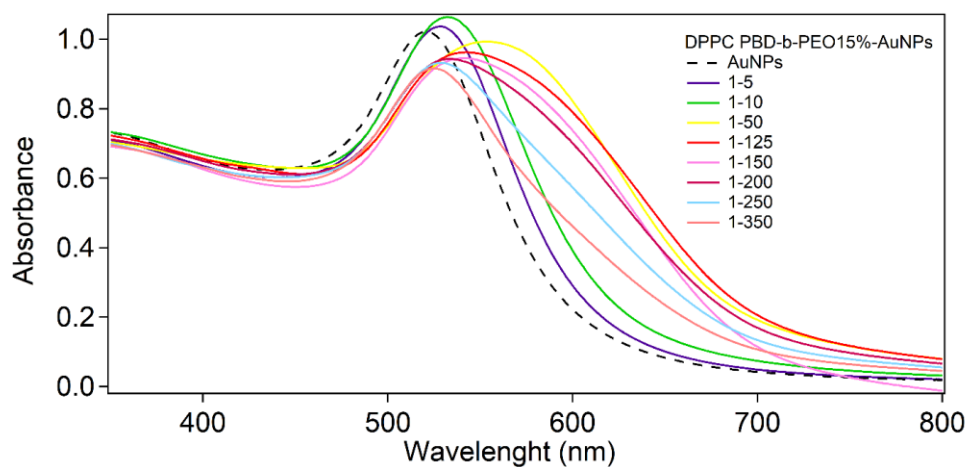


Figure S8. UV-Vis spectra of DPPC PBD-b-PEO 15% at decreasing vesicles/AuNPs ratios.

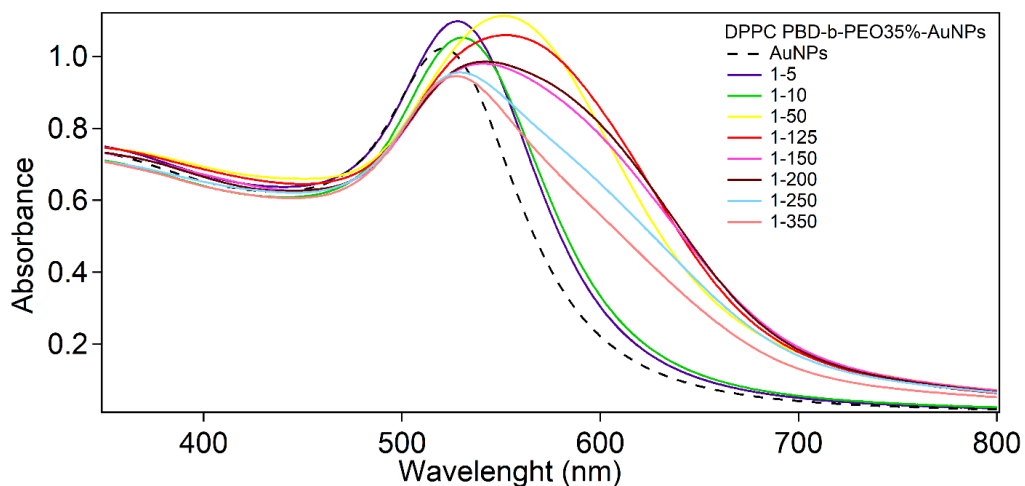


Figure S9. UV-Vis spectra of DPPC PBD-b-PEO 35% at decreasing vesicles/AuNPs ratios.

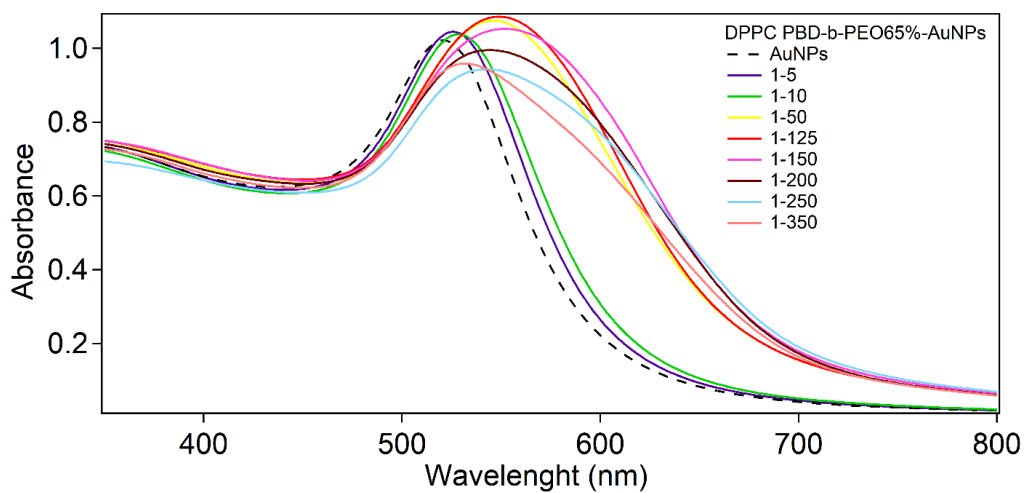


Figure S10. UV-Vis spectra of DPPC PBD-b-PEO 65% at decreasing vesicles/AuNPs ratios

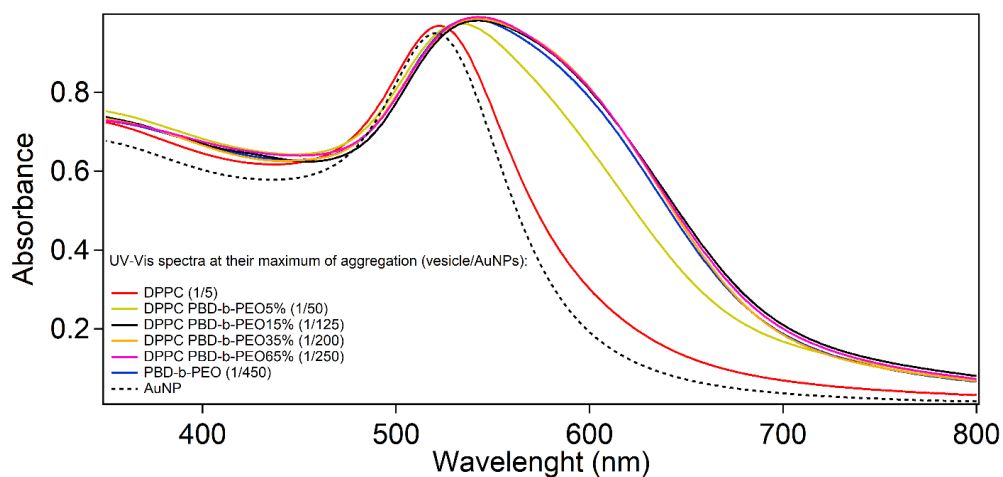


Figure S11. UV-Vis spectra of all the vesicles at the value of vesicle/AuNPs in which the nanoparticles aggregate the most.

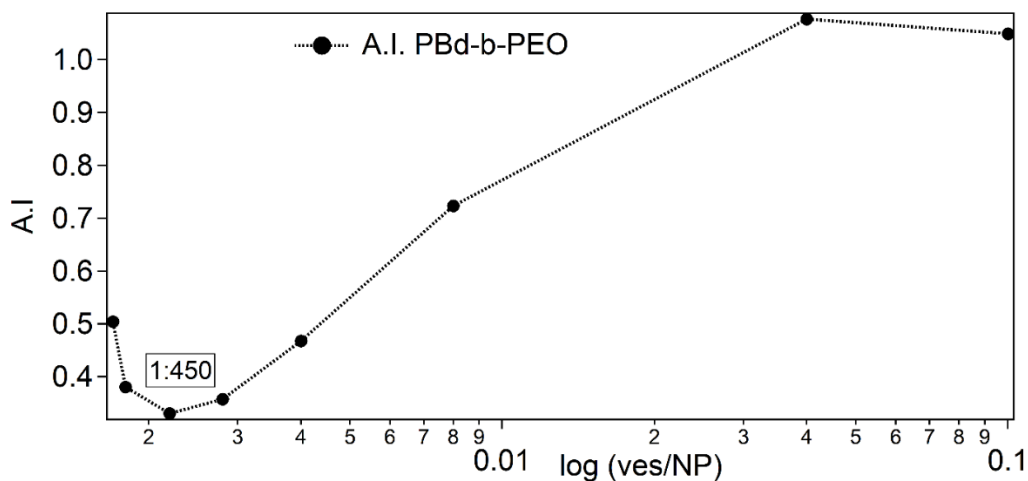


Figure S12. A.I. vs $\log(\text{ves/NP})$ plot for PBD-b-PEO.

Small Angle X-Ray Scattering (SAXS)

VES/AuNPs for DPPC PBD-b-PEO5%	Interparticle distance (nm)
1/10	14.3

1/50	11.6
1/125	11.6
1/250	11.6

Table S6. Interparticle distance calculated for different Vesicles/AuNPs ratio for the sample DPPC PBD-b-PEO5%.

VES/AuNPs for DPPC PBD-b-PEO15%	Interparticle distance (nm)
1/25	13.2
1/125	11.6
1/250	11.6
1/500	11.6

Table S7. Interparticle distance calculated for different Vesicles/AuNPs ratio for the sample DPPC PBD-b-PEO15%.

VES/AuNPs for DPPC PBD-b-PEO35%	Interparticle distance (nm)
1/25	14.3
1/200	11.6
1/350	11.6
1/500	11.6

Table S8. Interparticle distance calculated for different Vesicles/AuNPs ratio for the sample DPPC PBD-b-PEO35%.

VES/AuNPs for DPPC PBD-b-PEO65%	Interparticle distance (nm)
1/25	13.9

1/125	11.9
1/250	11.3
1/500	11.3
1/850	11.3

Table S9. Interparticle distance calculated for different Vesicles/AuNPs ratio for the sample DPPC PBD-b-PEO65%.

VES/AuNPs PBD-b-PEO	Interparticle distance (nm)
1/125	13.5
1/250	11.9
1/350	11.7
1/500	11.6
1/1450	11.6

Table S10. Interparticle distance calculated for different Vesicles/AuNPs ratio for the sample PBD-b-PEO.

VES/AuNPs for DPPC PBD-b-PEO5%	Fractal Dimensions
1/50	1.75 ± 0.03
1/125	1.38 ± 0.04
1/250	1.05 ± 0.04

Table S11. Fractal dimensions calculated for different Vesicles/AuNPs ratio for the sample DPPC PBD-b-PEO5%.

VES/AuNPs for DPPC PBD-b-PEO15%	Fractal dimensions
---------------------------------	--------------------

1/25	1.64 ± 0.04
1/125	1.89 ± 0.03
1/250	1.19 ± 0.03
1/500	1.15 ± 0.03

Table S12. Fractal dimensions calculated for different Vesicles/AuNPs ratio for the sample DPPC PBD-b-PEO15%.

VES/AuNPs for DPPC PBD-b-PEO35%	Fractal dimensions
1/25	1.23 ± 0.04
1/200	1.94 ± 0.02
1/350	1.52 ± 0.03
1/500	1.62 ± 0.03

Table S13. Fractal dimensions calculated for different Vesicles/AuNPs ratio for the sample DPPC PBD-b-PEO35%.

VES/AuNPs for DPPC PBD-b-PEO65%	Fractal dimensions
1/25	1.53 ± 0.06
1/125	2.56 ± 0.06
1/250	2.51 ± 0.04
1/500	1.50 ± 0.04
1/850	0.99 ± 0.04

Table S14. Fractal dimensions calculated for different Vesicles/AuNPs ratio for the sample DPPC PBD-b-PEO65%.

VES/AuNPs PBD-b-PEO	Fractal dimensions
---------------------	--------------------

1/125	2.84 ± 0.01
1/250	3.90 ± 0.06
1/350	2.75 ± 0.06
1/500	2.31 ± 0.05
1/1450	1.35 ± 0.04

Table S15. Fractal dimensions calculated for different Vesicles/AuNPs ratio for the sample PBD-b-PEO.

VES/AuNPs for DPPC	Fractal dimensions
1/10	1.47
1/25	0.52
1/50	0.47
1/125	0.090

Table S16. Fractal dimensions calculated for different Vesicles/AuNPs ratio for the sample DPPC.

Interaction of Metallic Nanoparticles With Biomimetic Lipid Liquid Crystalline Cubic Interfaces (Paper III)

Jacopo Cardellini, Costanza Montis, Francesco Barbero, Ilaria De Santis, Lucrezia Caselli, and Debora Berti, *Front. Bioeng. Biotechnol.* 2022; 10, 848687.



Interaction of Metallic Nanoparticles With Biomimetic Lipid Liquid Crystalline Cubic Interfaces

Jacopo Cardellini^{1,2}, Costanza Montis^{1,2}, Francesco Barbero^{2,3}, Ilaria De Santis^{1,2}, Lucrezia Caselli^{1,2,4*} and Debora Berti^{1,2}

¹Department of Chemistry "Ugo Schiff", University of Florence, Florence, Italy, ²CSGI, Consorzio Sistemi a Grande Interfase, University of Florence, Sesto Fiorentino, Italy, ³Department of Chemistry, University of Turin, Turin, Italy, ⁴Department of Pharmacy, University of Copenhagen, Copenhagen, Denmark

OPEN ACCESS

Edited by:

Pier Paolo Pompa,
Italian Institute of Technology (IIT), Italy

Reviewed by:

Borislav Angelov,
Institute of Physics (ASCR), Czechia
Maria Ada Malvindi,
HiQ-Nano srl, Italy

*Correspondence:

Lucrezia Caselli
lucrezia.caselli@sund.ku.dk

Specialty section:

This article was submitted to
Nanobiotechnology,
a section of the journal
Frontiers in Bioengineering and
Biotechnology

Received: 04 January 2022

Accepted: 07 February 2022

Published: 15 March 2022

Citation:

Cardellini J, Montis C, Barbero F,
De Santis I, Caselli L and Berti D (2022)
Interaction of Metallic Nanoparticles
With Biomimetic Lipid Liquid
Crystalline Cubic Interfaces.
Front. Bioeng. Biotechnol. 10:848687.
doi: 10.3389/fbioe.2022.848687

In the past decades, events occurring at the nano-bio interface (i.e., where engineered nanoparticles (NPs) meet biological interfaces such as biomembranes) have been intensively investigated, to address the cytotoxicity of nanomaterials and boost their clinical translation. In this field, lamellar synthetic model membranes have been instrumental to disentangle non-specific interactions between NPs and planar biological interfaces. Much less is known on nano-biointeractions occurring at highly curved biological interfaces, such as cubic membranes. These non-lamellar architectures play a crucial -but far from understood-role in several biological processes and occur in cells as a defence mechanism against bacterial and viral pathologies, including coronaviruses infections. Despite its relevance, the interaction of cubic membranes with nano-sized objects (such as viral pathogens, biological macromolecules and synthetic NPs) remains largely unexplored to date. Here, we address the interaction of model lipid cubic phase membranes with two prototypical classes of NPs for Nanomedicine, i.e., gold (AuNPs) and silver NPs (AgNPs). To this purpose, we challenged lipid cubic phase membranes, either in the form of dispersed nanoparticles (i.e., cubosomes) or solid-supported layers of nanometric thickness, with citrate-stabilized AuNPs and AgNPs and monitored the interaction combining bulk techniques (UV-visible spectroscopy, Light and Synchrotron Small-Angle X-ray Scattering) with surface methods (Quartz Crystal Microbalance and Confocal Laser Scanning Microscopy). We show that the composition of the metal core of NPs (i.e., Au vs Ag) modulates their adsorption and self-assembly at cubic interfaces, leading to an extensive membrane-induced clustering of AuNPs, while only to a mild adsorption of isolated AgNPs. Such differences mirror opposite effects at the membrane level, where AuNPs induce lipid extraction followed by a fast disruption of the cubic assembly, while AgNPs do not affect the membrane morphology. Finally, we propose an interaction mechanism accounting for the different behaviour of AuNPs and AgNPs at the cubic interface, highlighting a prominent role of NPs' composition and surface chemistry in the overall interaction mechanism.

Keywords: gold nanoparticles, silver nanoparticles, biomimetic systems, nano-bio interface, lipid liquid crystals, cubosomes, nano-bio interactions, cubic membranes

1 INTRODUCTION

During the last decades, inorganic nanoparticles (NPs) have been extensively investigated as possible building blocks for the development of therapeutic/diagnostic systems for biomedical applications: from the diagnosis and treatment of pathologies, to the recovery of damaged tissues, to the targeted, specific delivery of drugs, to the theranostics of serious diseases such as cancer, bacterial and viral infections, (Salvioni et al., 2017; Anees Ahmad et al., 2020; Yaqoob et al., 2020), the designed nanomedicine applications of inorganic NPs and, in particular, of metallic NPs, are countless (Alkilany et al., 2013; Muthu et al., 2014; Lombardo et al., 2019).

Despite this extremely promising potential, the clinical translation of NPs is still very limited, also due to a lack of comprehension and control of the NPs biological fate once in living organisms (Nel et al., 2009). Understanding the energetic contributions that rule interactions at the nano-biointerface (i.e. where NPs meet biological barriers, specifically cell membranes), is very challenging, due to the high compositional heterogeneity of biomembranes and the intrinsic variability of the biological environment. In this context, model membranes of lamellar nature (i.e., composed of a flat lipid bilayer (Montis et al., 2014a)) have proved to be instrumental to unravel non-specific interactions of nanomaterials with lipid interfaces and relate their behavior with the therapeutic efficacy and/or toxicity of NPs in biological organisms (Hélix-Nielsen, 2018; Pfeiffer et al., 2019; Montis et al., 2020a).

Conversely, the interaction of NPs with more complex membranous architectures, characterized by a non-lamellar nature, is practically unexplored. The so-called “cubic membranes”, for instance, are biologically relevant structures characterized by a high membrane curvature and translational order (Almshergji et al., 2006). Their 3D structure possess a cubic symmetry and consists of bicontinuous aqueous non-intersecting nanochannels separated by a lipid bilayer (Mezzenga et al., 2019). Several reports demonstrated the permanent or transient-occurrence of such a non-lamellar phase in cell membranes under starvation, viral infection, oxidative stress and other pathological conditions (Deng and Mieczkowski, 1998; Almshergji et al., 2009; Mezzenga et al., 2019). Importantly, it has been found that coronavirus infections (e.g. SARS-CoV-2, SARS-CoV, or MERS-CoV) are connected with the formation of cubic membranes in host cells (Knoops et al., 2008; Zhang et al., 2020; Deng and Angelova, 2021), which has been proposed as an evolutionary defence mechanism. Moreover, this membrane organization plays crucial roles in several biological processes, such as membrane fusion and fission.

On the synthetic side, these natural highly curved biological membranes inspired the development of artificial lipid-based architectures of cubic geometry, currently used in several technological fields, ranging from protein crystallization (Cherezov et al., 2002; Meikle et al., 2017), to nanomedicine (Yaghmur and Mu, 2021) and nutritional science (Yaghmur, 2019).

Synthetic cubic lipid systems can be formulated as “cubosomes” (Gustafsson et al., 1996), i.e. water-dispersed

nanosized particles with internal cubic structure. The colloidal stability of such particles in water is traditionally provided by amphiphilic copolymers adsorbed onto their surface (Chong et al., 2015), even though novel classes of stabilizer-free cubosomes emerged more recently (Zabara et al., 2019). Cubosomes have an enormous potential as vectors for *in vivo* targeted delivery of drugs, antimicrobials and active principles (Barriga et al., 2019; Zabara et al., 2019), due to the extraordinarily high encapsulation efficiency of both hydrophilic and hydrophobic molecules, compared to more traditional liposomal carriers. The formulation of hybrid inorganic NPs/cubosome systems can further extend their potential in nanomedicine, providing the lipid matrix with stimuli-responsive features. In this respect, understanding the interactions of inorganic NPs with the lipid interface of cubosomes has proved instrumental for the successful design of smart hybrid carriers for magnetically guided delivery and controlled release of drugs (Montis et al., 2015; Mendozza et al., 2018; Caselli et al., 2021a).

Beside this promising applicative potential, investigating the interaction of NPs with cubosomes offers a fresh perspective on nano-biointeractions, shifting the focus to the interface of cubic biomembranes. In this respect, artificial cubic phase systems, such as solid-supported cubic phase films, have been proposed as possible biomimetic platforms only recently (Dabkowska et al., 2017a; Dabkowska et al., 2017b; Caselli et al., 2022). These synthetic mimics aim at shedding some light on the mysterious role of cubic membranes in Nature, as well as investigating their response to nano-sized objects, from artificial nanomaterials to biological NPs, e.g. virus and biogenic vesicles. As an example, in a recent work we demonstrated that synthetic cubic phase membranes are significantly more resistant than lamellar ones against the destructive effect of positively charged AuNPs with different morphologies (Caselli et al., 2022). This effect was connected to the different geometry of the membrane, able to drive profound differences in the interactions established at the nano-bio interface.

However, except for few pioneering studies in the field, the interaction of such cubic interfaces with NPs still represents an almost unexplored research field.

In the present work, we studied the interaction of prototypical metallic NPs for medical applications (i.e. Ag- and AuNPs) with stabilizer-free cubosomes, synthesized according to recent preparation protocols (Zabara et al., 2019). We employed cubosomes either dispersed in water or adsorbed onto a solid support. Such artificial lipid models allowed us to study the effect of the core NPs composition (i.e. Ag- vs AuNPs) on cubic phase membranes, under simplified and controlled conditions. From the membrane side, the absence of a steric stabilizer on cubosomes enabled to investigate the interaction of NPs with a “naked” cubic interface, not mediated by a polymeric layer, in more similar conditions as the ones in living cells. From the NPs side, citrated Ag- and AuNPs were selected. Citrate anions are weakly associated to the metallic surface and are easily displaced by biomolecules commonly present in living organisms, such as serum proteins and membrane lipids (Perera et al., 2018; Wang

et al., 2019; Montis et al., 2020b). Thus, the selected particles allow a direct comparison of the interaction of two different metallic surfaces with the cubic lipid interface, minimizing the mediation of the coating agent. With this aim, we monitored the interaction of Ag- and AuNPs with cubosomes through a combination of bulk techniques (e.g. UV-vis spectroscopy (UV-vis) and Small Angle X-ray Scattering (SAXS)) and surface methods, i.e. Quartz Crystal Microbalance (QCM) and Confocal Laser Scanning Microscopy (CLSM). Overall, we show how the interaction crucially depends on the composition of the metallic NPs, leading to weaker interactions with the AgNPs and to irreversible clustering of AuNPs on the cubic phase membrane. These findings broaden our current knowledge of the chemical-physical parameters which govern the interaction at the nano-biointerface, extending the investigation to cubic interfaces of high biological relevance.

2 MATERIALS AND METHODS

2.1 Materials

Tetrachloroauric (III) acid, silver (I) nitrate, trisodium citrate dihydrate, Glycerol monooleate (GMO), and tannic acid were provided by Sigma-Aldrich (St. Louis, MO). 1,2-dioleoyl-sn-glycero-3-phosphocholine (DOPC) and 1,2-dioleoyl-3-trimethylammonium-propane (DOTAP) were provided by Avanti Polar Lipids, as well as 18:1 Cyanine 5 Phosphatidylethanolamine hydrophobic dye. The lipid dye β -Bodipy TM FL C12-HPLC were provided by Thermofisher. All chemicals were used as received. Milli-Q grade water was used in all preparations (conductivity: 0.056 μ S/cm, resistivity: 18.2 M Ω cm at room temperature).

2.2 Synthesis of AuNPs

Anionic gold nanospheres were synthesized according to a kinetically controlled seeded growth method (Bastús et al., 2011).

2.2.1 Synthesis of Au seeds

Briefly, 250 ml of a 2.2 mM sodium citrate aqueous solution was brought to boiling temperature under constant and vigorous magnetic stirring in a three-necked flask. When the solution reached the boiling temperature, 1 ml of HAuCl₄ was injected. The solution was further boiled for 10 min until it acquired a light pink colour. The resulting seeds are citrate coated particles of about 10 nm.

2.2.2 Growth of AuNPs

After the seed formation, 25 ml of seed dispersion were extracted, and 25 ml of sodium citrate 2.2 mM were injected. The reaction was cooled until 85–90°C. 1 ml of HAuCl₄ 25 mM was added in the flask. The colour of the solution turns red, and the resulting particle size is about 21 nm. The growth process was repeated twice to obtain AuNPs with the required size.

2.3 Synthesis of AgNPs

Anionic silver nanospheres were synthesized according to a kinetically controlled seeded growth method (Bastús et al., 2014).

2.3.1 Synthesis of Ag seeds

As for Au nanospheres, 100 ml of a 5 mM sodium citrate aqueous solution was brought to boiling temperature under constant and vigorous magnetic stirring in a three-necked flask. Then 200 μ L of tannic acid 2,5 mM and 1 ml of AgNO₃ were injected sequentially (delay time 3 min). After 10 min, 25 ml of Ag seeds were extracted, and 25 ml of sodium citrate 5 mM were added.

2.3.2 Growth of AgNPs

After the seed formation, the reaction mixture was cooled until 90°C. Then, 250 μ L of tannic acid (2,5 mM) and 250 μ L of AgNO₃ (5 mM) were sequentially injected (time delay ~ 1 min). The solution was heated for another 10 min before the particle characterization.

2.4 Liposomes and Cubosomes Preparation

For the preparation of DOPC (1,2-Dioleoyl-sn-glycero-3-phosphocholine)/DOTAP (Dioleoyl-3-trimethylammonium propane) (70/30 mol%) liposomes for QCM measurements, the proper amount of the two lipids were firstly dissolved in chloroform in 40 ml glass vials. For CLSM measurements, the lipid dye β -Bodipy TM FL C12-HPLC (Thermofisher), dissolved in chloroform, was added to the mixture at a 0.1% mol concentration with respect to the total lipid (DOPC + DOTAP) amount, and a lipid film was obtained by evaporating the solvent under a stream of nitrogen and overnight vacuum drying. The film was then swollen and suspended in a 100 mM NaCl water solution by vigorous vortex mixing to obtain a final 0.5 mg/ml lipid concentration. The resultant multilamellar vesicles (MVLs) in water were tip sonicated with a Digital Sonifier Model 450 (Branson, Hampton, NH, United States), provided with a Horn Tip (diameter 25.4 mm), in an intermittent-pulse mode (5 s), with a power of 400 W (amplitude 50%), for 15 min to obtain a homogeneous dispersion of unilamellar vesicles with a narrow size distribution. Glycerol monooleate (GMO)-based cubosomes were prepared according to a recent protocol (Zabara et al., 2019). A proper amount of GMO was weighted and suspended in in ultrapure milli-Q water by vigorous vortex mixing to obtain a final 4 mg/ml lipid concentration. The resultant dispersion was tip-sonicated for 30 min. For CLSM measurements, the cubosomes dispersion was added to a dry film of a lipid dye (18:1 Cyanine 5 Phosphatidylethanolamine), previously formed on the bottom of a glass vial from a methanol solution, to obtain a final dye's concentration within cubosomes of 0.1% mol.

2.5 UV-Visible Spectroscopy

UV-Vis spectra were collected with a Cary 3500 UV-Vis spectrophotometer.

2.6 Small Angle X-Ray Scattering

Small Angle X-Ray Scattering profiles were measured on AuNPs, AgNPs and hybrid dispersions using a Xeuss 3.0HR (Xenocs) instrument equipped with a Genix3D (Cu) X-Ray source and a Dectris 1 M Eiger detector. Samples were contained in glass capillary tubes of thickness 1.5 mm. Data from each sample

were acquired at Sample-Detector (S-D) distances of 450 and 1800 mm for 300 s. Intensities were normalized with respect to transmission and sample thickness. After data reduction, the contribution of the sample holder and solvent (water) was subtracted from the sample intensity. The wave vector range (Q-range) accessed in the experiments was The data were analysed with the SasView software. The GMO cubosomes dispersion was analysed at SAXS beamline of synchrotron radiation Elettra, Trieste (Italy) operated at 2 GeV and 300 mA ring current. The experiments were carried with and SAXS signal was detected with Pilatus 3 1 M detector in q-range from 0,009 to 0,7 recording the SAXS curves in a glass capillary.

2.7 Cryo-TEM

3 μL of GMO-based cubosomes were applied on glow-discharged Quantifoil Cu 300 R2/2 grids and plunge frozen in liquid ethane using an FEI Vitrobot Mark IV (Thermo Fisher Scientific). Excess liquid was removed by blotting for 1 s (blot force 1) using filter paper under 100% humidity and 10°C. Cryo-EM data were collected at Florence Center for Electron Nanoscopy (FloCEN), University of Florence (Italy), on a Glacios (Thermo Fisher Scientific) at 200 kV equipped with a Falcon III detector operated in counting mode. Images were acquired using EPU software with a physical pixel size of 2,5 Å and a total electron dose of $\sim 50e^{-}\text{Å}^{-2}$ per micrograph.

2.8 ζ -Potential Measurements

Zeta Potential determination was performed using a Brookhaven Instrument 90 Plus (Brookhaven, Holtsville, NY). Each measurement was an average of ten repetitions of 1 minute each and repeated ten times. Zeta potentials were obtained from the electrophoretic mobility u , according to Helmholtz-Smoluchowski equation:

$$\zeta = \frac{\eta}{\epsilon} \times u \quad (1)$$

with η being the viscosity of the medium, ϵ the dielectric permittivity of the dispersing medium. The Zeta Potential values are reported as averages from ten measurements.

2.9 Quartz Crystal Microbalance

QCM experiments were performed on a Q-Sense E1 instrument (Q-Sense, Gothenburg, Sweden). The instrument was equipped with a flow liquid cells (0.5 ml internal volume), containing a quartz sensor with 4.95 MHz fundamental resonance frequency, mounted horizontally. The active surface of the sensors ($\sim 1 \text{ cm}^2$) was coated with a thin SiO_2 layer ($\sim 100 \text{ nm}$ thick). Prior to use, the sensors were bath sonicated in pure acetone and ethanol, then extensively washed with Milli-Q water and dried with nitrogen flux. After that a plasma cleaner was used for 10 min to completely oxidize the surface. The experiments were performed at room temperature and solvent exchange in the measurement chamber was achieved with a peristaltic pump. First, the sensors were placed in the chambers and water was injected at a flow rate of 0.5 ml/min, the frequencies (f) were measured for the odd harmonics (1st–13th). A stable baseline for f of the different harmonics was ensured before the injection of

TABLE 1 | Physicochemical properties of NPs obtained by UV-Vis, SAXS, and ζ -potential measurements. The reported concentration values correspond to the concentration of NPs in the aqueous dispersion, obtained from the synthesis. Before each measurement, AgNPs concentration has been adjusted by dilution, to match the one of AuNPs ($8.3 \times 10^{-10} \text{ M}$).

	Conc.(M)	λ_{max} (nm)	Size (nm)	ζ -pot.(mV)
AuNPs	8.3×10^{-10}	519	20 ± 1	-22.5 ± 1
AgNPs	1.8×10^{-8}	406	22 ± 1	-18.9 ± 0.3

the vesicles. The QCM curves reported are normalized by the overtone number.

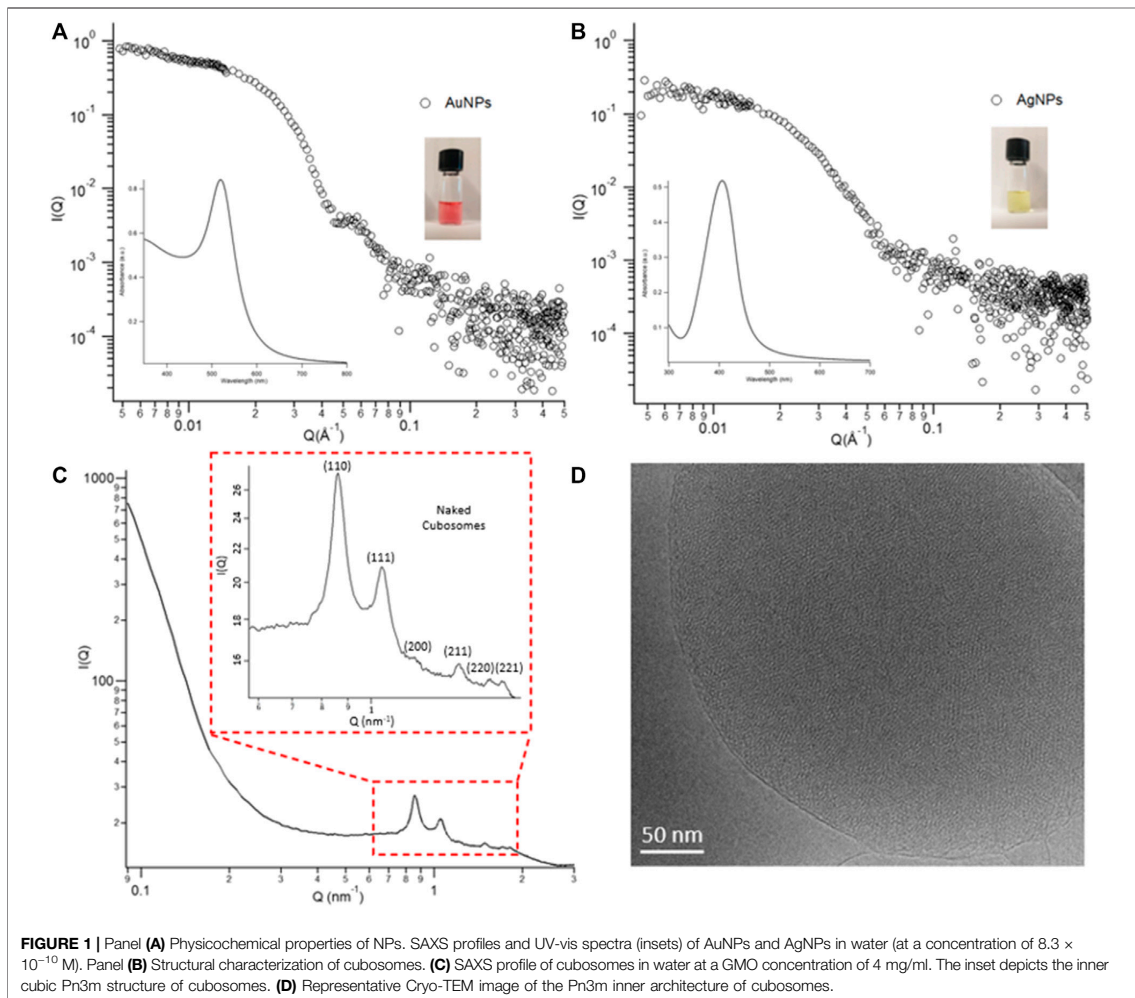
2.10 Confocal Laser Scanning Microscopy

A Leica CLSM TCS SP8 confocal microscope, operating in inverted mode, with a 63×1.3 numerical aperture water immersion objective, was used to image the lipid-based surface structures in water excess. The β -Bodipy TM FL C12-HPLC (ThermoFisher) lipophilic dye was used to label DOPC/DOTAP liposomes; the fluorescence of this probe was excited at 488 nm and collected in the 498–530 nm emission range with a Phomultiplier tube (PMT). The fluorescence of 18:1 Cyanine 5 Phosphatidylethanolamine (Avanti Polar Lipids) was used to label GMO cubosomes, employing an excitation wavelength of 633 nm, while the fluorescence was collected in the 650–700 nm emission range with a PMT. Images were taken with a resolution of 512×512 pixels using a 400 Hz bidirectional scan with each scanning line averaged four times. Leica software was used to create three-dimensional reconstructions of the z-stacks.

3 RESULTS

3.1 Metallic NPs and Cubosomes

Metallic NPs possess unique optical properties due to Surface Plasmon Resonance. Depending on composition, size, shape, and chemical environment, nanometals exhibit different absorption in the UV-Visible spectral region, endowing their dispersions with a characteristic colour. Au and Ag nanospheres typically show size-dependent shades of red and yellow, respectively, with progressive darkening as NPs' size increases. Here, spherical citrate-capped Au- and AgNPs were synthesized following a fast and reproducible protocol (Bastús et al., 2011; Bastús et al., 2014) consisting in the production and homogeneous growth of particles' seeds. The concentration, size, surface properties, as well as the optical features of NPs, are summarized in Table 1 (see also S.1 of Supplementary Material for further characterization). The average size of NPs was determined with Small-Angle X-Ray Scattering (Figures 1A,B). The gyration radii of the particles were obtained through a model-free Guinier analysis of the SAXS profiles of Figures 1A,B, reported in section S.1 of Supplementary Material. Considering spherical particles, we obtained AuNPs and AgNPs of about 20 nm in size and low polydispersity (Table 1). AgNPs and AuNPs UV-Vis spectra in water are characterized by an intense absorbance centred at 406 and



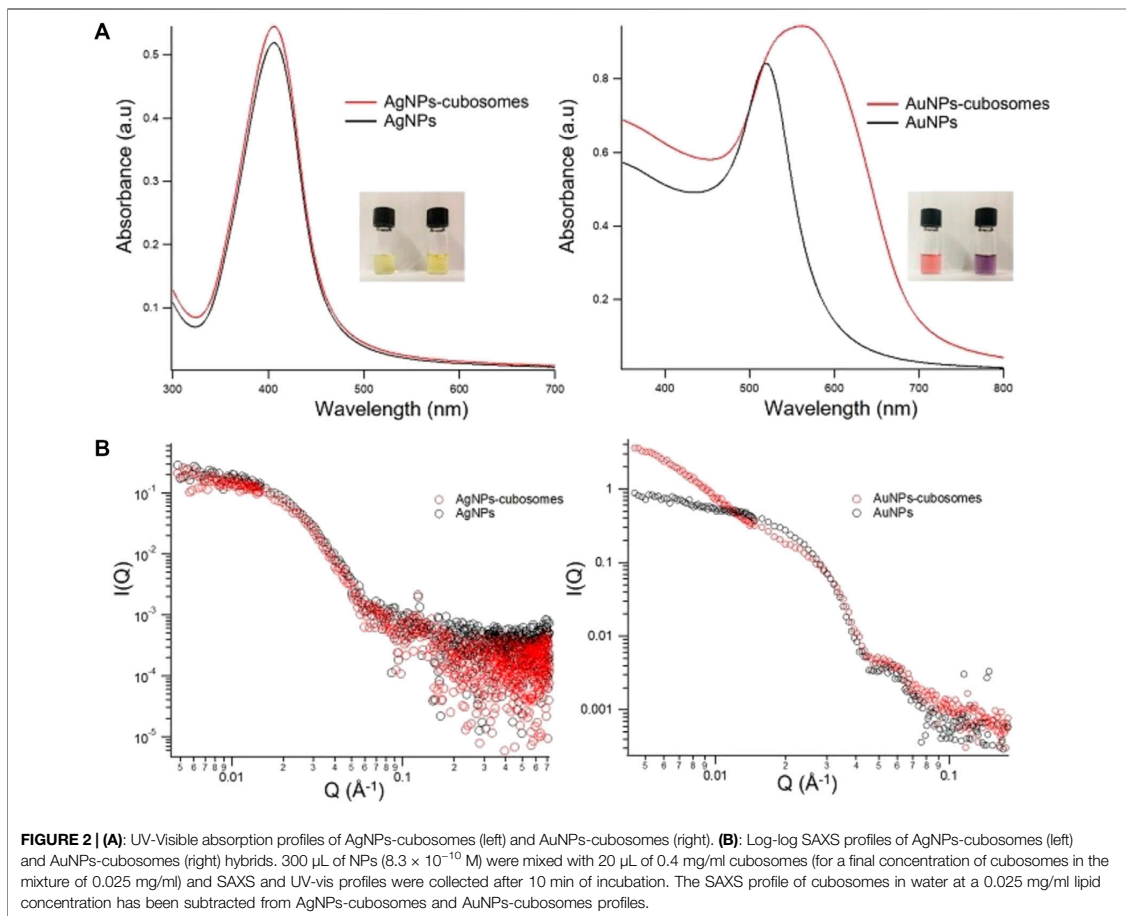
519 nm respectively (see insets in **Figures 1A,B**), in agreement with previous reports on particles of similar size (Bastús et al., 2011; Bastús et al., 2014). The anionic capping agents of NPs (citrate molecules for AuNPs, and citrate and tannic acid (mole ratio $\sim 500/1$) molecules for AgNPs), confer an overall negative surface charge to the particles' surface, been determined through zeta potential measurements (**Table 1**).

Stabilizer-free glycerol monooleate (GMO)/water cubosomes at a 4 mg/ml lipid concentration have been prepared by dispersing the GMO bulk phase in water excess, according to a recently published protocol. (Zabara et al., 2019). **Figure 1C** reports the structural features of their internal architecture. The multiple Bragg peaks in the scattering profile are consistent with a highly ordered lipid cubic phase with a Pn3m space group of a spacing parameter equal to 10.4 nm (see **S.2.2 of Supplementary Material**). This structure is characterized by two sets of interwoven aqueous

nanochannels, lined by a lipid bilayer. Direct images of the internal architecture of cubosomes have been collected with Cryo-TEM performed at the FloCEN facility at the University of Florence (**Figure 1D** and **Supplementary Figure S9**). The average hydrodynamic diameter of cubosomes (d_h) was evaluated through Dynamic Light Scattering measurements by analysing the autocorrelation function with a CONTIN Laplace inversion. The obtained cubosomes are characterized by an average diameter peaked at $d_h = 240$ nm and negative ζ -potential (-34 ± 1) (see **Supplementary Figures S5, S6** for further details).

3.2 AuNPs and AgNPs Interacting With Cubosomes

Figure 2A shows representative UV-vis spectra obtained by incubating 20 μ L of 0.4 mg/ml cubosomes with 300 μ L of



0.83 nM Ag or AuNPs dispersions. Since the optical properties of metallic particles are connected to the interparticle distance, the optical variations in the absorbance of metallic NPs can be used to monitor their aggregation. Generally, such aggregation provokes the broadening of the plasmonic peak, the red shift of its maximum, and even the occurrence of a new red-shifted peak depending on the morphology of the aggregates (Cardellini et al., 2022). All these variations, easily monitorable through UV-Vis Spectroscopy, represent an excellent tool to determine the interaction of NPs with their environment in biomimetic studies, colorimetric assays, and biosensing applications, as we recently presented in different studies. (Montis et al., 2014b; Busatto et al., 2018; Montis et al., 2020b; Zendrini et al., 2020; Caselli et al., 2021b). In our case, as displayed from UV-Vis spectra and pictures in **Figure 2**, the plasmonic features of the AgNPs dispersion remain almost unchanged even after 10 min of incubation with the cubosomes' dispersion. On the contrary, the colour of the AuNPs dispersion quickly turns from red to purple, associated to a prominent red shift of the maximum of the

characteristic plasmonic peak. This is due to the coupling of the surface plasmon modes of proximal NPs, indicating the decrease of the interparticle distance and formation of aggregates. Such a spontaneous aggregation of AuNPs is a concentration-dependent process. The aggregation of the particles gradually increases as the concentration of the cubosomes decreases (see **Supplementary Figure S12** for UV-Vis characterization). The higher extent of aggregation, observed at low cubosomes' amounts, is the clear evidence that the NPs aggregation is a membrane-templated phenomenon that only occurs on the cubosomes' surface.

To gain structural information on cubosomes/NPs hybrids, we performed SAXS measurements (**Figure 2B**). It is worth noticing that in our experimental conditions, the scattering signal of cubosomes is negligible, due to the higher electronic density of metallic NPs. Consequently, any variation in the scattering profiles can be exclusively related to variations in the NPs arrangement. In agreement with UV-vis results, the scattering profile of AgNPs is not affected by the presence of cubosomes,

indicating a very weak (or absent) interaction. In the case of AuNPs/cubosomes hybrids, the colour change reported in the UV-vis spectra is associated with an increase in the slope of the scattering profile at low- q . The power-law dependence observed in this region, highlighted by a linear trend with positive slope in the $I(q)$ vs q double logarithmic plot, can be related to the formation of NPs fractal aggregates on the cubosomes' membrane.

Overall, our findings underline dramatic differences in the interaction of NPs with cubosomes, depending on the metallic composition of the particles. Despite the very similar physical and chemical properties (size, morphology, concentration, and surface coating) shared by Ag- and AuNPs, the behavior of the hybrid systems is highly different. Specifically, AuNPs spontaneously cluster on the cubosomes membrane, pointing out that the attractive forces overcome the electrostatic repulsion, while the aggregation is inhibited in the case of AgNPs. However, UV-vis spectroscopy and SAXS measurements only focus on the behaviour of the inorganic NPs, without providing any information on their effect on the cubic membrane.

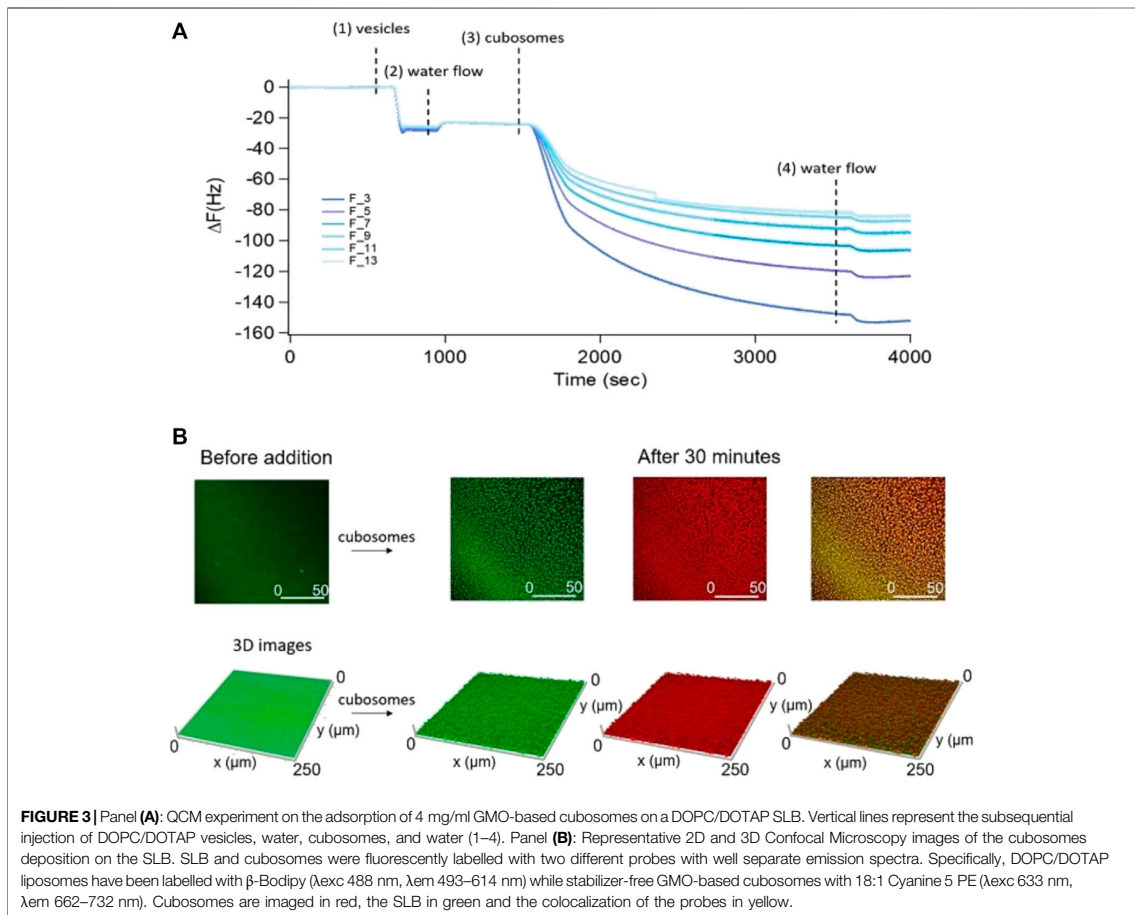
3.3 Cubosomes Deposition on the Lipid Bilayer

The preparation of model lipid membranes in the form of cubosomes adsorbed onto a solid support allowed us to exploit surface techniques (such as QCM and Confocal Microscopy) which allow for monitoring the modifications induced by NPs on the cubic membrane. Such an investigation will complement the information obtained from solution techniques (SAXS and UV-Vis spectroscopy), providing new fundamental insights on the interaction from the membrane perspective. Moreover, it enabled to set the focus exclusively on phenomena occurring at the nanobio interface (i.e., where metallic NPs meet cubic interfaces), ruling out possible bulk effects.

The preparation of solid-supported nanometric assemblies of cubic nature is not straightforward. Most of the studies so far focuses on the interaction of inorganic NPs with model bulk cubic phases (not suitable for surface studies and not well representative of real membranes, characterized by a nanometric thickness). More recently, new methods have been engineered to obtain thinner cubic phase films, with micro (Dabkowska et al., 2017a; Caselli et al., 2022) or nanometric (Ridolfi et al., 2021) thickness. These approaches are based on the spin coating of lipids dissolved in organic solvents (such as chloroform, hexane, and ethanol), generally toxic and complex to get rid of. Here, we exploited a novel approach, which does not require the use of organic solvents. This process is based on the spontaneous deposition and self-assembly of cubosomes onto a solid support, leading to the formation of a thin (i.e. nanometric) cubosomes carpet. Considering that the absorption of GMO-based cubosomes does not take place on bare hydrophilic SiO_2 substrates due to the negative zeta-potential of these lipid particles, we promoted the adsorption of cubosomes by functionalizing SiO_2 substrates with a slightly positive Supported Lipid Bilayer (SLB). Considering the negative surface charge of cubosomes, the electrostatic interaction with the positively charged SLB is

expected to promote a quantitative coverage of the substrate by cubosomes. We prepared the SLB through the adsorption and fusion on a hydrophilic SiO_2 substrate of 0.5 mg/ml DOPC (1,2-dioleoyl-sn-glycero-3-phosphocholine)/DOTAP (1,2-dioleoyl-3-trimethylammonium-propane) vesicles (70/30 mol%) dispersed in a 0.1 M NaCl aqueous solution. **Figure 3A** shows the formation of the DOPC/DOTAP SLB onto the SiO_2 support and the subsequent deposition of cubosomes, monitored by QCM. With this technique, the decrease of the resonance frequency (ΔF) can be related to the adsorbed mass on the sensor. First, we formed the SLB by injecting DOPC/DOTAP vesicles in the chamber measurements (step 1) in **Figure 3A** with a low flow rate (0.1 ml/min). Once injected into the chamber, the vesicles adhered to the SiO_2 substrate, provoking a slight decrease of ΔF . Then, the chamber was rinsed with ultrapure water 2) to promote vesicles' rupture due to the osmotic shock caused by the ionic strength gradient developed across the lipid membrane of vesicles. The inner water content of the vesicles was subsequently released leading to a tiny increase of the ΔF , reaching a stable value of -25 Hz, in perfect agreement with previous reports on SLB formation (Montis et al., 2016). Once the DOPC/DOTAP bilayer was formed, the cubosomes dispersion was injected in the chamber 3). As demonstrated by the high decrease in ΔF , the electrostatic interaction between the lipid bilayer and stabilizer-free cubosomes leads to the instantaneous and massive adsorption of cubosomes. The cell was subsequently rinsed with water (0.5 ml/min flow rate) to check the stability of the cubosomes layer 4); no major variations in ΔF were observed, accounting for the irreversible binding of cubosomes to the SLB, which prevents their detachment under water flow.

As a complementary analysis to directly visualize the formation of the cubosomes layer and obtain structural information at the microscale on coverage, we performed Confocal Laser Scanning Microscopy (CLSM) measurements. For this purpose, we labelled liposomes and cubosomes with two different probes (0.1% mol) with well-separated emission spectra. Representative side and top view 2D images and 3D reconstructions of the SLB before the addition of cubosomes are reported in the Supplementary Material (**Supplementary Figure S10**). **Figure 3B** reports representative top view 2D images and 3D reconstructions of the SLB/cubosomes system, collected after 30 min of incubation of 1 mg/ml cubosomes with the lipid bilayer (see **Supplementary Figure S11**, for corresponding side view 2D images). Here, fluorescence from cubosomes is represented in red, the one from the DOPC/DOTAP SLB in green, while their superposition in yellow. The addition of the cubosomes' dispersion to the lipid bilayer results in the homogeneous deposition of the cubic particles (red spots) on the SLB (green layer) without membrane disruption. After 30 min, the lipid bilayer is homogeneously covered by a layer of cubosomes. The adsorption kinetic has been also monitored live (see **Supplementary Movie S1**), showing that only few minutes (<3 min) are required to reach the fully covered state shown in **Figure 3B**. To gain further insight on the process of deposition of cubosomes, we collected CSLM images of the SLB/cubosomes system, obtained by incubating cubosomes at different concentrations (from 0.05 mg/ml to 1 mg/ml) and monitoring the deposition during the first minutes of interaction (**Figures**

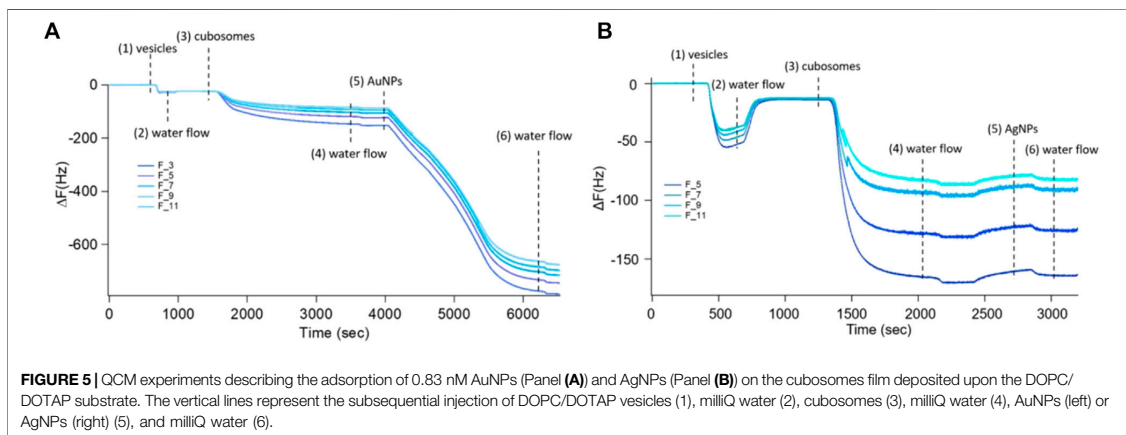
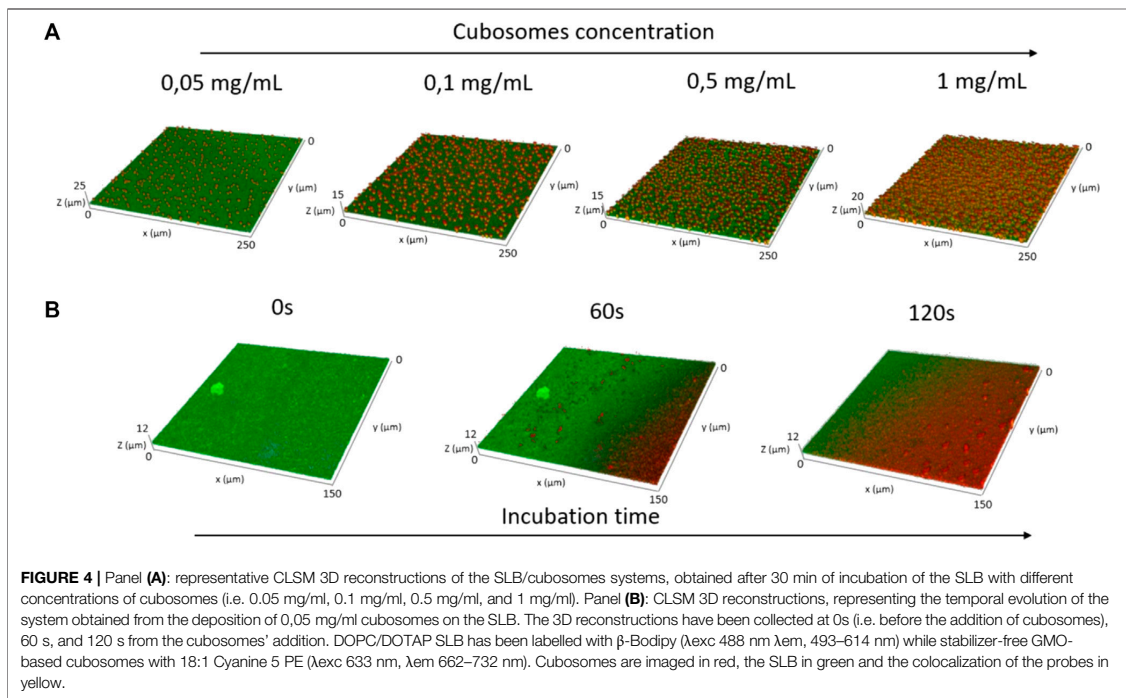


4A,B4). We found that the deposition of cubosomes is strictly dependent on concentration. Specifically, the pattern of cubosomes on the SLB gets less and less densely packed with decreasing concentrations of cubosomes (Figure 4A). Interestingly, the concentration of cubosomes also affects their dynamic of deposition, which appears much slower for low cubosomes' amounts (see also Supplementary Movie S2). With a 0.05 mg/ml cubosomes' concentration, the kinetic of the process is slow enough to allow us to monitor the deposition process in detail, by capturing the morphology of the system under non-equilibrium conditions (i.e. before reaching the final equilibrium forms depicted in Figure 4A). Figure 4B reports representative 3D reconstructions of the mixed SLB/cubosomes (0.05 mg/ml) system at short incubation times (<5 min). In these experimental conditions, we noticed that the (green) SLB assumes a homogeneous red coloration within the first seconds from the addition of cubosomes. This is likely to be due to a fast exchange of material, which includes the fluorescent probe, occurring when cubosomes firstly dock on the SLB substrate.

After that, the characteristic red spots start to pattern the support, quickly reaching an equilibrium configuration (within 10 min). The intrinsic resolution limit in CSLM does not allow to unambiguously assess whether such red spots are single -and isolated-cubosomes, or small cubosomes clusters. However, the negative surface charge of cubosomes (see Section 3.1) implies a strong electrostatic attraction with the positively charged surface of the SLB, responsible for their adsorption; on the contrary, the net repulsion between different cubosomes of same charge is likely to prevent their aggregation on the SLB, leading to the formation a pattern of single -and self-avoiding- cubosomes, such as the one observed in Figures 3, 4.

3.4 AuNPs and AgNPs Interacting With Thin Films of Cubosomes

Figure 5 displays the NPs adsorption on the cubosomes' film monitored with QCM. After the formation and stabilization of the thin film of cubosomes (see Section 3.2, steps 1–3), the system



was extensively rinsed with milliQ water (step 4) to remove the excess of non-adsorbed cubosomes. Right after, water dispersions of AuNPs or AgNPs (**Figure 5B**) at a concentration of 0.83 nM were injected into the measuring cell at 0.1 ml/min flow rate (step 5). The resulting interaction perfectly mirrors what observed for the corresponding dispersed systems. AuNPs strongly interact with the substrate, producing an immediate and dramatic decrease in the oscillation frequency (**Figure 5A**); this

indicates an elevated mass adsorption, which starts immediately and reaches its maximum within the first 30 min of interaction. Importantly, flushing milliQ water at a considerable flow rate (i.e. 0.5 ml/min) does not induce any appreciable removal of the adsorbed AuNPs (step 6), which accounts for a significant AuNPs-cubosomes interaction strength. On the contrary, no relevant shifts of the oscillation frequency were detected following the injection of AgNPs in the

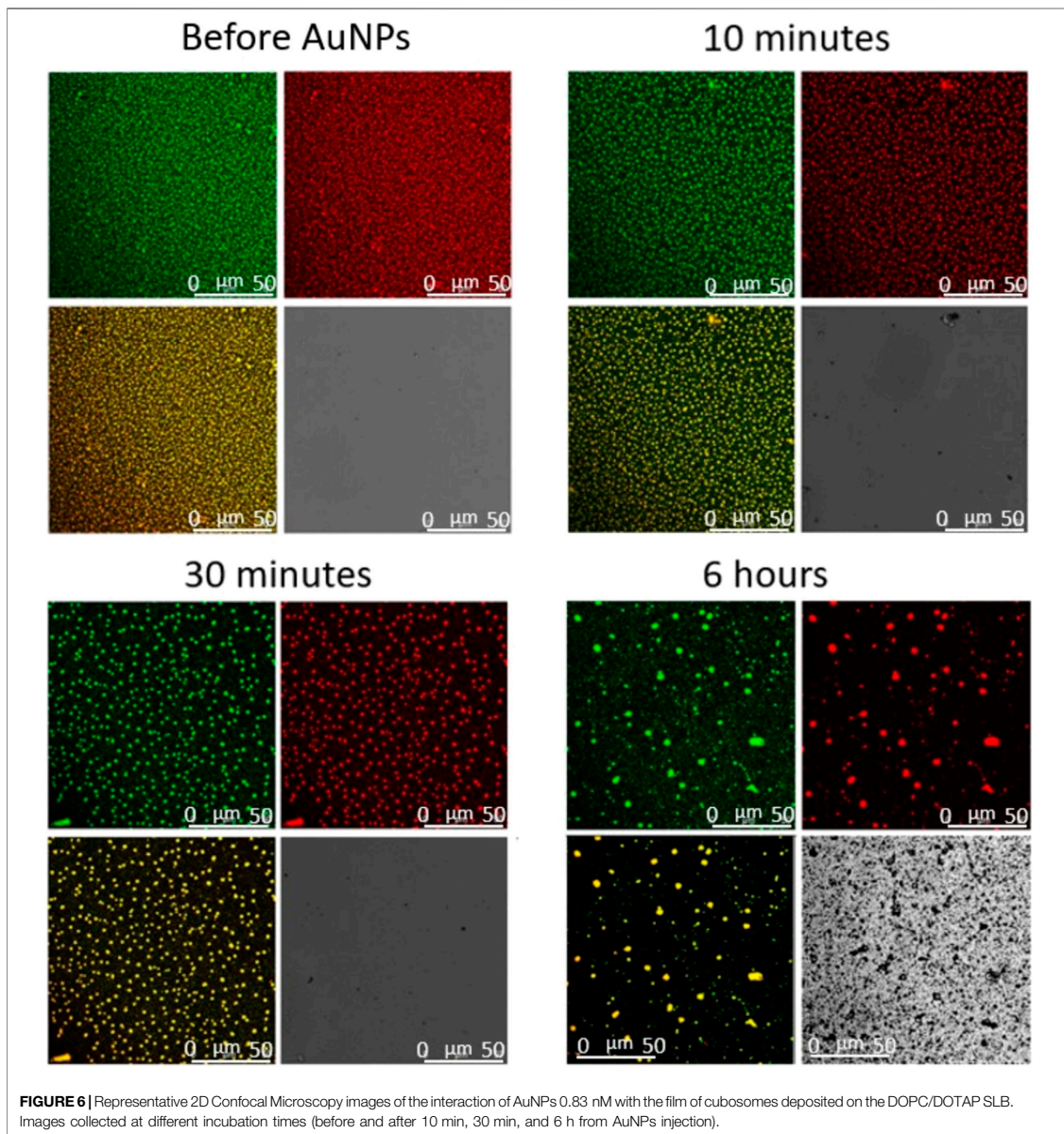


FIGURE 6 | Representative 2D Confocal Microscopy images of the interaction of AuNPs 0.83 nM with the film of cubosomes deposited on the DOPC/DOTAP SLB. Images collected at different incubation times (before and after 10 min, 30 min, and 6 h from AuNPs injection).

QCM chamber (**Figure 5B**), even after 10 min from the injection. Thus, in this latter case, just a negligible (or even absent) number of particles interact with -and adsorb on-the substrate.

On the same systems, we performed Confocal Microscopy measurements to gain information on the morphological modification possibly induced by NPs on the cubosomes film. Such modifications, conveniently monitored at the micron-scale, would account for the impact of NPs on representative portions

($50 \times 50 \mu\text{m}$ squared areas) of the cubosomes membrane. With the same set-up employed previously (see **Section 3.2**), we simultaneously collected the fluorescent signals from the supported DOPC/DOTAP bilayer and the GMO-based cubosomes, to investigate the impact of NPs at different depths of the lipid assembly. Moreover, we observed the interaction in transmission mode as well, to monitor the possible formation of NPs clusters.

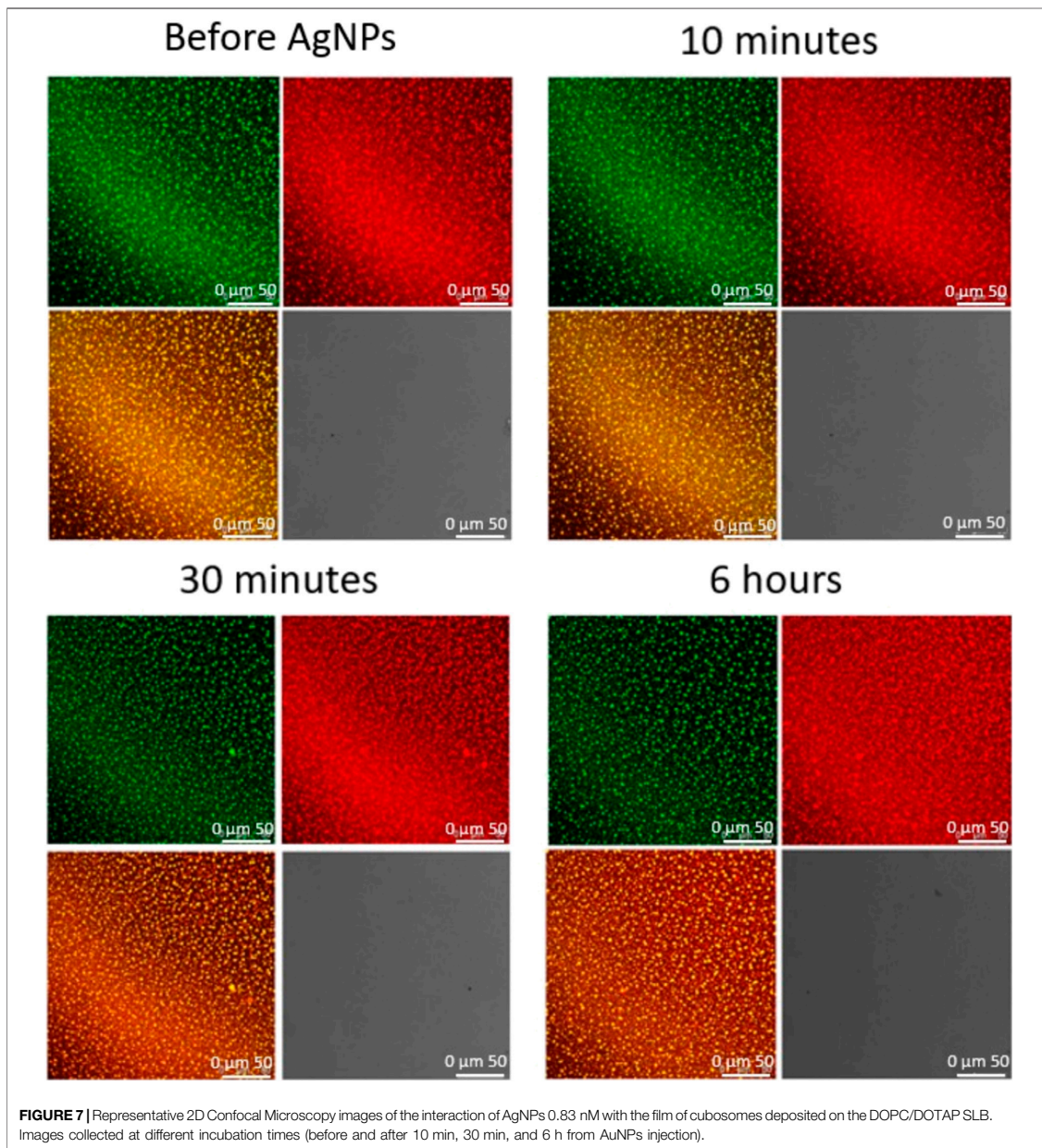
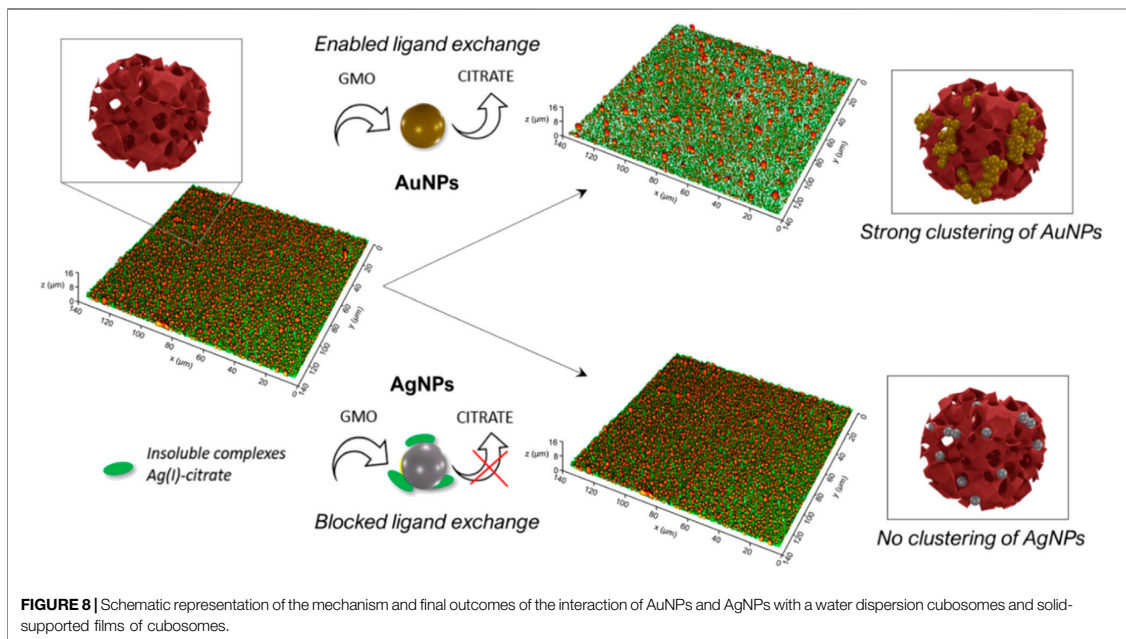


Figure 6 shows representative top-view fluorescence and transmission images of AuNPs interacting with the cubosomes layer adsorbed on the DOPC/DOTAP SLB. The time-evolution of the substrate morphology was monitored over a time-period of 6 h. Before injection of the particles, the substrate is characterized by a stable and densely packed cubosomes' array. Once the particles' dispersion (0.83 nM) is

introduced, the red spots (cubosomes) in the fluorescence image progressively increase in size, hinting to the agglomeration of adsorbed cubosomes. Mirroring the same trend, the SLB below (green fluorescence) becomes less compact. At the same time, the absolute fluorescence intensity of both the lipid bilayer and cubosomes dramatically decreases, suggesting that a lipid extraction



process takes place. After 6 h of interaction, only few large aggregates of mixed lipid composition are still present on the substrate, while the cubosomes layer has completely lost its characteristic packing. The loss of compactness occurs through a progressive dewetting-like process, in which pores are formed within the membrane, similarly to what previously was observed for lamellar membranes interacting with biologically relevant molecules, e.g. polyunsaturated ω -3 fatty acids (Angelova et al., 2019); here, the lipid assembly gradually loses adhesion to the glass substrate and retracts into large lipid agglomerates, likely due to the lipid removal induced by AuNPs. In addition, the transmission image shows micron-sized AuNPs (dark spots), which extensively cover the glass surface.

The very same experiment was performed incubating the cubosomes carpet with AgNPs at the same concentration (Figure 7). Fully in line with previous measurements, the top-view images show that citrated AgNPs do not affect the morphology of the substrate in the first 6 h of interaction. Moreover, the transmission signal doesn't present any sign of NPs aggregation in the chosen experimental time.

Overall, confocal microscopy investigation showed that the interaction with the cubosomes layer is strictly dependent on the particle composition. After a relatively long incubation time, AgNPs don't affect the morphology of the substrate and no micron-sized clusters of particles are detected. On the contrary, the effect of AuNPs is much stronger. AuNPs start to interact with the substrate extracting lipids from both the lipid bilayer and the cubosomes. The homogeneous cubosomes' pattern becomes less and less densely packed with time. After

6 h of incubation the substrate is almost completely disrupted, concentrated in isolated spots, and partially substituted by extended AuNPs clusters.

4 DISCUSSION

In this study we compared for the first time the interaction of a highly curved biomimetic interface of cubic nature with two prototypical metallic nanoparticles for biomedical applications: AuNPs and AgNPs, characterized by a citrate surface coating and a spherical shape. SAXS and UV-vis data, performed in solution, provided information on the variation of the NPs arrangement and interaction at the nanoscale, while Confocal Microscopy gave access to alterations of the micron-sized morphology of the cubic phase supported membrane. Being the selected NPs almost identical in terms of size, concentration and surface coating, our experimental results revealed that the interaction is governed—both at the nano and at the microscale—by the metallic composition of the particles. In particular, we showed that: 1) at the nanoscale: AuNPs quickly cluster on the cubosomes membrane, leading to the formation of NPs' fractal aggregates. On the contrary, the presence of the cubic phase membrane does not induce appreciable aggregation of AgNPs; 2) at the micron-scale: the ordered array of SLB-supported cubosomes gets readily un-packed and concentrated into separated dewetted-like spots by the action of AuNPs, while it is almost unaffected upon contact with AgNPs.

In recent works, a combination of computational and experimental results highlighted that the spontaneous

aggregation of citrated AuNPs on vesicles of lamellar nature is triggered by the fast release of citrate anions at the AuNPs surface (Montis et al., 2020b; Salassi et al., 2021; Cardellini et al., 2022). Such release occurs upon adhesion of AuNPs to the vesicles' membrane, which drives the displacement of citrate anions by the lipids composing the vesicles' membrane (i.e., a citrate/lipid ligand exchange). This causes a loss of electrostatic stabilization of AuNPs, driving their aggregation on the membrane of vesicles. It is reasonable to assume that, in the present case, the aggregation of AuNPs on the cubic membrane occurs through a similar mechanism, i.e., through a ligand exchange between citrate anions, weakly bonded to the gold surface, and the lipids (GMO) constituting the membrane of cubosomes. This ligand exchange, driven by hydrophobic and Van der Waals forces between the gold surface and the lipid molecules, would initiate the AuNPs aggregation on the surface of cubosomes dispersed in aqueous solution (UV-Vis and SAXS data of **Figure 2**), and provoke the lipid extraction and substrate removal observed on solid-supported cubosomes films (**Figure 6**). **Figure 8** (upper part) schematizes such mechanism of interaction and its final outcomes on both dispersed and solid-supported cubosomes.

From this perspective, the different behavior of AgNPs may be explained considering that citrate molecules cannot be as easily displaced from the silver surface as from the gold one. As reported in several works (Djokić, 2008; Anees Ahmad et al., 2020; William et al., 2021), citrate anions form water-insoluble complexes with Ag(I) ions, originated from solubilised Ag at the silver surface. Such complexes lie on the surface of AgNPs, partially -or completely-covering it, and are not readily displaceable at the lipid/water interface. Thus, once AgNPs are mixed with the cubosomes, the formation of these complexes would hamper the ligand-exchange reaction with lipids, preventing the citrate anions release (see **Figure 8**, downer part). As a result, no clustering of AgNPs is revealed on dispersed cubosomes (see UV-Vis and SAXS data of **Figure 2**), and no lipid removal and membrane disruption are observed in solid-supported cubosomes (see also CLSM data of **Figure 7**).

5 CONCLUSION

In the past years, the interaction of inorganic NPs and biomimetic membranes has been intensively investigated to increase our fundamental knowledge on nano-bio interfaces, develop novel synthetic smart hybrid nanomaterials and to predict their biological fate. However, most of these studies focused on planar lamellar membranes. Only recently, synthetic cubic lipid assemblies have been introduced in the library of biomimetic systems, to provide fundamental insight into the role of non-lamellar interfaces in natural systems, such as cubic membranes. Despite these very recent advancements, the biological role of cubic interfaces and their response to NPs adhesion remains an almost unexplored research field. Here for the first time, we present a physicochemical investigation of the interaction of cubic phase interfaces -both as cubosomes dispersions in water and as thin layers adsorbed on a substrate-

with two prototypical NPs particularly relevant for biomedical applications, i.e. AgNPs and AuNPs. The cubosomes' surface array here introduced, represents a particularly convenient structural platform to test NPs' behavior towards cubic phase lipid biomimetic interfaces.

Through an ensemble of different techniques, we disentangled the impact of such NPs on cubic phase structures at different length scales, i.e., from the nano- to the micron-scale. As observed for synthetic lamellar systems, citrated AuNPs cluster on the membrane of dispersed cubosomes, and extensively aggregate on a solid-supported cubosomes' film, leading to its disruption. On the contrary, AgNPs with the same size and identical surface coating, do not affect the morphology of the solid-supported cubosomes films and don't cluster on dispersed cubosomes. This experimental evidence may be related to the binding energy of the citrate molecules to the different metallic surfaces. Citrate anions are weakly associated to the gold surface and can be easily released through a ligand-exchange with the lipids, promoting the aggregation of AuNPs. Conversely, citrate anions form insoluble complexes with the Ag(I) ions at the silver surface, which stabilizes the colloidal dispersion and hampers the interaction with cubic membranes. These results contribute shedding light on the prominent role of the nature and association between ligands and metallic NPs surfaces in determining the events at nano-bio interfaces of cubic nature.

DATA AVAILABILITY STATEMENT

The original contributions presented in the study are included in the article/**Supplementary Material**, further inquiries can be directed to the corresponding author.

AUTHOR CONTRIBUTIONS

DB and LC contributed to conception and design of the study. FB, LC, JC, and IS synthesized gold and silver nanoparticles. LC, JC, and IS performed experiments. LC, JC, and CM performed the analysis of data. JC wrote the first draft of the manuscript. DB, CM, and LC contributed to manuscript revision. All authors read and approved the submitted version.

FUNDING

This work has been supported by the European Community through the evFOUNDRY project (H2020-FETOpen, ID: 801367) and the BOW project (H2020-EIC-FETPROACT-2019, ID: 952183).

ACKNOWLEDGMENTS

We also acknowledge MIUR-Italy ("Progetto Dipartimenti di Eccellenza 2018–2022, ref. B96C1700020008" allocated to

Department of Chemistry “Ugo Schiff”) and Ente Cassa di Risparmio di Firenze for the economic support. The Elettra Synchrotron SAXS facility (Basovizza, Trieste, Italy) is acknowledged for beam-time. We acknowledge the Florence Center for Electron Nanoscopy (FloCEN), University of Florence.

REFERENCES

Alkilany, A. M., Lohse, S. E., and Murphy, C. J. (2013). The Gold Standard: Gold Nanoparticle Libraries to Understand the Nano-Bio Interface. *Acc. Chem. Res.* 46, 650–661. doi:10.1021/ar300015b

Almsherqi, Z. A., Kohlwein, S. D., and Deng, Y. (2006). Cubic Membranes: a Legend beyond the Flatland* of Cell Membrane Organization. *J. Cel Biol.* 173, 839–844. doi:10.1083/jcb.200603055

Almsherqi, Z. A., Landth, T., Kohlwein, S. D., and Deng, Y. (2009). Chapter 6 Cubic Membranes. *Int. Rev. Cel Mol. Biol.* 274, 275–342. doi:10.1016/s1937-6448(08)02006-6

Anees Ahmad, S., Sachi Das, S., Khatoon, A., Tahir Ansari, M., Afzal, M., Saquib Hasnain, M., et al. (2020). Bactericidal Activity of Silver Nanoparticles: A Mechanistic Review. *Mater. Sci. Energ. Tech.* 3, 756–769. doi:10.1016/j.mset.2020.09.002

Angelova, A., Angelov, B., Garamus, V. M., and Drechsler, M. (2019). A Vesicle-To-Sponge Transition via the Proliferation of Membrane-Linking Pores in ω -3 Polyunsaturated Fatty Acid-Containing Lipid Assemblies. *J. Mol. Liquids* 279, 518–523. doi:10.1016/j.molliq.2019.01.124

Barriga, H. M. G., Holme, M. N., and Stevens, M. M. (2019). Cubosomes: The Next Generation of Smart Lipid Nanoparticles? *Angew. Chem. Int. Ed.* 58, 2958–2978. doi:10.1002/anie.201804067

Bastús, N. G., Comenge, J., and Puentes, V. (2011). Kinetically Controlled Seeded Growth Synthesis of Citrate-Stabilized Gold Nanoparticles of up to 200 Nm: Size Focusing versus Ostwald Ripening. *Langmuir* 27, 11098–11105. doi:10.1021/la201938u

Bastús, N. G., Merkoçi, F., Piella, J., and Puentes, V. (2014). Synthesis of Highly Monodisperse Citrate-Stabilized Silver Nanoparticles of up to 200 Nm: Kinetic Control and Catalytic Properties. *Chem. Mater.* 26, 2836–2846. doi:10.1021/cm500316k

Busatto, S., Giacomini, A., Montis, C., Ronca, R., and Bergese, P. (2018). Uptake Profiles of Human Serum Exosomes by Murine and Human Tumor Cells through Combined Use of Colloidal Nanoplasmonics and Flow Cytofluorimetric Analysis. *Anal. Chem.* 90, 7855–7861. doi:10.1021/acs.analchem.7b04374

Cardellini, J., Caselli, L., Lavagna, E., Salassi, S., Amenitsch, H., Calamai, M., et al. (2022). Membrane Phase Drives the Assembly of Gold Nanoparticles on Biomimetic Lipid Bilayers. *J. Phys. Chem. C*. doi:10.1021/acs.jpcc.1c08914

Caselli, L., Mendoza, M., Muzzi, B., Toti, A., Montis, C., Mello, T., et al. (2021). Lipid Cubic Mesophases Combined with Superparamagnetic Iron Oxide Nanoparticles: A Hybrid Multifunctional Platform with Tunable Magnetic Properties for Nanomedical Applications. *Ijms* 22 (17), 9268. doi:10.3390/ijms22179268

Caselli, L., Ridolfi, A., Cardellini, J., Sharpnack, L., Paolini, L., Brucale, M., et al. (2021). A Plasmon-Based Nanoruler to Probe the Mechanical Properties of Synthetic and Biogenic Nanosized Lipid Vesicles. *Nanoscale Horiz.* 6, 543–550. doi:10.1039/d1nh00012h

Caselli, L., Ridolfi, A., Mangiapi, G., Maltoni, P., Moulin, J.-F., Berti, D., et al. (2022). Interaction of Nanoparticles with Lipid Films: The Role of Symmetry and Shape Anisotropy. *Phys. Chem. Chem. Phys.* 24, 2762–2776. doi:10.1039/d1cp03201a

Cherezov, V., Clogston, J., Misquitta, Y., Abdel-Gawad, W., and Caffrey, M. (2002). Membrane Protein Crystallization in Meso: Lipid Type-Tailoring of the Cubic Phase. *Biophysical J.* 83, 3393–3407. doi:10.1016/s0006-3495(02)75339-3

Chong, J. Y. T., Mulet, X., Boyd, B. J., and Drummond, C. J. (2015). Steric Stabilizers for Cubic Phase Lyotropic Liquid Crystal Nanodispersions (Cubosomes). *Adv. Planar Lipid Bilayers Liposomes* 21, 131–187. doi:10.1016/bs.adplan.2014.11.001

SUPPLEMENTARY MATERIAL

The Supplementary Material for this article can be found online at: <https://www.frontiersin.org/articles/10.3389/fbioe.2022.848687/full#supplementary-material>

Dabkowska, A. P., Hirst, C., Valdeperas, M., Clifton, L. A., Montis, C., Nöjd, S., et al. (2017). Temperature Responsive Lipid Liquid crystal Layers with Embedded Nanogels. *Chem. Commun.* 53, 1417–1420. doi:10.1039/c6cc09426k

Dabkowska, A. P., Valdeperas, M., Hirst, C., Montis, C., Pålsson, G. K., Wang, M., et al. (2017). Non-lamellar Lipid Assembly at Interfaces: Controlling Layer Structure by Responsive Nanogel Particles. *Interf. Focus* 7 (4), 20160150. doi:10.1098/rsfs.2016.0150

Deng, Y., and Angelova, A. (2021). Coronavirus-Induced Host Cubic Membranes and Lipid-Related Antiviral Therapies: A Focus on Bioactive Plasmalogens. *Front. Cel Dev. Biol.* 9, 1–21. doi:10.3389/fcell.2021.630242

Deng, Y., and Mieczkowski, M. (1998). Three-dimensional Periodic Cubic Membrane Structure in the Mitochondria of Amoebae *Chaetosphaerium carolinensis*. *Protosplasma* 203, 16–25. doi:10.1007/bf01280583

Djokić, S. (2008) Synthesis and Antimicrobial Activity of Silver Citrate Complexes. *Bioinorg. Chem. Appl.* 2008 436458. doi:10.1155/2008/436458

Gustafsson, J., Ljusberg-Wahren, H., Almgreen, M., and Larsson, K. (1996). Cubic Lipid-Water Phase Dispersed into Submicron Particles. *Langmuir* 1220, 4611–4613. doi:10.1021/la960318y

Hélix-Nielsen, C. (2018). Biomimetic Membranes as a Technology Platform: Challenges and Opportunities. *Membranes* 8 (3), 44. doi:10.3390/membranes8030044

Knoops, K., Kikkert, M., Van Den Worm, S. H. E., Zevenhoven-Dobbe, J. C., Van Der Meer, Y., Koster, A. J., et al. (2008). SARS-coronavirus Replication Is Supported by a Reticulovesicular Network of Modified Endoplasmic Reticulum. *PLoS Biol.* 6, 1957–1974. doi:10.1371/journal.pbio.0060226

Lombardo, D., Kiselev, M. A., and Caccamo, M. T. (2019). Smart Nanoparticles for Drug Delivery Application: Development of Versatile Nanocarrier Platforms in Biotechnology and Nanomedicine. *J. Nanomater.* 2019, 1–26. doi:10.1155/2019/3702518

Meikle, T. G., Drummond, C. J., Separovic, F., and Conn, C. E. (2017). Membrane-mimetic Inverse Bicontinuous Cubic Phase Systems for Encapsulation of Peptides and Proteins. *Adv. Biomembranes Lipid Self-Assembly* 25, 63–94. doi:10.1016/bs.abl.2017.01.002

Mendoza, M., Montis, C., Caselli, L., Wolf, M., Baglioni, P., and Berti, D. (2018). On the Thermotropic and Magnetotropic Phase Behavior of Lipid Liquid Crystals Containing Magnetic Nanoparticles. *Nanoscale* 10, 3480–3488. doi:10.1039/c7nr08478a

Mezzenga, R., Seddon, J. M., Drummond, C. J., Boyd, B. J., Schröder-Turk, G. E., and Sagalowicz, L. (2019). Nature-Inspired Design and Application of Lipidic Lyotropic Liquid Crystals. *Adv. Mater.* 31 (35), 1900818. doi:10.1002/adma.201900818

Montis, C., Baglioni, P., and Berti, D. (2014). Monitoring the Interaction of Nucleolipoplexes with Model Membranes. *Soft Matter* 10, 39–43. doi:10.1039/c3sm52254g

Montis, C., Caselli, L., Valle, F., Zandrini, A., Carlà, F., Schweins, R., et al. (2020). Shedding Light on Membrane-Templated Clustering of Gold Nanoparticles. *J. Colloid Interf. Sci.* 573, 204–214. doi:10.1016/j.jcis.2020.03.123

Montis, C., Castrorlorio, B., Mendoza, M., Salvatore, A., Berti, D., and Baglioni, P. (2015). Magnetocubosomes for the Delivery and Controlled Release of Therapeutics. *J. Colloid Interf. Sci.* 449, 317–326. doi:10.1016/j.jcis.2014.11.056

Montis, C., Gerelli, Y., Fragneto, G., Nylander, T., Baglioni, P., and Berti, D. (2016). Nucleolipid Bilayers: A Quartz crystal Microbalance and Neutron Reflectometry Study. *Colloids Surf. B: Biointerfaces* 137, 203–213. doi:10.1016/j.colsurfb.2015.07.039

Montis, C., Maiolo, D., Alessandri, I., Bergese, P., and Berti, D. (2014). Interaction of Nanoparticles with Lipid Bilayers: A Multiscale Perspective. *Nanoscale* 6, 6452–6457. doi:10.1039/c4nr00838c

Montis, C., Salvatore, A., Valle, F., Paolini, L., Carlà, F., Bergese, P., et al. (2020). Biogenic Supported Lipid Bilayers as a Tool to Investigate Nano-Bio Interfaces. *J. Colloid Interf. Sci.* 570, 340–349. doi:10.1016/j.jcis.2020.03.014

- Muthu, M. S., Leong, D. T., Mei, L., and Feng, S.-S. (2014). Nanotheranostics → Application and Further Development of Nanomedicine Strategies for Advanced Theranostics. *Theranostics* 4, 660–677. doi:10.7150/thno.8698
- Nel, A. E., Mädler, L., Velegol, D., Xia, T., Hoek, E. M. V., Somasundaran, P., et al. (2009). Understanding Biophysicochemical Interactions at the Nano-Bio Interface. *Nat. Mater* 8, 543–557. doi:10.1038/nmat2442
- Perera, G. S., Athukorale, S. A., Perez, F., Pittman, C. U., and Zhang, D. (2018). Facile Displacement of Citrate Residues from Gold Nanoparticle Surfaces. *J. Colloid Interf. Sci.* 511, 335–343. doi:10.1016/j.jcis.2017.10.014
- Pfeiffer, T., De Nicola, A., Montis, C., Carlà, F., Van Der Vegt, N. F. A., Berti, D., et al. (2019). Nanoparticles at Biomimetic Interfaces: Combined Experimental and Simulation Study on Charged Gold Nanoparticles/Lipid Bilayer Interfaces. *J. Phys. Chem. Lett.* 10, 129–137. doi:10.1021/acs.jpcclett.8b03399
- Ridolfi, A., Humphreys, B., Caselli, L., Montis, C., Nylander, T., Berti, D., et al. (2021). Nanoscale Structural and Mechanical Characterization of Thin Bicontinuous Cubic Phase Lipid Films. *Colloids Surf. B Biointerfaces*, 210 112231. doi:10.1016/j.colsurfb.2021.112231
- Salassi, S., Caselli, L., Cardellini, J., Lavagna, E., Montis, C., Berti, D., et al. (2021). A Martini Coarse Grained Model of Citrate-Capped Gold Nanoparticles Interacting with Lipid Bilayers. *J. Chem. Theor. Comput.* 17 (10), 6597–6609. doi:10.1021/acs.jctc.1c00627
- Salvioni, L., Galbiati, E., Collico, V., Alessio, G., Avvakumova, S., Corsi, F., et al. (2017). Negatively Charged Silver Nanoparticles with Potent Antibacterial Activity and Reduced Toxicity for Pharmaceutical Preparations. *Ijn* Vol. 12, 2517–2530. doi:10.2147/ijn.s127799
- Wang, X., Wang, X., Bai, X., Yan, L., Liu, T., Wang, M., et al. (2019). Nanoparticle Ligand Exchange and its Effects at the Nanoparticle-Cell Membrane Interface. *Nano Lett.* 19, 8–18. doi:10.1021/acs.nanolett.8b02638
- William, N., Bamidoro, F., Beales, P. A., Drummond-Brydson, R., Hondow, N., Key, S., et al. (2021). Tuning Stable noble Metal Nanoparticles Dispersions to Moderate Their Interaction with Model Membranes. *J. Colloid Interf. Sci.* 594, 101–112. doi:10.1016/j.jcis.2021.03.009
- Yaghmur, A., and Mu, H. (2021). Recent Advances in Drug Delivery Applications of Cubosomes, Hexosomes, and Solid Lipid Nanoparticles. *Acta Pharmaceutica Sinica B* 11, 871–885. doi:10.1016/j.apsb.2021.02.013
- Yaghmur, A. (2019). Nanoencapsulation of Food Ingredients by Cubosomes and Hexosomes. *Lipid-Based Nanostructures for Food Encapsulation Purposes* 2, 483–522. doi:10.1016/b978-0-12-815673-5.00012-x
- Yaqoob, S. B., Adnan, R., Rameez Khan, R. M., and Rashid, M. (2020). Gold, Silver, and Palladium Nanoparticles: A Chemical Tool for Biomedical Applications. *Front. Chem.* 8, 1–15. doi:10.3389/fchem.2020.00376
- Zabara, M., Senturk, B., Gontsarik, M., Ren, Q., Rottmar, M., Maniura-Weber, K., et al. (2019). Multifunctional Nano-Biointerfaces: Cytocompatible Antimicrobial Nanocarriers from Stabilizer-Free Cubosomes. *Adv. Funct. Mater.* 29 (35), 1904007. doi:10.1002/adfm.201904007
- Zendrini, A., Paolini, L., Busatto, S., Radeghieri, A., Romano, M., Wauben, M. H. M., et al. (2020). *Front. Bioeng. Biotechnol.* 7, 1–10. doi:10.3389/fbioe.2019.00452
- Zhang, J., Lan, Y., and Sanyal, S. (2020). Membrane Heist: Coronavirus Host Membrane Remodeling during Replication. *Biochimie* 179, 229–236. doi:10.1016/j.biochi.2020.10.010

Conflict of Interest: The authors declare that the research was conducted in the absence of any commercial or financial relationships that could be construed as a potential conflict of interest.

Publisher's Note: All claims expressed in this article are solely those of the authors and do not necessarily represent those of their affiliated organizations, or those of the publisher, the editors and the reviewers. Any product that may be evaluated in this article, or claim that may be made by its manufacturer, is not guaranteed or endorsed by the publisher.

Copyright © 2022 Cardellini, Montis, Barbero, De Santis, Caselli and Berti. This is an open-access article distributed under the terms of the Creative Commons Attribution License (CC BY). The use, distribution or reproduction in other forums is permitted, provided the original author(s) and the copyright owner(s) are credited and that the original publication in this journal is cited, in accordance with accepted academic practice. No use, distribution or reproduction is permitted which does not comply with these terms.

Supplementary Material

Interaction of Metallic Nanoparticles with Biomimetic Lipid Liquid Crystalline Cubic Interfaces

Jacopo Cardellini^{1,2}, Costanza Montis^{1,2}, Francesco Barbero^{2,3}, Ilaria De Santis,^{1,2} Lucrezia Caselli^{1,2,4,*} and Debora Berti^{1,2}

¹Department of Chemistry “Ugo Schiff”, University of Florence, Via della Lastruccia 3, Sesto Fiorentino, Florence 50019, Italy

²CSGI, Consorzio Sistemi a Grande Interfase, University of Florence, Sesto Fiorentino, Italy

³Present Address Department of Chemistry, University of Turin, francesco.barbero@unito.it

⁴Department of Pharmacy, University of Copenhagen, DK-2100 Copenhagen, Denmark

*** Correspondence:**

Dr. Lucrezia Caselli

lucrezia.caselli@sund.ku.dk

Keywords: gold nanoparticles, silver nanoparticles, biomimetic systems, cubic phases, cubosomes, nano-bio interface, lipid liquid crystals, nano-bio interactions.

	<i>Index</i>	<i>Page</i>
S.1	<i>Supplementary Characterization of Gold and Silver Nanoparticles</i>	3
S.1.1	Small Angle X-ray Scattering	3
S.1.2	UV-Vis Spectroscopy: AuNPs	5
S.1.3	UV-Vis Spectroscopy: AgNPs	6
S.2	<i>Supplementary Characterization of Cubosomes</i>	7
S.2.1	Dynamic Light Scattering and Zeta-Potential	7
S.2.2	Small Angle X-ray Scattering	8
S.2.3	Cryo-TEM	9
S.3	<i>Supplementary Characterization of cubic thin films</i>	9

Supplementary Material

S.3.1	DOPC/DOTAP Supported Lipid Bilayer formation	9
S.4	<i>Supplementary Characterization of AuNPs-cubosomes hybrids</i>	10
S.4.1	UV-vis Spectroscopy: Effect of cubosomes concentration	10
S.5	<i>Bibliography</i>	11

S.1 Supplementary Characterization of Gold and Silver Nanoparticles

S1.1 Small Angle X-ray Scattering

SAXS measurements on AuNPs aqueous dispersion were carried out in sealed glass capillaries of 1,5 mm diameter.

In diluted solution without interparticle interaction, the structure factor $S(Q)$ can be approximated equal to 1, and the scattering intensity $I(q)$ assumes the following form:

$$I(Q) = n\Delta\rho^2 V_p^2 P(Q) \quad (1)$$

Where n is the number density of the objects in the dispersion, $\Delta\rho$ is the contrast between the solvent and the scattering objects, V_p is the particle's volume and $P(Q)$ is the form factor. Within the Guinier approximation¹, valid for diluted and monodispersed particles, $P(Q)$ can be expressed as:

$$P(Q) = 1 - \frac{Q^2 R_g^2}{3} \quad (2)$$

And substituting equation (1) we can obtain:

$$I(Q) = n\Delta\rho^2 V_p^2 \exp\left(-\frac{Q^2 R_g^2}{3}\right) \quad (3)$$

And in logarithmic form:

$$\ln I(Q) = \text{const} - \frac{Q^2 R_g^2}{3} \quad (4)$$

Then, according to the Guinier approximation, when $S(Q)=1$, the slope of scattering profile in the low Q region in a $\ln I(Q)$ vs Q^2 plot can be associated to the average gyration radius of the particles if the equation $QR_g < 1$ is respected. Finally, we can extract the particle's radius, assuming a spherical shape, exploiting the following relation:

$$R = \sqrt{\frac{5}{3}} R_g \quad (5)$$

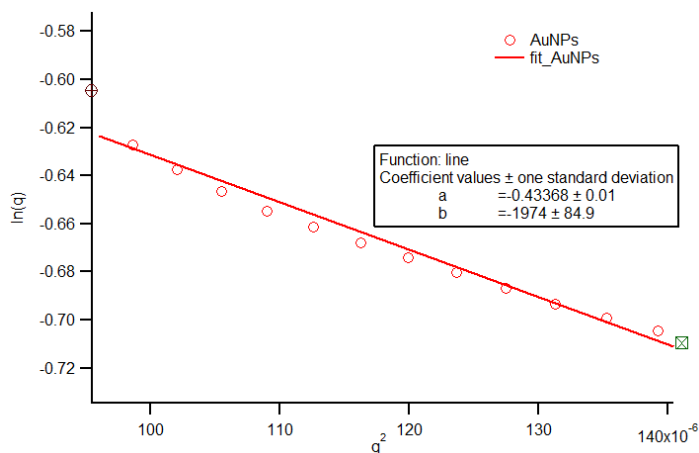


Figure S1 Guinier approximation for gold nanoparticles: $\ln I(q)$ vs q^2 plot. The slope of linear fitting (solid red line) of the scattering intensity in the Guinier Region (red markers) is related to the gyration radius of the particles. The size and polydispersity obtained from the fitting procedure are summarized in the Table S1 below.

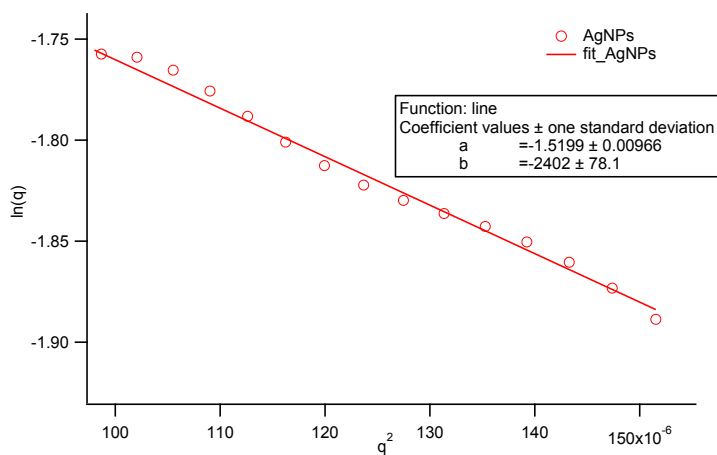


Figure S2 Guinier approximation for silver nanoparticles: $\ln I(q)$ vs q^2 plot. The slope of linear fitting (solid red line) of the scattering intensity in the Guinier Region (red markers) is related to the gyration radius of the particles. The size and polydispersity obtained from the fitting procedure are summarized in the Table S1 below.

R_{core} (nm)	
AuNPs	20 ± 1
AgNPs	22 ± 1

Table S1 Nanoparticles radii obtained for AuNPs and AgNPs for the analysis of the SAXS profiles according to the Guinier approximation.

UV-vis Spectroscopy: AuNPs

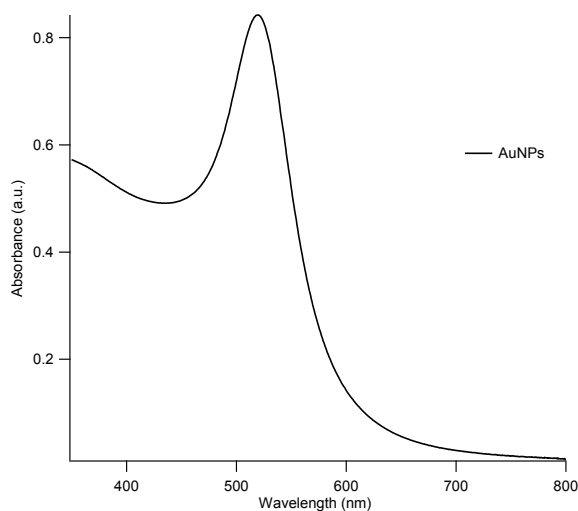


Figure S3 UV-Vis spectra of AuNPs after 1:3 dilution in water ($2.77 \times 10^{-10} M$). The plasmon absorption peak is at around 520 nm.

To further evaluate the AuNPs size through UV-Vis spectroscopy we exploited the following equation²:

$$d = \exp \left(B_1 \frac{A_{spr}}{A_{450}} - B_2 \right) \quad (6)$$

with d diameter of gold nanoparticles, A_{spr} absorbance at the surface plasma resonance peak, A_{450} absorbance at the wavelength of 450 nm and B_1 and B_2 are dimensionless parameters, taken as 3 and 2,2, respectively. The diameter value obtained is of 20 nm.

The concentration of citrated gold nanoparticles was determined via UV-Vis spectrometry, using the Lambert-Beer law ($E(\lambda) = \varepsilon(\lambda)lc$), taking the extinction values $E(\lambda)$ at the LSPR maximum, i.e. $\lambda = 520$ nm. The extinction coefficient $\varepsilon(\lambda)$ of gold nanoparticles dispersion was determined by the method reported in literature³, by the following equation:

$$\ln(\varepsilon) = k \ln(d) + a \quad (7)$$

with d core diameter of nanoparticles, and k and a dimensionless parameters ($k = 3,32111$ and $a = 10,80505$). The arithmetic mean of the sizes obtained by optical and scattering analyses was selected, leading to a $\varepsilon(\lambda)$ of $2.0 \cdot 10^8 \text{ M}^{-1} \text{ cm}^{-1}$. The final concentration of the citrated AuNPs is therefore $\sim 8.3 \cdot 10^{-10} \text{ M}$.

UV-vis Spectroscopy: AgNPs

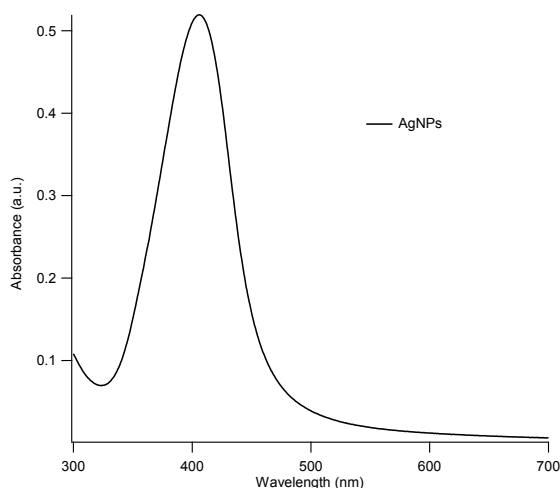


Figure S4 UV-Vis absorption spectra of AgNPs after 1:3 dilution in water ($1.6 \times 10^{-9} \text{ M}$). The plasmon absorption peak is at 520 nm.

To confirm the AgNPs size evaluated by SAXS we exploited the UV-vis spectroscopy according the following equation⁴:

$$d = 0.11 (\lambda_{\max})^2 - 89.99 (\lambda_{\max}) + 17,775.94 \quad (8)$$

where d is the diameter and λ_{\max} is the wavelength corresponding to the maximum absorption peak. Exploiting this equation, we found a nanoparticle's diameter equal to $d=18.8$ nm.

The concentration of citrated AgNPs was determined via UV-Vis spectrometry, using the Lambert-Beer law ($E(\lambda) = \varepsilon(\lambda)lc$). The extinction coefficient $\varepsilon(\lambda)$ of silver nanoparticles dispersion was determined by the method reported in literature, according to the following equation:

$$\varepsilon = 0.202e^{0.251d} \quad (9)$$

The final concentration obtained for AgNPs is 1.8×10^{-8} M. Finally, before each measurement, the AgNPs dispersion was diluted to the same concentration of AuNPs (8.3×10^{-10} M).

Supplementary Characterization of Cubosomes

Dynamic Light Scattering and Zeta-Potential

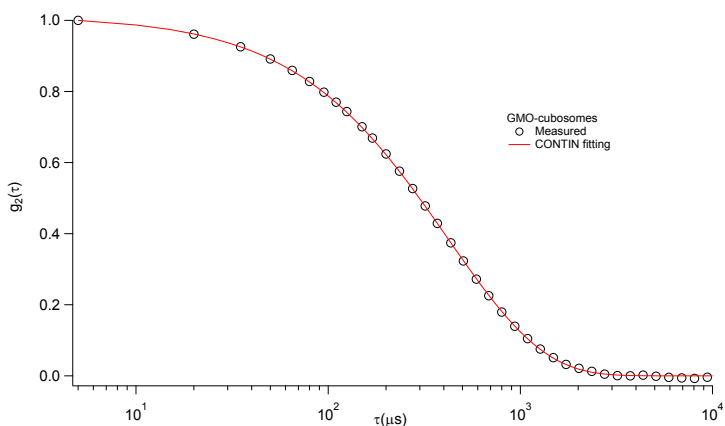


Figure S5 *Dynamic Light Scattering curve of GMO-cubosomes dispersion analyzed with a Contin through the Laplace inversion according to the CONTIN algorithm⁵.*

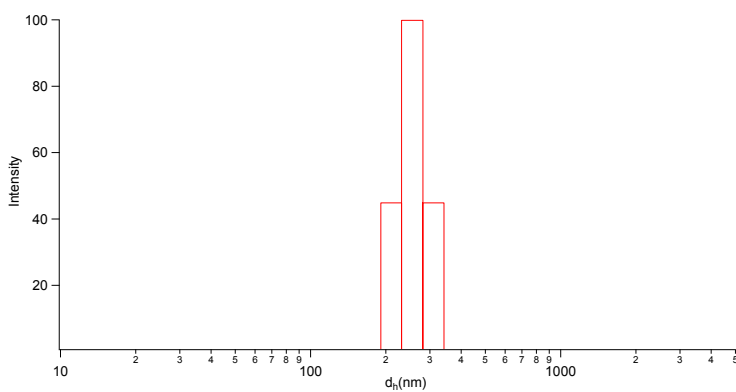


Figure S6 *Size distribution of cubosomes obtained by the Contin analysis.*

Small Angle X-Ray Scattering

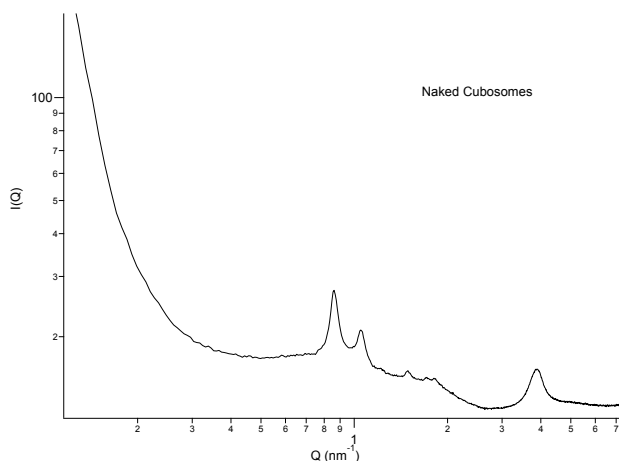


Figure S7 Comparison between the scattering intensity of water and the scattering intensity of 10 μL of liposome dispersions (12 nM) in 300 μL of water.

In order to obtain the spacing parameter of the Pn3m cubic phase we exploit the following equation⁶:

$$Q_{hkl} = \frac{2\pi}{d} * (h^2 + k^2 + l^2)^{1/2} \quad (10)$$

Where h, k and l are the Miller indexes representing the crystallographic planes of the liquid crystallin phase and Q_{hkl} is the q position measured for each reflex. In the case of a Pn3m phase, the characteristic values of $(h^2 + k^2 + l^2)^{1/2}$ are $\sqrt{2}$, $\sqrt{3}$, $\sqrt{4}$, $\sqrt{6}$, $\sqrt{8}$ and $\sqrt{9}$. Thus, plotting $x=Q_{hkl}(1/\text{\AA})$ vs $y=(h^2+k^2+l^2)^{1/2}$, the spacing parameter d can be obtained by the slope b of the linear fitting, reported in figure S7, according to the following equation:

$$d = \frac{2\pi}{b} \quad (11)$$

The evaluated spacing parameter is 10.4 nm.

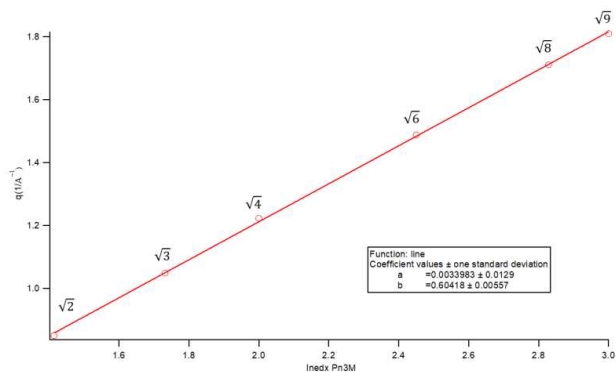


Figure S8 Comparison between the scattering intensity of water and the scattering intensity of 10 μL of liposome dispersions (12 nM) in 300 μL of water.

Cryo-TEM

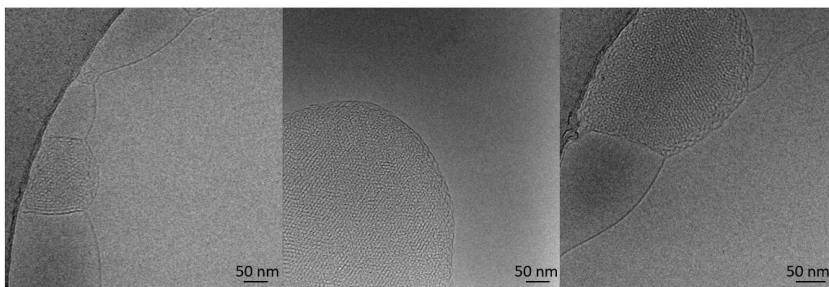


Figure S9 Further examples of cryo-TEM images of stabilizer-free GMO cubosomes.

Supplementary Characterization of cubic thin films

DOPC/DOTAP Supported Lipid Bilayer formation

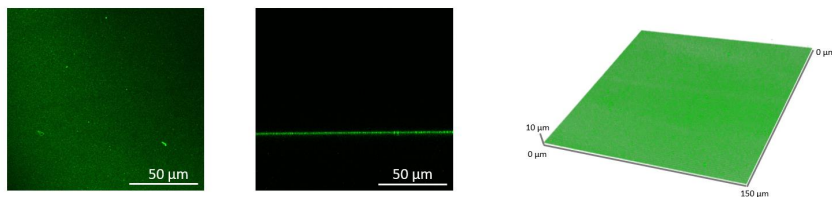


Figure S10 Top view (left), side view (middle) and 3D view (right) of DOPC/DOTAP supported lipid bilayer collected with Confocal Microscopy.

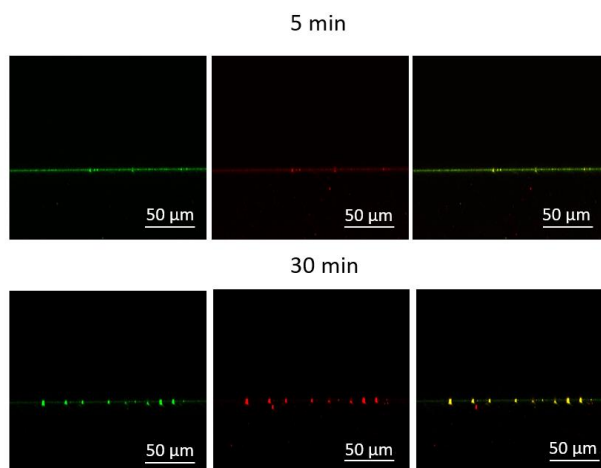


Figure S11 Side views of the cubosomes deposition on the DOPC/DOTAP SLB 5 min (top) and 30 min (bottom) after the cubosomes injection. Cubosomes are imaged in red, the SLB in green and the colocalization of the probes in yellow.

Supplementary Characterization of AuNPs-cubosomes hybrids

UV-vis Spectroscopy: Effect of cubosomes concentration

We monitored the AuNPs aggregation varying the cubosomes concentration. 300 μL of AuNPs 8.3×10^{-10} M were incubated with 0, 15, 30, 60, and 120 μL of cubosomes 4 mg/mL and the optical variations of the dispersion were evaluated after 10 minutes of interaction. Figure S12 displays the collected UV-visible spectra. As shown, increasing the number of cubosomes, the optical variation of the original AuNPs spectrum become less pronounced. This experimental evidence underlines that the AuNPs clustering is templated by the cubosomes, and the particles aggregation occurs on the membrane. Moreover, it is maximized by decreasing the available surface for aggregation until the saturation of this surface is reached. These findings are totally in agreement with the self-assembly of citrated AuNPs on synthetic vesicles composed of zwitterionic phospholipid, extensively studied in a recent work.⁷

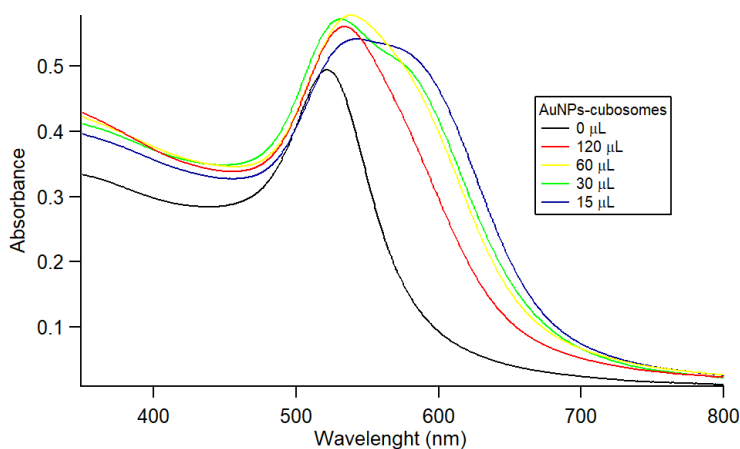


Figure S12 UV-Vis spectra of AuNP (0.83 M) in the presence of different amounts of GMO-based cubosomes (120 μL , 60 μL , 30 μL , 15 μL and 0 μL of 4 mg/mL cubosomes).

Bibliography

- 1 H. B. Stuhmann, *Prog. Cryst. Growth Charact.*, 1989, **18**, 1–19.
- 2 W. Haiss, N. T. K. Thanh, J. Aveyard and D. G. Fernig, 2007, **79**, 4215–4221.
- 3 X. Liu, M. Atwater, J. Wang and Q. Huo, 2007, **58**, 3–7.
- 4 M. Sikder, J. R. Lead, G. T. Chandler and M. Baalousha, *Sci. Total Environ.*, 2018, **618**, 597–607.
- 5 S. W. Provencher, *Comput. Phys. Commun.*, 1982, **27**, 229–242.
- 6 C. A. F. Peters and J. Kortazzi, *Astron. Nachrichten*, 1873, **82**, 145–148.
- 7 C. Montis, L. Caselli, F. Valle, A. Zandrini, F. Carlà, R. Schweins, M. Maccarini, P. Bergese and D. Berti, *J. Colloid Interface Sci.*, 2020, **573**, 204–214.

A plasmon-based nanoruler to probe the mechanical properties of synthetic and biogenic nanosized lipid vesicles (Paper IV)

Lucrezia Caselli, Andrea Ridolfi, Jacopo Cardellini, Lewis Sharpnack, Lucia Paolini, Marco Brucale, Francesco Valle, Costanza Montis, Paolo Bergese, and Debora Berti, *Nanoscale Horizons*, 2021, 6, 543–550.



Cite this: DOI: 10.1039/d1nh00012h

Received 8th January 2021,
Accepted 7th April 2021

DOI: 10.1039/d1nh00012h

rsc.li/nanoscale-horizons

A plasmon-based nanoruler to probe the mechanical properties of synthetic and biogenic nanosized lipid vesicles†

Lucrezia Caselli,^{ab} Andrea Ridolfi,^{abc} Jacopo Cardellini,^{ab} Lewis Sharpnack,^d
Lucia Paolini,^{be} Marco Brucalè,^{bc} Francesco Valle,^{ib} Costanza Montis,^{*ab}
Paolo Bergese,^{ib} and Debora Berti^{ib} *^{ab}

Nanosized lipid vesicles are ubiquitous in living systems (e.g. cellular compartments or extracellular vesicles, EVs) and in formulations for nanomedicine (e.g. liposomes for RNA vaccine formulations). The mechanical properties of such vesicles are crucial in several physicochemical and biological processes, ranging from cellular uptake to stability in aerosols. However, their accurate determination remains challenging and requires sophisticated instruments and data analysis. Here we report the first evidence that the surface plasmon resonance (SPR) of citrated gold nanoparticles (AuNPs) adsorbed on synthetic vesicles is finely sensitive to the vesicles' mechanical properties. We then leverage this finding to show that the SPR tracking provides quantitative access to the stiffness of vesicles of synthetic and natural origin, such as EVs. The demonstration of this plasmon-based "stiffness nanoruler" paves the way for developing a facile, cost-effective and high-throughput method to assay the mechanical properties of dispersions of vesicles of nanometric size and unknown composition at a collective level.

Introduction

Membrane-delimited compartments (e.g., cells, organelles and nanosized vesicles of biological origin, such as enveloped viruses¹ or extracellular vesicles (EVs)^{2,3}) are among the basic units of living organisms. Importantly, they are also widespread

New concepts

Citrated gold nanoparticles (AuNPs) undergo membrane-templated self-assembly when challenged with nanosized lipid vesicles. We show that the stiffness of the target vesicle finely modulates the extent of AuNPs aggregation, which can be easily monitored by UV-Vis spectrophotometry. Leveraging this discovery, we propose a novel experimental method to assess the mechanical properties of synthetic and natural vesicles. Through a "stiffness index", S.I., we quantify the extent of AuNPs aggregation and define its functional dependence on the mechanical properties of the vesicles. This method was validated on a set of synthetic lipid vesicles of known stiffness and then tested on a sample of biogenic extracellular vesicles (EVs). The "plasmon-based stiffness nanoruler" is a reproducible, sensitive, high-throughput, and readily accessible method, which overcomes many of the hurdles still hampering an accurate determination of the rigidity of nanovesicles. In addition, it can easily and readily probe the properties of tiny sample amounts, which represents a considerable advantage for biological samples, usually available in low quantities due to purification costs. This new method will advance our understanding of the role of rigidity of nanovesicles in modulating their biological behavior, from the pharmacokinetics of liposomal formulation for drug delivery to the uptake of natural vesicles and viruses.

structural motifs in bio-inspired nanomaterials, such as liposomes,⁴ virosomes⁵ or polymerosomes.⁶ The mechanical properties of such membrane compartments regulate the response to external stimuli, which is crucial in a host of biologically-relevant interactions at the nanoscale.^{7–11} A well-known example is the mechanical response of cells and membrane bound-organelles, which is the key in numerous biological processes (e.g. cell fusion, growth and differentiation, endo- and exocytosis, uptake of nanoparticles or viruses,^{12–14} etc.) and in the onset of pathological cell conditions.^{15–18} More recent reports have highlighted that the mechanical response of EVs (membrane-delimited nanoparticles secreted by all cell types and essential mediators of cell signalling^{2,3,19}) is a biomarker for malignant conditions of parental cells.^{20,21} In addition, the nanomechanics of pathogens, including viruses with a lipid envelope (e.g. Moloney murine leukemia virus and HIV²²), was recently connected to their infectivity.²³ Mechanical properties

^a Department of Chemistry, University of Florence, Via della Lastruccia 3, Sesto Fiorentino, Florence 50019, Italy. E-mail: debora.berti@unifi.it, costanza.montis@unifi.it

^b Consorzio Sistemi a Grande Intefase, Department of Chemistry, University of Florence, Sesto Fiorentino, Italy

^c Consiglio Nazionale delle Ricerche, Istituto per lo Studio dei Materiali Nanostrutturati (CNRISMN), via Gobetti 101, Bologna 40129, Italy

^d ESRF–The European Synchrotron, Grenoble 38043, France

^e Department of Molecular and Translational Medicine, University of Brescia, Brescia, Italy

^f Consorzio Interuniversitario Nazionale per la Scienza e la Tecnologia dei Materiali, Florence, Italy

† Electronic supplementary information (ESI) available. See DOI: 10.1039/d1nh00012h

are also crucial for the interaction of synthetic nanostructures with the biological environment: the deformability of liposomes or polymeric vesicles for drug or vaccine delivery deeply affects their pharmacokinetics in the bloodstream and the internalization route.²⁴

Although central in several research areas, the accurate assessment of the mechanical properties of synthetic or natural vesicles still poses a challenge.^{25,26} Traditional methods, such as shape fluctuation optical analysis,²⁷ micropipette aspiration,²⁸ X-ray scattering^{29,30} and neutron spin-echo,³¹ provide insights into biologically-relevant descriptors of the mechanical response of the lipid membrane, such as the bilayer's bending rigidity.^{27–31} However, these techniques are cost- and/or time-consuming and often yield discrepant results, as pointed out in several reports.^{25,26,32–34} More recently, techniques that actively probe the mechanical properties at a whole-vesicle level, rather than those of the lipid shell, are gaining the central stage;³⁵ examples include optical tweezers and Atomic Force Microscopy (AFM) operating modes, such as Dynamic Mechanical Analysis, Quantitative Imaging and Lorentz Contact Resonance.²⁰ Most of these methods rely on contact mechanic models for interpreting the measured mechanical properties of the probed objects; however, there is still disagreement on which model is best suited for describing the nanomechanics of a lipid vesicle.³⁶ As a consequence, classical AFM-based force spectroscopy (AFM-FS) indentation experiments still represent a common choice for the nanomechanical analysis of vesicles,^{37–39} since they allow determining the overall mechanical response of vesicles to applied deformations, *i.e.* their “stiffness”, in a model-free approach. The measured stiffness includes contributions both from the membrane shell and the enclosed volume, accounting for the mechanical properties of the internal pool, volume variations upon deformation, osmotic imbalance, *etc.* Unfortunately, all these experimental methods probe a single particle at a time and require sophisticated instruments or/and highly experienced users.³⁵

Here, we propose AuNPs as nanoprobes of the stiffness of membranous nano-objects, with typical submicron sizes. This approach overcomes many limitations of the currently available methods, measurements can be performed with a UV-Vis spectrophotometer and limited data analysis is required. In the following, this communication will (i) explore how the stiffness of liposomes modulates the surface plasmon resonance (SPR) of AuNPs adsorbed on their membrane and (ii) propose this previously unnoticed relationship as the working principle of a new, accessible and robust spectrophotometric method to evaluate the stiffness of both synthetic and natural lipid vesicles of unknown composition.

The SPR of AuNPs is finely sensitive to the chemical environment and the interparticle distance, which underpins their application as nanoscale probes.⁴⁰ The coupling between the SPR of proximal AuNPs, which results from AuNPs close approach or aggregation, was exploited for the first time by El-Sayed and co-workers as a plasmon ruler⁴¹ and is nowadays used in a number of bioanalytical assays.^{42,43} The CONAN (Colloidal NANoplasmonic) assay is a recent example, where the AuNPs SPR shift upon incubation with EVs is exploited to

determine their purity and concentration;^{44–46} in this latter case, the SPR shift arises from the spontaneous aggregation of AuNPs on the lipid membrane of vesicles (of both synthetic and natural origin, as EVs). This membrane-induced aggregation has been the focus of several recent investigations.^{47–52} Specifically, the membrane-induced aggregation of AuNPs has been interpreted as on-off mechanism to date,^{53,54} switchable by the physical state of the membrane: fluid-phase bilayers, characterized by free lipid diffusion and low rigidity, would promote aggregation, resulting in a marked change of AuNPs SPR profile. Conversely, the aggregation of AuNPs would be completely inhibited on tightly packed gel-phase membranes, characterized by a higher rigidity. At variance with the literature, we demonstrate that the SPR shift of AuNPs also interest gel-phase membranes and is rather modulated by the stiffness of the vesicles through a precise functional dependence: this allows defining a “stiffness nanoruler”, able to discriminate vesicles within the same physical state (whether it is gel or fluid) on the basis of their mechanical behaviour. In analogy with the plasmon nanoruler, introduced as distance-sensor,⁴¹ this plasmon-based descriptor leverages the unique sensitivity of AuNPs SPR to determine the mechanical properties of lipid vesicles. As a proof-of-principle of applicability to complex natural systems, we tested the assay on EVs, whose stiffness is of prominent relevance in cellular adhesion and uptake³⁵ and a characteristic that distinguish EVs deriving from malignant and non-malignant cells.^{20,21}

Results and discussion

We prepared a library of unilamellar liposomes having a similar average diameter (~ 100 nm) and low polydispersity indexes (see ESI† for details on preparation and characterization) from a set of synthetic phosphatidylcholines (PC) differing for length and/or degree of unsaturation of the acyl chains (Fig. 1a). The free-standing bilayers, either in the gel or fluid phase at room temperature (Fig. 1a), display different rigidities.^{56–59} Given their very similar size distributions and the absence of any osmotic imbalance between the lumen and the external medium, the rigidity of the lipid shells can be considered the sole responsible for the overall stiffnesses of the vesicles.

Fig. 1b reports representative AFM-FS force/distance plots of single-vesicle indentation events for each lipid.^{60,61} The slope of the linear regime occurring immediately after the contact point represents the stiffness of the vesicles; the stiffnesses in Fig. 1c were obtained by averaging the values for multiple vesicles (see ESI† for further details). Taken together, the entire series of stiffness values measured on the selected library of synthetic PC standards can be regarded as a stiffness gauge in which the rigidity monotonically increases from DOPC to DSPC vesicles, in line with the literature.^{25,62} This set will be used to validate the stiffness plasmon nanoruler.

The vesicles ($20 \mu\text{l}$ of a water dispersion at a 0.35 nM vesicles' concentration) were then challenged with $100 \mu\text{l}$ of 6.7 nM water dispersion of negatively charged citrated AuNPs (13 ± 0.6 nm diameter, zeta potential: -36 ± 2 mV), to obtain a

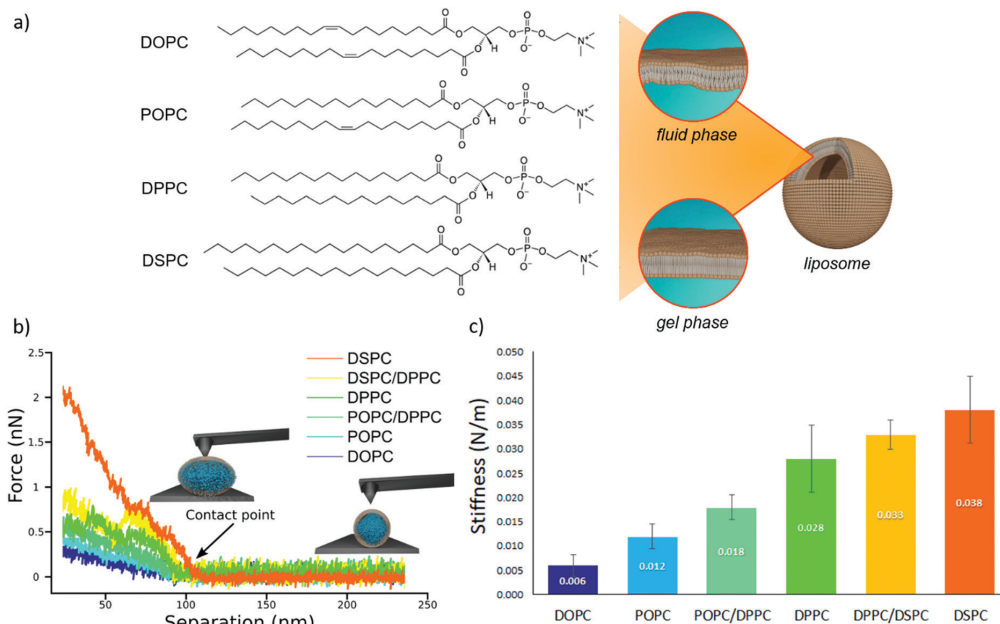


Fig. 1 AFM characterization of vesicles stiffnesses. (a) Chemical formulas of the four lipids used for the preparation of liposomes (1,2-distearoyl-*sn*-glycero-3-phosphocholine (DSPC), 1,2-dipalmitoyl-*sn*-glycero-3-phosphocholine (DPPC), 1-palmitoyl-2-oleoyl-*sn*-glycero-3-phosphocholine (POPC) and 1,2-dioleoyl-*sn*-glycero-3-phosphocholine (DOPC)); depending on the molecular composition, the lipid bilayer enclosing a liposome exhibits a different degree of molecular packing at room temperature, which determines the phase (*i.e.*, fluid or gel) of the membrane. (b) AFM force-distance curves for the different vesicles batches, together with graphical representation of vesicles deformation induced by the AFM tip at two different separation distances. Liposomes samples are DOPC; POPC, POPC/DPPC (50/50 mol%), DPPC, DPPC/DSPC (50/50 mol%) and DSPC vesicles; (c) stiffness values (N m^{-1}) of the different vesicles, determined through AFM-FS; All error bars represent the uncertainties obtained by bootstrapping (1000 repetitions of 5 draws, with replacement).

final liposomes/AuNPs molar ratio of $\sim 1/100$. The changes in the SPR profile were monitored after 15 minutes of incubation at room temperature (Fig. 2a). These experimental conditions were carefully selected on the basis of our recent investigation on POPC liposomes interacting with citrated AuNPs.⁵²

The AuNPs dispersion in the absence of lipid vesicles shows a well-defined SPR peak centred at 522 nm (red curve); upon mixing with liposomes, an immediate colour change is visible to the naked eye (inset, Fig. 2a), which clearly depends on the composition of the target membrane. Going from DSPC to DOPC, we observe colour shifts from red to increasingly dark shades of violet and blue. The variation in the SPR profile gradually increases as the stiffness of vesicles decreases. Specifically, from the stiffest vesicles (DSPC) to the softest ones (DOPC), the progressive emergence of a high-wavelength shoulder can be observed, eventually resulting in a secondary plasmon peak at about 625 nm (see Fig. 2a).

This new spectral feature is the hallmark of the aggregation of AuNPs, whose spatial proximity produces the coupling of the individual AuNPs plasmons.

To get insights into the structure of AuNPs aggregates, we performed Small Angle X-ray Scattering (SAXS) for DOPC, POPC, DPPC and DSPC liposomes challenged with AuNPs (Fig. 2b).

The power-law dependence in the low- q region highlights the presence of AuNPs clusters on fluid-phase bilayers, with a fractal dimension which increases as the stiffness of vesicles decreases (Fig. 2b, inset, and ESI^\dagger).⁶³ The spatial correlation between AuNPs was determined from the structure factor $S(q)$, inferred from the high- q region of the scattering profiles (Fig. 2b, inset, and ESI^\dagger). The position of the $S(q)$ correlation peaks for fluid-phase liposomes is consistent with AuNP-AuNP center-to-center distances comparable with the particle diameter and decreasing with vesicles' stiffness (14.5 nm and 14.1 nm for POPC and DOPC, respectively). For liposomes in the gel phase, no low- q upturn of intensity was detected and the positional correlation corresponds to significantly higher AuNP-AuNP distances (*i.e.*, 30.5 nm and 30.2 nm for DSPC and DPPC, respectively), hinting at the presence of multiple AuNPs adsorbed on the same liposomal surface, but not aggregated.

According to recent reports, the aggregation of AuNPs on lecithin vesicles is switched on and off by the membrane phase:^{53,54} aggregation is inhibited on gel-phase bilayers (*e.g.* DPPC and DSPC at r.t.) and promoted by fluid-phase membranes (*e.g.* DOPC and POPC at r.t.), with no differences observed for bilayers in the same phase.^{53,54} Conversely, the UV-Vis and SAXS data here shown provide additional insights, highlighting that – in

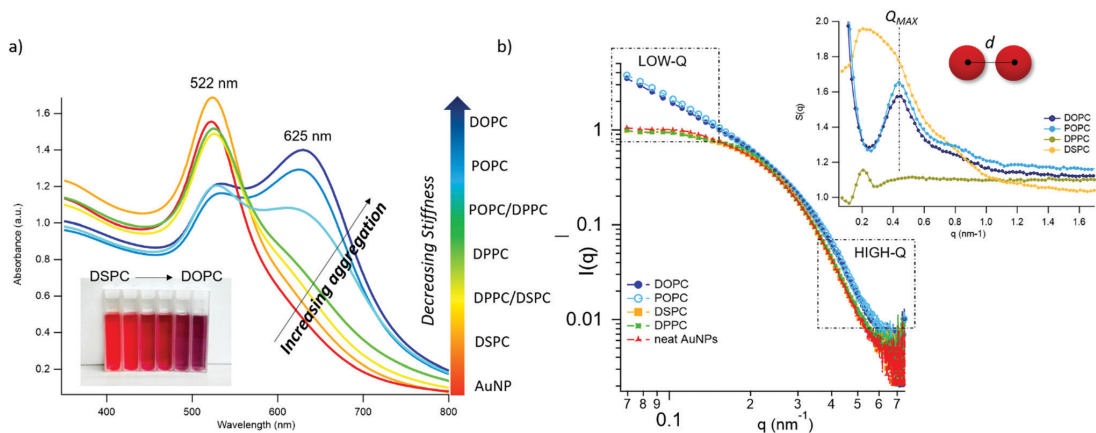


Fig. 2 AuNPs interaction with lipid bilayers of different stiffness. (a) UV-Vis spectra of AuNPs (6.7 nM) incubated with synthetic vesicles (0.2 nM) (liposomes/AuNPs number ratio 1/100). Inset: Visual appearance of the same samples. (b) SAXS profiles of NPs with and without vesicles (1:8 vesicles/AuNPs molar ratio). Under these conditions, the scattering from vesicles (subtracted from the scattering of AuNPs-vesicles mixtures) is negligible and the observed signal is only due to AuNPs. The power law dependence at low- q is connected to the presence of AuNPs clusters and to their morphology. The power-law exponents for DOPC/AuNPs and POPC/AuNPs complexes, *i.e.* -1.54 and -1.50 respectively (see ESI†), are consistent with an increasing fractal dimension of clusters as the stiffness of vesicles decreases. The absence of such power-law for gel-phase liposomes is related to non-aggregated AuNPs, preserving their original diameter. The right inset is the structure factor ($S(q)$) vs. q , extracted from the high- q range of vesicles/AuNPs profiles (see ESI†).

these experimental conditions – AuNPs clustering on lipid vesicles is not abruptly switched-on by varying the membrane physical state: the slight – but still evident – differences in the AuNPs SPR induced by vesicles with the same physical state but different rigidities demonstrate that AuNPs aggregation is rather modulated by the membrane rigidity in a “continuous fashion”.

This dependence can be exploited to set-up a UV-Vis spectroscopic assay to probe the mechanical properties of lipid

vesicles. With this aim, we analysed the optical spectra to extract a quantitative descriptor. The so-called “stiffness index”, S.I., (see Fig. 3a), accounting for the main variations in the AuNPs SPR profile, was used to build-up an empirical ‘AuNPs spectral response’ vs. ‘vesicles’ stiffness’ scale. The S.I. for each AuNPs/vesicles hybrid is calculated dividing the area subtended by the absorbance spectrum in the 560–800 nm range by the area relative to the total spectral range (350–800 nm). The results are then normalized for the S.I. of neat AuNPs

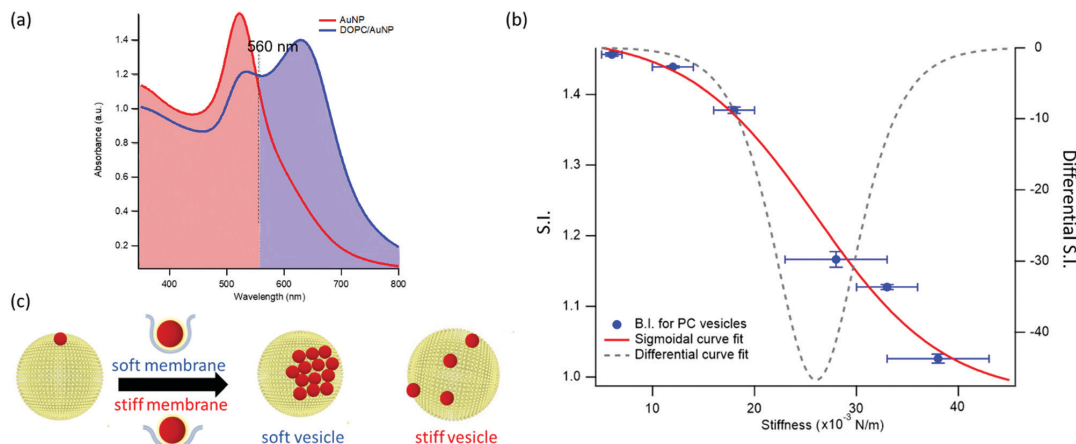


Fig. 3 Quantification of liposomes-induced variation in the AuNPs SPR profile. (a) Visual description of the stiffness index (S.I.); (b) S.I. values (blue spots) with relative errors bars plotted as a function of membrane stiffness. The red curve is the sigmoidal curve fit, while the grey dashed curve is the first derivative of the sigmoidal curve fit with respect to stiffness (see ESI† for details on fitting parameters). (c) Mechanism of interaction between AuNPs and vesicles characterized by different stiffness. The adhesion of an AuNP on a soft membrane is followed by a significant AuNP wrapping by the membrane, resulting into AuNPs aggregation on the vesicle surface. The AuNP docking on a stiffer membrane results in a lower wrapping extent, preventing AuNPs clustering.

(which is then equal to 1 by definition) to obtain positive integer values of S.I., which gradually increase with increasing AuNPs aggregation extent.

Fig. 3b reports the S.I. (blue dots) obtained for the liposome set plotted as a function of vesicles' stiffness, obtained from AFM-FS measurements (Fig. 1). Each point represents the average value obtained from five independent batches, which highlights a particularly high reproducibility (see Table S5 of ESI† for standard deviations of each vesicles' batch).

The dependence of the S.I. on stiffness can be expressed by a sigmoidal law, with the following expression:

$$\text{S.I.} = \frac{b}{1 + \exp\left(\frac{c - S}{d}\right)} + a \quad (1)$$

with S the stiffness obtained from AFM-FS and a , b , c and d constant fitting parameters (see red profile in Fig. 3b for the best fitting curve and ESI† for further details).

For this set of synthetic vesicles, having superimposable size distributions and a luminal content identical to the external medium, the stiffness differences observed in AFM-FS are only due to a membrane contribution, which results from the different composition of the bilayers. As it is well-established, the mechanical response of a lipid bilayer is mainly controlled by its bending rigidity,²⁵ quantified by the bilayer bending modulus. Therefore, in these experimental conditions, it is the bilayer bending modulus that determines the overall stiffness of the vesicles and in turn the extent of AuNPs aggregation (*i.e.* the S.I.).

Interestingly, in a recent simulation Lipowsky and co-authors⁶⁴ report a sigmoidal correlation between the wrapping efficiency of spherical NPs interacting with model membranes and the bilayer bending modulus. This relation holds for fixed NPs radius and membrane-NPs adhesion energy, which perfectly matches our experimental conditions (*i.e.* NPs of defined size and vesicles with fixed PC headgroups).

This finding is fully in line with a recent report,⁵² where AuNPs wrapping, modulated by the membrane bending modulus, is recognized as the main driver for the membrane-templated aggregation of AuNPs, through the mechanism sketched in Fig. 3c: briefly, AuNPs adsorb on the vesicle's surface due to Van der Waals attractive interactions and get partially wrapped by the membrane. This wrapping drives a ligand exchange between the membrane lipids and the AuNPs stabilizing agent, *i.e.* the citrate anion, whose release reduces the interparticle electrostatic energy barrier and leads to the aggregation of AuNPs. Importantly, the extent of AuNPs aggregation is modulated by the wrapping efficiency, which is related to the bending rigidity of the membrane. Our results, reporting the first experimental evidence of a sigmoidal relation between AuNPs aggregation and membrane bending rigidity, reconcile this latter mechanism with the theoretical predictions proposed by Lipowsky *et al.*, who first connected the wrapping ability of a membrane to its bending modulus through a sigmoidal law.

The dependence of the S.I. on the stiffness of vesicles (eqn (1)) allows a quantitative estimate of the mechanical properties of membrane-enclosed compartments of unknown composition. The method here proposed possess high reproducibility and sensitivity. In fact, it is able to robustly discriminate systems with very close stiffnesses (*i.e.* differences as small as 0.006 N m^{-1}), as POPC and DOPC liposomes, whose mechanical properties are usually not distinguishable with many other techniques.^{62,65}

In addition, the presence of a sigmoidal law, which exhibits the highest variation of S.I. in the central region of the selected set of stiffnesses (see grey dashed curve of Fig. 3b, representing the first derivative of the sigmoidal fit) provides maximum sensitivity in the region where the rigidities of natural membranes usually fall (*i.e.* $0.02\text{--}0.025 \text{ N m}^{-166}$).

We chose EVs to further validate the method and to provide evidence of its applicability on membranous nanoparticles, which are more challenging both in terms of compositional

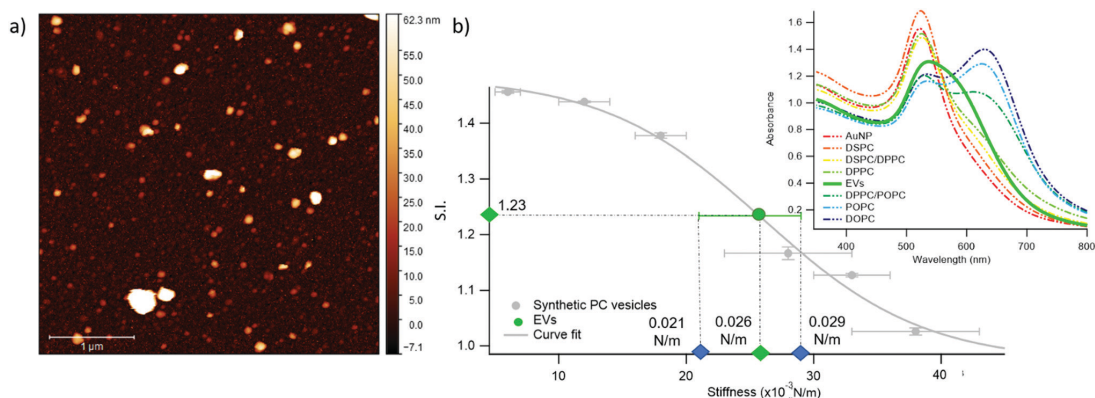


Fig. 4 Quantification of Extracellular Vesicles (EVs)-induced variation in the SPR profile of AuNPs. (a) Representative AFM image of EVs; (b) Sigmoidal trend of the S.I. as a function of membrane stiffness. The EVs' S.I. (1.23 ± 0.01), evaluated through UV-Vis spectroscopy, and stiffness, predicted by the sigmoidal law (0.026 N m^{-1}), are reported as green points in the graph. The green error bar represents the stiffness interval obtained through AFM-FS for EVs. The right inset reports the UV-Vis spectra of AuNPs (6.7 nm) in the presence of synthetic PC vesicles (dashed curves) and EVs (solid green curve) at a vesicles' concentration of 0.35 nM .

and structural complexity, as well as in analyte availability. Specifically, we assayed a sample of EVs from the murine cell line TRAMP-C2, with size and z-potential similar to the PC synthetic liposomes (see ESI† for details). The EVs were separated from the cell culture medium and characterized according to international guidelines;⁶⁷ in particular, we used the protocols described in Paolini *et al.* (medium EVs),⁶⁸ to obtain a pure – *i.e.* not containing exogenous proteins (which would otherwise affect the EVs interaction with AuNPs^{44,48}) – EVs dispersion in water. The morphology of EVs was investigated by liquid imaging AFM (see Fig. 4a), showing the characteristic spherical cap shape of EVs adhered onto a substrate and an average diameter of 74.3 nm (refer to ESI† for further details).

The stiffness of EVs, determined through AFM-FS as previously described for PC liposomes, falls in the middle of the stiffness interval defined by the synthetic standards used for calibration ($0.025 \pm 0.004 \text{ N m}^{-1}$), in between the values obtained for DPPC and DPPC/POPC liposomes (see Fig. 1c). 20 μl of EVs (0.35 nM) were mixed with 100 μl of AuNPs in the same conditions (AuNPs/vesicles molar ratio, incubation time and temperature) previously employed for synthetic liposomes and the SPR profile change of AuNPs was recorded through UV-Vis spectroscopy (right inset of Fig. 4b).

In full agreement with the AFM analysis, this SPR profile variation, S.I. = 1.23 ± 0.01 , is intermediate between the ones of DPPC, S.I. = 1.16 ± 0.01 , and DPPC/POPC, S.I. = 1.377 ± 0.005 . This result demonstrates that the correlation between AuNPs aggregation and vesicles' stiffness, observed in liposomes, also holds for the case of far more complex nanosized vesicles of biological origin. More importantly, the value of stiffness estimated from the S.I. of the AuNPs/EVs hybrid according to the calibration trend (*i.e.*, $0.0259 \pm 0.0005 \text{ N m}^{-1}$) falls right in the middle of the EVs stiffness range determined through AFM (Fig. 4b): this striking agreement proves the predictive ability of this new optical method, showing that the nanoplasmonic properties of AuNPs can be effectively harnessed to assess the stiffness of membrane-confined objects with high sensitivity.

Conclusions

The determination of the stiffness of synthetic and natural vesicles is particularly challenging. Here, we show that the SPR of AuNPs can be exploited to quantify this property: combining UV-Vis Spectroscopy, Small Angle X-ray Scattering and AFM-based Force Spectroscopy, we prove that AuNPs aggregation, induced by the interaction with lipid membranes and quantified by an empirical index S.I., exhibits a clear dependence on the mechanical properties of synthetic vesicles. This dependence, expressed by a sigmoidal law, can be used to estimate the stiffness of biological membrane compartments, *e.g.* EVs, of unknown composition and properties. Similarly to the plasmon ruler developed by El-Sayed *et al.*,⁴¹ where the SPR of AuNPs is used to probe their mutual distance, we define a “stiffness nanoruler”, where the plasmon resonance is applied to probe the nano-mechanics of a target membrane. The method requires cheap

reagents and a standard wet lab facility, while keeping competitive reproducibility and sensitivity. From the sample side, it allows for examination of volumes as small as 15 μl (with a concentration of particles in the 10^{-8} M range) which is not accessible today to any other method. This allows to minimize the amounts of vesicles required, which is paramount for biological samples, where low amounts of analyte are yearned due to the origin of the samples (*e.g.* human biological fluids) and/or complex and time-consuming separation protocols. Moreover, differently from other methods – such as AFM and micropipette – which probe the stiffness of single objects, it provides the ensemble-averaged stiffness, *i.e.* accounting for possible variability across the population, with short-time (few minutes) data acquisition.

Conflicts of interest

There are no conflicts to declare.

Acknowledgements

This work has been supported by the European Community through the eFOUNDry project (H2020-FETopen, ID: 801367) and the BOW project (H2020-EIC-FETPROACT-2019, ID: 952183). We also acknowledge MIUR-Italy (“Progetto Dipartimenti di Eccellenza 2018–2022, ref. B96C1700020008” allocated to Department of Chemistry “Ugo Schiff”) and Ente Cassa di Risparmio di Firenze for the economic support. We thank the SPM@ISMN research facility for support in the AFM experiments. The European Synchrotron Radiation Facility (ESRF) is acknowledged for provision of beam-time.

References

- 1 W. Lucas and K. M. David, *Encyclopedia of Life Sciences*, 2010, pp. 1–7.
- 2 M. Yáñez-mó and E. Al, *J. Extracell. Vesicles*, 2015, **14**, 27066.
- 3 G. Raposo and P. D. Stahl, *Nat. Rev. Mol. Cell Biol.*, 2019, **20**, 509–510.
- 4 G. Bozzuto and A. Molinari, *Int. J. Nanomed.*, 2015, **10**, 975–999.
- 5 A. Huckriede, L. Bungener, T. Stegmann, T. Daemen, J. Medema, A. M. Palache and J. Wilschut, *Vaccine*, 2005, **23**, S26.
- 6 X. Zhang and P. Zhang, *Curr. Nanosci.*, 2016, **13**, 124–129.
- 7 M. Mendozza, L. Caselli, A. Salvatore, C. Montis and D. Berti, *Soft Matter*, 2019, **15**(44), 8951–8970.
- 8 A. E. Nel, L. Mädler, D. Velegol, T. Xia, E. M. Hoek, P. Somasundaran, F. Klaessig, V. Castranova and M. Thompson, *Nat. Mater.*, 2009, **8**(7), 543–557.
- 9 C. M. Beddoes, C. P. Case and W. H. Briscoe, *Adv. Colloid Interface Sci.*, 2015, **218**, 48–68.
- 10 P. K. K. Nagayama, *Particles at Fluid Interfaces and Membranes: Attachment of Colloid Particles*, Elsevier Science, 1st edn, 2001.
- 11 K. L. Chen and G. D. Bothun, *Environ. Sci. Technol.*, 2014, **48**, 873–880.

- 12 M. Simunovic, C. Prévost, P. Bassereau and P. Bassereau, *Philos. Trans. R. Soc., A*, 2016, **374**, 20160034.
- 13 P. B. Canham, *J. Theor. Biol.*, 1970, **26**, 61–81.
- 14 E. A. Evans, *Biophys. J.*, 1974, **14**, 923–931.
- 15 A. C. Dumitru, M. Poncin, L. Conrard, Y. F. Dufrêne, D. Tyteca and D. Alsteens, *Nanoscale Horiz.*, 2018, **3**, 293–304.
- 16 I. Safeukui, P. A. Buffet, G. Deplaine, S. Perrot, V. Brousse, A. Sauvanet, B. Aussilhou, P. H. David, S. Dokmak, A. Couvelard, D. Cazals-hatem, O. Mercereau-puijalon and N. Mohandas, *Blood Adv.*, 2018, **2**, 1–4.
- 17 C. Alibert, B. Goud and J. Manneville, *Biol. Cell.*, 2017, **109**, 167–189.
- 18 D. Vorselen, S. M. van Dommelen, R. Sorkin, M. C. Piontek, J. Schiller, S. T. Döpp, S. A. A. Kooijmans, B. A. van Oirschot, B. A. Versluijs, M. B. Bierings, R. van Wijk, R. M. Schiffelers, G. J. L. Wuite and W. H. Roos, *Nat. Commun.*, 2018, **9**, 1–9.
- 19 G. Van Niel, G. D. Angelo and G. Raposo, *Nat. Rev. Mol. Cell Biol.*, 2018, **19**, 213–228.
- 20 B. Whitehead, L. P. Wu, M. L. Hvam, H. Aslan, M. Dong, L. Dyrskjøt, M. S. Ostenfeld, S. M. Moghimi and K. A. Howard, *J. Extracell. Vesicles*, 2015, **4**, 1–11.
- 21 L. Paolini, A. Zendrini and A. Radeghieri, *Biomarkers Med.*, 2018, **12**(4), 383–391.
- 22 C. Carrasco, M. Castellanos, P. J. De Pablo and M. G. Mateu, *Proc. Natl. Acad. Sci. U. S. A.*, 2008, **105**, 4150–4155.
- 23 W. H. Roos, *Semin. Cell Dev. Biol.*, 2018, **73**, 145–152.
- 24 P. Guo, D. Liu, K. Subramanyam, B. Wang, J. Yang, J. Huang, D. T. Augustine and M. A. Moses, *Nat. Commun.*, 2018, **9**(1), 1–9, DOI: 10.1038/s41467-017-02588-9.
- 25 J. F. Nagle, M. S. Jablin, S. Tristram-nagle and K. Akabori, *Chem. Phys. Lipids*, 2015, **185**, 3–10.
- 26 D. Bochicchio and L. Monticelli, *The Membrane Bending Modulus in Experiments and Simulations: A Puzzling Picture*, Elsevier Inc., 1st edn, 2016, vol. 23.
- 27 N. Bezlyepkina, R. L. Knorr, R. Lipowsky and R. Dimova, *Soft Matter*, 2010, **6**, 1472–1482.
- 28 J. R. Henriksen and J. H. Ipsen, *Eur. Phys. J. E: Soft Matter Biol. Phys.*, 2004, **167**, 149–167.
- 29 J. Pan, S. Tristram-nagle and J. F. Nagle, *Phys. Rev. E: Stat., Nonlinear, Soft Matter Phys.*, 2009, **80**, 021931.
- 30 C. Length, G. Fragneto, T. Charitat, E. Bellet-amalric and R. Cubitt, *Langmuir*, 2003, **19**, 7695–7702.
- 31 M. Mell, L. H. Moleiro, Y. Hertle, P. Fouquet, R. Schweins, T. Hellweg and F. Monroy, *Eur. Phys. J. E: Soft Matter Biol. Phys.*, 2013, **36**, 75.
- 32 D. Marsh, *Chem. Phys. Lipids*, 2006, **144**, 146–159.
- 33 J. F. Nagle, *Faraday Discuss.*, 2013, **161**, 11–29.
- 34 R. Dimova, *Adv. Colloid Interface Sci.*, 2014, **208**, 225–234.
- 35 M. C. Piontek, R. B. Lira and W. H. Roos, *Biochim. Biophys. Acta, Gen. Subj.*, 2019, 129486.
- 36 M. LeClaire, J. Gimzewski and S. Sharma, *Nano Sel.*, 2021, **2**, 1–15.
- 37 D. Vorselen, M. C. Piontek, W. H. Roos and G. J. L. Wuite, *Front. Mol. Biosci.*, 2020, **7**, 1–14.
- 38 S. Li, F. Eghiaian, C. Sieben, A. Herrmann and I. A. T. Schaap, *Biophys. J.*, 2011, **100**, 637–645.
- 39 A. Calò, D. Reguera, G. Oncins, M. A. Persuy, G. Sanz, S. Lobasso, A. Corcelli, E. Pajot-Augy and G. Gomila, *Nanoscale*, 2014, **6**, 2275–2285.
- 40 V. Amendola, R. Pilot and M. Frasconi, *J. Phys.: Condens. Matter*, 2017, **29**, 203002.
- 41 P. K. Jain, W. Huang and M. A. El-sayed, *Nano Lett.*, 2007, **7**, 2080–2088.
- 42 W. Zhao, M. M. Ali, S. D. Aguirre, M. A. Brook and Y. Li, *Anal. Chem.*, 2008, **80**, 8431–8437.
- 43 C. C. Chang, C. P. Chen, T. H. Wu, C. H. Yang, C. W. Lin and C. Y. Chen, *Nanomaterials*, 2019, **9**, 1–24.
- 44 D. Maiolo, L. Paolini, G. Di Noto, A. Zendrini, D. Berti, P. Bergese and D. Ricotta, *Anal. Chem.*, 2015, **87**(8), 4168–4176.
- 45 A. Zendrini, L. Paolini, S. Busatto, A. Radeghieri, M. Romano, M. H. M. Wauben, M. J. C. van Herwijnen, P. Nejsun, A. Borup, A. Ridolfi, C. Montis and P. Bergese, *Front. Bioeng. Biotechnol.*, 2020, **7**, 452.
- 46 A. Mallardi, N. Nuzziello, M. Liguori, C. Avolio and G. Palazzo, *Colloids Surf., B*, 2018, **168**, 134–142.
- 47 A. Ridolfi, L. Caselli, C. Montis, G. Mangiapia, D. Berti, M. Brucale and F. Valle, *J. Microsc.*, 2020, **280**(3), 194–203.
- 48 C. Montis, D. Maiolo, I. Alessandri, P. Bergese and D. Berti, *Nanoscale*, 2014, **6**(12), 6452–6457.
- 49 C. Montis, V. Generini, G. Boccalini, P. Bergese, D. Bani and D. Berti, *J. Colloid Interface Sci.*, 2018, **516**, 284–294.
- 50 J. Liu, *Langmuir*, 2016, **32**, 4393–4404.
- 51 F. Wang and J. Liu, *Nanoscale*, 2015, **7**, 15599–15604.
- 52 C. Montis, L. Caselli, F. Valle, A. Zendrini, F. Carlà, R. Schweins, M. Maccarini, P. Bergese and D. Berti, *J. Colloid Interface Sci.*, 2020, **573**, 204–214.
- 53 K. Sugikawa, T. Kadota, K. Yasuhara and A. Ikeda, *Angew. Chem., Int. Ed.*, 2016, **55**, 4059–4063.
- 54 F. Wang, D. E. Curry and J. Liu, *Langmuir*, 2015, **31**, 13271–13274.
- 55 R. Sorkin, R. Huisjes, F. Boškovic, D. Vorselen, S. Pignatelli, Y. Ofir-birin, J. K. F. Leal, J. F. Schiller, D. Mullick, W. H. Roos, G. Bosman, N. Regev-rudzki, R. M. Schiffelers and G. J. L. Wuite, *Small*, 2018, **1801650**, 1–8.
- 56 J. F. Nagle, J. Pan, S. Tristram-nagle and N. Kuc, *Biophys. J.*, 2008, **94**, 117–124.
- 57 R. Dimova, B. Pouligny and C. Dietrich, *Biophys. J.*, 2000, **79**, 340–356.
- 58 C. Lee, W. Lin and J. Wang, *Phys. Rev. E: Stat., Nonlinear, Soft Matter Phys.*, 2001, **64**, 020901.
- 59 K. R. Mecke and T. Charitat, *Langmuir*, 2003, **19**, 2080–2087.
- 60 U. C. Afm, S. Sharma, H. I. Rasool, V. Palanisamy, C. Mathisen, M. Schmidt, D. T. Wong and J. K. Gimzewski, *ACS Nano*, 2010, **4**, 1921–1926.
- 61 M. Krieg, G. Fl, D. Alsteens, B. M. Gaub, W. H. Roos, G. J. L. Wuite, H. E. Gaub, C. Gerber and Y. F. Dufr, *Nat. Rev. Phys.*, 2019, **1**, 41–57.
- 62 J. F. Nagle, *Chem. Phys. Lipids*, 2017, **205**, 18–24.
- 63 L. A. Feigin and D. S. Svergun, *Structure Analysis by Small Angle X-Ray and Neutron Scattering*, Plenum Press, New York, Princeton, 1987.
- 64 M. Raatz, R. Lipowsky and T. R. Weikl, *Soft Matter*, 2014, **10**, 3570–3577.

- 65 G. Niggemann, M. Kummrow, W. Helfrich, G. Niggemann, M. Kummrow, W. H. The and B. Rigidity, *J. Phys. II*, 1995, 5, 413–425.
- 66 A. Ridolfi, M. Brucale, C. Montis, L. Caselli, L. Paolini, A. Borup, A. T. Boysen, F. Loria, M. J. C. van Herwijnen, M. Kleinjan, P. Nejsun, N. Zarovni, M. H. M. Wauben, D. Berti, P. Bergese and F. Valle, *Analytical chemistry*, 2020, 92(15), 10274–10282.
- 67 C. Théry and E. Al, *J. Extracell. Vesicles*, 2018, 7, 1535750.
- 68 L. Paolini, S. Federici, G. Consoli, D. Arceri, A. Radeghieri, I. Alessandri and P. Bergese, *J. Extracell. Vesicles*, 2020, 9(1), 1741174.

Supporting Information for:

A plasmon-based nanoruler to probe the mechanical properties of synthetic and biogenic nanosized lipid vesicles

Lucrezia Caselli, Andrea Ridolfi, Jacopo Cardellini, Lewis Sharpnack, Lucia Paolini, Marco Brucale, Francesco Valle, Costanza Montis, Paolo Bergese and Debora Berti

	Page
Supplementary Materials and Methods	S2
<i>Materials</i>	<i>S2</i>
<i>Synthesis of citrated AuNPs</i>	<i>S2</i>
<i>Preparation of liposomes</i>	<i>S3</i>
<i>Preparation of liposomes/AuNPs hybrids</i>	<i>S3</i>
<i>UV-vis spectroscopy</i>	<i>S4</i>
<i>Small Angle X-ray Scattering</i>	<i>S4</i>
<i>Atomic Force Microscopy</i>	<i>S7</i>
<i>Transmission Electron Microscopy</i>	<i>S9</i>
<i>Dynamic Light Scattering</i>	<i>S9</i>
<i>Z-Potential</i>	<i>S10</i>
Supplementary Characterization of Gold Nanoparticles	S11
<i>Transmission Electron Microscopy</i>	<i>S11</i>
<i>Small Angle X-Ray Scattering</i>	<i>S11</i>
<i>Dynamic Light Scattering and Z-Potential</i>	<i>S13</i>
<i>UV-Vis Spectroscopy</i>	<i>S14</i>
Supplementary Characterization of Liposomes	S16
<i>Dynamic Light Scattering and Z-Potential</i>	<i>S16</i>
<i>Evaluation of liposomes concentration</i>	<i>S16</i>
Supplementary Characterization of EVs	S18
<i>Z-Potential</i>	<i>S18</i>
<i>AFM characterization of synthetic and natural lipid vesicles</i>	<i>S18</i>

Supplementary Characterization of liposomes/AuNPs hybrids	S22
<i>Small-Angle X-Ray Scattering</i>	<i>S22</i>
<i>UV-Vis Spectroscopy</i>	<i>S24</i>
Bibliography	S27

Supplementary Materials and Methods

Materials

Tetrachloroauric (III) acid ($\geq 99.9\%$) and trisodium citrate dihydrate ($\geq 99.9\%$) for the synthesis of AuNPs were provided by Sigma-Aldrich (St. Louis, MO). 1,2-dioleoyl-sn-glycero-3-phosphocholine (DOPC) ($>99\%$), 1-palmitoyl-2-oleoyl-sn-glycero-3-phosphocholine (POPC) ($\geq 98.0\%$), 1,2-dipalmitoyl-sn-glycero-3-phosphocholine (DPPC) ($>99\%$) and 1,2-distearoyl-sn-glycero-3-phosphocholine (DSPC) ($>99\%$) for the liposomes preparation were provided by Sigma-Aldrich (St. Louis, MO). All chemicals were used as received. Milli-Q grade water was used in all preparations.

Synthesis of citrated AuNPs

Anionic gold nanospheres of 16 nm in size were synthesized according to the Turkevich-Frens method^{1,2}. Briefly, 20 mL of a 1mM HAuCl₄ aqueous solution was brought to boiling temperature under constant and vigorous magnetic

stirring. 2 mL of 1% citric acid solution were then added and the solution was further boiled for 20 minutes, until it acquired a deep red color. The nanoparticles dispersion was then slowly cooled down to room temperature.

Preparation of liposomes

The proper amount of lipid was dissolved in chloroform and a lipid film was obtained by evaporating the solvent under a stream of nitrogen and overnight vacuum drying. The film was then swollen and suspended in warm (50 °C) milliQ-water by vigorous vortex mixing, in order to obtain a final 4 mg/ml lipid concentration. The resultant multilamellar liposomes in water were subjected to 10 freeze-thaw cycles and extruded 10 times through two stacked polycarbonate membranes with 100 nm pore size at room temperature, to obtain unilamellar liposomes with narrow and reproducible size distribution. The filtration was performed with the Extruder (Lipex Biomembranes, Vancouver (Canada)) through Nuclepore membranes.

Preparation of liposomes/AuNPs hybrids

The hybrid samples preparation procedure for Figure 2a of the main text is the following: 20 μ L of liposomes (previously diluted to a final lipid concentration of 0.04 mg/ml) or extracellular vesicles were placed inside a 500 μ L UV-Vis

plastic cuvette. Then 100 μL of citrated gold nanoparticles ($6.7 \cdot 10^{-9}$ M, see “Synthesis citrated Gold Nanoparticles” and “Supplementary Characterization of Gold Nanoparticles” of SI) were added, in order to have a final concentration (inside the cuvette) of $\sim 5 \cdot 10^{-11}$ M and of $\sim 5 \cdot 10^{-9}$ M for liposomes and AuNPs, respectively, and liposomes/AuNPs number ratio of $\sim 1/100$. This liposomes/AuNPs number ratio was selected on the basis of our previous publication³, which highlights that the aggregation of AuNPs on POPC vesicles -and subsequent AuNPs SPR variations- is promoted by low liposomes amounts within the mix. Thus, such a ratio allows for maximizing the liposomes-induced AuNPs SPR spectral shift for an enhanced sensitivity of the plasmon-based nanoruler assay. Then, samples were incubated for 15 minutes, after that the UV-Vis spectra were recorded.

The hybrid samples preparation procedure for Figure 2b of the main text is the following: fixed volumes (768.9 μL) of AuNPs dispersion ($6.7 \cdot 10^{-9}$ M) were added to 20 μL of liposomes (see Table S4 of SI for liposomes concentration), in order to have a final AuNPs/liposomes number ratio of ~ 8 . Samples were incubated for 15 minutes, then placed in glass capillaries of 1 mm diameter and Small-Angle X-Ray profiles acquired.

UV-vis spectroscopy

UV-Vis spectra were measured with a JASCO UV-Vis spectrophotometer.

Small Angle X-ray Scattering

SAXS measurements for the characterization of AuNPs were carried out on a S3-MICRO SAXS/WAXS instrument (HECUS GmbH, Graz, Austria) which consists of a GeniX microfocus X-ray sealed Cu K α source (Xenocs, Grenoble, France) of 50 W power which provides a detector focused X-ray beam with $\lambda = 0.1542$ nm Cu K α line. The instrument is equipped with two one-dimensional (1D) position sensitive detectors (HECUS 1D-PSD-50 M system). Each detector is 50 mm long (spatial resolution 54 $\mu\text{m}/\text{channel}$, 1024 channels) and covers the SAXS q-range ($0.003 < q < 0.6 \text{ \AA}^{-1}$). The temperature was controlled by means of a Peltier TCCS-3 Hecus. The analysis of SAXS curves was carried out using Igor Pro.⁴ SAXS measurement on AuNPs aqueous dispersion was carried out in a sealed glass capillary of 1.5 mm diameter. To analyze gold nanospheres' curves we chose a model function with a spherical form factor and a Schulz size distribution:⁵ it calculates the scattering for a polydisperse population of spheres with uniform scattering length density. The distribution of radii is a Schulz distribution given by the following equation:

$$f(R) = (z + 1)^{z+1} x^z \frac{\exp[-(z + 1)x]}{R_{avg} \Gamma(z + 1)}$$

where R_{avg} is the mean radius, $x = R/R_{avg}$ and z is related to the polydispersity. The form factor is normalized by the average particle volume, using the 3rd moment of R :

$$\langle V \rangle = \frac{4\pi}{3} \langle R^3 \rangle = \frac{4\pi}{3} \langle R \rangle^3 \frac{(z+3)(z+2)}{(z+1)^2}$$

The scattering intensity is:

$$I(q) = \left(\frac{4\pi}{3}\right)^2 N_0 \Delta\rho^2 \int_0^\infty f(R) R^6 F^2(qR) dR$$

where N_0 is the total number of particles per unit volume, $F(R)$ is the scattering amplitude for a sphere and $\Delta\rho$ is the difference in scattering length density between the particle and the solvent.

SAXS measurements for the characterization of AuNPs/liposomes hybrids were collected at beamline ID02 at the European Synchrotron Radiation Facility (ESRF, Grenoble, France) ⁶. A scattering vector (of magnitude q) range of $0.007 \leq q \leq 0.2 \text{ nm}^{-1}$ was covered with two sample–detector distances (1 and 10 m) and a single-beam setting for an X-ray monochromatic radiation wavelength with a wavelength of $\lambda = 0.10 \text{ nm}$ (12.46 keV). The beam diameter was adjusted to $72.4 \mu\text{m}$ in the horizontal (x) direction and $42.3 \mu\text{m}$ in the vertical (y) direction (full width at half-maximum at the sample). Assuming a Gaussian distribution, the portion of the beam that is hitting outside the channel can be estimated. When the channel is centered, this is $\sim 0.3\%$ but closer to the edge and more beam overlaps the edge. The beamstop diameter was 2 mm. As a detector, a 2D Rayonix MX-

170HS with a pixel size of $44 \times 44 \mu\text{m}^2$ was used, which was housed in an evacuated flight tube, at a sample-to-detector distance of alternatively 10 m (leading to an available q -range of $0.007\text{-}0.02 \text{ nm}^{-1}$) or 1 m (leading to an available q -range of $0.07\text{-}0.2 \text{ nm}^{-1}$). The exposure times for the background- and sample measurements were 0.5 s for the case of 1 m sample-to-detector distance and 0.3 s for the case of 10 m sample-to-detector distance. Measured scattering patterns were normalized to an absolute intensity scale after applying standard detector corrections and then azimuthally averaged to obtain the one-dimensional intensity profiles, denoted by $I(q)$.

Atomic Force Microscopy (AFM)

Surface Preparation and Sample Deposition

All AFM experiments were performed on poly-L-lysine (PLL) coated glass coverslips. All reagents were acquired from Sigma-Aldrich Inc (www.sigmaaldrich.com) unless otherwise stated. Microscopy borosilicate glass slides (15mm diameter round coverslips, Menzel Gläser) were first immersed in a 3:1 mixture of 96% H_2SO_4 and 50% aqueous H_2O_2 ('oxidising piranha') solution for 2 h in order to remove any organic residue present on their surface; after that, they were cleaned in a sonicator bath (Elmasonic Elma S30H) for 30 minutes in acetone, followed by 30 minutes in isopropanol and 30 minutes in ultrapure water (Millipore Simplicity UV). Clean slides were incubated overnight

in a 0.0001% (w/v) PLL solution at room temperature, thoroughly rinsed with ultrapure water and dried with nitrogen. A 10 μ l-droplet of the vesicle-containing solution under study was deposited on a PLL-functionalized glass slide and left to adsorb for 10 minutes at 4°C, then inserted in the AFM fluid cell (see below) without further rinsing. The concentration of each vesicle-containing solution was adjusted in order to maximize the surface density of isolated, individual vesicles and minimize clusters of adjoining vesicles.

AFM Setup

All AFM experiments were performed in ultrapure water at room temperature on a Bruker Multimode (equipped with Nanoscope V electronics, a sealed fluid cell and a type JV piezoelectric scanner) using Bruker SNL-A probes (triangular cantilever, nominal tip curvature radius 2-12 nm, nominal elastic constant 0.35 N/m, calibrated with the thermal noise method).

AFM Imaging

Imaging was performed in PeakForce mode. In order to minimize vesicle deformation or rupture upon interaction with the probe, the applied force setpoint was kept in the 150-250 pN range. Lateral probe velocity was not allowed to exceed 5 μ m/s. Feedback gain was set at higher values than those usually employed for optimal image quality in order to ensure minimal probe-induced vesicle deformation upon lateral contact along the fast scan axis (please refer to Ridolfi et al. ⁷ for further details). The average height value of all bare substrate

zones was taken as the baseline zero height reference. Image background subtraction was performed using Gwyddion 2.53.16⁸.

AFM-based Force Spectroscopy (AFM-FS)

The mechanical characterization of vesicles via AFM force spectroscopy was performed by first scanning the sample (see previous paragraph) to locate individual vesicles. The chosen vesicles were then imaged reducing the scan size for achieving higher accuracy. We recorded a series of force/distance curves at multiple XY positions (typically around 64-100 curves arranged in a square array covering the vesicle initial location) for each individual vesicle. In most cases, only a few curves showed the mechanical fingerprint of an intact vesicle response to indentation: a linear deformation upon applied pressure during probe penetration. Of these, we first discarded those curves with probe-vesicle contact points occurring at probe-surface distances below vesicle height as measured by imaging. Remaining traces (typically 1-3 per vesicle) were analyzed to calculate vesicle stiffness (ks).

Transmission Electron Microscopy

Transmission electron microscopy (TEM) images were acquired with a STEM CM12 Philips electron microscope equipped with an OLYMPUS Megaview G2 camera, at CeME (CNR Florence Research Area, Via Madonna del Piano, 10 - 50019 Sesto Fiorentino). A drop of citrated AuNPs, diluted ten times, was placed

on 200 mesh carbon-coated copper grids with a diameter of 3 mm and a thickness of 50 μm (Agar Scientific) and dried at room temperature. Then, the sample was analyzed at an accelerating voltage of 100 keV.

Dynamic Light Scattering

DLS measurements at $\theta = 90^\circ$ were performed using a Brookhaven Instrument 90 Plus (Brookhaven, Holtsville, NY). Each measurement was an average of ten repetitions of one minute each and repeated ten times. The autocorrelation functions were analyzed through the cumulant fitting stopped to the second order or with Laplace inversion according to CONTIN algorithm, allowing an estimate of the hydrodynamic diameter of particles.

Z-Potential Measurements

Zeta potential measurements were performed using a Zeta Potential Analyzer (Zeta Plus, Brookhaven Instruments Corporation, Holtsville, NY). Zeta potentials were obtained from the electrophoretic mobility u , according to Helmholtz-Smoluchowski equation: $\zeta = (\eta/\epsilon) \times u$ with η being the viscosity of the medium, ϵ the dielectric permittivity of the dispersing medium. The Zeta Potential values are reported as averages from ten measurements.

Supplementary Characterization of Gold Nanoparticles

Transmission Electron Microscopy

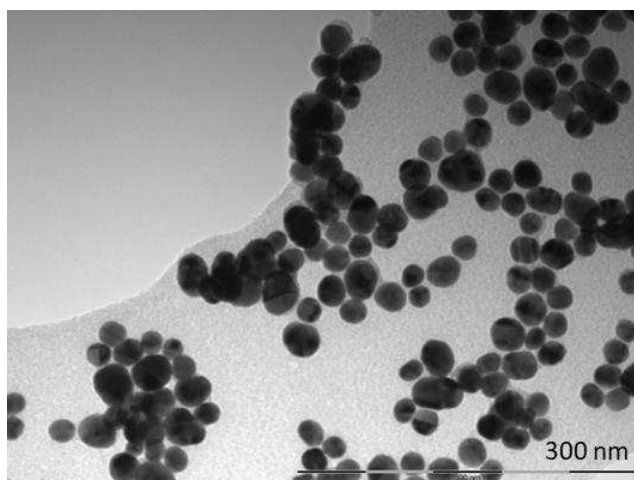


Figure S1 Representative Transmission electron microscopy (TEM) images of citrated gold nanoparticles acquired with a STEM CM12 Philips electron microscope, at CeME (CNR Florence Research Area, Via Madonna del Piano, 10 - 50019 Sesto Fiorentino). The sample was placed on a 200 mesh carbon-coated copper grid.

Small Angle X-ray Scattering

The analysis of SAXS curves was carried out using Igor Pro.⁴ SAXS measurements on AuNPs aqueous dispersion were carried out in sealed glass capillaries of 1.5 mm diameter. To analyze gold nanospheres' curves we chose a model function with a spherical form factor and a Schulz size distribution:⁵, it calculates the scattering for a polydisperse population of spheres with uniform scattering length density. The distribution of radii is a Schulz distribution given by the following equation:

$$f(R) = (z + 1)^{z+1} x^z \frac{\exp[-(z + 1)x]}{R_{avg} \Gamma(z + 1)}$$

where R_{avg} is the mean radius, $x = R/R_{avg}$ and z is related to the polydispersity. The form factor is normalized by the average particle volume, using the 3rd moment of R :

$$\langle V \rangle = \frac{4\pi}{3} \langle R^3 \rangle = \frac{4\pi}{3} \langle R \rangle^3 \frac{(z + 3)(z + 2)}{(z + 1)^2}$$

The scattering intensity is:

$$I(q) = \left(\frac{4\pi}{3}\right)^2 N_0 \Delta\rho^2 \int_0^\infty f(R) R^6 F^2(qR) dR$$

where N_0 is the total number of particles per unit volume, $F(R)$ is the scattering amplitude for a sphere and $\Delta\rho$ is the difference in scattering length density between the particle and the solvent. The structural parameters (Table S1) of citrated gold nanoparticles were evaluated from the SAXS profile of their water dispersion (Figure S2) according to the models reported in the Materials and Methods section of SI.

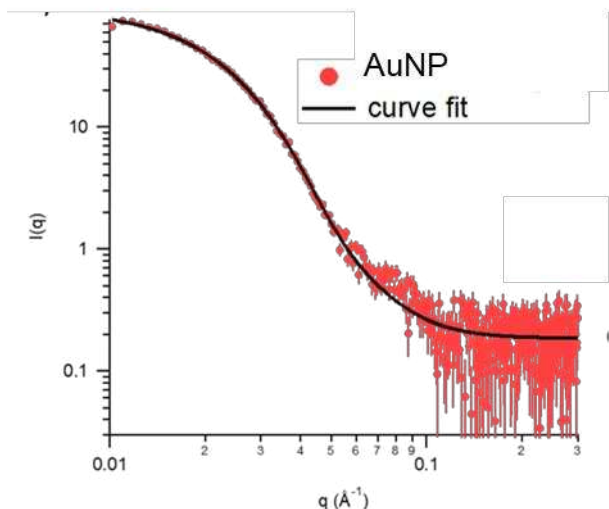


Figure S2 Experimental SAXS curve (red markers) obtained for AuNPs and curve fit (solid black line) according to the Schulz spheres model from the NIST package SANS Utilities. The size and polydispersity obtained from the fitting procedure are summarized in the Table S1 below.

	R_{core} (nm)	poly
AuNP	6.5	0.3

Table S1 Structural parameters of the nanoparticles obtained from the analysis of SAXS curves according to the the Schulz spheres model.

Dynamic Light Scattering and Z-Potential

AuNPs hydrodynamic diameter and surface charge in MilliQ water were evaluated through Dynamic Light Scattering and Zeta-Potential, respectively,

and reported in Table S2.

	D_h (nm)	Z-Potential (mV)
AuNPs	15.8 ± 0.3	-36 ± 2

Table S2 Hydrodynamic diameter obtained from Dynamic Light Scattering and Zeta Potential values of AuNPs.

UV-vis Spectroscopy

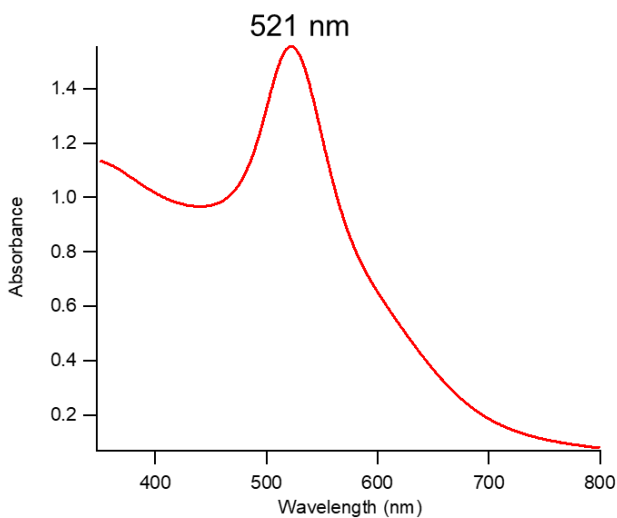


Figure S3 UV-Vis absorption spectra of AuNPs after 1:5 dilution in water. The plasmon absorption peak is at around 521 nm.

The size of AuNPs was further evaluated from UV-Vis Spectroscopy by the following equation ⁹:

$$d = \exp \left(B_1 \frac{A_{spr}}{A_{450}} - B_2 \right)$$

with d diameter of gold nanoparticles, A_{spr} absorbance at the surface plasma resonance peak, A_{450} absorbance at the wavelength of 450 nm and B_1 and B_2 are dimensionless parameters, taken as 3 and 2.2, respectively. The diameter value obtained is of 13.5 nm.

The concentration of citrated gold nanoparticles was determined via UV-Vis spectrometry, using the Lambert-Beer law ($E(\lambda) = \varepsilon(\lambda)lc$), taking the extinction values $E(\lambda)$ at the LSPR maximum, i.e. $\lambda = 521$ nm. The extinction coefficient $\varepsilon(\lambda)$ of gold nanoparticles dispersion was determined by the method reported in literature ¹⁰, by the following equation:

$$\ln(\varepsilon) = k \ln(d) + a$$

with d core diameter of nanoparticles, and k and a dimensionless parameters ($k = 3.32111$ and $a = 10.80505$). The arithmetic mean of the sizes obtained by optical and scattering analyses was selected, leading to a $\varepsilon(\lambda)$ of $2.8 \cdot 10^8 \text{ M}^{-1} \text{ cm}^{-1}$. The final concentration of the citrated AuNPs is therefore $\sim 5.6 \cdot 10^{-9} \text{ M}$.

Supplementary Characterization of Liposomes

Dynamic Light Scattering and Zeta-Potential

	D_h (nm)	Zeta P
DOPC	118.6 ± 0.2	-16 ± 1
POPC	103.8 ± 0.1	-19 ± 3
POPC/DPPC	92.1 ± 0.2	-22 ± 1
DPPC	115.7 ± 0.1	-13 ± 1
DPPC/DSPC	104 ± 0.2	-10 ± 1
DSPC	127.7 ± 0.2	-19 ± 1

Table S3 Hydrodynamic diameter obtained from Dynamic Light Scattering and Zeta Potential values of synthetic liposomes.

Evaluation of Liposomes concentration

The lipid concentration in the starting colloidal dispersion was estimated to be 4 mg/mL from the initial lipid and water amounts employed in the formation and swelling of lipid films (see “Preparation of liposomes” in the Materials and Methods section), assuming the absence of lipid loss due to the extrusion procedure. The liposomes concentration in the final dispersion was subsequently

calculated considering the hydrodynamic diameter of each liposomal batch (Table S3 of SI). In particular, from the liposomes' average diameter, the liposomal surface area (surface area= $4\pi r^2$) can be calculated; the doubled surface can be subsequently divided by the lipid cross section (0.5 nm^2) in order to obtain the lipid number per liposome, assuming that approximately one half of the lipids is localized in the external leaflet of a liposomes, since the bilayer thickness, about 4-5 nm, is negligible with respect to the liposomes' average diameter. Eventually, the total weighted lipid concentration was divided by the total number of lipids per liposome, yielding the real liposome concentration, which is reported in Table S4 for each liposomes' dispersion.

	Concentration (M)
DOPC	$3.2 \cdot 10^{-8}$
POPC	$3.1 \cdot 10^{-8}$
POPC/DPPC	$3.6 \cdot 10^{-8}$
DPPC	$3.1 \cdot 10^{-8}$
DPPC/DSPC	$3.8 \cdot 10^{-8}$
DSPC	$3.5 \cdot 10^{-8}$

Table S4 Final liposomes' concentration in each liposomal batch.

Supplementary Characterization of EVs

Zeta Potential

The Zeta Potential of EVs dispersion in milliQ water was measured as described in the “Material and Methods” section of SI and is equal to -21 ± 3 mV.

AFM characterization of synthetic and natural lipid vesicles

AFM Mechanical Characterization

According to the Canham-Helfrich theory, the mechanical response of a vesicle to an applied force is elastic; this behavior is reflected in the linear relationship between the force and tip penetration, in the AFM force-distance curves, right after the contact point (see Fig.1b in the main text). Calculating the slope of this linear part, gives the value of the vesicle stiffness, a mechanical parameter that accounts for multiple contributions, the most relevant being the intrinsic membrane rigidity (the bending modulus) and the vesicle luminal, i.e. internal, pressure. The latter contribution describes the vesicle pressurization following the deformation applied by the AFM tip. This deformation generates a volume variation that increases the pressure within the vesicle. While the bending modulus is an intrinsic descriptor of the lipid membrane bending rigidity, the internal pressure and hence the stiffness depend on the size of each vesicle. Indeed, the volume variation associated with a given tip penetration varies with

the vesicle size (i.e. the same penetration will result in higher volume variations for smaller vesicles); as a consequence, vesicles that are heterogenous in size will be subjected to different pressurizations following similar indentation events. However, both the measured liposomes and EVs are characterized by low polydispersity, this allows considering the stiffness a size-independent parameter. Moreover, since all the tested liposomes were characterized by similar size distributions and same polar headgroups, they will experience similar pressurizations and electrostatic attractions to the substrate; as a result, we can assume that changes in their stiffness are entirely ascribable to differences in their membrane rigidity, which can be recapitulated by the bending modulus. Membrane rigidity may vary depending on the phase behavior of the lipid bilayer, a temperature dependent parameter. All the measurements were performed at 28°C, where neat DOPC and POPC vesicles are in the fluid phase, while DPPC and DSPC ones are in the gel phase. In fluid-state membranes, lipid molecules can diffuse freely within the bilayer plane, while in gel- state membranes lipids are more tightly packed and their motion is more constrained. As a consequence, gel- phase bilayers are expected to be stiffer than fluid- phase ones. Our results from the Force Spectroscopy FS analysis (Figure 1c, main text) confirms this behavior, with DPPC and DSPC vesicles being substantially stiffer than DOPC and POPC ones. Two other important parameters that can affect the stiffness of a lipid bilayer are the chain length and its degree of saturation; e. g. DSPC

possesses two fully saturated chains, longer than all the other measured ones, resulting in the highest measured stiffness. Overall, the obtained stiffness values for neat DOPC, POPC, DPPC and DSPC vesicles (Figure 1c, main text) are in good agreement with results from recent AFM-FS investigations on similar vesicles¹¹. Another interesting aspect to highlight is that the stiffnesses measured for the hybrid lipid vesicles (POPC/DPPC and DPPC/DSPC) have intermediate values with respect to liposomes made of the two pure components.

AFM-based characterization of EVs size distribution, concentration and purity

AFM imaging was employed to obtain the size distribution of the EVs sample. A total of 166 EVs were imaged; from the topography of the AFM images, assuming the vesicle surface area conservation and by applying simple geometric consideration (see Ridolfi et al.¹² for further details) it is possible to obtain the values of the diameter that the vesicles would have had in solution, prior to their adsorption to the surface (we refer to this parameter as “Size”). Figure S4 displays the size distribution for the EVs sample used in this study. The measured EVs have a mean size of 74 nm with a standard deviation of 30 nm.

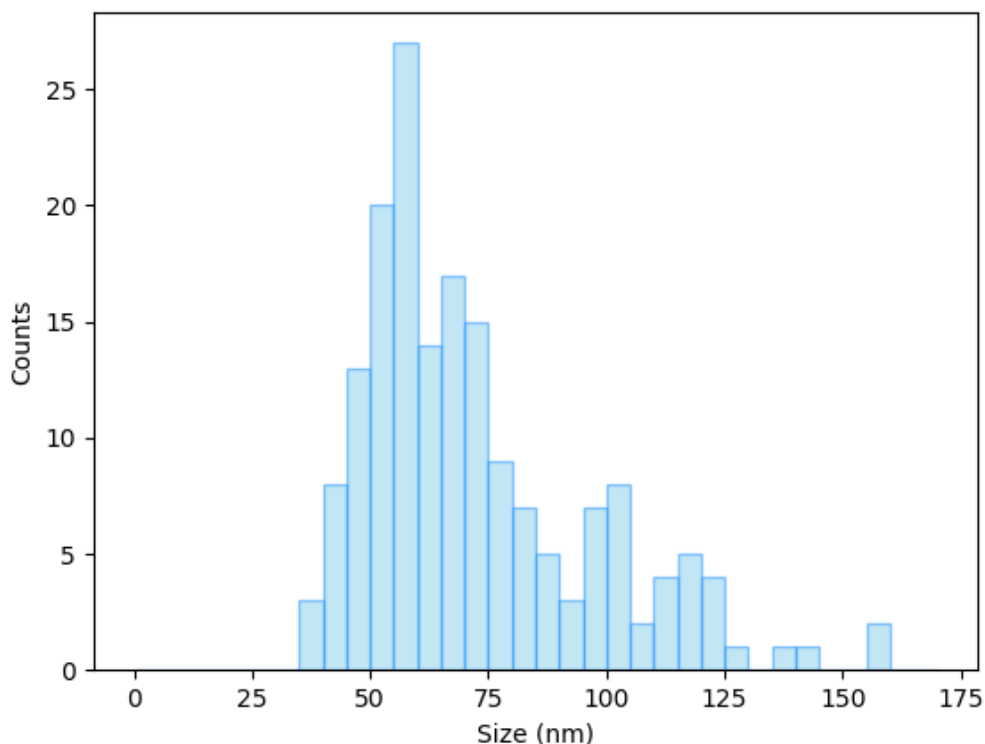


Figure S4: EVs size distribution obtained from the AFM imaging analysis. The size of the EVs (reported in the horizontal axis), indicates the diameter that the vesicles would have had in solution, prior to their adsorption.

Exploiting the AFM-based characterization method developed by Ridolfi et al.⁷, it is also possible to detect the presence of contaminants that, from a physico-chemical point of view, do not behave like a lipid vesicle; the method is based on the calculation of the contact angle (CA) that each vesicle displays after adsorption on the surface. Both synthetic lipid vesicles and EVs are characterized by a narrow distribution of CA over the whole range of characteristic sizes. Figure S5 shows the CA values of each of the imaged EVs, plotted against their

size; as can be seen, the scatterplot displays only the fingerprint of the typical vesicle-like behavior, ruling out the presence of any contaminant on the surface.

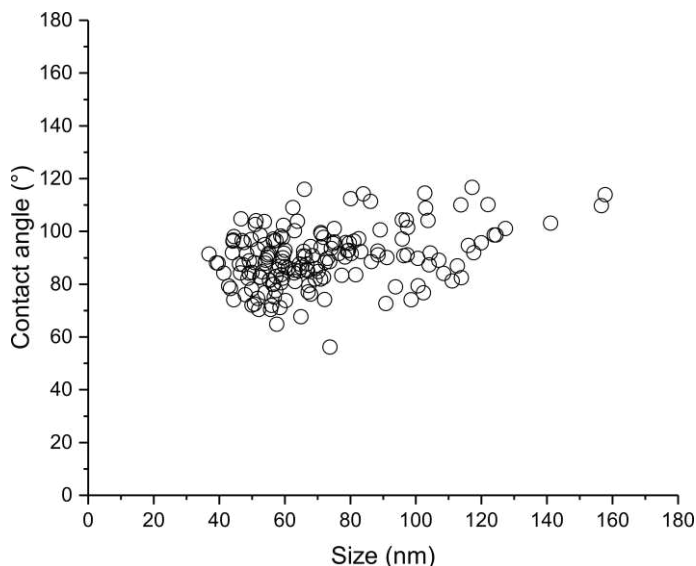


Figure S5: Scatterplot showing the contact angle of each EV, plotted against their respective size. According to this characterization, the EVs show the typical vesicle-like behavior, i.e. narrow CA distribution over the entire range of sizes (average CA value is 90° and the standard deviation is 11°); pointing to the absence of any spherical contaminant.

AFM imaging was also used to estimate the starting concentration of the EVs sample. To do this, we compared the number of DPPC liposomes (coming from a solution with a known concentration and having a size distribution similar to the EVs) adsorbed on the glass surface with the number of EVs adsorbed on the same glass surface. This represents only a qualitative procedure and it is based on different assumptions: i) the interactions of DPPC liposomes with the glass surface are similar to the EVs ones, ii) the recorded images are representative of both the vesicles samples, iii) the size distributions of the two samples are

similar to each other. The concentration of the DPPC starting solution is 0.02 mg/ml; analysing the AFM images, we recorded a total of 329 vesicles in 4 different images, giving an average of 82.25 vesicles per image. Measuring EVs from TRAMP cells, we sampled 5 images, obtaining a total number of 166 EVs; 33.20 EVs per image. From proportionality considerations, it is possible to estimate the concentration of the EVs, spotted on the glass coverslips, using the following expression:

$$\text{DPPC concentration (mg/ml)} : \text{DPPC liposomes per image} = \text{EVs concentration (mg/ml)} : \text{EVs per image}$$

From the expression we obtained a concentration of 0.008 mg/ml for the EVs sample. Since the EVs starting solution have been diluted six times before being spotted on the glass surface, the starting concentration is ~0.048 mg/ml.

Supplementary Characterization of liposomes/AuNPs hybrids

Small-Angle X-Ray Scattering

SAXS measurements on liposomes/AuNPs hybrids were recorded at ID02 beamline, ESRF (Grenoble, France), using a sample-to-detector distance of 10 m. The analysis of SAXS curves was carried out using Igor Pro⁴. SAXS measurements on liposomes/AuNPs aqueous dispersion were carried out in

sealed glass capillaries of 1 mm diameter.

The SAXS profiles of DOPC liposomes/AuNPs and POPC liposomes/AuNPs in Figure 2b were fitted according to a linear fit in the $0.0695\text{-}0.1142\text{ nm}^{-1}q$ -range, to obtain the slope values reported in the main text (-1.5404 ± 0.00297 for DOPC and -1.4987 ± 0.00612 for POPC). The fitting yielded a chisquare of 0.000239052 and 0.00106975 , for DOPC/AuNPs and POPC/AuNPs respectively.

The SAXS results of inset of Figure 2b were collected at ID02 beamline, ESRF (Grenoble, France), using a sample-to-detector distance of 1 m.

The scattering intensity ($I(q)$) is defined by the following equation:

$$I(q) = KN_p V_p^2 (\Delta\rho)^2 P(q)S(q) + B$$

With k instrumental constant, N_p scattering nanoparticles' number per unit volume, V_p nanoparticle's volume, $\Delta\rho$ contrast of the experiment, B background intensity, $P(q)$ e $S(q)$ form and structure factors, respectively.

In order to obtain the structure factor of the liposome/AuNPs complex, we divided the scattering intensity of the liposomes/AuNPs hybrid by the scattering intensity of the neat AuNPs dispersion (at a suitable dilution of 1:10):

$$\frac{I(q)_{Hyb}}{I(q)_{NP}} \sim \frac{S(q)_{Hyb}P(q)_{Hyb}}{S(q)_{NP}P(q)_{NP}}$$

For a diluted AuNPs dispersion the structure factor can be considered equal to 1. In addition, in the high- q region ($0.1\text{-}1.6\text{ nm}^{-1}$), the form factor of

liposomes/AuNP hybrids can be approximated to the one of neat AuNPs, leading to the following:

$$\frac{I(q)_{Hyb}}{I(q)_{NP}} = S(q)_{Hyb}$$

The mean interparticle distance between the AuNPs within the aggregates (d) can be obtained from the $S(q)$ vs q (nm^{-1}) plot (see inset of Figure 2b of the main text), by the following equation:

$$d = \frac{2\pi}{q_{max}}$$

With q_{max} q value corresponding to the maximum of the correlation peaks reported in the inset of figure 2b (main text).

UV-Vis Spectroscopy

The S.I. mean values for each liposomes/AuNPs mixtures are reported in Table S5, together with the relative standard deviation obtained from five repeated measurements on different samples (see “Preparation of liposomes/AuNPs hybrids” of SI).

	S.I. mean value	Standard deviation
DOPC	1.456	0.002
POPC	1.438	0.001
POPC/DPPC	1.377	0.005
DPPC	1.16	0.01
DPPC/DSPC	1.127	0.003

DSPC	1.026	0.006
------	-------	-------

Table S5 S.I. mean value and standard deviation for each liposomes/AuNPs hybrid.

The fitting parameters describing the sigmoidal best fit (eqn. 1 of the main text) for the S.I. values of liposomes plotted versus the AFM-determined stiffness, reported in Figure 3b of the main text, are the following:

a	b	c	d	Chi square
1.4831 ± 0.0485	-0.51151 ± 0.131	0.026043 ± 0.00266	0.0063004 ± 0.00265	0.0015

Table S6 Fitting parameters obtained by fitting the S.I. vs stiffness values of Figure 3c (main text) through the sigmoidal best fit (refer eqn 1 of main text for description of parameters).

The extent of AuNPs aggregation was also evaluated using different optical indexes, both taken from literature and defined in our lab.

In particular, as an alternative to the bending index defined in the main text, which is based on the determination of the area under the absorbance curve associated to AuNP aggregation, we defined another optical parameter (S.I. (2)). This alternative bending index allows evaluating AuNPs aggregation extent by calculating the intensity difference between the free AuNPs primary plasmon band (at 521 nm) and the aggregated AuNPs secondary plasmon peak, whose maximum is located at about 625 nm (see Figure S6). This result is then divided by the wavelength interval ($\Delta\lambda$) between the two peaks and normalized for the S.I. of neat AuNPs.

$$S.I. (2) = \frac{I_{625} - I_{521}}{\Delta\lambda}$$

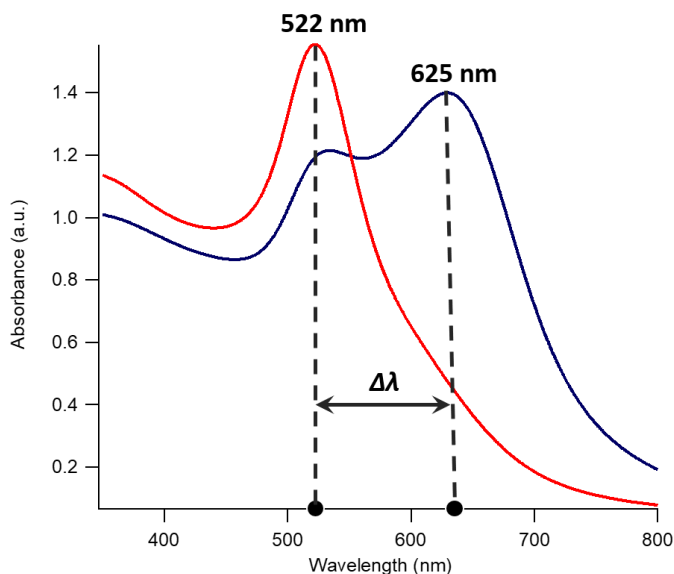


Figure S6 Visual description of the S.I. (2) evaluation.

We also selected another optical index from literature ($A.I_{CONAN}$)^{13,14}, which is commonly used to describe the aggregation of AuNPs on natural and synthetic vesicles and defined as follows:

$$A.I_{CONAN} = \frac{I_{521}}{I_{650} + I_{800}}$$

with I_{521} , I_{650} and I_{800} UV-Vis absorbances at 521, 650 and 800 nm respectively.

Both the S.I. (2) and the $A.I_{CONAN}$ show a sigmoidal behaviour as a function of membrane stiffness, as reported in Figure S7 and Table S7.

	S.I. (2)	A.I. CONAN
DOPC	-0.1965 ± 0.0004	0.785 ± 0.014
POPC	-0.14 ± 0.03	0.83 ± 0.17
POPC/DPPC	0.12 ± 0.03	1.02 ± 0.05
DPPC	0.71 ± 0.06	1.99 ± 0.24
DPPC/DSPC	0.76 ± 0.01	2.36 ± 0.05
DSPC	1.04 ± 0.02	3.28 ± 0.24

Table S7 S.I. (2) and A.I. CONAN mean values and standard deviations for each liposomes/AuNPs hybrid.

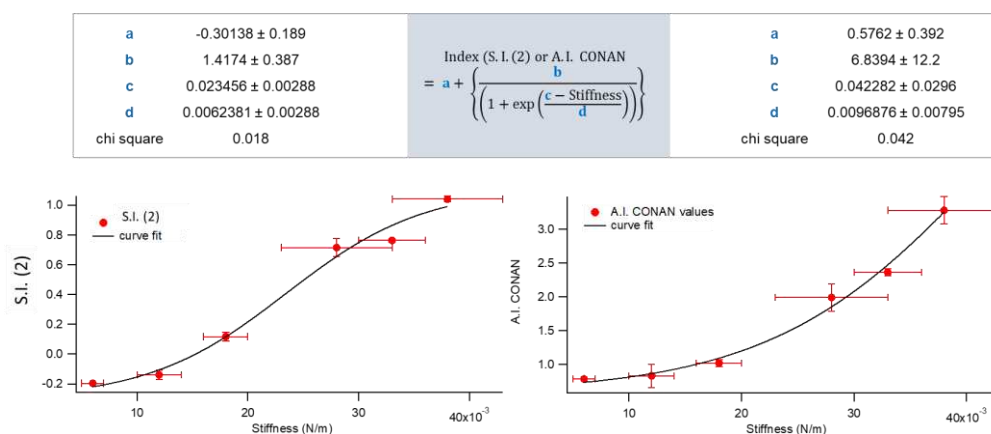


Figure S7 S.I. (2) and A.I. CONAN mean values and as a function of membrane stiffness. The sigmoidal fit curve is shown in black, together with the corresponding equation and fitting parameters (top inset).

Bibliography

- 1 J. Turkevich, P. C. Stevenson and J. Hillier, *Discuss. Faraday Soc.*, 1951, **11**, 55–75.
- 2 G. Frens, *Nat. Phys. Sci.*, 1973, **241**, 20–22.
- 3 C. Montis, L. Caselli, F. Valle, A. Zendrini, F. Carlà, R. Schweins, M. Maccarini, P. Bergese and D. Berti, *J. Colloid Interface Sci.*, 2020, **573**, 204–214.
- 4 S. R. Kline, *J. Appl. Crystallogr.*, 2006, **39**, 895–900.
- 5 M. Kotlarchyk and S.-H. Chen, *J. Chem. Phys.*, 1983, **79**, 2461.
- 6 T. Narayanan, M. Sztucki, P. Van Vaerenbergh, J. Gorini, L. Claustre, F. Sever and J. Morse, *J. Appl. Crystallogr.*, 2018, **51**, 1511–1524.
- 7 A. Ridolfi, M. Brucale, C. Montis, L. Caselli, L. Paolini, A. Borup, A. T. Boysen, F. Loria, M. J. C. Van Herwijnen, M. Kleinjan, P. Nejsun, N. Zarovni, M. H. M. Wauben, D. Berti, P. Bergese and F. Valle, *Anal. Chem.*, 2020, **92**, 10274–10282.
- 8 D. Nečas and P. Klapetek, *Cent. Eur. J. Phys.*, 2012, **10**, 181–188.
- 9 W. Haiss, N. T. K. Thanh, J. Aveyard and D. G. Fernig, *Anal. Chem.*, 2007, **79**, 4215–4221.
- 10 X. Liu, M. Atwater, J. Wang and Q. Huo, *Colloids Surfaces B Biointerfaces*, 2007, **58**, 3–7.
- 11 D. Vorselen, F. C. Mackintosh, W. H. Roos and G. J. L. Wuite, *ACS Nano*, 2017, **11**, 2628–2636.
- 12 A. Ridolfi, M. Brucale, C. Montis, L. Caselli, L. Paolini, A. Borup, A. T. Boysen, F. Loria, M. J. C. van Herwijnen, M. Kleinjan, P. Nejsun, N. Zarovni, M. H. M. Wauben, D. Berti, P. Bergese and F. Valle, *Anal. Chem.*, 2020, **92**, 10274–10282.
- 13 S. Busatto, A. Giacomini, C. Montis, R. Ronca and P. Bergese, *Anal. Chem.*, 2018, **90**, 7855–7861.
- 14 R. Carney, A. Zendrini, L. Paolini, S. Busatto and A. Radeghieri, *Front. Bioeng. Biotechnol.*, 2020, **7**, 1–10.

Probing the coverage of nanoparticles by biomimetic membranes via nanoplasmonics (Paper V)

Jacopo Cardellini, Andrea Ridolfi, Melissa Donati, Valentina Giampietro, Mirko Severi, Marco Brucale, Francesco Valle, Paolo Bergese, Costanza Montis, Lucrezia Caselli, and Debora Berti (Manuscript in preparation)

Probing the coverage of nanoparticles by biomimetic membranes via nanoplasmonics

Jacopo Cardellini^{1,2}, Andrea Ridolfi^{1,2,3,4}, Melissa Donati¹, Valentina Giampietro¹, Mirko Severi¹, Marco Brucale^{2,3}, Francesco Valle^{2,3}, Paolo Bergese^{2,5,6}, Costanza Montis^{1,2}, Lucrezia Caselli^{1,2,7}, and Debora Berti^{1,2}*

1 Department of Chemistry “Ugo Schiff”, University of Florence, Florence, Italy

2 CSGI, Consorzio Sistemi a Grande Interfase, University of Florence, Sesto Fiorentino, Italy

3 Istituto per lo Studio dei Materiali Nanostrutturati, Consiglio Nazionale delle Ricerche, 40129 Bologna, Italy

4 Department of Physics and Astronomy and LaserLaB Amsterdam, Vrije Universiteit Amsterdam, Amsterdam, The Netherlands (current affiliation)

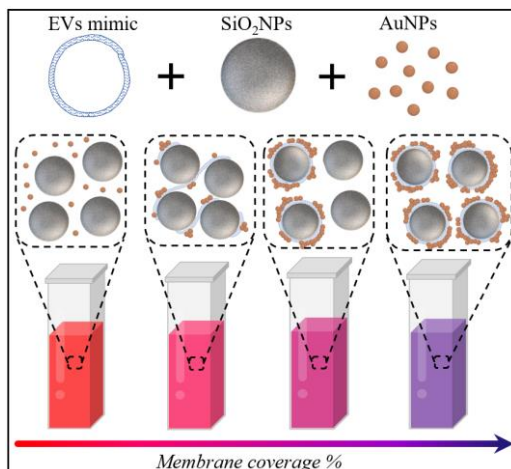
5 Department of Molecular and Translational Medicine, University of Brescia, Brescia, Italy

6 Consorzio Interuniversitario Nazionale per la Scienza e la Tecnologia dei Materiali, Florence, Italy

7 Department of Pharmacy, University of Copenhagen, DK-2100 Copenhagen, Denmark (current affiliation)

*E-mail: lucrezia.caselli@sund.ku.dk (corresponding author)

Keywords: (lipid-coated nanoparticles, gold nanoparticles, nanoplasmonic, biomimetic nanoparticles, silica nanoparticles, camouflaged nanoparticles, Extracellular Vesicles membrane)



Although promising for biomedicine, the clinical translation of inorganic nanoparticles (NPs) is limited by low biocompatibility and stability in biological fluids. A common strategy to circumvent this drawback consists in disguising the active inorganic core with a coating of (synthetic or natural) lipid bilayers, reminiscent of the structure of cell membrane, to redefine the chemical and biological identity of NPs. While recent reports introduced membrane-coating procedures for NPs, a robust and accessible method to quantify the integrity of the bilayer coverage is not yet available.

To fill this gap, we prepared SiO₂NPs with different membrane coverage degrees and monitored their interaction with AuNPs combining microscopic, scattering, and optical techniques. The membrane-coating on SiO₂NPs induces spontaneous clustering of AuNPs, whose extent depends on the coating integrity. Remarkably, we discovered a linear correlation between the membrane coverage and a spectral descriptor for the AuNPs' plasmonic resonance, spanning a wide range of coating yields. These results provide a fast, and cost-effective assay to monitor the compatibilization of NPs with biological environments, essential for bench tests and scale-up. In addition, we introduce a robust and scalable method to prepare SiO₂/AuNPs hybrids through spontaneous self-assembly, with a high-fidelity structural control mediated by a lipid bilayer.

1. Introduction

Over the last decades, numerous efforts have been devoted to the exploitation of the unique properties of inorganic nanoparticles (NPs) for biomedical applications. Despite the large number of NPs developed for biomedical purposes and reports illustrating their in-vitro potential, the route for effective clinical translation is still very limited, due to multiple issues¹⁻⁵, including poor colloidal stability and limited circulation time in biological fluids, cytotoxic effects, poor targeting ability and uncontrolled accumulation in specific tissues, which eventually leads to low efficacy and unwanted side effects.⁶ In a simplistic view, these drawbacks could be considered to be related to a general issue, i.e. the inherent exogenous, synthetic nature of inorganic NPs, and their size range, which – being close to that of biomolecules and biological assemblies – can lead to unpredictable behavior when inserted into a biological environment.

Coating NPs with a lipid membrane of either synthetic or natural origin is one of the most promising strategies to circumvent this issue, which led to a new class of nanomaterials, i.e., membrane-camouflaged biomimetic NPs. While retaining the physicochemical properties of the core (inorganic) material, the lipid shell of these systems provides biomimetic surface functions, such as immune escape ability and modulation, specific molecular recognition and targeting, enhanced cell adhesion, reduced toxicity, and long circulation time.⁷⁻

¹¹ Among the possible sources for membrane camouflaging, synthetic lipid bilayers, whose composition can be conveniently tailored to resemble that of biological membranes, are commonly employed as bioinspired coatings to improve the biocompatibility and pharmacokinetics of NPs,^{12,13} as well as to enhance their colloidal stability¹⁴. Lipid bilayers can be easily functionalized to introduce targeting properties^{15,16}, steering the carriers towards specific sites, protecting them from the biological environment, and preventing the uncontrolled leakage of drugs.¹³ More sophisticated coatings^{17,18}, employing

natural cell membranes (e.g., of red^{19–23} and white^{24–26} blood cells, cancer cells^{27,28,29}, stem cells³⁰, platelets^{31,32}, and bacterial walls^{33,34,35}), are currently the focus of intensive research, which has already led to the development of hybrid NPs with superior properties for drug delivery^{36,37}, in vitro imaging^{19,38,39}, diagnosis and treatment of cancer^{40,41}, bacterial infections^{42,43} and other diseases⁴⁴, anticancer vaccination⁴⁵ and detection of viral pathogens⁴⁶.

In the palette of natural camouflages, the biomembrane of Extracellular Vesicles' (EVs') represents one of the latest -and more promising- frontiers.⁴⁷ EVs are biogenic vesicles naturally secreted by cells, containing lipids, proteins, nucleotides, and metabolites in the inner pool.⁴⁸ As compared to other natural membrane coatings, EVs provide unmet targeting abilities, which are connected to their role in cell-cell chemical communication as nano-shuttles for proteins, lipids, and RNA^{49,50,51}. Provided by its endogenous origin, the EV membrane also offers near non-immunogenicity, resistance to macrophage uptake^{52,53} and the ability to cross the blood-brain barrier^{54,55}, as well as enhanced endocytosis efficiency.⁵⁶ Coating NPs with the EVs membrane has recently proved as a powerful tool to achieve immune evasion-mediated targeting⁵⁷ and selective accumulation at the tumor site^{57,58}, e.g., through receptor-mediated endocytosis.⁵⁹

Despite a consistent growth of the library of available membrane-coated NPs, achieving complete membrane coverage and developing efficient and reliable methods to quantify its integrity remain a significant hurdle. An incomplete membrane coating drastically decreases the colloidal stability of NPs^{60,61,62}, and may promote cargo leakage in drug-delivery systems⁶³. Moreover, the integrity of the membrane coating modulates the efficiency of macrophage clearance⁶⁴ and affects the internalization mechanism of biomimetic NPs⁶⁵, as well as their biomedical functions^{66,67,68}.

So far, the characterization of the coating integrity has primarily relied on microscopy techniques (e.g., Electron, Confocal Laser Scanning, and Atomic Force microscopies)^{69,70,71}, Dynamic Light Scattering (DLS)⁷² and Zeta Potential measurements^{73,72,74}. However, microscopy techniques do not provide ensemble-averaged characterization and generally require specialized equipment and ad-hoc sample preparation. On the other side, scattering-based methods and other traditional approaches (e.g., colloidal stability test in phosphate-buffered saline or fetal bovine serum⁶⁵, and sodium dodecyl sulfate-polyacrylamide gel electrophoresis^{72,75}), fail in providing a quantitative estimate of the coating extent. More sophisticated techniques, such as mass spectrometry (MS) or liquid chromatography-tandem MS^{76,77,78}, only give a rough estimation of the coating degree, i.e., heavily affected by strong assumptions on the morphology and structure of the coating itself.

Here, we report a new colorimetric and spectrophotometric method for quantitatively assessing the membrane coating extent, based on the plasmonic properties of citrated gold nanoparticles (AuNPs).

AuNPs spontaneously interact with free-standing lipid bilayers, leading to membrane adhesion and AuNPs clustering^{79,80,81,82,83,84}. Recently, we have shown how the spontaneous clustering of AuNPs on synthetic and natural lipid vesicles (such as EVs) can be exploited to gain information on the characteristics of the vesicles themselves, such as their concentration⁸⁵, stiffness^{86,87}, and the presence of protein contaminants⁸⁸. Overall, AuNPs plasmonic properties are emerging as convenient, highly sensitive and robust probes for lipid interfaces.

Given these unique properties, we here test the ability of AuNPs to probe and possibly quantify the membrane coating degree on the surface of inorganic NPs. To this purpose, we prepare biomimetic NPs with a silica inorganic core and a synthetic membrane shell, whose composition mimics the typical one of EVs. Through a combination of structural and spectrophotometric techniques, we

investigate the interaction of such membrane-coated SiO₂NPs (M-SiO₂NPs) with AuNPs, as a function of the membrane coating integrity. Finally, we leverage these findings to estimate the extent of the lipid coverage of M-SiO₂NPs, through a simple and fast colorimetric assay.

2. Results and Discussion

2.1. Formation of biomimetic membrane-coated SiO₂NPs (M-SiO₂NPs)

As model inorganic particles, we selected commercial anionic SiO₂NPs, given their well-known surface chemistry and the wide range of applications in biomedical research^{89,90}. To form the lipid coating, we used DOPC (1,2-dioleoyl-sn-glycero-3-phosphocholine)/Sphingomyelin/Cholesterol (0.87/0.38/1.00 mol%) vesicles, characterized by an average hydrodynamic diameter of 110 nm (PDI 0.150) and a ζ -potential of -15.2 ± 1.3 mV (see section S2 of SI). This composition has been selected to mimic the prototypical lipid membrane of Extracellular Vesicles (EVs), typically enriched in sphingomyelin and cholesterol as compared to parental cells.⁹¹

The lipid coating of SiO₂NPs was obtained through a slight modification of a well-established protocol⁹² (described in the Materials and Methods section). Briefly, this method relies in mixing SiO₂NPs in ultrapure water with a high stoichiometric excess of liposomes ($\geq 1/50$ SiO₂NPs/liposomes number ratio), formed in an aqueous medium with high osmolality. The adhesion of vesicles on the SiO₂NPs surface, driven by Van der Waals attractive forces, is quickly followed by membrane rupture, triggered by the transmembrane gradient of osmotic pressure between the inner aqueous pool of vesicles and the dispersing medium.

M-SiO₂NPs were imaged through Cryogenic electron microscopy (Cryo-EM), with Figure 1a and 1b displaying representative Cryo-EM images at different magnifications. While only very few intact vesicles (see Figure 1a, top part, and section S2.1 for additional images) appear to sit onto the SiO₂

surface, most of SiO₂NPs are either totally (Fig.1b blue arrows) or partially (Fig.1b blue arrows) surrounded by a nanometric layer, closely following the particle morphology, with an electron density that is intermediate between the ones of SiO₂ and the surrounding medium. This layer can be reasonably identified as the bilayer, originally constituting the lipid membrane of vesicles. To gain additional information on the thickness of the surrounding layer, the samples were also imaged by liquid-Atomic Force Microscopy (AFM). Representative AFM images of SiO₂NPs and M-SiO₂NPs are displayed in Figure S2.2, while Figure 1c reports the size distributions obtained for the two samples; the average diameter for the SiO₂NPs is 125 ± 10 nm, while the one of M-SiO₂NPs is 140 ± 15 nm. The 15 nm difference between the two average diameters is compatible with the presence of a lipid bilayer entirely covering most of the particles of the M-SiO₂NP sample.

In addition, we characterized the lipid coating at an ensemble-averaged level, performing DLS and ζ -Potential measurements (Figure 1d). The DLS autocorrelation functions for bare and M-SiO₂NPs (Figure 1d) were analyzed through a cumulant fitting stopped at the second order⁹³. The inset in Figure 1d summarizes the main results. The hydrodynamic diameter of uncoated SiO₂NPs, inferred from the corresponding autocorrelation function, is 165 nm (PDI 0.067). It is worth highlighting that the hydrodynamic size of SiO₂NPs is remarkably larger (~40 nm) than the primary particle diameter determined by AFM, which is in line with previous reports⁹⁴. In contrast, the autocorrelation function of M-SiO₂NPs decays at longer times, consistent with an increase of hydrodynamic diameter up to 210 nm (PDI 0.1), which is compatible with an extensive formation of a lipid bilayer on the SiO₂NPs. Moreover, the characteristic ζ -Potential increases from -40 ± 1 mV (for SiO₂NPs) to -22 ± 1 mV (for M-SiO₂NPs), which is very close to the one of liposomes (-15 ± 1 mV), further confirmation of the effective lipid coverage of the SiO₂NPs' surface.

Lastly, we quantified the extent of the SiO₂ surface covered by the lipid bilayer employing Inductively Coupled Plasma-Atomic Emission Spectrometry (ICP-AES). This technique allows for exact quantification of the Si and P atoms in the final M-SiO₂NPs samples, from which the ratio between the covered and bare SiO₂ surfaces can be inferred through simple geometrical models (see section S5.1 in SI). It is worth stressing that these models heavily rely on specific assumptions about the packing of lipid molecules within the membrane formed on SiO₂ (see section 2.3 of SI); consequently, the technique can only provide a rough estimation of the degree of coverage of the SiO₂NPs surface. Through this approach, a coverage % of 88 ± 8 was estimated for the sample reported in Fig 1.

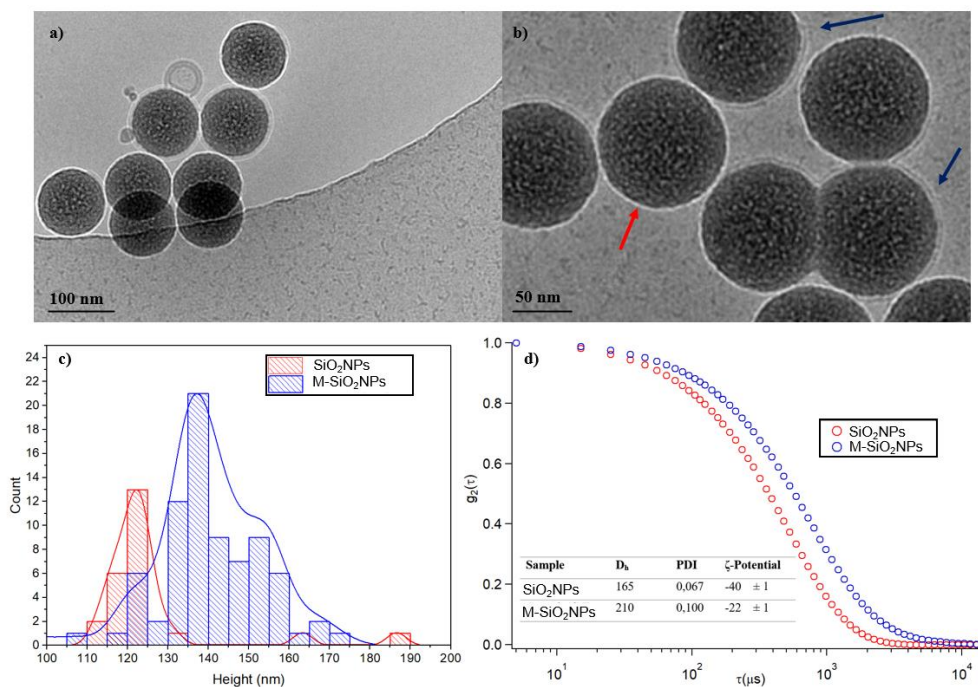


Figure 1. a) and b) Cryo-EM images of M-SiO₂NPs at different magnifications (blue and red arrows identify coated and uncoated areas, respectively); c) Size distribution of SiO₂NPs (red) and M-SiO₂NPs (blue) obtained by liquid-AFM imaging; d) Autocorrelation functions of 0.08 mg/mL water dispersion of

SiO₂NPs (red) and M-SiO₂NPs (blue). The inset shows the hydrodynamic diameter (extrapolated by a cumulant fitting) and the ζ -potential values of each sample.

2.2. *The interaction of M-SiO₂NPs with citrated gold nanoparticles*

Once the formation of M-SiO₂NPs was demonstrated via different complementary techniques as discussed in the previous paragraph, we tested the possibility to probe the lipid layer covering the NPs utilizing the plasmonic properties of AuNPs.

To this purpose, 1.15 nM bare SiO₂NPs (control sample) were first challenged by 6.13 nM Turkevich-Frens AuNPs with an average diameter of 12 nm and -35 mV ζ -Potential (see section S3 of SI for AuNPs characterization), for a final SiO₂NPs/AuNPs number ratio of \sim 1/30. The sample was imaged via Cryo-EM (Figure 2a), showing that AuNPs do not interact with bare SiO₂NPs, which is expected for the electrostatic repulsion between the two inorganic surfaces, both having a highly negative ζ -Potential.

Conversely, when AuNPs are incubated with M-SiO₂NPs under the same conditions, a completely different effect is visible: as shown in Figure 2b (see also section S4.1 for additional images), AuNPs spontaneously cluster on M-SiO₂NPs, forming AuNPs-decorated M-SiO₂NPs composites. This phenomenon, which did not occur with the bare SiO₂NPs, is clearly induced by the presence of a lipid bilayer on the SiO₂ surface, which mediates the adhesion and clustering of AuNPs on M-SiO₂NPs.

Cryo-TEM results were complemented by an ensemble-averaged characterization performed through DLS (see section S4.2 of SI), which provided the mean size and polydispersity of SiO₂NPs/AuNPs and M-SiO₂NPs/AuNPs mixed samples. This characterization showed no interaction between AuNPs and bare SiO₂NPs, testified by the presence of two distinct populations within the SiO₂NPs/AuNPs samples, whose sizes perfectly

matches the ones of free AuNPs (~20 nm) and free SiO₂NPs (~170 nm). In contrast, a single population of bigger size (~230 nm) was detected for M-SiO₂NPs/AuNPs samples, consistent with the formation of composites in which M-SiO₂NPs are decorated by a layer of AuNPs.

Remarkably, the clustering of AuNPs on M-SiO₂NPs led to an evident color change of the AuNPs dispersion from red to purple/blue (see insets of Figures 2c and 2d) within 10 minutes of incubation, which can be noticed by the naked eye and is connected to a variation of AuNPs' plasmonic properties. Conversely, bare SiO₂NPs do not induce significant color variations in the AuNPs' dispersion.

The corresponding spectral variations were quantified by means of UV-Vis spectroscopy (results displayed in Figures 2c and 2d). In line with visual observation, the interaction of AuNPs with bare SiO₂NPs does not significantly alter the plasmonic features of AuNPs, consisting of the characteristic plasmonic primary peak located at 520 nm (red trace). On the contrary, the interaction with M-SiO₂NPs causes a red-shift of the plasmon resonance peak of AuNPs and the occurrence of an additional red-shifted shoulder, a well-established signature of plasmon coupling^{87,95}, consistent with AuNPs aggregation.

As already anticipated, a similar coupling of the plasmons of AuNPs has been observed for AuNPs interacting with natural or synthetic vesicles and conveniently used for determining the concentration, purity and rigidity of such soft objects^{51,96}. Here for the first time, we show that this phenomenon can also be activated on rigid nanoparticles (such as inorganic SiO₂NPs), thanks to the mediating action of a lipid bilayer covering their surface.

The clustering of AuNPs on free-standing bilayers was previously found to be promoted by the bending ability of the lipid membrane^{85,87,95,97}; on the contrary, it was expected to be strongly suppressed (or fully prevented) for

lipid interfaces formed on rigid supports (e.g., the inorganic core of NPs), where membrane bending ability is strongly reduced.

To shed light on this aspect, we directly compared the UV-Vis spectra of AuNPs incubated with M-SiO₂NPs with the ones of AuNPs interacting with liposomes presenting the same membrane composition (see section S4.3 of SI); the results showed that the rigid core of SiO₂ strongly decreases the aggregation of AuNPs on the lipid membrane, without, however, completely preventing it. In fact, the clustering extent of AuNPs on M-SiO₂NPs is sufficient to detect an apparent color change in AuNPs dispersion and, accordingly, a variation in the corresponding UV-Vis absorbance spectra.

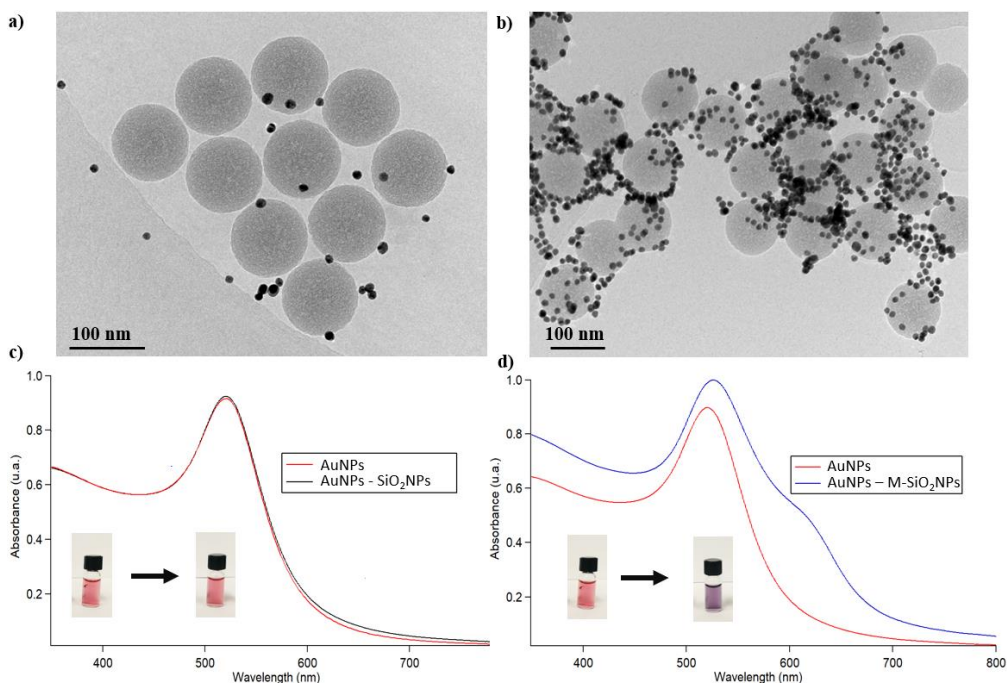


Figure 2. Cryo-EM images of (a) SiO₂NPs - AuNPs (b) M-SiO₂NPs - AuNPs composites and UV-visible spectra of AuNPs incubated with (c) SiO₂NPs and (d) M-SiO₂NPs. The UV-Vis spectrum of bare AuNPs (red curve) is also reported as a control sample. The visual appearance of AuNPs before and after

the incubation with SiO₂NPs and M-SiO₂NPs is reported in the insets of the graphs.

2.3 A nanoplasmonic assay to quantify lipid coverage in M-SiO₂NPs

Having demonstrated that the self-assembly of citrated AuNPs occurs on lipid-coated SiO₂NPs and not on bare ones, we explored how the plasmonic variations of AuNPs are affected by the extent of lipid coverage of the SiO₂NPs.

To this aim, we applied the same transmembrane osmotic shock-based protocol for synthesizing several SiO₂NPs samples with different degrees of coating (see Materials and Methods section). While a NPs/vesicles ratio $\geq 1/50$ is required to obtain an almost full coverage of the silica surface (i.e., ~88%, see previous paragraphs), the coverage extent can be tuned by varying the SiO₂NPs/vesicles ratio during incubation. Employing SiO₂NPs/vesicles ratios of 1/50, 1/15, 1/10, 1/5, 1/3, and 1/1, we realized different hybrids and characterized them through ICP-AES, DLS, and ζ -potential (see section 4.4). Table 1 provides a full overview of such characterization.

Sample	D _h (nm)	PDI	ζ -Potential (mV)	SiO ₂ NPs coverage
Vesicles	115	0.115	-11.2 ± 1.1	/
SiO ₂ NPs	165	0.067	-40.2 ± 0.9	0%
1/50	210	0.100	-22.7 ± 1.3	88 ± 8%
1/15	193	0.122	-26.2 ± 1.2	68 ± 7%
1/10	189	0.164	-28.6 ± 0.7	60 ± 6%
1/5	193	0.152	-30.3 ± 1.4	53 ± 5%
1/3	414	0.363	-37.1 ± 3.2	33 ± 3%
1/1	621	0.335	-36.5 ± 3.5	13 ± 1%

Increasing coverage

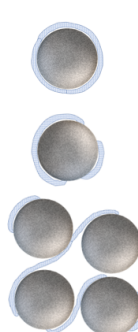


Table 1. Hydrodynamic diameter, ζ -potential values of SiO₂NPs, bare vesicles, and M-SiO₂NPs obtained using different SiO₂NPs-vesicles ratios. The last

column reports the SiO₂NPs coverage percentage, calculated from the concentration of P and Si measured by ICP-AES for each composition (see SI section S2.3). The inset displays a schematic representation of how the coverage affects the size and stability of the hybrids.

The results obtained from ICP-AES measurements were used for a rough estimation of the coating degrees of SiO₂NPs (see SI section S2.3). The coating fraction ranged from 13% to 88% by increasing the number of vesicles employed in the incubation step. The size, colloidal stability, and surface charge of the M-SiO₂NPs with different coating degrees were assessed by DLS and ζ -Potential. The ζ -Potential of the M-SiO₂NPs decreases in a monotonous trend, passing from -23 ± 1 mV for the 1/50 SiO₂NPs/vesicle ratio to -37 ± 4 mV for the 1/1 one, which is very close to the value obtained for bare SiO₂NPs. These results are consistent with an increased extent of particle coverage as the number of vesicles per SiO₂NP increases.

On the other hand, the hydrodynamic size of M-SiO₂NPs (around 200 nm) is stable in the range 1/50 to 1/5 SiO₂NPs/vesicle ratio, while for higher ratios (i.e., 1/3 and 1/1) the samples display an abrupt increase in the size, reaching very high hydrodynamic diameters (400-600 nm) and polydispersity (around 0.3-0.4). For these dispersions, we observed low colloidal stability, with massive precipitation within 1 h from preparation. This observation can be explained considering that, for high SiO₂NPs/vesicle ratios, the coverage on SiO₂NPs is only partial. In agreement with some recent reports, a lipid surface coverage lower than 40% induces abrupt precipitation⁹⁸ due to the presence of membrane patches on the silica surface, triggering the bridging between different -and partially coated- particles^{61,62} (inset in table 1).

In the present case, it is reasonable to assume that, for colloiddally unstable samples, the vesicles' amount is too low to completely coat the available SiO₂ surface, and, therefore, most of the SiO₂NPs will present a

discontinuous surface coverage. The lipid edges of the bilayer patches represent very high-energy spots, which promote interaction with other uncompleted bilayer shells, inducing particle bridging, and precipitation. In this hypothesis, the dispersions' stability, only achieved for lower SiO₂NPs/vesicle ratios (<50%), can be considered an indirect proof of the formation of intact bilayer shells around the surface of a significant fraction of the SiO₂NPs.

We then investigated the interaction of AuNPs with M-SiO₂NPs presenting different coating degrees through UV-vis spectroscopy (Figure 3a). For this purpose, the M-SiO₂NPs were incubated with AuNPs under the same experimental conditions described in section 2.2. The incubation provokes a gradual color variation of the original AuNPs dispersion (see Figure 3a inset), from a ruby red to different shades of purple; this is associated with a broadening of the plasmonic primary signal and the appearance of a red-shifted shoulder (Figure 3a), previously also observed for the 1/50 SiO₂NPs/vesicles sample (section 2.2). Interestingly, the extent of such variations (especially in terms of the intensity of the red-shifted shoulder) depends on the fraction of membrane-covered SiO₂NPs surface. Specifically, the red-shifted shoulder gets gradually more pronounced with increasing membrane coverage.

To characterize the structure of the AuNP aggregates, we performed Synchrotron Small Angle X-Ray Scattering (SAXS) measurements (Elettra, Trieste, Italy). Figure 3b displays the SAXS profiles obtained for the bare AuNPs and M-SiO₂NPs/AuNPs adducts. The scattering signal arises from a form factor $P(q)$, which accounts for the shape and size of the dispersed objects, and from a structure factor $S(q)$, which depends on interparticle interactions. In our experimental conditions, considering the much higher concentration of the AuNPs, the SiO₂NPs contribution to the scattering profiles can be regarded as negligible (see Figure S11 in section S4.4). Therefore, the SAXS profiles shown in Figure 3b are only due to the combination of the $P(q)$ and the $S(q)$ of

AuNPs, providing specific information on their structure and aggregation extent. In particular, in the low- q range ($0.082 < \text{nm}^{-1} < 0.161$), we notice a power-law dependence between the scattering intensity and q , highlighted by a linear trend in a double-log representation of the profiles. For low scattering vectors values, the scattering signal accounts for the morphology of particles and aggregates. According to the Porod approximation⁹⁹, this dependence can be related to the mass fractal dimension of the probed objects, which accounts for the dimensionality of the AuNPs clusters. Specifically, the absolute values of the slopes of the log-log plots can be associated with a Porod coefficient which represents the fractal dimension of the aggregates. The evaluated slope decreases from -0.53 to -1.44 as the membrane coverage increases, as reported in the inset of Figure 3b. In a model-free fashion, such a slope evolution suggests that the aggregation of AuNPs creates larger and more densely packed clusters with increasing SiO₂NPs coverage. Overall, the structural information gained from the SAXS profiles strongly agrees with the plasmonic variations monitored in the UV-Vis spectra.

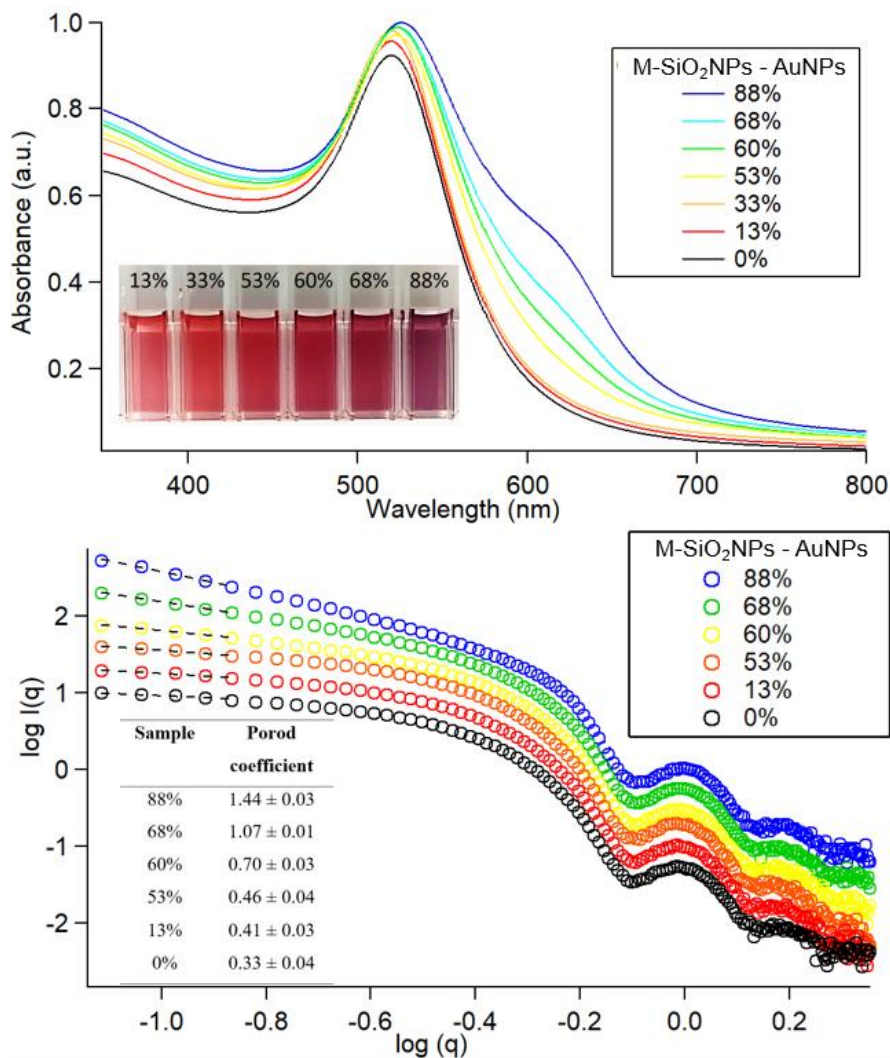


Figure 3. (Top) UV-visible spectra of 6.13 nM AuNPs interacting with 1.15 nM M-SiO₂NPs with different degrees of coverage, collected after 10 min of incubation; (bottom) SAXS profiles of M-SiO₂NPs -AuNPs mixtures with varying degrees of SiO₂NPs membrane coverage collected after 10 minutes of incubation. The inset displays the Porod coefficients extracted from the linear fits (dashed black lines) of the double log plots.

The results from SAXS and UV-Vis show that AuNPs clustering on M-SiO₂NPs is spontaneous and strictly modulated by the coated surface fraction

of SiO₂NPs. The plasmonic properties of AuNPs conveniently monitor such dependence, through both color and spectral variations of the AuNPs/M-SiO₂NPs dispersion. It is then possible to infer the coating degree from a colorimetric assay by introducing a quantitative descriptor of the plasmonic variations of the AuNPs dispersion.

To this aim, we selected an optical index recently used to quantify the variation of optical properties of AuNPs dispersions in the presence of synthetic free-standing vesicles¹⁰⁰. This aggregation index (A.I.) is calculated by dividing the area subtended by the absorbance spectrum in the 560–800 nm range by the total spectral range area (350–800 nm). The results are then normalized for the A.I. of neat AuNPs, so that the A.I. of neat AuNPs' dispersion is equal to 1 and, increasing the particle aggregation, the A.I. value increases. Table 2 summarizes the A.I.s for each M-SiO₂NPs /AuNPs sample, where the coating degrees vary.

SiO₂NPs coverage	A.I.
88%	1.81 ± 0.05
68%	1.63 ± 0.04
60%	1.45 ± 0.03
53%	1.35 ± 0.02
33%	1.14 ± 0.01
13%	1.07 ± 0.02
0%	1

Table 2. *A.I. values obtained for each different membrane coverage of SiO₂NPs.*

Figure 4 shows the so-determined A.I. values plotted *versus* the membrane coverage % of SiO₂NPs (inferred quantitatively by ICP-AES).

While the gradual color variation of AuNPs (bottom inset in figure 4) can already provide some qualitative hints on the degree of membrane coverage, the A.I. and the coverage extent of SiO₂NPs are linked by a precise functional relation, which paves the way for developing a spectrophotometric assay for the quantitative determination of membrane coverage. Specifically, the A.I. increases linearly with membrane coverage (r-squared 0.98) over a wide range of coating yields (35-90%). The fitting accuracy decreases when SiO₂NPs with a coverage <35% are included in the linear regression, yielding an r-squared of 0.95 (see section 5.2 of SI). This is probably due to the poor colloidal stability of the M-SiO₂NPs in low coverage conditions, leading to uncontrolled precipitation of M-SiO₂NPs/AuNPs complexes (see Fig. S14 of SI for the correlation between the hydrodynamic size of M-SiO₂NPs and the optical response of AuNPs).

While several qualitative methods (e.g., colloidal stability tests⁶⁵, and sodium dodecyl sulfate-polyacrylamide gel electrophoresis⁷²) can easily detect a very poor (<35%) or absent coverage on NPs, this approach offers a precise -and quantitative- determination of membrane integrity at intermediate and/or high membrane coverage levels, which represents the compositional range of interest for the application of NPs in the biomedical field; as a matter of fact, most of the membrane-related surface functionalities of NPs vanish at low coverages⁶⁶⁻⁶⁸, while only higher levels of coverage ensure colloidal stability^{60,62} of NPs and partial (or complete) preservation of the biological functions⁶⁵ of their membrane shell.

Moreover, it is worth noticing that, since the aggregation of AuNPs is induced by the presence of the lipid bilayer coating, the assay does not depend on the chemical nature of the nanoparticles' inorganic core and could be extended to NPs with different compositions and physicochemical features.

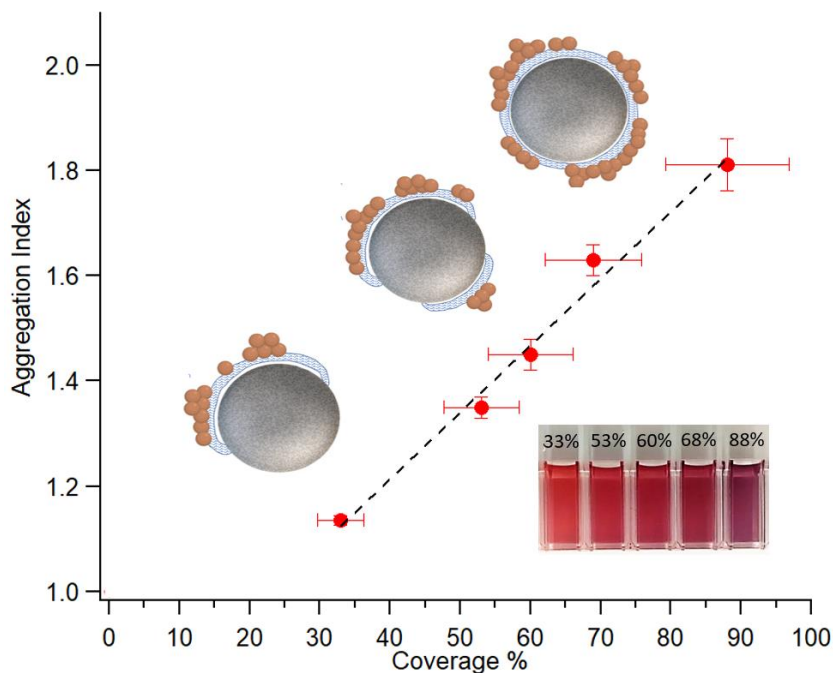


Figure 4. A.I. as a function of SiO_2NPs membrane coverage, with sketches of $\text{AuNPs}/\text{M-SiO}_2$ hybrids highlighting how the integrity of the membrane coating affects AuNPs binding and aggregation. Inset: visual appearance of AuNPs incubated with SiO_2NPs at different membrane coverages.

3. Conclusion

In the last years, the production of lipid bilayer-coated materials has proved a powerful approach to increase the biocompatibility of inorganic NPs, reduce adverse side effects, and improve their efficiency. To reach this overarching goal, high-fidelity structural control and the availability of analytical methods amenable for scale-up production are critical. Here we described a straightforward and quantitative assay for determining the extent biomimetic lipid bilayer coverage on inorganic nanoparticles. Based on previous works, we leveraged the plasmonic properties of Turkevich-Frens AuNPs and their sensitivity to the AuNP aggregation extent to develop an

effective method for the quantification of lipid membrane coating on inorganic NPs. By challenging SiO₂NPs of different -and known- lipid coverage degrees with AuNPs, we show that, in the region of colloidal stability, the plasmonic descriptor of AuNPs' optical properties linearly varies with the amount of lipid coverage and that this dependence can be leveraged for estimating the coverage extent.

As a difference from the already available methods^{69-71,76-78}, such assay provides a fast and high-throughput readout of membrane integrity at an ensemble-averaged level, which only requires cheap reagents, standard lab instrumentation, and limited users experience.

From a different -but equally important- perspective, we also showed that a lipid membrane can drive and control the self-assembly of AuNPs on an inorganic nanosized scaffold, which enables the possibility to create complex hybrid materials composed of an inorganic core, a lipid bilayer shell and a further plasmonic shell of tuneable optical properties. The easiness of preparation, which exploits the spontaneous self-assembly of AuNPs, can inspire the production of multicomponent biocompatible nanomaterials with high structural fidelity and mild experimental conditions.

4. Experimental Section/Methods

4.1 Materials

Tetrachloroauric (III) acid and trisodium citrate dihydrate were provided by Sigma-Aldrich (St. Louis, MO). 1,2-Dioleoyl-sn-glycero-3-phosphocholine (DOPC), N-palmitoyl-D-erythro-sphingosylphosphorylcholine (sphingomyelin) and cholesterol were provided by Avanti Polar Lipids. Sucrose, sodium chloride (NaCl), sodium citrate, and calcium chloride (CaCl₂) were provided by Sigma Aldrich. All chemicals were used as received. Milli-Q-grade water was used in all preparations. Silica Nanoparticles were provided by HiQ-Nano (Arnesano, Lecce, Italy) and are stable in an aqueous buffer and

are characterized by a hydrophilic surface with terminal Si-OH functional groups.

4.2 Preparation of SiO₂ NPs

The commercial batch was thoroughly homogenized by vortexing, followed by 30 min bath sonication before use. Subsequently, it was diluted in milliQ water to obtain a final SiO₂ concentration of 1.6 mg/mL right before mixing with liposomes.

4.3 Preparation of liposomes

To prepare the EVs-mimicking liposomes, the proper amount of DOPC, Sphingomyelin, and cholesterol was dissolved in chloroform (0.87/0.37/1 mol%/mol%), and a lipid film was obtained by evaporating the solvent under a stream of nitrogen and overnight vacuum drying. The film was then swollen and suspended in a warm (40 °C) water solution of sucrose (650 mM), sodium chloride (150 mM), and sodium citrate (10 mM) by vigorous vortex mixing to obtain a final lipid concentration of 7 mg/ml. The resultant multilamellar vesicles (MVL) in water were subjected to 10 freeze–thaw cycles and extruded 10 times through two stacked polycarbonate membranes with a 100 nm pore size at room temperature to obtain unilamellar vesicles (ULV) with a narrow and reproducible size distribution. The filtration was performed with the Extruder (Lipex Biomembranes, Vancouver, Canada) through Nucleopore membranes.

4.4 Preparation of membrane-coated Silica Nanoparticles (M-SiO₂NPs)

To prepare fully coated SiO₂-NPs, 1 mL of a dispersion of uncoated SiO₂-NPs in ultrapure water (1.6 mg/mL) was mixed with 1 mL of liposomes dispersion (7 mg/mL) at high stoichiometric excess of liposomes (approximately 1/50 SiO₂-NPs/liposomes number ratio), formed in an aqueous environment with high osmolality (650 mM sucrose, 10 mM Sodium Citrate, 150 mM NaCl, 10 mM CaCl₂). The formation of the lipid coating on SiO₂NPs starts with the

adhesion of the vesicles on the SiO₂NPs surface due to Van der Waals interactions; this is followed by membrane rupture driven by the transmembrane gradient of osmotic pressure between the inner aqueous pool and the dispersing medium (SiO₂NPs were initially dispersed in ultrapure water). The excess of intact liposomes was then removed through centrifugation (6000 rpm x 30 min each), after which the supernatant was discarded, and the precipitate (containing M-SiO₂NPs) collected and redispersed in ultrapure water. This last step was repeated 6 times to fully remove the excess of intact vesicles. To account for possible material loss during the centrifugation cycles, the final concentration of M-SiO₂NPs was quantified by ICP-AES (see section S2.3).

To prepare M-SiO₂-NPs with different degrees of coverage we employed the same protocol varying the initial SiO₂NPs/vesicle ratio. Specifically, 1 mL SiO₂-NPs in ultrapure water (1.6 mg/mL) was mixed with 1 mL of liposomes properly diluted to obtain SiO₂NPs/vesicle ratios of approximately 1/15, 1/10, 1/5, 1/3, and 1/1. The intact liposomes were removed through centrifugation (6000 rpm x 30 min each), and the precipitate was collected and redispersed in 1 mL of ultrapure water.

4.5 Synthesis of AuNPs

Anionic gold nanospheres (AuNPs) of 12 nm in size were synthesized according to the Turkevich–Frens method.^{101,102} Briefly, 20 mL of a 1 mM HAuCl₄ aqueous solution was brought to the boiling temperature under constant and vigorous magnetic stirring. 2 mL of a 1% citric acid solution were then added to the mixture. The solution was further boiled for 10 min until it acquired a deep red color. The nanoparticle solution was then slowly cooled to room temperature.

4.6 Cryo-EM

3 μL of each sample at a SiO_2NPs concentration of 1.15 nm were applied on glow-discharged Quantifoil Cu 300 R2/2 grids. The samples were plunge frozen in liquid ethane using an FEI Vitrobot Mark IV (Thermo Fisher Scientific) instrument. The excess liquid was removed by blotting for 1 s (blot force of 1) using filter papers under 100% humidity and at 10 $^\circ\text{C}$. Cryo-EM data were collected at the Florence Center for Electron Nanoscopy (FloCEN), University of Florence (Italy), on a Glacios (Thermo Fisher Scientific) instrument at 200 kV equipped with a Falcon III detector operated in the counting mode. Images were acquired using EPU software with a physical pixel size of 2.5 \AA and a total electron dose of $\sim 50 \text{ e}^-/\text{\AA}^2$ per micrograph.

4.7 Atomic Force Microscopy (AFM)

NPs were deposited on top of poly-L-lysine (PLL) coated glass coverslips. All reagents were purchased from Sigma-Aldrich Inc (www.sigmaaldrich.com) unless otherwise stated. Menzel Gläser coverslips were cleaned in Piranha solution for 2h and washed in a sonicator bath (Elmasonic Elma S30H) for 30' in acetone, followed by 30' in isopropanol and 30' in ultrapure water (Millipore Simplicity UV). Before each experiment, glass coverslips were treated with air plasma (Pelco Easiglow) and immersed into a 0.01 mg/mL PLL solution in Borate buffer (pH 8.33) at room temperature for 30 minutes. After being thoroughly rinsed with ultrapure water and dried with nitrogen, the coverslips were ready to be used for the AFM experiments. A 10 μl droplet of the SiO_2NPs dispersion was deposited on top of the coverslips and left equilibrating for 15 minutes before being inserted into the AFM fluid cell. The concentrations of SiO_2NP dispersions were adjusted via trial and error to avoid the formation of NP-clusters, which would ultimately prevent the quantitative determination of their morphology. AFM experiments were performed in PeakForce mode at room temperature on a Bruker Multimode 8 equipped with Nanoscope V electronics, a sealed fluid cell, a type JV piezoelectric scanner

and Bruker SNL10-A probes (with nominal tip radius 2-12 nm and spring constant 0.35 N/m), calibrated according to the thermal noise method¹⁰³. A 50 mM MgCl₂, 100 mM KCl solution was used as imaging buffer in order to reduce the electrical double layer (EDL) interaction region between the AFM tip and the NPs¹⁰⁴. NP height was used to obtain the respective size distributions; given that NPs are spherical rigid objects, their height coincides with the NP diameter and being unaffected by tip convolution effects, represents a reliable parameter for size estimation.

4.8 Dynamic Light Scattering (DLS) and ζ -Potential

DLS measurements at $\theta = 90^\circ$ and the ζ -potential determination were performed using a Brookhaven Instrument 90 Plus (Brookhaven, Holtsville, NY). Each measurement was an average of 10 repetitions of 1 min each, and measurements were repeated 10 times. The autocorrelation functions (ACFs) were analyzed through cumulant fitting stopped at the second order for samples characterized by a single monodisperse population, allowing an estimate of the hydrodynamic diameter of particles and the polydispersity index. ζ -potentials were obtained from the electrophoretic mobility u according to the Helmholtz–Smoluchowski equation $\zeta = \left(\frac{\eta}{\epsilon}\right) \times \mu$ (1), where η is the viscosity of the medium and ϵ is the dielectric permittivity of the dispersing medium. The ζ -potential values are reported as averages from 10 measurements.

4.9 Inductively Coupled Plasma - Atomic Emission Spectrometry (ICP-AES)

The determination of Si and P content in the samples was performed in triplicate by using a Varian 720-ES Inductively Coupled Plasma Atomic Emission Spectrometer (ICP-AES). An accurately measured amount of each sample was diluted to a final volume of 5 mL with 1% suprapure HNO₃ obtained by sub-boiling distillation. Each sample was thus spiked with 100 μ L of Ge 50 mg/L standard solution used as the internal standard. Calibration

standards were prepared by gravimetric serial dilution from a commercial stock standard solution of Si and P at 1000 mg L⁻¹. The analytic wavelengths used for Si and P determination were 251.611 and 213.618 nm, respectively, whereas for Ge we used the line at 209.426 nm. The operating conditions were optimized to obtain the maximum signal intensity, and between each sample, a rinse solution constituted of 2% v/v HNO₃ was used to avoid memory effects.

4.10 UV-vis spectroscopy

UV-vis spectra were recorded with a Cary 3500 UV-vis spectrophotometer. 50 μL of either naked SiO₂NPs or M-SiO₂NPs (at a SiO₂ concentration of 1.15 nM with different degrees of coverage) were mixed with 300 μL of 6.13 nM AuNPs and incubated for 10 minutes at room temperature in PMMA UV-vis micro cuvettes (maximum volume 1.5 mL). Then, 700 μL of MilliQ water were added to the samples and after 10 minutes, the spectra were simultaneously recorded with a multiple sample holder in the spectral range 350-800 nm.

4.11 Small Angle X-ray Scattering

M-SiO₂NPs - AuNPs hybrids were characterized at the SAXS beamline of the synchrotron radiation source Elettra (Trieste, Italy), which was operated at 2 GeV and a 300mA ring current. The experiments were carried out with $\lambda = 1.5 \text{ \AA}$, and the SAXS signal was detected with a Pilatus 3 1M detector in the q-range from 0.009 to 0.7 \AA^{-1} . The SAXS curves were recorded in a glass capillary.

Acknowledgments

This work has been supported by the European Community through the BOW project (H2020-EIC-FETPROACT2019, ID 952183). We also acknowledge MIUR-Italy (“Progetto Dipartimenti di Eccellenza 2018–2022, ref B96C1700020008”) allocated to the Department of Chemistry “Ugo Schiff”) and Ente Cassa di Risparmio di Firenze for economic support. The Elettra

Synchrotron SAXS facility (Basovizza, Trieste, Italy) is acknowledged for beam time. We acknowledge the Florence Center for Electron Nanoscopy (FloCEN) at the University of Florence.

References

- 1 S. Gavas, S. Quazi and T. M. Karpiński, *Nanoscale Res. Lett.*, 2021, **16**, 173.
- 2 S. Hua, M. B. C. de Matos, J. M. Metselaar and G. Storm, *Front. Pharmacol.*, DOI:10.3389/fphar.2018.00790.
- 3 M. Henriksen-Lacey, S. Carregal-Romero and L. M. Liz-Marzán, *Bioconjug. Chem.*, 2017, **28**, 212–221.
- 4 M. Hofmann-Antenbrink, D. W. Grainger and H. Hofmann, *Nanomedicine Nanotechnology, Biol. Med.*, 2015, **11**, 1689–1694.
- 5 S. Barua and S. Mitragotri, *Nano Today*, 2014, **9**, 223–243.
- 6 E. Pedziwiatr-Werbicka, K. Horodecka, D. Shcharbin and M. Bryszewska, *Curr. Med. Chem.*, 2020, **28**, 346–359.
- 7 X. Zhen, P. Cheng and K. Pu, *Small*, 2019, **15**, 1–19.
- 8 M. Wu, W. Le, T. Mei, Y. Wang, B. Chen, Z. Liu and C. Xue, *Int. J. Nanomedicine*, 2019, **Volume 14**, 4431–4448.
- 9 R. H. Fang, C. M. J. Hu, B. T. Luk, W. Gao, J. A. Copp, Y. Tai, D. E. O'Connor and L. Zhang, *Nano Lett.*, 2014, **14**, 2181–2188.
- 10 L. Zhang, X. Zhang, G. Lu, F. Li, W. Bao, C. Song, W. Wei and G. Ma, *Small*, 2019, **15**, 1–13.
- 11 M. Zhou, Y. Xing, X. Li, X. Du, T. Xu and X. Zhang, *Small*, 2020, **16**, 1–11.
- 12 M. M. Van Schooneveld, E. Vucic, R. Koole, Y. Zhou, J. Stocks, D. P. Cormode, C. Y. Tang, R. E. Gordon, K. Nicolay, A. Meijerink, Z. A. Fayad and W. J. M. Mulder, *Nano Lett.*, 2008, **8**, 2517–2525.
- 13 A. Luchini and G. Vitiello, *Front. Chem.*, 2019, **7**, 1–16.

- 14 J. Yang, J. Tu, G. E. M. Lamers, R. C. L. Olsthoorn and A. Kros, *Adv. Healthc. Mater.*, 2017, **6**, 1–7.
- 15 K. S. Butler, P. N. Durfee, C. Theron, C. E. Ashley, E. C. Carnes and C. J. Brinker, *Small*, 2016, **12**, 2173–2185.
- 16 G. D. Bothun, *J. Nanobiotechnology*, 2008, **6**, 1–10.
- 17 M. Sancho-Albero, M. del M. Encabo-Berzosa, M. Beltrán-Visiedo, L. Fernández-Messina, V. Sebastián, F. Sánchez-Madrid, M. Arruebo, J. Santamaría and P. Martín-Duque, *Nanoscale*, 2019, **11**, 18825–18836.
- 18 M. Sancho-Albero, B. Rubio-Ruiz, A. M. Pérez-López, V. Sebastián, P. Martín-Duque, M. Arruebo, J. Santamaría and A. Unciti-Broceta, *Nat. Catal.*, 2019, **2**, 864–872.
- 19 C.-M. J. Hu, L. Zhang, S. Aryal, C. Cheung, R. H. Fang and L. Zhang, *Proc. Natl. Acad. Sci.*, 2011, **108**, 10980–10985.
- 20 C. Ferrel, S. Rayamajhi, T. Nguyen, R. Marasini, T. Saravanan, F. Deba and S. Aryal, *ACS Appl. Bio Mater.*, 2021, **4**, 6974–6981.
- 21 J. Peng, Q. Yang, W. Li, L. Tan, Y. Xiao, L. Chen, Y. Hao and Z. Qian, *ACS Appl. Mater. Interfaces*, 2017, **9**, 44410–44422.
- 22 Q. Pei, X. Hu, X. Zheng, S. Liu, Y. Li, X. Jing and Z. Xie, *ACS Nano*, 2018, **12**, 1630–1641.
- 23 J. P. Thawani, A. Amirshaghghi, L. Yan, J. M. Stein, J. Liu and A. Tsourkas, *Small*, 2017, **13**, 1–9.
- 24 S. Krishnamurthy, M. K. Gnanasammandhan, C. Xie, K. Huang, M. Y. Cui and J. M. Chan, *Nanoscale*, 2016, **8**, 6981–6985.
- 25 H. Zhao, L. Li, J. Zhang, C. Zheng, K. Ding, H. Xiao, L. Wang and Z. Zhang, *ACS Appl. Mater. Interfaces*, 2018, **10**, 31124–31135.
- 26 L. Rao, Z. He, Q.-F. Meng, Z. Zhou, L.-L. Bu, S.-S. Guo, W. Liu and X.-Z. Zhao, *J. Biomed. Mater. Res. Part A*, 2017, **105**, 521–530.
- 27 Z. Chen, P. Zhao, Z. Luo, M. Zheng, H. Tian, P. Gong, G. Gao, H. Pan, L. Liu, A. Ma, H. Cui, Y. Ma and L. Cai, *ACS Nano*, 2016, **10**,

10049–10057.

- 28 C. Liu, D. Wang, S. Zhang, Y. Cheng, F. Yang, Y. Xing, T. Xu, H. Dong and X. Zhang, *ACS Nano*, 2019, **13**, 4267–4277.
- 29 J.-Y. Zhu, D.-W. Zheng, M.-K. Zhang, W.-Y. Yu, W.-X. Qiu, J.-J. Hu, J. Feng and X.-Z. Zhang, *Nano Lett.*, 2016, **16**, 5895–5901.
- 30 Z. Gao, L. Zhang, J. Hu and Y. Sun, *Nanomedicine Nanotechnology, Biol. Med.*, 2013, **9**, 174–184.
- 31 X. Geng, D. Gao, D. Hu, Q. Liu, C. Liu, Z. Yuan, X. Zhang, X. Liu, Z. Sheng, X. Wang and H. Zheng, *ACS Appl. Mater. Interfaces*, 2020, **12**, 55624–55637.
- 32 Q. Jiang, K. Wang, X. Zhang, B. Ouyang, H. Liu, Z. Pang and W. Yang, *Small*, 2020, **16**, 2001704.
- 33 C.-H. Luo, C.-T. Huang, C.-H. Su and C.-S. Yeh, *Nano Lett.*, 2016, **16**, 3493–3499.
- 34 D. T. Riglar and P. A. Silver, *Nat. Rev. Microbiol.*, 2018, **16**, 214–225.
- 35 V. Gujrati, S. Kim, S.-H. Kim, J. J. Min, H. E. Choy, S. C. Kim and S. Jon, *ACS Nano*, 2014, **8**, 1525–1537.
- 36 T. Kang, Q. Zhu, D. Wei, J. Feng, J. Yao, T. Jiang, Q. Song, X. Wei, H. Chen, X. Gao and J. Chen, *ACS Nano*, 2017, **11**, 1397–1411.
- 37 Y. Fu, G. He, Z. Liu, J. Wang, M. Li, Z. Zhang, Q. Bao, J. Wen, X. Zhu, C. Zhang and W. Zhang, 2022, **2202337**, 1–11.
- 38 J. Li, X. Zhen, Y. Lyu, Y. Jiang, J. Huang and K. Pu, *ACS Nano*, 2018, **12**, 8520–8530.
- 39 L. Rao, B. Cai, L.-L. Bu, Q.-Q. Liao, S.-S. Guo, X.-Z. Zhao, W.-F. Dong and W. Liu, *ACS Nano*, 2017, **11**, 3496–3505.
- 40 X. Zhen, P. Cheng and K. Pu, *Small*, 2019, **15**, 1804105.
- 41 L. Zhu, Y. Zhong, S. Wu, M. Yan, Y. Cao, N. Mou, G. Wang, D. Sun and W. Wu, *Mater. Today Bio*, 2022, **14**, 100228.
- 42 J. R. Fitzgerald, T. J. Foster and D. Cox, *Nat. Rev. Microbiol.*, 2006, **4**,

445–457.

- 43 C.-M. J. Hu, R. H. Fang, J. Copp, B. T. Luk and L. Zhang, *Nat. Nanotechnol.*, 2013, **8**, 336–340.
- 44 Q. Zhang, D. Dehaini, Y. Zhang, J. Zhou, X. Chen, L. Zhang, R. H. Fang, W. Gao and L. Zhang, *Nat. Nanotechnol.*, 2018, **13**, 1182–1190.
- 45 R. H. Fang, C.-M. J. Hu, B. T. Luk, W. Gao, J. A. Copp, Y. Tai, D. E. O'Connor and L. Zhang, *Nano Lett.*, 2014, **14**, 2181–2188.
- 46 H.-W. Chen, Z.-S. Fang, Y.-T. Chen, Y.-I. Chen, B.-Y. Yao, J.-Y. Cheng, C.-Y. Chien, Y.-C. Chang and C.-M. J. Hu, *ACS Appl. Mater. Interfaces*, 2017, **9**, 39953–39961.
- 47 P. Fathi, L. Rao and X. Chen, *View*, 2021, **2**, 20200187.
- 48 R. Van Der Meel, M. H. A. M. Fens, P. Vader, W. W. Van Solinge, O. Eniola-Adefeso and R. M. Schiffelers, *J. Control. Release*, 2014, **195**, 72–85.
- 49 G. Raposo and W. Stoorvogel, *J. Cell Biol.*, 2013, **200**, 373–383.
- 50 H. Saari, E. Lázaro-Ibáñez, T. Viitala, E. Vuorimaa-Laukkanen, P. Siljander and M. Yliperttula, *J. Control. Release*, 2015, **220**, 727–737.
- 51 S. Busatto, A. Giacomini, C. Montis, R. Ronca and P. Bergese, *Anal. Chem.*, 2018, **90**, 7855–7861.
- 52 S. Kamerkar, V. S. LeBleu, H. Sugimoto, S. Yang, C. F. Ruivo, S. A. Melo, J. J. Lee and R. Kalluri, *Nature*, 2017, **546**, 498–503.
- 53 S. EL Andaloussi, I. Mäger, X. O. Breakefield and M. J. A. Wood, *Nat. Rev. Drug Discov.*, 2013, **12**, 347–357.
- 54 S. EL Andaloussi, S. Lakhali, I. Mäger and M. J. A. Wood, *Adv. Drug Deliv. Rev.*, 2013, **65**, 391–397.
- 55 M. J. Haney, N. L. Klyachko, Y. Zhao, R. Gupta, E. G. Plotnikova, Z. He, T. Patel, A. Piroyan, M. Sokolsky, A. V. Kabanov and E. V. Batrakova, *J. Control. Release*, 2015, **207**, 18–30.
- 56 O. M. Elsharkasy, J. Z. Nordin, D. W. Hagey, O. G. de Jong, R. M.

- Schiffelers, S. EL Andaloussi and P. Vader, *Adv. Drug Deliv. Rev.*, 2020, **159**, 332–343.
- 57 C. Liu, W. Zhang, Y. Li, J. Chang, F. Tian, F. Zhao, Y. Ma and J. Sun, *Nano Lett.*, 2019, **19**, 7836–7844.
- 58 G. Cheng, W. Li, L. Ha, X. Han, S. Hao, Y. Wan, Z. Wang, F. Dong, X. Zou, Y. Mao and S.-Y. Zheng, *J. Am. Chem. Soc.*, 2018, **140**, 7282–7291.
- 59 J. Wang, Y. Dong, Y. Li, W. Li, K. Cheng, Y. Qian, G. Xu, X. Zhang, L. Hu, P. Chen, W. Du, X. Feng, Y. Di Zhao, Z. Zhang and B. F. Liu, *Adv. Funct. Mater.*, 2018, **28**, 1–14.
- 60 A. H. Bahrami, M. Raatz, J. Agudo-canalejo, R. Michel, E. M. Curtis, C. K. Hall, M. Gradzielski, R. Lipowsky, T. R. Weigl, M. Raphael, C. E. M. H. C. K, G. Michael and L. Rein-, *Adv. Colloid Interface Sci.*, , DOI:10.1016/j.cis.2014.02.012.
- 61 R. Michel and M. Gradzielski, *Int. J. Mol. Sci.*, 2012, **13**, 11610–11642.
- 62 S. Mornet, O. Lambert, E. Duguet and A. Brisson, *Nano Lett.*, 2005, **5**, 281–285.
- 63 J. Liu, X. Jiang, C. Ashley and C. J. Brinker, *J. Am. Chem. Soc.*, 2009, **131**, 7567–7569.
- 64 J. Van Deun, Q. Roux, S. Deville, T. Van Acker, P. Rappu, I. Miinalainen, J. Heino, F. Vanhaecke, B. G. De Geest, O. De Wever and A. Hendrix, *Cells*, 2020, **9**, 1797.
- 65 L. Liu, X. Bai, M.-V. Martikainen, A. Kårlund, M. Roponen, W. Xu, G. Hu, E. Tasciotti and V.-P. Lehto, *Nat. Commun.*, 2021, **12**, 5726.
- 66 M. Hadjidemetriou, Z. Al-Ahmady, M. Mazza, R. F. Collins, K. Dawson and K. Kostarelos, *ACS Nano*, 2015, **9**, 8142–8156.
- 67 F. Persson, J. Fritzsche, K. U. Mir, M. Modesti, F. Westerlund and J. O. Tegenfeldt, *Nano Lett.*, 2012, **12**, 2260–2265.

- 68 R. C. Van Lehn, M. Ricci, P. H. J. Silva, P. Andreozzi, J. Reguera, K. Voitchovsky, F. Stellacci and A. Alexander-Katz, *Nat. Commun.*, 2014, **5**, 4482.
- 69 A. E. LaBauve, T. E. Rinker, A. Nouredine, R. E. Serda, J. Y. Howe, M. B. Sherman, A. Rasley, C. J. Brinker, D. Y. Sasaki and O. A. Negrete, *Sci. Rep.*, 2018, **8**, 13990.
- 70 D. B. Tada, E. Suraniti, L. M. Rossi, C. A. P. Leite, C. S. Oliveira, T. C. Tumolo, R. Calemczuk, T. Livache and M. S. Baptista, *J. Biomed. Nanotechnol.*, 2014, **10**, 519–528.
- 71 C. Gao, Q. Huang, C. Liu, C. H. T. Kwong, L. Yue, J.-B. Wan, S. M. Y. Lee and R. Wang, *Nat. Commun.*, 2020, **11**, 2622.
- 72 W. Liu, M. Zou, T. Liu, J. Zeng, X. Li, W. Yu, C. Li, J. Ye, W. Song, J. Feng and X. Zhang, *Nat. Commun.*, 1–12.
- 73 L. Zhang, Y. Zhu, X. Wei, X. Chen, Y. Li, Y. Zhu, J. Xia, Y. Huang, Y. Huang, J. Wang and Z. Pang, *Acta Pharm. Sin. B*, 2022, **12**, 3427–3447.
- 74 J. Zhuang, H. Gong, J. Zhou, Q. Zhang and W. Gao, ,
- 75 W. Liu, M. Zou, T. Liu, J. Zeng, X. Li, W. Yu and C. Li, 2019, **1900499**, 1–10.
- 76 L. P. Arnett, M. W. Forbes, R. Keunen and M. A. Winnik, *Langmuir*, 2021, **37**, 14605–14613.
- 77 J. Y. Lee, H. Wang, G. Pyrgiotakis, G. M. DeLoid, Z. Zhang, J. Beltran-Huarac, P. Demokritou and W. Zhong, *Anal. Bioanal. Chem.*, 2018, **410**, 6155–6164.
- 78 X. Zhang, A. K. Pandiakumar, R. J. Hamers and C. J. Murphy, , DOI:10.1021/acs.analchem.8b03911.
- 79 K. Sugikawa, T. Kadota, K. Yasuhara and A. Ikeda, *Angew. Chemie - Int. Ed.*, 2016, **55**, 4059–4063.
- 80 F. Wang and J. Liu, *Nanoscale*, 2015, **7**, 15599–15604.

- 81 F. Wang, D. E. Curry and J. Liu, *Langmuir*, 2015, **31**, 13271–13274.
- 82 C. Montis, D. Maiolo, I. Alessandri, P. Bergese and D. Berti, *Nanoscale*, 2014, **6**, 6452–6457.
- 83 S. Salassi, L. Caselli, J. Cardellini, E. Lavagna, C. Montis, D. Berti and G. Rossi, *J. Chem. Theory Comput.*, , DOI:10.1021/acs.jctc.1c00627.
- 84 J. Cardellini, C. Montis, F. Barbero, I. De Santis, L. Caselli and D. Berti, *Front. Bioeng. Biotechnol.*, 2022, **10**, 1–15.
- 85 C. Montis, L. Caselli, F. Valle, A. Zandrini, F. Carlà, R. Schweins, M. Maccarini, P. Bergese and D. Berti, *J. Colloid Interface Sci.*, 2020, **573**, 204–214.
- 86 J. Cardellini, L. Caselli, E. Lavagna, S. Salassi, H. Amenitsch, M. Calamai, C. Montis, G. Rossi and D. Berti, *J. Phys. Chem. C*, 2022, **126**, 4483–4494.
- 87 L. Caselli, A. Ridolfi, J. Cardellini, L. Sharpnack, L. Paolini, M. Brucale, F. Valle, C. Montis, P. Bergese and D. Berti, *Nanoscale Horizons*, , DOI:10.1039/d1nh00012h.
- 88 D. Maiolo, L. Paolini, G. Di Noto, A. Zandrini, D. Berti, P. Bergese and D. Ricotta, *Anal. Chem.*, 2015, **87**, 4168–4176.
- 89 J. G. Croissant, K. S. Butler, J. I. Zink and C. J. Brinker, *Nat. Rev. Mater.*, 2020, **5**, 886–909.
- 90 A. Watermann and J. Brieger, *Nanomaterials*, , DOI:10.3390/nano7070189.
- 91 A. Llorente, T. Skotland, T. Sylvänne, D. Kauhanen, T. Róg, A. Orłowski, I. Vattulainen, K. Ekroos and K. Sandvig, *Biochim. Biophys. Acta - Mol. Cell Biol. Lipids*, 2013, **1831**, 1302–1309.
- 92 P. J. Chung, H. L. Hwang, K. Dasbiswas, A. Leong and K. Y. C. Lee, *Langmuir*, 2018, **34**, 13000–13005.
- 93 P. A. Hassan, S. Rana and G. Verma, *Langmuir*, 2015, **31**, 3–12.

- 94 M. Kaasalainen, V. Aseyev, E. von Haartman, D. Ş. Karaman, E. Mäkilä, H. Tenhu, J. Rosenholm and J. Salonen, *Nanoscale Res. Lett.*, 2017, **12**, 74.
- 95 J. Cardellini, L. Caselli, E. Lavagna, S. Salassi, H. Amenitsch, M. Calamai, C. Montis, G. Rossi and D. Berti, *J. Phys. Chem. C*, 2022, **126**, 4483–4494.
- 96 A. Zandrini, L. Paolini, S. Busatto, A. Radeghieri, M. Romano, M. H. M. Wauben, M. J. C. van Herwijnen, P. Nejsun, A. Borup, A. Ridolfi, C. Montis and P. Bergese, *Front. Bioeng. Biotechnol.*, 2020, **7**, 1–10.
- 97 J. Cardellini, C. Montis, F. Barbero, I. De Santis, L. Caselli and D. Berti, *Front. Bioeng. Biotechnol.*, , DOI:10.3389/fbioe.2022.848687.
- 98 S. Savarala, F. Monson, M. A. Ilies and S. L. Wunder, *Langmuir*, 2011, **27**, 5850–5861.
- 99 L. A. Feigin and D. I. Svergun, *Structure Analysis by Small-Angle X-Ray and Neutron Scattering*, Springer US, Boston, MA, 1987.
- 100 L. Caselli, A. Ridolfi, J. Cardellini, L. Sharpnack, L. Paolini, M. Brucale, F. Valle, C. Montis, P. Bergese and D. Berti, *Nanoscale Horizons*, 2021, **6**, 543–550.
- 101 J. Turkevich, P. C. Stevenson and J. Hillier, *Discuss. Faraday Soc.*, 1951, **11**, 55–75.
- 102 G. Frens, *Nat. Phys. Sci.*, 1973, **241**, 20–22.
- 103 J. L. Hutter and J. Bechhoefer, *Rev. Sci. Instrum.*, 1993, **64**, 1868–1873.
- 104 D. J. Müller, D. Fotiadis, S. Scheuring, S. A. Müller and A. Engel, *Biophys. J.*, 1999, **76**, 1101–1111.

Supporting Information for:

Probing the coverage of nanoparticles by biomimetic membranes via nanoplasmonics

Jacopo Cardellini, Andrea Ridolfi, Melissa Donati, Valentina Giampietro, Mirko Severi, Marco Brucale, Francesco Valle Paolo Bergese, Costanza Montis, Lucrezia Caselli, and Debora Berti

	Page
1 Supplementary Characterization of Liposomes	2
<i>1.1 Dynamic Light Scattering and Z-Potential</i>	2
<i>1.2 Evaluation of liposomes concentration</i>	2
2 Supplementary Characterization of Coated SiNPs	4
<i>2.1 Cryo-TEM</i>	4
<i>2.2 Atomic Force microscopy</i>	4
<i>2.3 Evaluation of the degree of coverage</i>	5
3 Supplementary Characterization of AuNPs	6
<i>3.1 Small Angle X-ray Scattering</i>	7
<i>3.2 Dynamic Light Scattering</i>	8
<i>3.3 UV-vis spectroscopy</i>	9
4 Supplementary Characterization of Coated SiNPs/AuNPs hybrids	11
<i>4.1 Cryo-TEM</i>	11
<i>4.2 Dynamic Light Scattering</i>	12
<i>4.3 UV-vis spectroscopy</i>	15
<i>4.4 Small Angle X-ray Scattering</i>	16
5 Supplementary Characterization of Coated SiNPs with different coverage	18
<i>5.1 Dynamic Light Scattering</i>	18
<i>5.2 Nanoplasmonic assay for the quantification of the SiNPs lipid coverage</i>	18
Bibliography	21

1 Supplementary Characterization of Liposomes

1.1 Dynamic Light Scattering and Z-Potential

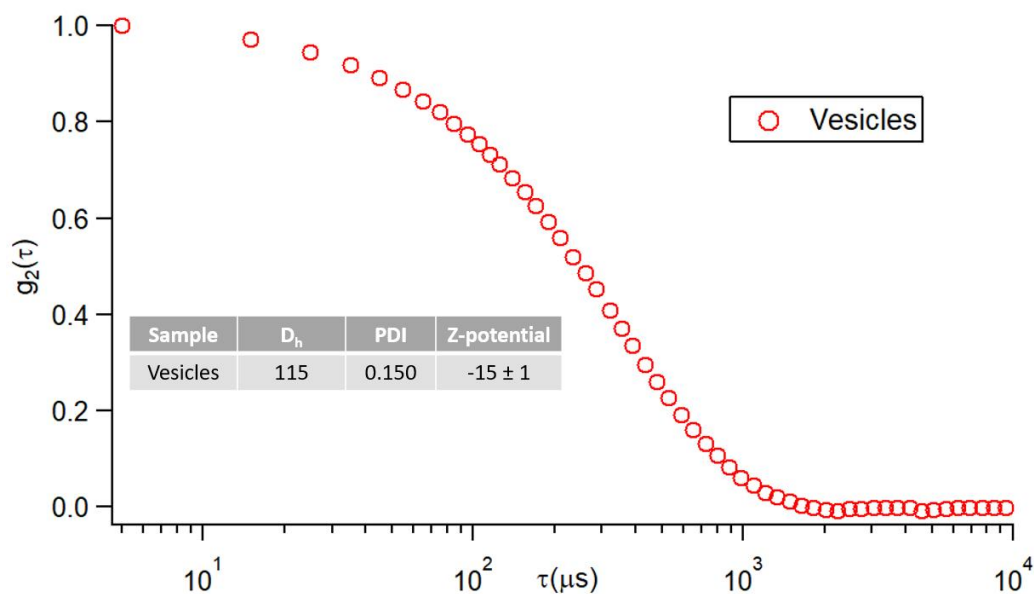


Fig S1: Autocorrelation function collected for the vesicles' dispersion at a concentration of 0.35 mg/mL. The table in the inset shows the hydrodynamic diameter and the polydispersity index (PDI), evaluated with the cumulant analysis, and the surface ζ -potential.

1.2 Evaluation of Liposomes concentration

The lipid concentration in the starting colloidal dispersion was estimated to be 7 mg/mL from the initial lipid and water amounts employed in the formation and swelling of lipid films, assuming the absence of lipid loss due to the extrusion procedure. The liposomes concentration in the final dispersion was subsequently

calculated considering their hydrodynamic diameter (Fig. S1). In particular, the liposomal surface area (surface area= $4\pi r^2$) can be extracted from the liposome diameters; the doubled surface can be subsequently divided by the lipid cross section (approximately 0.5 nm^2) in order to obtain the lipid number per liposome, assuming that approximately one half of the lipids is localized in the external leaflet of a liposome, since the bilayer thickness, about 4-5 nm, is negligible with respect to the liposomes' average diameter. Eventually, the total weighted lipid concentration was divided by the total number of lipids per liposome. A liposome concentration of 7.998×10^{13} vesicles/mL was obtained, corresponding to a molar concentration of $13 \times 10^{-8} \text{ M}$. The liposomal dispersions were diluted to reach a final concentration of $5 \cdot 10^{13}$ vesicles/mL before use (corresponding to a molar concentration of $9.5 \times 10^{-8} \text{ M}$).

2 Supplementary Characterization of M-SiO₂NPs

2.1 Cryo-TEM

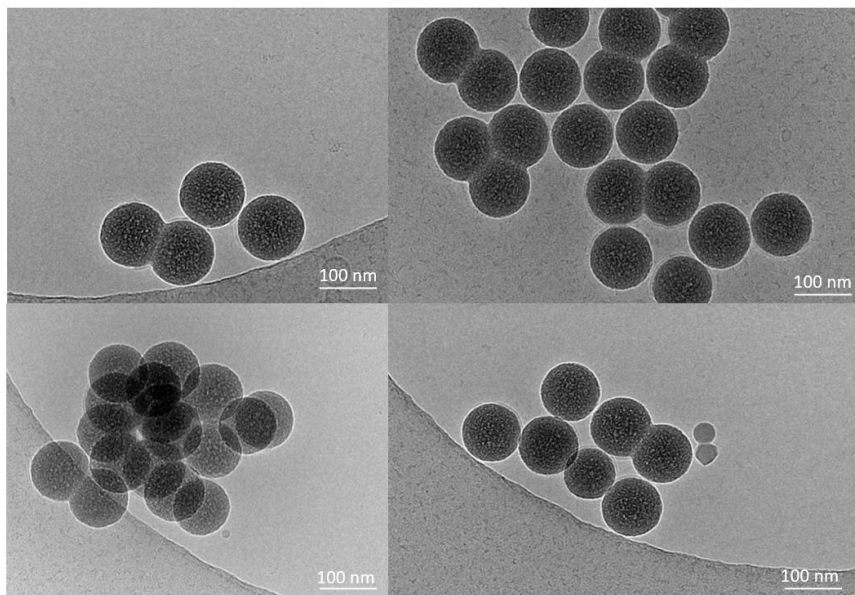


Fig S2: Cryo-TEM images of SiO₂NPs with a membrane coverage of 88%.

2.2 Atomic Force Microscopy

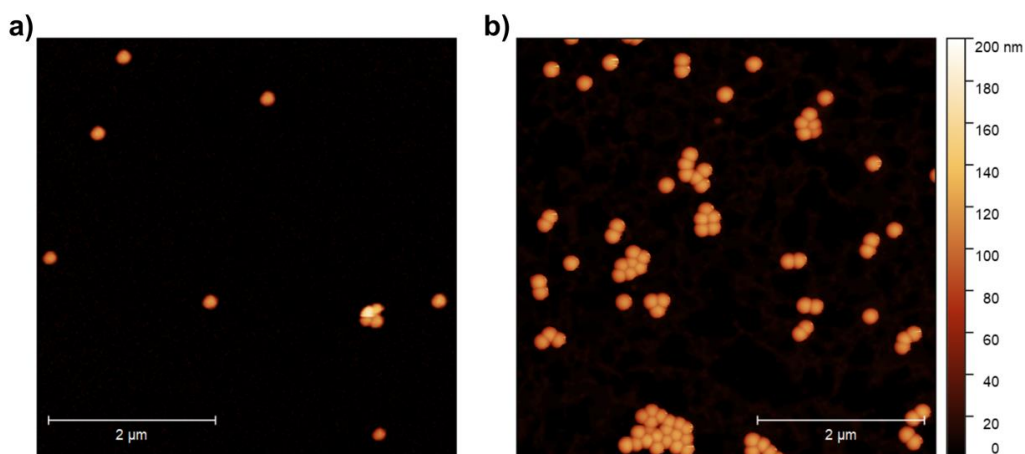


Fig S3: Representative AFM images of a) SiO₂NPs and b) M-SiO₂NPs.

2.3 Evaluation of the degree of coverage

To evaluate the degree of lipid coverage of each sample, we performed ICP-AES measurements. With this method we were able to determine (in terms of mg per

liters) the amount of P and Si within the dispersion. The obtained values were reported in table S1. Starting from such values we evaluated the lipid coverage of SiO₂NPs for each formulation, according to the following procedure. The amount of P was used for calculating the moles of lipids in the samples. Considering AFM results, the size of M-SiO₂NPs is approximately 140 nm. Thus, the amount of lipids needed for the formation of a lipid bilayer around a single SiO₂NP can be approximated to be equal to the amount of lipid composing a liposome of 140 nm in diameter (following the procedure reported in section S1.2).

For evaluating the concentration of SiO₂NPs in each sample after 6 cycles of centrifugation, the total mass of SiO₂NPs was obtained starting from the amount of Si measured by the ICP-MS analysis. Then, the mass of a single SiO₂NP was obtained from the density of the SiO₂NP ($d=1.9 \text{ g/cm}^3$) and the volume of a single SiO₂NP of 120 nm in diameter (904320 nm^3). The number of SiO₂NPs present in the sample was obtained by dividing the total mass of SiO₂NPs for the mass of a single SiO₂NP. Finally, to obtain the percentage of covered SiO₂NP surface, the total number of lipids (calculated from ICP-AES data as described above) was divided by the number of lipids theoretically needed for fully covering the number of SiO₂NPs present in the sample.

The obtained results are reported in table S3. Each sample was diluted to a SiO₂ concentration of 1.15 nm before each further measurement.

Sample	P mg/L	Si mg/L	SiNPs coverage
50/1	8.9 ± 0.8	596.3	88 ± 8 %
15/1	7.2 ± 0.7	626.3	68 ± 7 %
10/1	5.9 ± 0.6	579.0	60 ± 6 %
5/1	5.0 ± 0.5	557.4	53 ± 5 %
3/1	3.2 ± 0.3	570.9	33 ± 3 %
1/1	1.0 ± 0.1	462.3	13 ± 1 %

Table S1: mg/L concentration of the samples obtained by ICP-AES measurements.

3 *Supplementary Characterization of Gold Nanoparticles*

3.1 Small Angle X-ray Scattering

SAXS measurements on AuNPs aqueous dispersion were carried out in sealed glass capillaries of 1.5 mm diameter.

The structural parameters (Table S2) of citrated gold nanoparticles were evaluated from the SAXS profile of their diluted water dispersion (2.06 n M) (Figure S1), according to a spherical form factor and a Schulz size distribution. In our concentration range, we can safely assume that there are no interparticle interactions, and that the structure factor $S(Q)$ is equal to 1 in the whole range of scattering vectors. Thus, the scattering profile of the particles derives from their form factor, $P(Q)$. The SAXS spectrum reported in Figure S1 is fully consistent with the characteristic $P(Q)$ of spherical particles with an average diameter of about 5.8 nm.

The clear presence of $P(Q)$ oscillations in the high Q region is consistent with a relatively low polydispersity of the synthesized AuNPs.

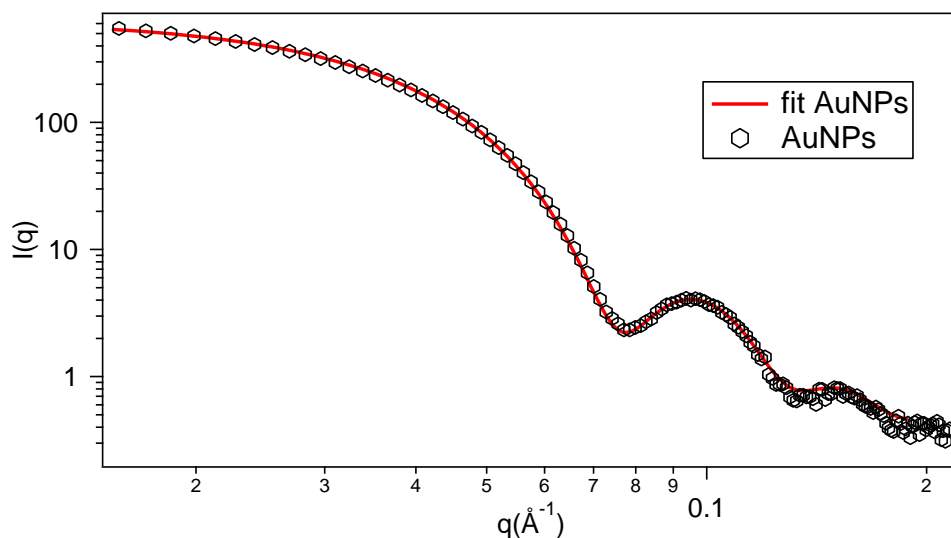


Figure S4: Experimental SAXS curve (red markers) obtained for AuNPs, and curve fit (solid black line) according to the Schulz spheres model from the analysis software package SasView. The size and polydispersity obtained from the fitting procedure are summarized in the Table S1 below.

	R_{core} (nm)	poly
AuNP	5.8	0.095

Table S2: Structural parameters of the nanoparticles obtained from the analysis of SAXS curves according to the Schulz spheres model.

3.2 Dynamic Light Scattering and ζ -Potential

AuNPs hydrodynamic diameter and surface charge in MilliQ water were evaluated

through Dynamic Light Scattering and ζ -Potential, respectively, and reported in inset of figure S5.

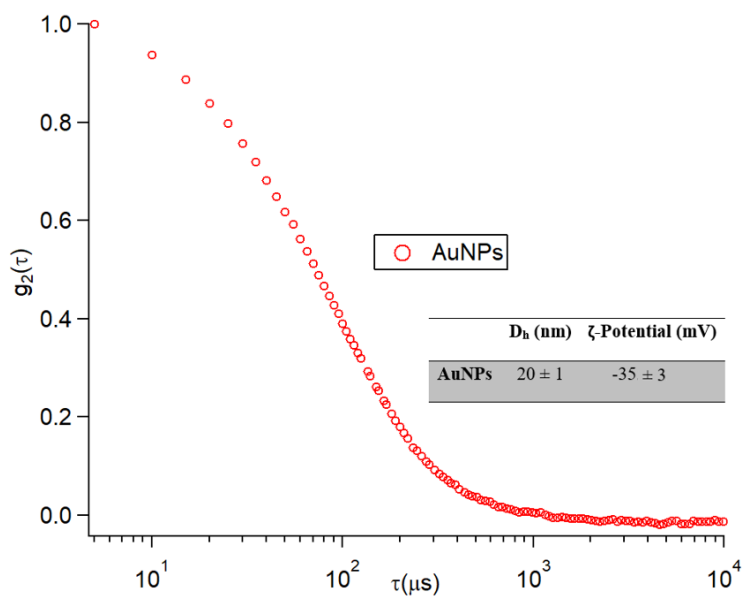


Figure S5: Hydrodynamic diameter obtained from Dynamic Light Scattering and surface ζ -Potential of AuNPs.

3.3 UV-vis Spectroscopy

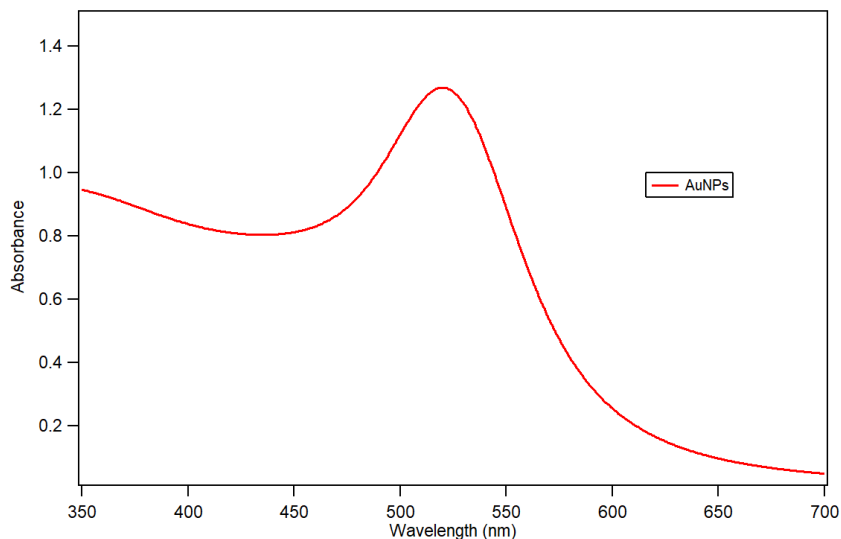


Figure S6 UV-Vis absorption spectra of AuNPs after 1:3 dilution in water (2.06 nM). The plasmon absorption peak is at around 520 nm.

To further evaluate the AuNPs size through UV-Vis spectroscopy we exploited the following equation¹:

$$d = \exp \left(B_1 \frac{A_{spr}}{A_{450}} - B_2 \right)$$

with d diameter of gold nanoparticles, A_{spr} absorbance at the surface plasma resonance peak, A_{450} absorbance at the wavelength of 450 nm and B_1 and B_2 are dimensionless parameters, taken as 3 and 2.2, respectively. The diameter value obtained is of 12.3 nm.

The concentration of citrated gold nanoparticles was determined via UV-Vis spectrometry, using the Lambert-Beer law ($E(\lambda) = \varepsilon(\lambda)lc$), taking the extinction

values $E(\lambda)$ at the LSPR maximum, i.e. $\lambda = 521$ nm. The extinction coefficient $\varepsilon(\lambda)$ of gold nanoparticles dispersion was determined by the method reported in literature², by the following equation:

$$\ln(\varepsilon) = k \ln(d) + a$$

with d core diameter of nanoparticles, and k and a dimensionless parameters ($k = 3,32111$ and $a = 10,80505$). The arithmetic mean of the sizes obtained by optical and scattering analyses was selected, leading to a $\varepsilon(\lambda)$ of $2.0 \cdot 10^8 \text{ m}^{-1} \text{ cm}^{-1}$. The final concentration of the citrated AuNPs is therefore $\sim 6.13 \cdot 10^{-9} \text{ M}$.

4 Supplementary Characterization of M-SiO₂NPs/AuNPs hybrids

4.1 Cryo-TEM

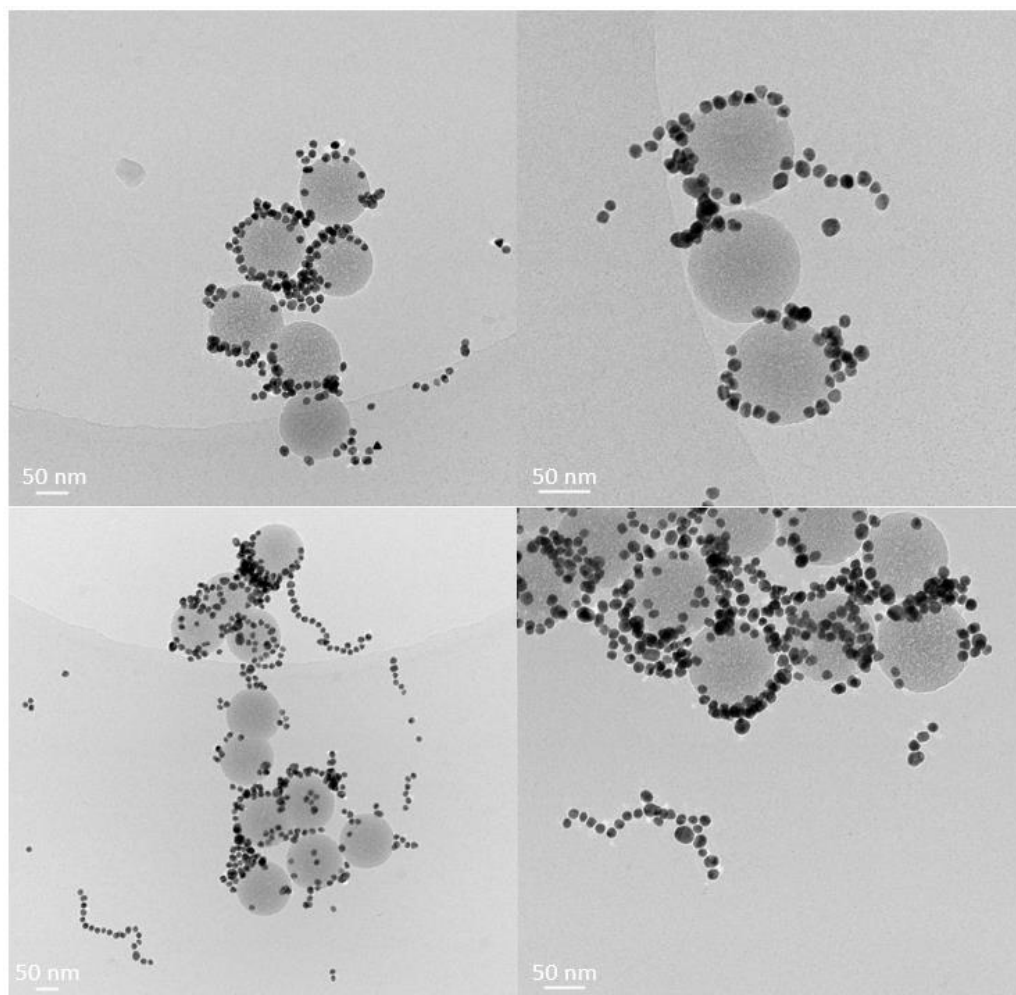


Figure S7: Cryo-TEM images of $M\text{-SiO}_2\text{NPs-AuNPs}$ hybrids. $M\text{-SiO}_2\text{NPs}$ are characterized by an almost complete membrane coverage (88%, estimated through ICP-AES).

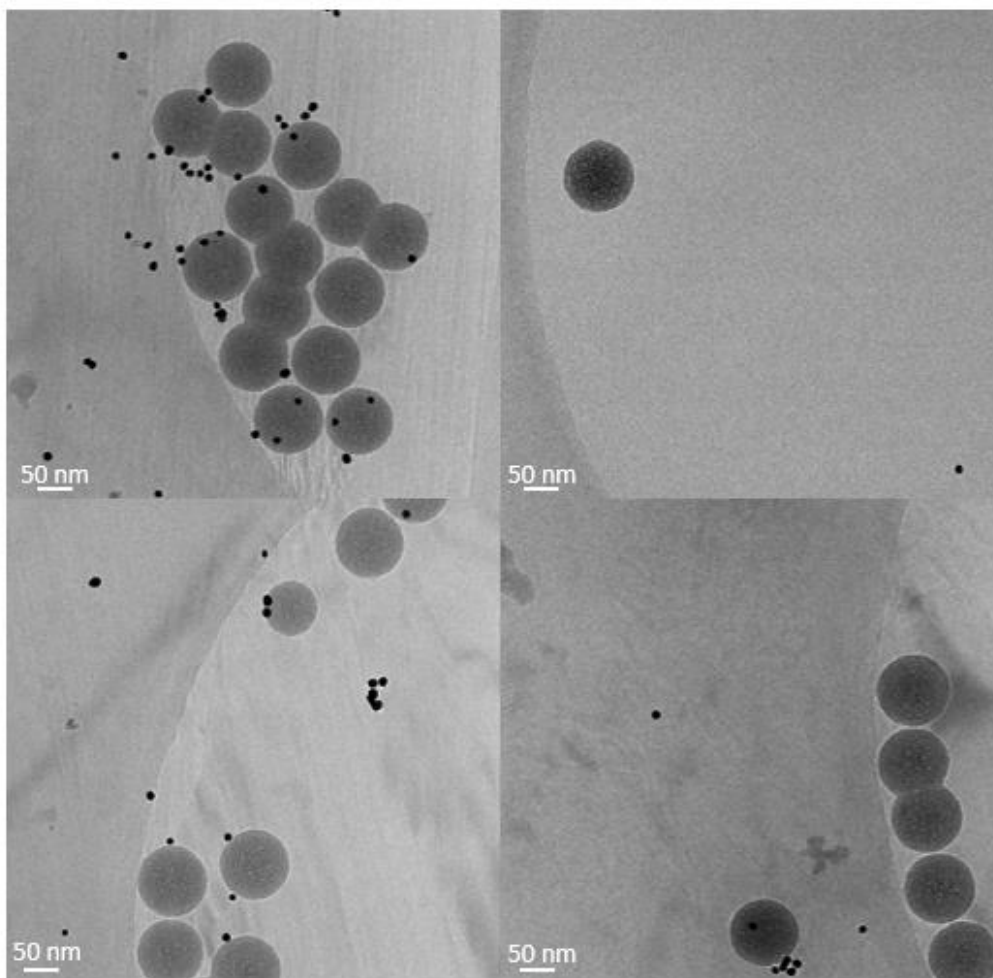


Figure S8: *Cryo-TEM images of naked SiO₂NPs incubated with the AuNPs dispersion.*

4.2 Dynamic light scattering

To gain more insights into the aggregation process, we performed DLS measurements on the very same samples used in cryo-TEM experiments. Figure S8 shows the normalized autocorrelation functions measured for the naked SiNPs, the naked SiNPs interacting with AuNPs, and the coated SiNPs interacting with AuNPs. The autocorrelation functions were analysed using a Non-Negatively constrained

Least Squares fitting (NNLS). This model, generally used for polydisperse suspensions undergoing Brownian motion, provides a size distribution of the dispersed particles, reported in section figure S8. As shown, the hydrodynamic diameter evaluated for the naked SiNPs is centered at about 170 nm, according to reported cumulant fitting in the main text. The interaction of AuNPs with M-SiO₂NPs leads to the formation of larger hybrid objects with a hydrodynamic diameter of about 230 nm. Concerning the naked SiNPs-AuNPs sample, the correlation function is bimodal, suggesting the presence of two separated populations presenting size distributions centred at 20 nm and 170 nm, respectively. Remarkably, the smallest population is consistent with the hydrodynamic dimensions of AuNPs, while the larger one shows very similar sizes to those measured for the uncoated SiNPs. The very fact that DLS measurements are consistent with the presence of two different populations, meaning that the dispersed objects possess very different diffusion coefficients, is a further confirmation that the interaction between AuNPs and SiNPs is mediated by the lipid coating.

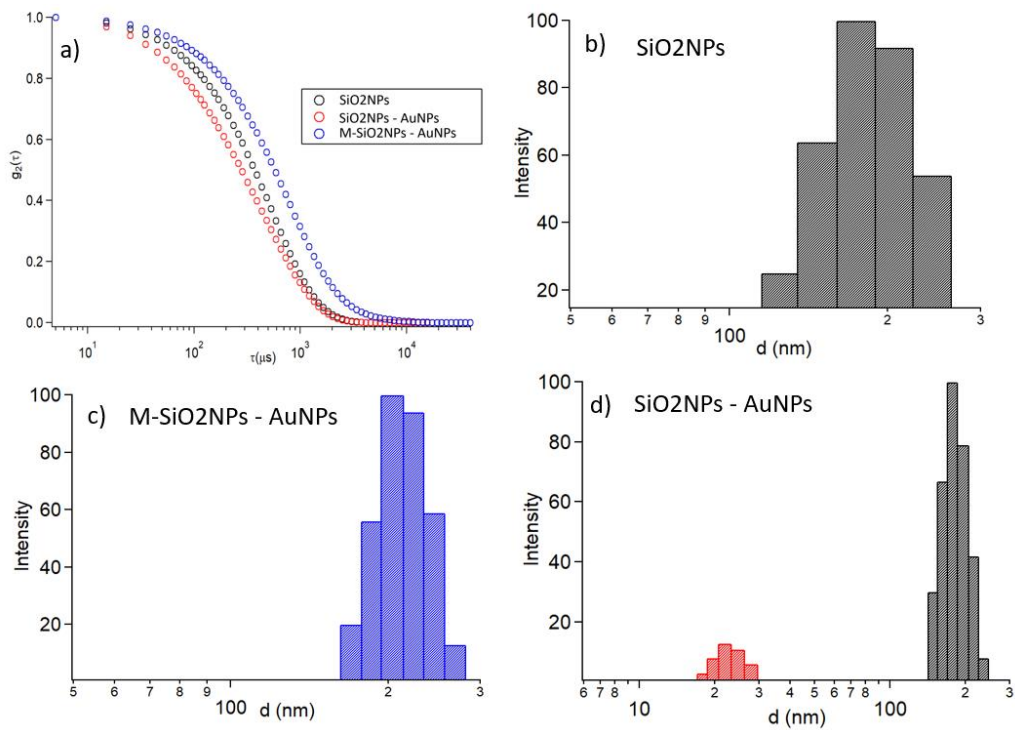


Figure S9: a) DLS autocorrelation functions of SiO₂NPs, SiO₂NPs – AuNPs, , M-SiO₂NPs – AuNPs, b) Size distributions obtained from the NNLS fitting of the DLS autocorrelation functions of diluted water dispersion of c) naked SiNPs, b) M-SiO₂NPs (with 88% membrane coverage)-AuNPs composites, and d) naked SiNPs-AuNPs mixture.

4.3 UV-vis spectroscopy

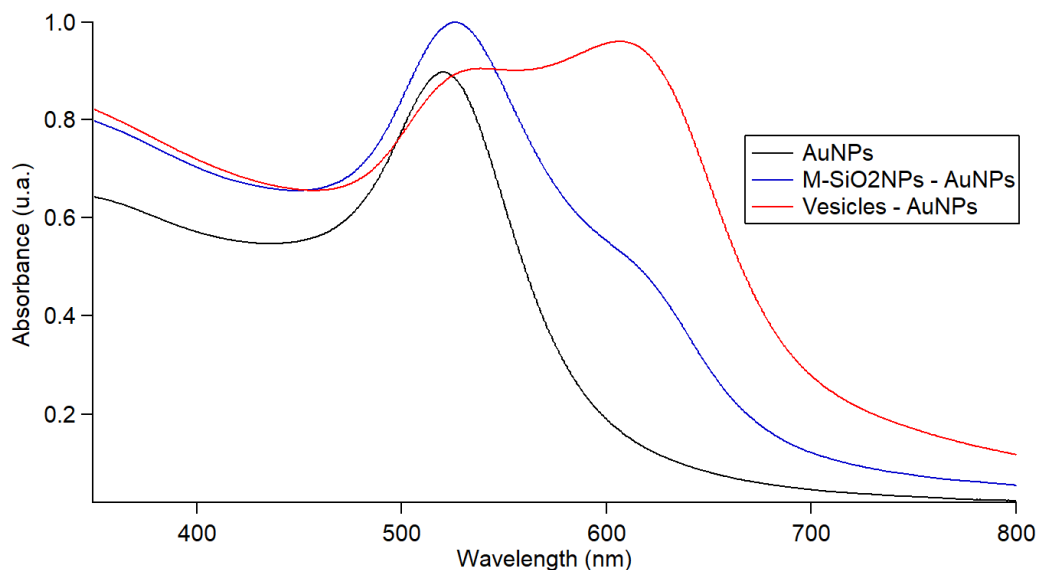


Figure S10: UV-vis spectroscopy comparing the plasmonic signal of bare AuNPs and AuNPs incubated with either M-SiO₂NPs (with 88% membrane coverage) or free-standing vesicles with the same lipid membrane composition. The concentration of AuNPs was 6.13 nM, while the concentration of vesicles and M-SiO₂NPs was 1.15 nM. The plasmonic variation of AuNPs interacting with the free-standing vesicles are much more pronounced, indicating the high AuNPs clustering.

4.4 Small-Angle X-Ray Scattering

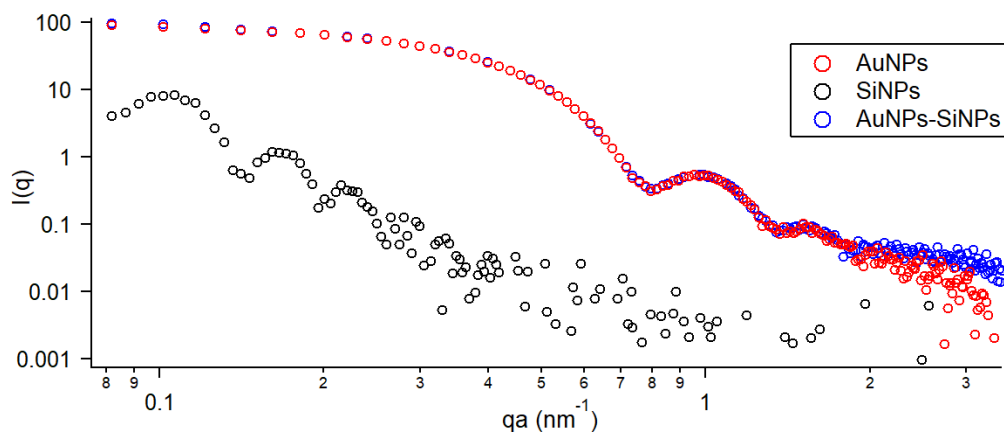


Figure S11: Comparison between SAXS profiles of bare AuNPs, SiO₂NPs, and SiO₂NPs -AuNPs mix obtained by adding 300 μ L of 6.13 nm of AuNPs to 50 μ L 1.15 nm of SiO₂NPs.

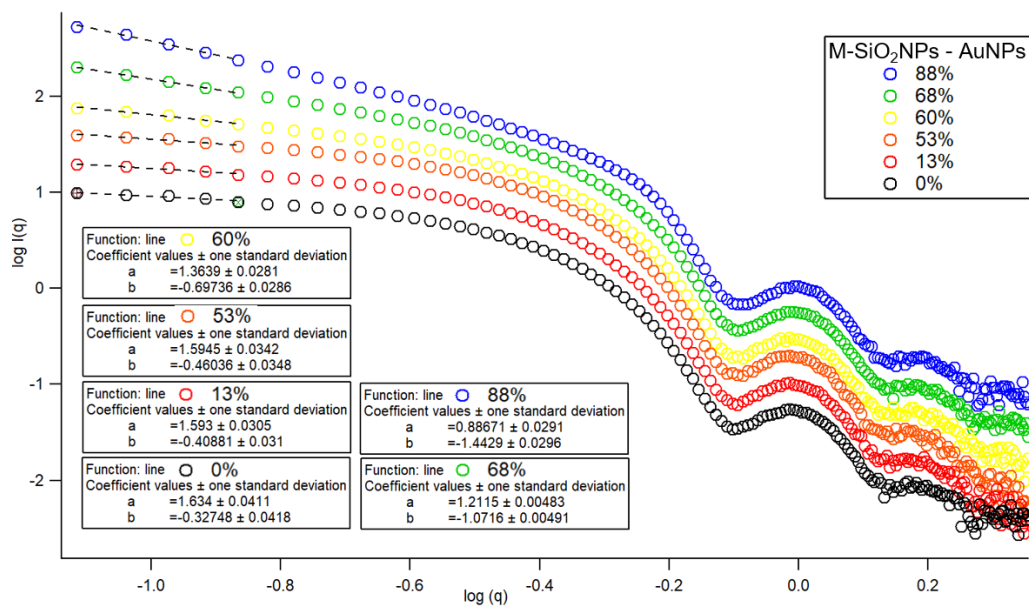


Figure S12: Log-Log SAXS profiles of M-SiO₂NPs-AuNPs mixtures with different degrees of SiO₂NPs membrane coverage collected after 10 minutes of incubation. The dashed lines represent the linear fitting in the Guinier region of the AuNPs

($0.082 < nm^{-1} < 0.161$). The “b” values in the squared boxes represent the slope values for the different SAXS profiles obtained from the fitting.

Sample	Porod coefficient
88%	1.44 ± 0.03
68%	1.07 ± 0.01
60%	0.70 ± 0.03
53%	0.46 ± 0.04
13%	0.41 ± 0.03
0%	0.33 ± 0.04

Table S3: Porod coefficient obtained from the slope of the linear fitting of the SAXS profiles in the low q region (Guinier region of the AuNPs $0.082 < nm^{-1} < 0.161$).

5 Characterization of the M-SiO₂NPs/AuNPs as a function of the degree of coverage

5.1 Dynamic Light Scattering

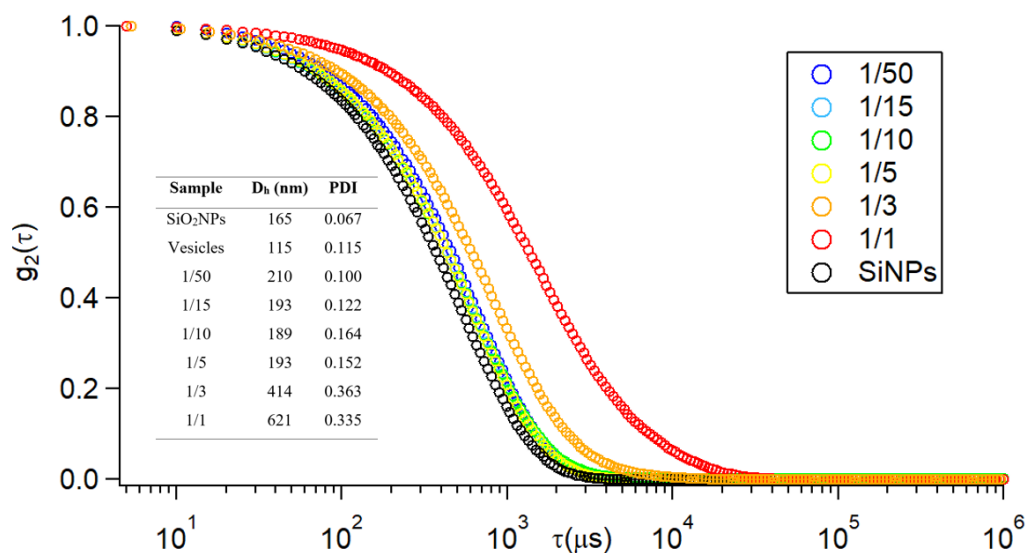


Figure S13: Normalized DLS curves obtained for M-SiO₂NPs with different coverages. The inset reports the hydrodynamic diameters and PDI of samples, showing the increase in the size of the samples with low coverages.

5.2 Nanoplasmonic assay for the quantification of the lipid coverage on SiO₂NPs

To set up a colorimetric assay for the estimation of the covered SiNPs (Figure S14), a quantitative descriptor of the plasmonic variations of AuNPs dispersion is required. With this purpose, we selected an aggregation index already used for quantifying the plasmonic variations induced by the presence of synthetic vesicles on the AuNPs dispersion³:

$$A. I. = \frac{\frac{A_{560-800}}{A_{350-800}}}{A. I._{AuNPs}}$$

Where $A_{560-800}$ is the area subtended by the absorbance spectrum in the 560-800 nm range, $A_{350-800}$ is the area of the entire spectrum, and $A. I._{AuNPs}$ represents the $\frac{A_{560-800}}{A_{350-800}}$ evaluated for the bare AuNPs dispersion.

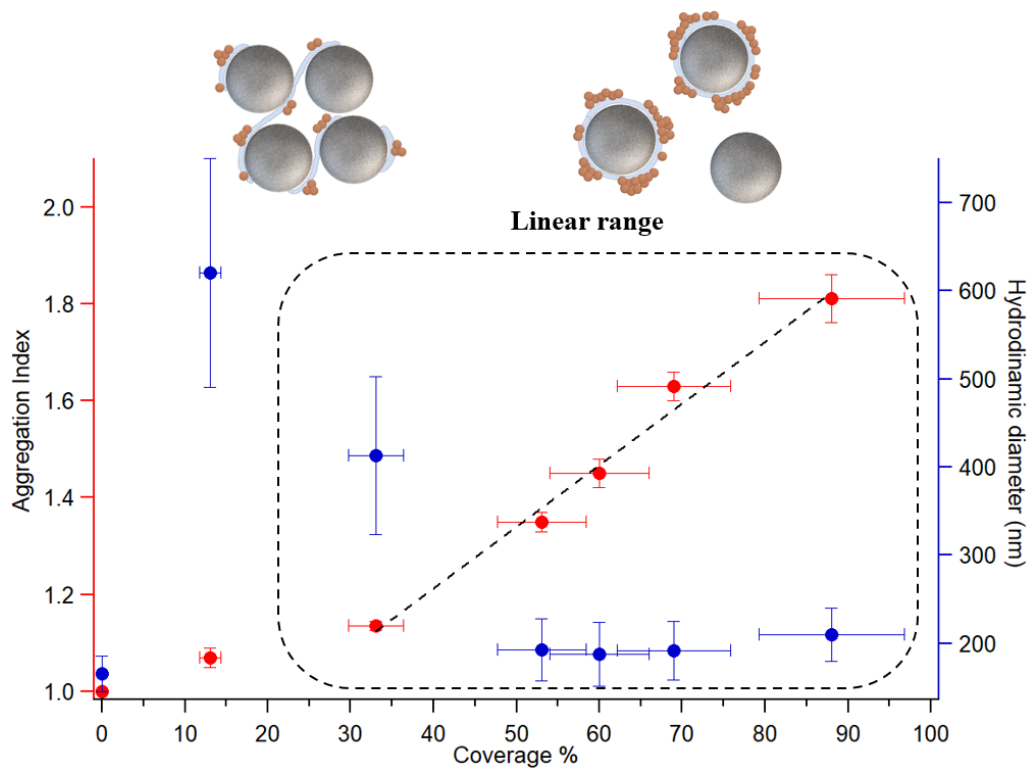


Figure S14: A.I. as a function of SiO₂NPs coverage. A.I. (left axis) and hydrodynamic diameter (right axis) as a function of SiO₂NPs membrane coverage (bottom axis). The linear fit for A.I. vs membrane coverage is also reported, in the 35-100% range of coverage, yielding a r-squared of 0.98.

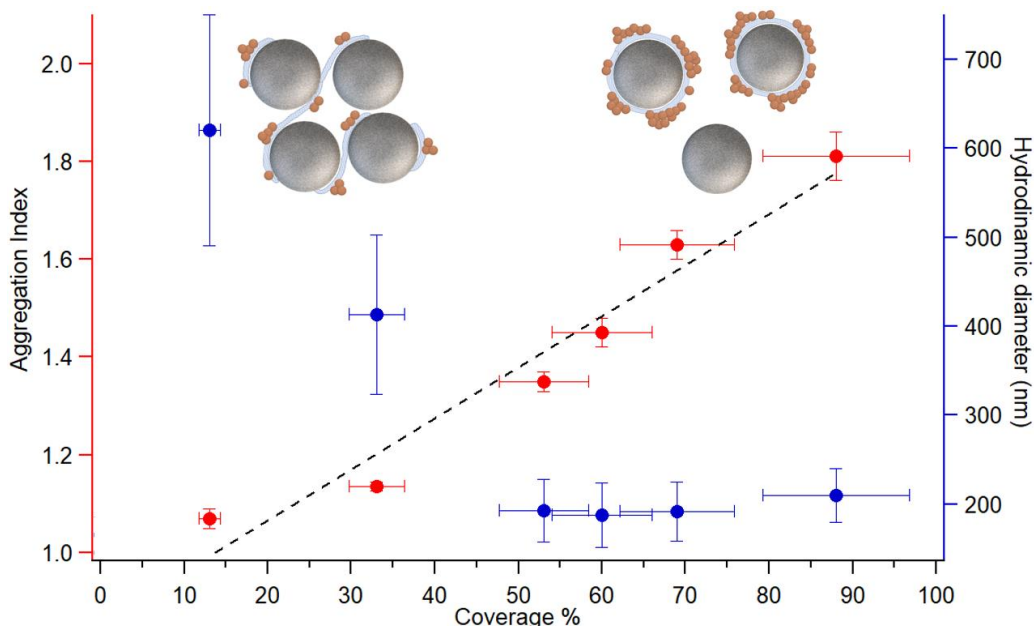


Figure S15: A.I. as a function of SiO₂NPs coverage. A.I. (left axis) and hydrodynamic diameter (right axis) as a function of SiO₂NPs membrane coverage (bottom axis). The linear fit for A.I. vs membrane coverage in the 13-100% range of coverage is reported. The goodness of fit decreases by the inclusion of the A.I. of the SiO₂NPs with a coverage of 13% (*r*-squared of 0.95).

Furthermore, to verify that the linearity of the spectral variation with the lipid coverage of SiNPs is independent of the selected A.I., we further analyzed the spectra with a different aggregation index (A.I. bis). Such A.I. bis was obtained as follow:

$$A.I. \text{ bis} = \frac{Abs_{max} - Abs_{600}}{\Delta\lambda}$$

Where Abs_{600} is the absorbance evaluated at 600 nm, Abs_{max} is the absorbance of the main peak of the dispersion, and $\Delta\lambda$ is the wavelength difference between 600 nm and the main peak. Each value is then normalized for the A.I. bis obtained from the bare AuNPs spectrum. This A.I. accounts of the spectral variation of the AuNPs spectra considering that the A.I. of bare AuNPs is always equal to 1 and, increasing

the particle aggregation, the A.I. value decreases. Table S5 summarized the evaluated A.I.s for each coating extent.

SiNPs coverage	A.I.
$88 \pm 8 \%$	0.70 ± 0.05
$68 \pm 7 \%$	0.78 ± 0.03
$60 \pm 6 \%$	0.85 ± 0.03
$53 \pm 5 \%$	0.91 ± 0.02
$33 \pm 3 \%$	1 ± 0.01
$13 \pm 1\%$	0.99 ± 0.02
0 %	1

Tab S4: A.I. bis values obtained for each different membrane coverage of SiNPs.

By plotting the calculated A.I.bis versus the coverage of SiNPs the linear trend of the A.I. with increasing the SiNPs coverage is confirmed for the samples for the lipid coverages higher than approximately 35% (Fig S15).

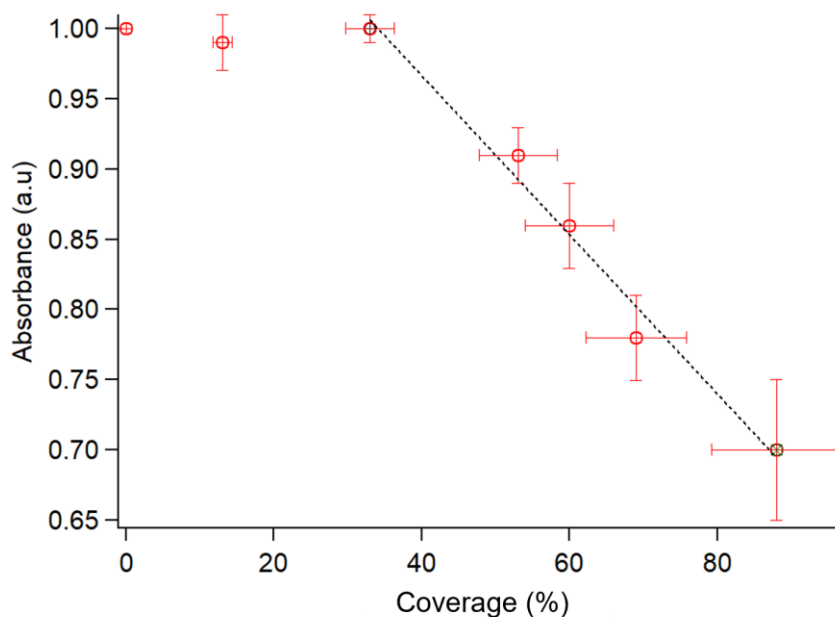


Figure S16: *Linear trend of the A.I. bis as a function of SiNPs coverage. The samples with low surface coverage (<35%) cannot be fitted by the linear regression.*

Bibliography

- 1 W. Haiss, N. T. K. Thanh, J. Aveyard and D. G. Fernig, 2007, **79**, 4215–4221.
- 2 X. Liu, M. Atwater, J. Wang and Q. Huo, 2007, **58**, 3–7.
- 3 L. Caselli, A. Ridolfi, J. Cardellini, L. Sharpnack, L. Paolini, M. Brucale, F. Valle, C. Montis, P. Bergese and D. Berti, *Nanoscale Horizons*, 2021, **6**, 543–550.

Self-assembly of magneto-plasmonic NPs on synthetic vesicles: hybrid nanomaterials for medical applications (Paper VI)

Jacopo Cardellini, Alessandro Surpi, Beatrice Muzzi, Valentina Pacciani, Claudio Sangregorio, Costanza Montis, Alek Dediu, and Debora Berti (Manuscript in preparation)

Self-assembly of magneto-plasmonic NPs on synthetic vesicles: hybrid nanomaterials for medical applications (Paper VI)

Jacopo Cardellini, Alessandro Surpi, Beatrice Muzzi, Valentina Pacciani, Claudio Sangregorio, Costanza Montis, Alek Dediu, and Debora Berti (Manuscript in preparation)

Abstract

1. Introduction

In the past years, several novel nanomaterials have been proposed as game-changer tools in the medical treatment of pathologies. In the nanometric lengthscale, materials gain completely novel characteristics, such as optical properties and magnetic responsiveness. By varying their chemical-physical nature (composition, shape, size, and surface functionalization), nanomaterials can be selectively directed toward specific targets. The possibility to control concentration, time, and site of nanoparticle (NP) delivery represents their major benefit, aiming at reducing the total amount of administrated drugs and the resulting side effects.

In this context, superparamagnetic nanoparticles (SPIONS) are among the most promising inorganic NPs. They can be spatially controlled with static and alternating magnetic fields, funding multiple applications in nanomedicine, ranging from the targeted delivery of drugs to contrast agents in magnetic resonance imaging (MRI) and the hyperthermic treatment of cancer cells. Furthermore, their engineering with an additional gold shell (AuMNPs) can eventually improve their potentiality. Besides its low reactivity and decent biocompatibility, the gold shell introduces the plasmonic properties of nanostructured gold. Furthermore, the well-known conjugation chemistry of gold paves the way for the production of a large library of core-shell NPs for multiple applications.

Despite their extraordinary potential, to date, the effective clinical application of NPs is still extremely limited, due to the lack of fundamental knowledge on their biological fate once introduced in living systems. A deep comprehension of the interaction mechanisms between inorganic nanomaterials and biological membranes represents a crucial point to boost their clinical translation.

Lipid particles represent the most applied nanomaterial in nanomedicine. Being composed of natural lipids, they possess very low toxicity and extended circulation time in bloodstream. The most prominent example is represented by liposomes. Several liposomal formulations are FDA-approved nanomaterial for drug delivery and, nowadays, they represent the starting scaffold for the development of RNA vaccines against Covid 19 and other viral infections.

Based on these reasons, a prominent strategy for improving the biocompatibility of inorganic nanoparticles leverage their combination with lipid scaffolds, forming lipid-inorganic hybrids. Such strategies are aimed at combining the hard properties of the particles, with the biocompatibility of lipid membranes, often giving rise to new synergistic properties. For instance, the NPs interaction with lipid membranes can locally concentrate the particles, affecting the collective properties of the hybrid.

In recent works, we demonstrated that hydrophilic citrated AuNPs spontaneously associate with the zwitterionic membrane of liposomes, according to a membrane-templated process. Such gold aggregation is strictly related to the vesicle's rigidity. Specifically, AuNPs extensively aggregate on soft membranes, while they can just randomly adhere to rigid ones. This aggregative phenomenon comports the spectral variations of the plasmonic properties of AuNPs and has been exploited in various colorimetric assays for the determination of rigidity and concentration of synthetic and natural vesicles, and for estimating the degree of lipid coating in membrane-camouflaged inorganic NPs. From an applicative standpoint, the size and morphology of the gold cluster and the colloidal stability of the hybrids can be finely controlled by varying the vesicle concentration and composition. This aggregative

strategy was successfully exploited in the synthesis of AuNPs-vesicles smart nanomaterials for biomedical application, merging the photothermal properties of gold aggregates and the biocompatibility and drug delivery potentiality of the lipid vesicles.

Here, we investigated the interaction of synthetic liposomes with hybrid citrated gold-magnetic nanoparticles (AuMNPs), aiming at the development of a novel synthetic strategy for the synthesis of controlled nanoparticles-liposomes adducts as engineered nanomaterials for nanomedicine. Specifically, we systematically studied the interaction of AuMNPs and two liposomal formulations with different membrane rigidity. The interaction was firstly monitored through UV-Vis spectroscopy, exploiting the plasmonic properties of nanostructured gold. Then, the morphology and NPs arrangement of the hybrids were directly imaged with Cryo Transmission Electron Microscopy, while their colloidal stability was monitored with Dynamic Light Scattering measurements. Eventually, magnetic mobility studies demonstrate that the magnetic responsiveness of the NPs-vesicles suprastructures is extremely enhanced compared one of the free dispersed particles and can be modulated by varying the NPs/vesicles ratio.

Overall, this work provides fundamental information on the membrane-templated formation of magnetic-liposome adducts, demonstrating how the spatial confinement of the particles on the liposome's membranes leads to the enhancement in magnetic responsivity. The understanding of the chemical-physical parameters that rule this phenomenon paves the way for the development of straightforward synthetic protocols of smart nanomaterials for biomedical purposes.

2. Materials and Methods

2.1 Materials

Tetrachloroauric (III) acid and trisodium citrate dihydrate were provided by Sigma-Aldrich (St. Louis,MO). 1,2-Dioleoyl-sn-glycero-3-phosphocholine (DOPC) and 1-

dipalmitoyl-sn-glycero-3-phosphocholine (DPPC) were provided by Avanti Polar Lipids. All chemicals were used as received. Milli-Q-grade water was used in all preparations.

2.2 Synthesis of AuMNPs

Anionic gold nanospheres 12 nm in size were synthesized according to the Turkevich–Frens method. Briefly, 20 mL of a 1 mM H₂AuCl₄ aqueous solution was brought to the boiling temperature under constant and vigorous magnetic stirring. The solution was then mixed to 2 mL of a 1% citric acid solution and was further boiled for 10 min until it acquired a deep red color. The nanoparticle solution was then slowly cooled to room temperature.

2.2 Synthesis of liposomes

To prepare the DOPC and DPPC liposomes, the proper amount of lipid was dissolved in chloroform, and a lipid film was obtained by evaporating the solvent under a stream of nitrogen and overnight vacuum drying. The film was then swollen and suspended in warm (50 °C) Milli-Q water by vigorous vortex mixing to obtain a final 4 mg/ml lipid concentration. The resultant multilamellar vesicles (MLV) in water were subjected to 10 freeze–thaw cycles and extruded 10 times through two stacked polycarbonate membranes with a 100 nm pore size at room temperature to obtain unilamellar vesicles (ULV) with a narrow and reproducible size distribution. The filtration was performed with the Extruder (Lipex Biomembranes, Vancouver, Canada) through Nuclepore membranes.

2.1 UV-Vis

UV–vis spectra were recorded with a Cary 3500 UV–vis spectrophotometer.

2.2 DLS

DLS measurements at $\theta = 90^\circ$ and the ζ -potential determination were performed using a Brookhaven Instrument 90 Plus (Brookhaven, Holtsville, NY). Each

measurement was an average of 10 repetitions of 1 min each, and measurements were repeated 10 times. The autocorrelation functions (ACFs) were analysed through cumulant fitting stopped at the second order for samples characterized by a single monodisperse population, allowing an estimate of the hydrodynamic diameter of particles and the polydispersity index. For polydisperse samples, the experimental ACFs were analyzed through the Laplace inversion according to the CONTIN algorithm. ζ -potentials were obtained from the electrophoretic mobility u according to Helmholtz–Smoluchowski equation $\zeta = \left(\frac{\eta}{\epsilon}\right) \times \mu$ (1) where η is the viscosity of the medium and ϵ is the dielectric permittivity of the dispersing medium. The ζ -potential values are reported as averages from 10 measurements.

2.3 H-TEM

2.4 Cryo-TEM

On glow-discharged Quantifoil Cu 300 R2/2 grids were applied 3 μ L of each sample. The samples were plunge frozen in liquid ethane using an FEI Vitrobot Mark IV (Thermo Fisher Scientific) instrument. Excess liquid was removed by blotting for 1 s (blot force of 1) using filter paper under 100% humidity and 10 °C. Cryo-EM data were collected at the Florence Center for Electron Nanoscopy (FloCEN), University of Florence, on a Glacios (Thermo Fisher Scientific) instrument at 200 kV equipped with a Falcon III detector operated in the counting mode. Images were acquired using EPU software with a physical pixel size of 2.5 Å and a total electron dose of $\sim 50 e^-/\text{Å}^2$ per micrograph.

3 Result and discussion

3.1 Particle characterization (DLS, UV-vis, TEM, Magnetic properties)

0.137 μ M AuMNPs nanoparticles were prepared according to a well-known protocol with little modifications (see section 2.x). A gold shell has been grown around 8 nm Fe₃O₄ seeds exploiting the reduction of a gold salt by the citrate molecules adsorbed

on the surface of seeds (see S.I. for the Fe_3O_4 NPs characterization). The so-obtained particles display plasmonic properties (Figure 1a) consistent with the formation of gold core-shell NPs. Specifically, the UV-vis spectrum shows a broad plasmonic signal peaked at about 538 nm, as reported in the literature. The hydrodynamic size of the particles in the colloidal dispersion was obtained through Dynamic Light Scattering measurements. Figure 1b shows the measured autocorrelation function (red circles) fitted with a Non-Negatively constrained Least Squares fitting (NNLS). The NNLS model, generally employed for colloidal dispersions containing polydispersed particles, clearly discriminates between two distinct size distributions (inset in Figure 1b). The bigger one, centered at about 45 nm, features the hydrodynamic size of the synthesized AuMNPs. On the other hand, the smaller population is peaked at about 10 nm and perfectly matches the dimensions of the ferric seeds.

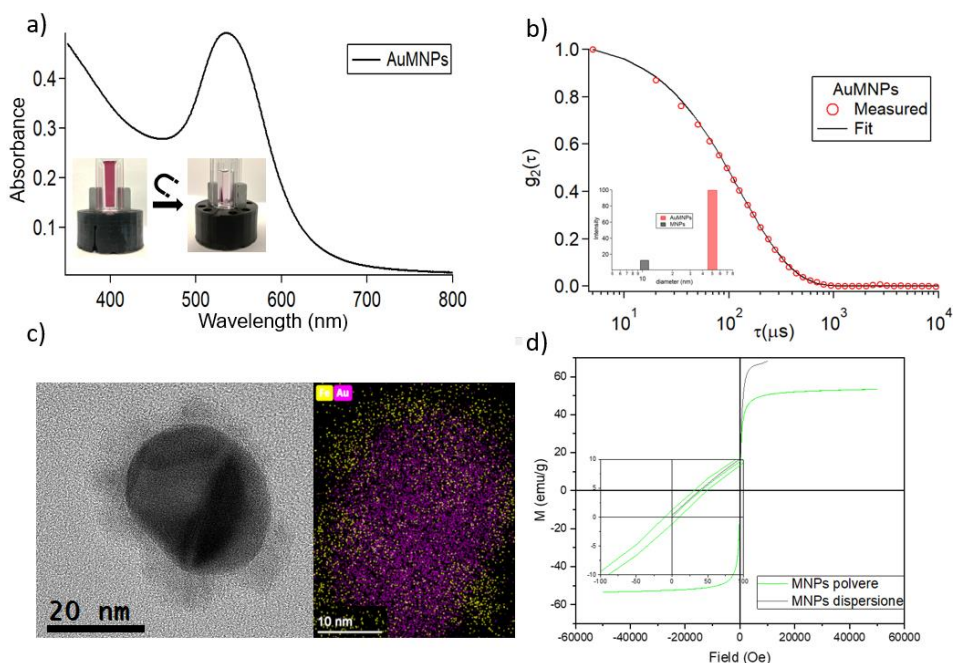


Figure 1:

3.2 Characterization of AuMNPs-liposomes hybrids

To investigate the interaction of the AuMNPs with zwitterionic liposomes with different rigidities, xx nM AuMNPs dispersion was challenged with DOPC and DPPC synthetic vesicles, and the spectral variations of the particles were monitored through UV-vis spectroscopy. Figure 2 displays the UV-vis spectra collected for the AuMNPs dispersion mixed with different concentrations of liposomes. Depending on the lipid formulations, the liposome's membrane displays very different viscoelastic properties. Specifically, DOPC lipids self-assemble in water forming soft vesicles with the bilayer in a liquid-crystalline phase. Conversely, at room temperature, DPPC molecules constitute a much more rigid membrane characterized by densely packed hydrophobic tails. Regarding the interaction with the citrated particles, the DOPC presence provokes the red-shift and broadening of the AuMNPs' original plasmonic peak, caused by the coupling of the plasmonic peak due to the spatial proximity of AuMNPs, and related to the particle aggregation. The decrease of the vesicle amount leads to the progressive enlargement of the plasmonic peak, underlying that the particle aggregation is maximized for the lower DOPC amounts. Such experimental result reveals that the AuMNPs aggregate on the soft vesicle membrane according to a membrane templated process, accordingly to what was previously observed for AuNPs. On the contrary, the interaction with rigid DPPC liposomes provokes much lower plasmonic variations and the plasmonic signal is negligibly affected by the vesicle amount. This behavior is consistent with the absorption of the particles to the DPPC membranes, and leads to the bathochromic shift of the original peak as a consequence of the change of the chemical environment of the particles. However, in this case, the limited signal broadening related to the weak plasmonic coupling suggests a limited particle aggregation.

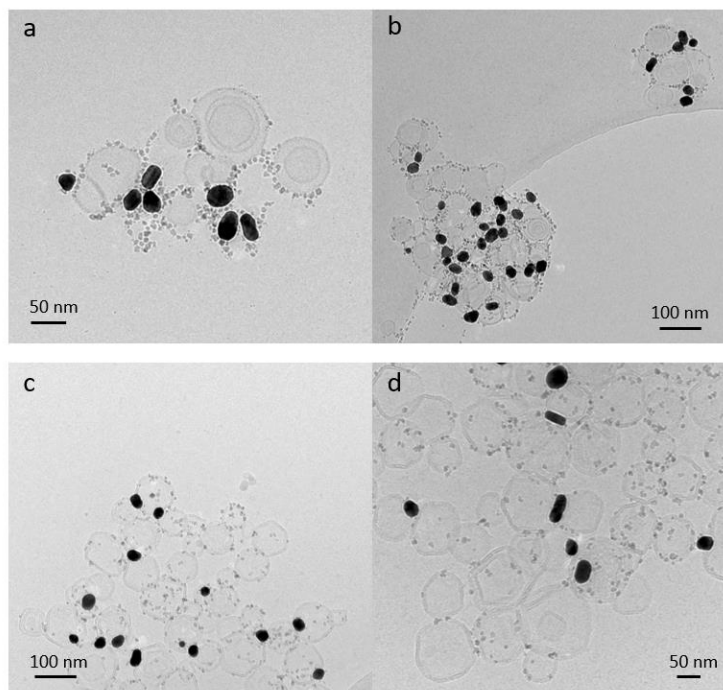


Figure 2: Cryo-TEM images of (a,b) DOPC-AuMNPs and (c,d) DOPC-AuMNP composites.

To obtain structural information on the AuMNPs-liposomes hybrids, we performed Cryo-EM measurements. Figure 3 shows representative Cryo-TEM images of DOPC and DPPC vesicles challenged with the AuMNPs dispersion after 10 minutes of interaction. First, we noticed that the AuMNPs dispersion is composed of two typologies of particles, in line with the DLS analysis. Specifically, the synthesis produced hybrid gold-magnetic nanoparticles dispersed together with several uncoated Fe₃O₄ magnetic seeds. Both the two kinds of dispersed particles adhere to soft and rigid vesicles without membrane disruption. However, we noticed a dramatic morphological difference between the formed suprastructures. On soft DOPC vesicles, the particles adhere to the lipid shell forming compact clusters, where particles are in direct contact with each other. The observed cluster morphology justifies the plasmon coupling observed in the UV-vis spectra. Regarding DPPC vesicles, the particles randomly adhere to the lipid scaffolds.

However, the particle clustering on the membrane is mostly inhibited, forming hybrids with a minor number of adsorbed particles per vesicle and, importantly, with a higher average NP-NP distance.

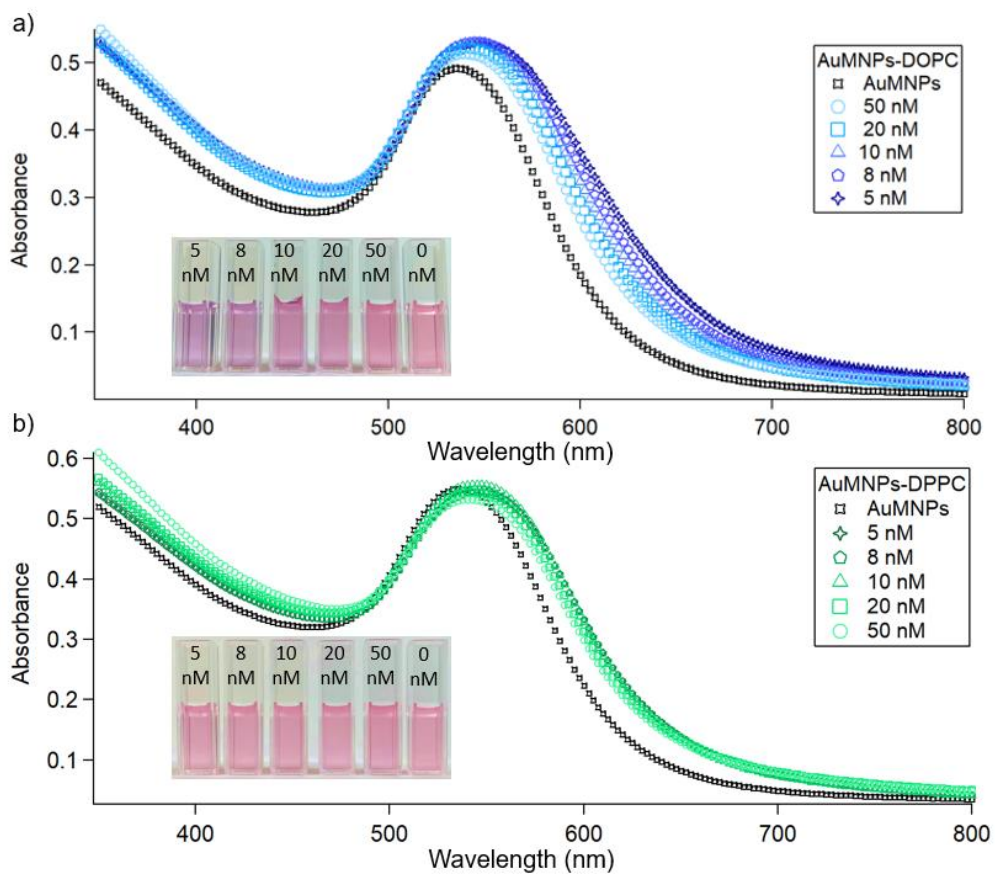


Figure 3: UV-Visible absorption profiles of AuMNPs-DOPC (a) and AuMNPs-DPPC (b) as a function of the liposome concentration (5 nM, 8 nM, 10 nM, 20 nM, and 50 nM). The insets in the figures report the color variation in the various sample.

These results imply that the phase of the membrane drives the aggregation of AuMNPs on the lipid membranes, leading to completely different morphologies of the hybrids.

To further characterize this phenomenon, we monitored the aggregative process in terms of size and colloidal stability with Dynamic Light Scattering. The AuMNPs-

vesicles hydrodynamic size was monitored as a function of incubation time, vesicle concentration and vesicle rigidity. First, several amounts of DPPC and DOPC vesicles were incubated for 10 minutes with $x.x$ nM AuMNPs dispersion, and figure 4 displays the autocorrelation functions obtained for each sample. Concerning the DOPC-AuMNPs system, the hydrodynamic diameter of the hybrids increases with increasing the number of particles per vesicle, passing from 160 nm to 350 nm. The evaluated size is consistent with the hydrodynamic dimension of a lipid vesicle surrounded by a nanoparticles crust. The interaction of AuMNPs with rigid DPPC vesicles leads to the formation of μm -sized objects, possessing dimensions not clearly dependent on the starting NPs/vesicles ratios, and characterized by an elevated polydispersity (population distribution ranging from 300-1000 nm). Moreover, the prepared samples appear cloudy and highly unstable. To gain a deep comprehension of the colloidal stability of the systems, the evolution of the hydrodynamic dimensions was monitored over time. For what concerns the DOPC sample, in all the selected vesicle concentrations, the interaction forms metastable objects, with steady hydrodynamic size in the first hour of incubation. On the contrary, the AuMNPs adhesion on DPPC vesicles provokes the formation of highly unstable objects which rapidly precipitate. As reported in the literature, the difference in colloidal stability can be attributed to the number of particles per vesicle. The soft bilayer triggers a membrane template NPs aggregation which leads, as confirmed by Cryo-EM images, to the massive particle docking to the lipid shell. The presence of this elevated number of NPs negatively charges the liposomal surface, electrostatically stabilizing the hybrids. In the case of DPPC, the elevated membrane rigidity inhibits the nanoparticle clustering, and the number of adsorbed NPs per vesicle is much lower. Reasonably, in this configuration, the particle number is not sufficient to electrostatically stabilize the lipid surface. On the other hand, the NPs presence introduces attractive contributions between the adsorbed nanoparticles and the surrounding vesicles, leading to a bridging process that highly destabilizes the colloidal dispersion, eventually leading to phase separation.

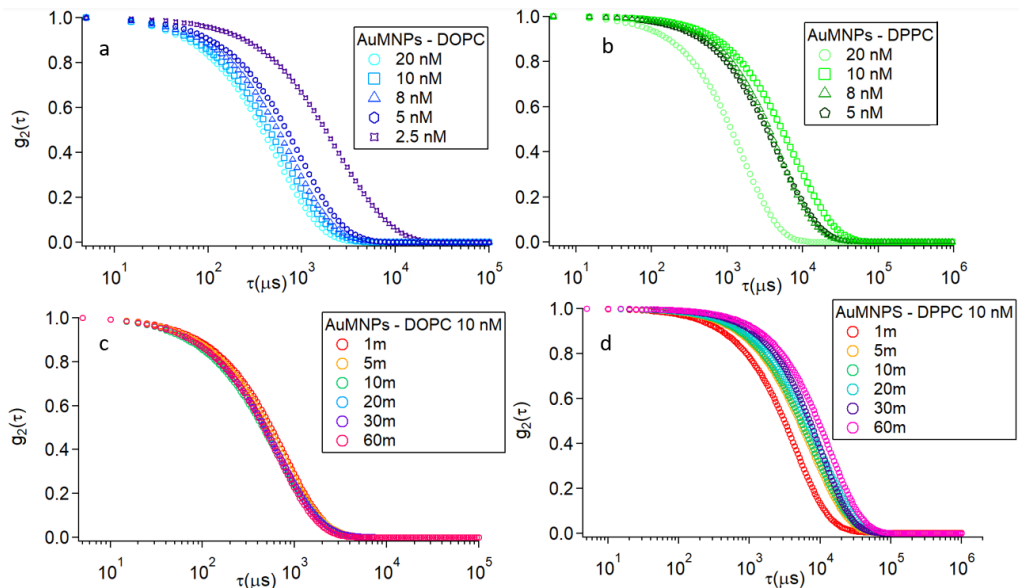


Figure 4: Autocorrelation functions collected for AuMNPs-DOPC (a) and AuMNPs-DPPC (b) hybrids as a function of the liposome concentration (20 nM, 10 nM, 8 nM, and 5 nM). Time evolution of the DLS curves of the AuMNPs-DOPC hybrids (c) and of the AuMNPs-DPPC hybrids(d).

In conclusion, according to an iterative interacting process extensively investigated for citrated Turkevich Frens AuNPs, the aggregative phenomenon of citrated AuMNPs on zwitterion vesicles is mainly driven by the liposomal membrane phase.

3.3 Contribution of small seeds and core-shell particles

DLS analysis, H-TEM, and Cryo-EM images demonstrate the coexistence of 8 nm Fe_3O_4 magnetic seeds and 40-50 nm AuMNPs. To understand if the membrane-templated aggregation on liposomes originates from the interaction of the small seeds, the core-shell particles, we separated the two populations and tested the interaction with DOPC vesicles. 1 mL of xx AuMNPs was centrifuged at 3000 rpm for 30 minutes. The supernatant is a water dispersion of the smaller particles and was used as obtained. The red precipitate containing the core-shell particles was further dispersed in 1 mL of milliQ water. The dispersions were incubated with DOPC liposomes and analysed through DLS measurements. Concerning the interaction

with the centrifugated particles, the analysis of the autocorrelation function displays the presence of two well-separated populations, centered at about 50 nm and at 120 nm, respectively matching the dimension of free dispersed AuMNPs particles and the characteristic size of DOPC liposomes. The ability of DLS to detect two different populations is a clear indication that the suspended particles possess different diffusion coefficients and are non-interacting objects. On the contrary, the interaction of the DOPC liposomes and the supernatant leads to the formation of hybrids with size and colloidal stability matching the one obtained for the AuMNPs. These experimental results reveal that the aggregative process is firstly triggered by the smaller ferric NPs and then involves the gold NPs, which aggregate modifying their plasmonic properties. On the contrary, in absence of small magnetic seeds, the interaction of the bigger particles with the lipid membranes is inhibited, as demonstrated by DLS and UV-vis spectroscopy.

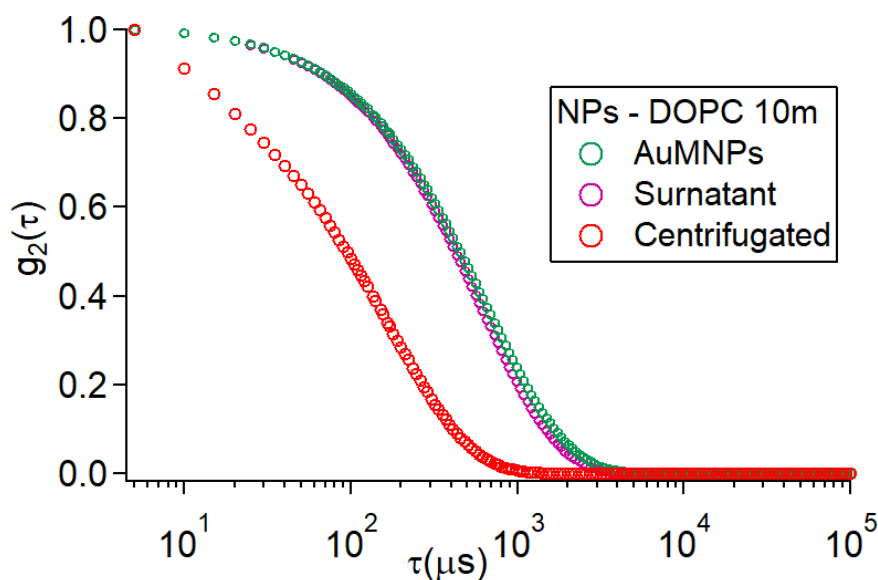


Figure 5:

3.4 Magnetic mobility of AuNPs-DOPC adducts

The last part of this work focuses on the investigation of the magnetic responsivity of the hybrids when an external magnetic gradient is applied. With this purpose, only the AuMNPs dispersion and stable DOPC-AuMNPs hybrids have been employed. In a dedicated experimental set-up developed at CNR-ISMN, a uniform solution of AuMNPs-liposomes or AuMNPs has been injected into a 500 μm -wide quartz capillary where a high-gradient magnetic field is generated by a couple of cubic permanent magnets placed symmetrically on the sides of the capillary. The transparent quartz capillary allows the optical investigation of the behavior of the magnetic particles under a magnetic field by a microscope-connected CCD camera. The injected batches of NPs-liposomes hybrids, characterized by different DOPC liposome concentrations (5 nM, 8 nM, 20 nM), are expected to display distinct magnetic moments due to the different number of NPs per vesicle. While the Brownian motion disperses the nanoobjects through the fluid volume, the external magnetic field generates a drift of the magnetic objects towards the highest field region (close to the external magnet). In the absence of hydrodynamic flows, the competition between the chaotic Brownian motion and the directional magnetic force dictates the time scale over which an equilibrium concentration of nanoparticles finally forms in the experimental system.

When injected in the capillary, the particles accumulate in the region closest to the magnet forming a disc-shaped dark area. The surface of this area grows over time with clearly distinct time dynamics for unconjugated AuMNPs and AuMNPs-liposome conjugates (figure 2.27a). For the conjugates with low liposome/AuMNP ratios (DOPC 5 nM and 8 nM), the disk grows until it reaches a seeming equilibrium condition in 1 and 3 hours, respectively. For the highest liposome/AuMNPs ratio (DOPC 20 nM) and the bare AuMNPs, the equilibrium condition is not reached within the times experimentally probed, and the surface area keeps growing.

Figure 2.27b displays the time evolution of the disc for all the investigated samples. As highlighted by inspecting the slopes of the linear fittings of the accretion of the

disc area during the time, the responsivity of the systems to the external magnetic field increases with decreasing the liposomes concentration. Reasonably, these experimental results can be explained by considering that increasing the number of magnetic particles per vesicle, the magnetic responsivity of the hybrids increases. Overall, albeit with very preliminary measurements, these results demonstrate that the membrane-templated aggregation of citrate-stabilized NPs can be instrumental in the production of novel nanomaterials possessing enhanced and controlled properties with respect to the starting precursors.

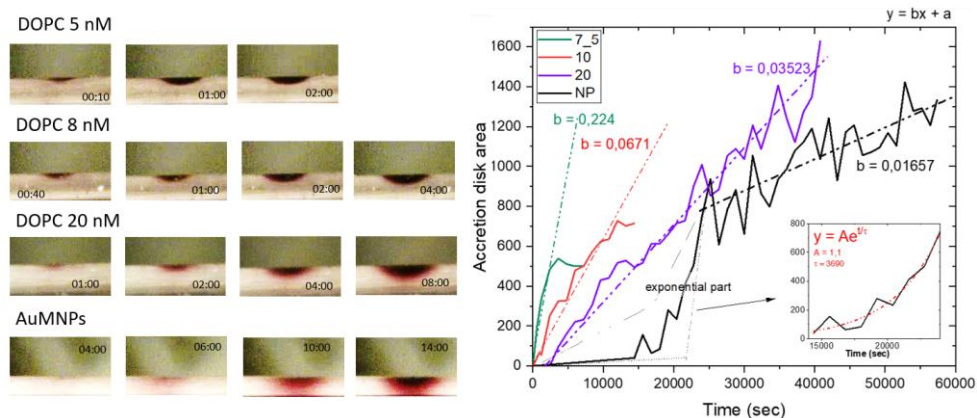


Figure 6: a) Representative collected images reporting the time evolution of the area of the accretion disk for AuMNPs-DOPC hybrids (DOPC 8 nM, 10 nM, and 20 nM) and AuMNPs; b) Accretion of the disk areas during the time. The slope of the linear fitting reflects the responsivity of the particles to the external magnetic field.

4 Conclusion

REFERENCES